The Dissertation Committee for David Keith Leigh Certifies that this is the approved version of the following Dissertation:

Improving Process Stability and Ductility in Laser Sintered Polyamide

Committee:

David L. Bourell, Supervisor

Joseph J. Beaman

Desiderio Kovar

Filippo Mangolini

Maria Juenger

Improving Process Stability and Ductility in Laser Sintered Polyamide

by

David Keith Leigh

Dissertation

Presented to the Faculty of the Graduate School of

The University of Texas at Austin

in Partial Fulfillment

of the Requirements

for the Degree of

Doctor of Philosophy

The University of Texas at Austin

May 2019

Dedication

I would like to dedicate this work to all the industrialists and academicians that have helped pioneer the field of additive manufacturing. These individuals, organizations and institutions have been dedicated to research in laser sintering and have helped champion a new era in sustainable manufacturing. This work has been made much easier through published research coupled with the economic drive of key industry partners that are committed to the real-world application of additive manufacturing.

Finally, to those that risked greatly and saw their dreams come true: Joe Allison, Andy Christianson, Rob Connelly, Greg Morris, and of course. . . Charlie Norton.

All hard work brings a profit, but mere talk leads only to poverty. Prov 14:23

Acknowledgements

First, I'd like to acknowledge the significant work that was done by the team at Harvest Technologies since the mid-1990s. This team developed processes and techniques and created a viable commercial venture that allowed for end-use laser sintered parts to be used in aerospace and showcase how 'rapid prototyping' was no longer a family of processes for concept models: especially Greg Reynolds, Ron Clemons, Barry Scott, Larry Thompson, John Broome, Bryan Ketterman, Caleb Farrell, Carlos Berumen, Jason Morgan and Alberto Perez. I'd also like to acknowledge the DTeaMer family that has remained a family even as they have been dispersed across a number of companies and industries. Thanks to Ben Fulcher for his assistance in the data analysis and programming, Joe LoBue for his work in helping me develop a viable thermal model, and Trevor Watt for general banter about the matter.

Finally, I'd like to thank fellow pilgrims that have been traveling the same journey from different parts of the world to include Dave Bourell, Joe Beaman, Tim Gornet, Tom Starr, Phill Dickens, Richard Hague, Neil Hopkinson, Candice Majewski, Chris Tuck, Gideon Levy, Manfred Schmid, Rethia Williams, Jeff DeGrange, Kent Firestone, Sheku Kamara, the SFF Symposium, SME RAPID community, and the wonderful AMUG family.

Abstract

Improved Process Stability and Ductility in Laser Sintered Polyamide

David Keith Leigh, PhD
The University of Texas at Austin, 2019

Supervisor: David L. Bourell

The desire to manufacture production parts using additive manufacturing has created an increased demand on the laser sintering technology to supply this need. A significant issue in laser sintered polymers is the variability of mechanical properties from build-to-build and the inability to determine the success or failure of the production process until the production builds are complete. Interlayer ductility of parts produced in the laser sintering process has been shown to be uncontrolled and unpredictable. This research focuses on improving interlayer ductility and establishing a baseline for modeling the time-temperature-transformation of production-grade, laser-sintered polymers.

The background shows that there has been a significant amount of research to map processing parameters to mechanical properties and that industry has been focused on recording processing parameters and mechanical properties as part of the quality record. The research shows trends in mechanical performance that are not adequately explained with current analytical techniques. The experimental research characterized the thermal attributes of the laser sintering process using onboard sensors, production build data, external thermal cameras, and in-situ thermocouples to map the thermal profile of a complete laser sintering build.

This information, used in conjunction with an array of over 80,000 production build tensile data points, provides the basis for a thermal model for laser sintered polymers. Current laser energy models in laser sintering are incomplete and do not consider many processing parameters available in the laser sintering process, focusing primarily on the build surface temperature and the laser energy applied to the part region. A more complete thermal model must also account for the energy exposure during the build. The thermal process model is developed to integrate the thermal history during the build and cooldown cycle as a metric of success. It will be shown that improved and more predictable ductility performance is achievable, and that a thermal process model can be used to characterize the energy input required over time to achieve optimal results. Ultimately, increased reliability in laser sintered polymer parts will increase their usage in commercial applications.

Table of Contents

List of Tables

List of Figures

List of Equations

1.0 INTRODUCTION

1.1 Dissertation Context

The central theme of this work involves the use of the polymer laser sintering process in a production environment. Laser sintering is one of the technologies in the powder bed fusion category of additive manufacturing and is a leader for end use parts applications due to its versatility and ability to process polymers, ceramics, and metals. Because of the wide range of material processing capabilities, laser sintering has opened the use of additive parts in many industrial applications.

Most of the work done regarding the maximizing of mechanical properties for end-use laser sintered parts has focused on the processing of the build layer. The work done in this study will illustrate the need for an understanding of the full thermal processing lifecycle of the laser sintered polymers. The background presented will show that fracture-limited ductility is a primary contributor to poor mechanical properties. This work will further illustrate that interlayer porosity at the interface boundary layers is a primary contributor to brittle fracture and limited ductility.

While prior work done to characterize laser sintering processing has focused on the build layer, the effect of elevated temperatures during the build has been largely ignored. ***The hypothesis of this work is that the energy required to melt coupled with the thermal profile of the build region are predictors of mechanical property performance.*** Theories on the physics of sintering can be used along with a detailed thermal model to provide a quantitative measure that can help determine mechanical property performance. Ultimately, a technique can be developed and used to improve machine architecture and the productivity and performance of laser sintering in a production environment.

1.2 Dissertation Structure

A full outline of the content of this dissertation is found in this section with a brief overview of preliminary and primary investigations and research objectives. There has been an attemptby the research community to quantify a thermal model for the energy required to create stronger laser sintered parts. While this model has become more sophisticated over time, the results and conclusions have been insufficient. Most of the literature quantifies the energy required to make stronger parts as defined primarily by yield stress. (Gibson I. a., 1997) (Caulfield, McHugh, & Lohfeld, 2006) (Majewski, Zarringhalam, & Hopkinson, 2008) (Starr, Gornet, & and Usher, 2011) The yield stress of laser-sintered nylon polymers is equivalent with other manufacturing technologies like compression molding, roto-molding, and injection molding. This previous work has stopped short of addressing parts that appear to be good (sufficient yield strength) yet fail when under the stress of real-life applications (brittle fracture). When measuring mechanical properties, poor part quality can be masked if elongation-at-break is not considered. The catalyst of the preliminary research is to understand the failure mechanisms that contribute to fracture-limited ductility.

1.2.1 PRELIMINARY INVESTIGATION AND RESEARCH OBJECTIVES

The key factors that were investigated during preliminary research were measurement and analysis of tensile specimens that were produced with laser sintered polyamide 11 (“nylon”) in a production environment under varying processing conditions. (Leigh, Fracture Behavior in Laser Sintering, 2011) The key research objectives were to:

1. Build tensile specimens with varying processing parameters and evaluate the modes of failure.

2. Classify the failure modes seen in laser sintering (delamination, fracture limited ductility and full plasticity failure).
3. Create a physical model of the interlayer bond and the coplanar porosity observed in laser sintered parts to correlate levels of porosity to failure modes.
4. Correlate the relative porosity of the interface boundary layer to the relative elongation.

1.2.2 PRIMARY INVESTIGATION AND RESEARCH OBJECTIVES

While the preliminary results identified the primary causes of fracture limited ductility as interlayer or interface boundary layer porosity, it stopped short of identifying processing parameters that could mitigate the limited ductility. During the preliminary research, it was observed that there was a correlation between time at temperature and mechanical properties. Of interest were tensile specimens built with the exact same processing parameters in the same location in a build yet had improved mechanical properties based on the depth of parts in the build. Stated a different way, parts were observed to possess improved mechanical properties if they were exposed to an elevated temperature for a longer time. The research objectives of this primary work are to:

1. Evaluate a production dataset of roughly 80,000 samples of laser-sintered nylon polyamide 11.
2. Correlate the elongation-at-break results with processing parameters and various levels of thermal exposure over time.
3. Thoroughly map the thermal characteristics of a standard polymer laser sintering production build using production processing sensors, an external thermal camera

to map the build surface temperature, and supplementary thermocouples to map the temperature of the part cake.

4. Build tensile specimens in a standard polymer laser sintering production build as a control build to correlate experimental data to the production dataset and use it as a baseline for further tests.
5. Modify the system architecture to create an elevated temperature over the full build processing time.
6. Build tensile specimens in the modified machine and compare the data to the control build.
7. Establish a thermal model of the polymer laser sintering process that can be used to simulate the thermal process over time of any voxel.
8. Adapt a formula derived from the Frenkel Theory of Sintering for use in correlating thermal-time exposure to mechanical properties.

Chapter 1	Introduction
Chapter 2	Background
Chapter 3	Hypothesis
Chapter 4	Theory and Modeling
Chapter 5	Experimental
Chapter 6	Results
Chapter 7	Discussion
Chapter 8	Conclusions
Chapter 9	Recommendations for Further Study
Appendix A	Production Case Study Statistical Data
Appendix B	MATLAB Program Source Code
Appendix C	Production Processing Parameters
Appendix D	Production Build Log Data
Appendix E	ANSYS Fluent Thermal Settings
Appendix F	ANSYS Fluent Macro Code

Table 1: Dissertation Structure

2.0 BACKGROUND

2.1 Early Rapid Prototyping Systems and Processes

A family of rapid prototyping processes were invented and developed in the late 1980s and early 1990s. These processes took advantage of new computer-aided drafting/design programs enabled by the ever-expanding computing power of a desktop system used by design engineers. (SME Staff, 2013) These new manufacturing processes used integration techniques to process digital solid models and then replicate the digital model with the layer-by-layer addition of materials to create a three-dimensional solid. These systems utilize three major steps to create the three-dimensional solid.

1. The first step of the process is the computational evaluation of a solid model and the subsequent creation of a set of cross-sectional vector fields referred to as "slices." Each slice has a field of x-y vectors that represent the cross-sectional area of the model, with the aggregate total of these slices making up the complete 3-dimensional object. Each slice is prepared based upon a predetermined "layer thickness" which is typically 0.004 inches to 0.010 inches. An illustration of the slicing algorithm process can be seen in Figure 1.

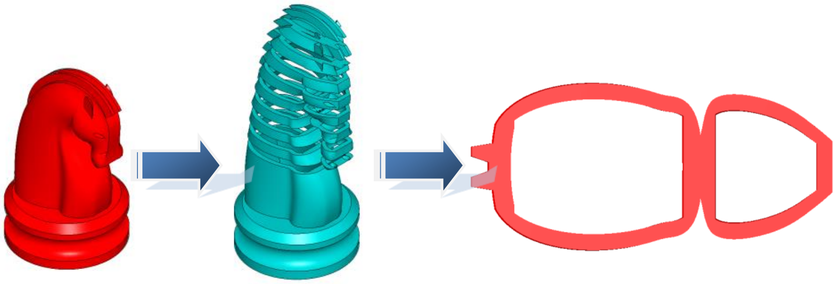

Figure 1: Illustration of CAD Model Slicing (Leigh, Fracture Behavior in Laser Sintering, 2011)

2. The second step of the process is to transfer each of the slices onto a substrate to make a three-dimensional representation of the solid model. The major systems that were used in the initial days of rapid prototyping are described in this chapter. The general process is to melt, fuse, polymerize, jet, or extrude these two-dimensional layers in sequence to build up, layer-by-layer, a representation of the intended designed part.
3. The final process step is to repeat this integration and formation step until complete. To completely build the full three-dimensional part, layers must continuously be sliced and fused together. The layer thickness of the process determines the thickness of the digital slice that is extracted from the digital model – typically represented by an .stl file which was developed by 3D Systems, Inc. and has become the de facto standard 3D printing file format (Jacobs, 1996)

It is important to understand the evolution of rapid prototyping to additive manufacturing with many of the early successes, industry adoption, and academic works being intertwined. The process of converting a CAD model into a single slice (Step 1 above) and the repeating of these processes seem straightforward, so most of the work has focused on the actual differentiated step of how a single layer is created in the respective rapid prototyping process.

The following descriptions of three early rapid prototyping systems are a summary obtained through http://www.efunda.com/processes/rapid_prototyping/. This engineering resource site has captured the narrative descriptions of these processes from the 1990s and helps show the initial justification for the use of laser sintering in end-use parts. (eFunda, Inc. , 2018)

2.1.1 STEREOLITHOGRAPHY (VAT PHOTOPOLYMERIZATION)

Stereolithography (SLA®) was the earliest of the rapid prototyping systems developed, making its debut in 1986 in Valencia, CA under the umbrella of 3D Systems Inc. This early system contributed to the narrative by creating a 3D communication file (.stl) that was used by the system to create the individual slices to be used to build the part. The process uses a vat of photopolymer, a permeable metal stage, and a UV laser to create parts by curing the top surface of the resin as seen in Figure 2.

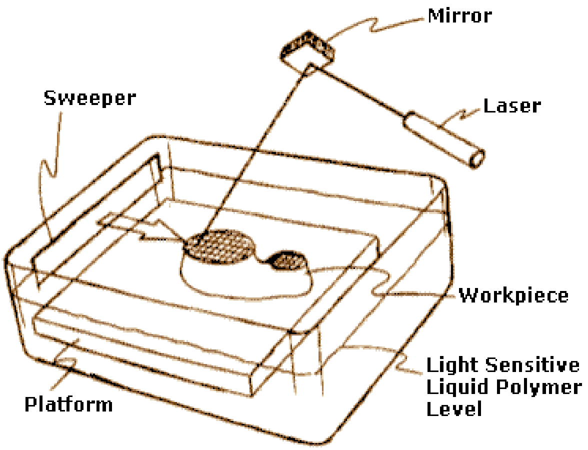

Figure 2: 3D Systems Stereolithography Process (eFunda, Inc. , 2018)

Stereolithography is still widely used today as an industrial prototyping and pattern system as well as a critical tool in the production of unique medical end-use parts. Some of the common applications used today include patterns for dental aligners, investment casting patterns, short-run tooling patterns, customized in-ear hearing aid shells, and medical and surgical planning models.

The sequence of steps in the stereolithography process is further illustrated in Figure 3. The process is carried out primarily by curing the top surface of the photopolymer with sufficient energy to get a solid part. Since the layers are small compared to the surface tension of the resin, a leveling mechanism must be used to apply resin to the top of thick cross sections and adequate time is required for the top surface to reach equilibrium. Once the part is completed, secondary cleaning and curing steps are required to get a useful part.

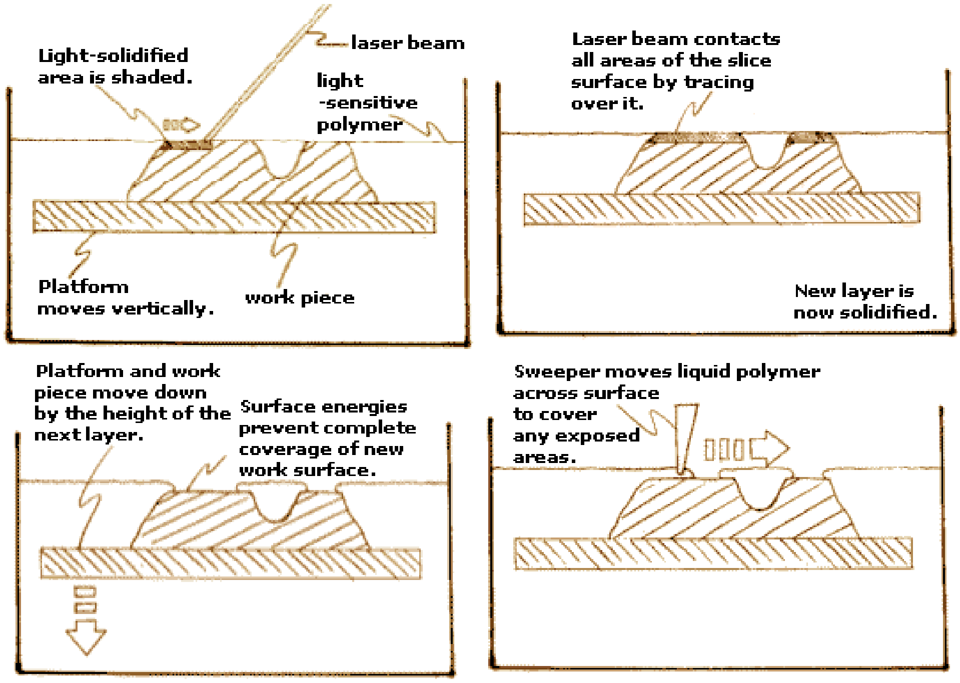

Figure 3: 3D Systems Stereolithography Process Sequence (eFunda, Inc. , 2018)

The primary limitations to the stereolithography process are the inherent strength of the photopolymer and the long-term stability and creep associated with these polymers. In recent years, this process has expanded its application base through companies like FormNext with the use of low-cost DLP light engines or the use of more functional photopolymers through companies like Carbon to address the demands of end-use consumer products.

2.1.2 SELECTIVE LASER SINTERING ® (POWDER BED FUSION)

A more detailed description of the laser sintering process (seen in Figure 4) will follow in Section 2.3 Laser Sintering, but the following from the efunda website illustrates the motivation for using laser sintering in high value and low volume end-use applications: considerably stronger than SLA; sometimes structurally functional parts are possible; ability to approximate common engineering plastics, and living hinges are possible with the thermoplastic-like materials. (eFunda, Inc. , 2018)

The site continues to illustrate the advantages of this 'prototyping' process that continued to fuel the development of production standards to use this digital technology in a new field of additive manufacturing:

> *Its chief advantages over Stereolithography (SLA) revolve around material properties. Many varying materials are possible, and these materials can approximate the properties of thermoplastics such as polycarbonate, nylon, or glass-filled nylon. (eFunda, Inc. , 2018)*

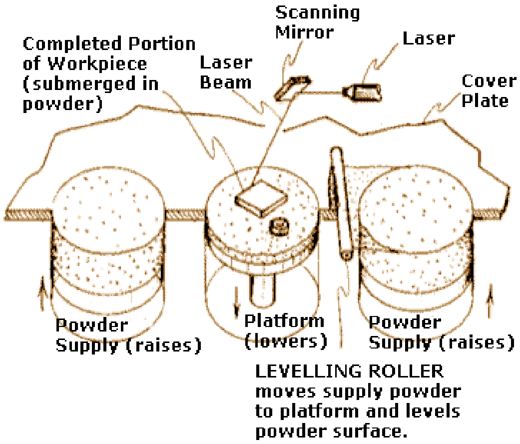

Figure 4: Illustration of the Laser Sintering Process (eFunda, Inc. , 2018)

2.1.3 FUSED DEPOSITION MODELING – FDM (MATERIAL EXTRUSION)

The FDM process was invented in 1988 by Scott Crump and commercialized through Stratasys of Eden Prairie, MN. The fundamental process involves extruding a thermoplastic material through a "print head" onto a substrate as seen in Figure 5. Multiple scan tracks are extruded and cool on the substrate that make up the individual layer. The part is created, and subsequent layers are added as the platform indexes away from the print head. Initial issues with layer-to-layer adhesion and melt quality were a large detractor and left FDM in the middle of many of the processes, not as accurate as SLA and not as strong as laser sintering.

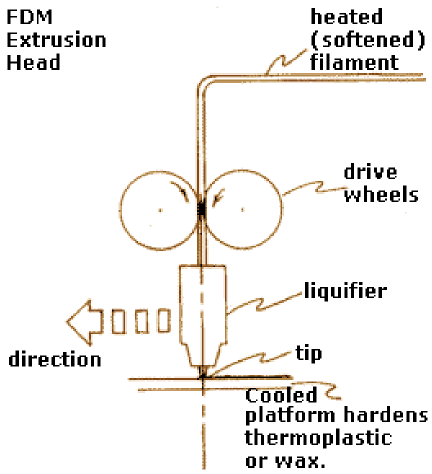

Figure 5: Illustration of Fused Deposition Modeling (FDM) (eFunda, Inc. , 2018)

A key advantage that started to arise was the ability to run an FDM machine in an office environment without the need for a large ecosystem of support equipment. While the applications were initially geared towards concept models, continued improvements in thermal management of the build chamber along with material development and extruder improvements have enabled the FDM process to be have the highest install base in the industry due to the broad adoption of the small desktop printers with pricing under $3,000 per unit.

2.2 Additive Manufacturing

Additive manufacturing is a family of manufacturing processes that use digital solid models to create three-dimensional solid by various layer-by-layer techniques. The use of the traditional prototyping techniques as a foundation for a new manufacturing solution has required a significant amount of effort to define industry standards to include terminology, product specifications, material specifications and process specifications. The success of polymer and metal laser sintering as described in the previous section and in multiple publications has provided enough justification for several companies and organizations to spearhead this early effort. (Wohlers, 2018) (Gebhardt, 2011) (Bourell, Beaman, Ming, & Rosen, 2009) (Levy, 2010) As a result, there has been publication of multiple standards, including the ISO/ASTM standards and the ASME draft standard for *Product Definition in Additive Manufacturing* on January 2018, which can be seen in Figure 6. Included in the standards is a classification of seven major categories of additive manufacturing: vat photopolymerization, material jetting, binder jetting, material extrusion, powder bed fusion, sheet lamination, and directed energy deposition. (ASTM F42 Committee) (F42.91, 2012)

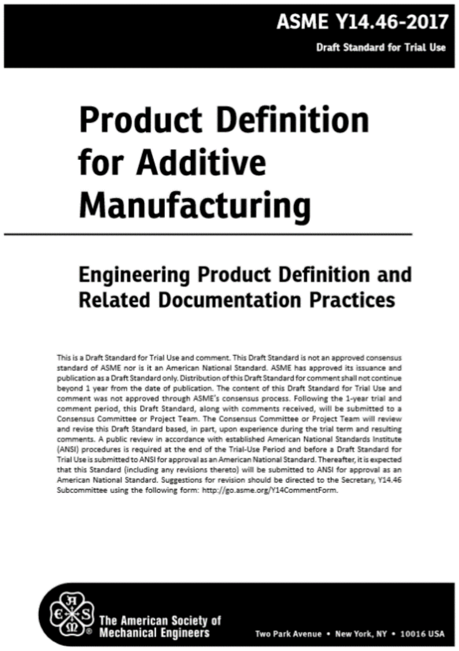

ASME Y14.46-2017
Draft Standard for Trial Use

Product Definition for Additive Manufacturing

Engineering Product Definition and Related Documentation Practices

This is a Draft Standard for Trial Use and comment. This Draft Standard is not an approved consensus standard of ASME nor is it an American National Standard. ASME has approved its issuance and publication as a Draft Standard only. Distribution of this Draft Standard for comment shall not continue beyond 1 year from the date of publication. The content of this Draft Standard for Trial Use and comment was not approved through ASME's consensus process. Following the 1-year trial and comment period, this Draft Standard, along with comments received, will be submitted to a Consensus Committee or Project Team. The Consensus Committee or Project Team will review and revise this Draft Standard based, in part, upon experience during the trial term and resulting comments. A public review in accordance with established American National Standards Institute (ANSI) procedures is required at the end of the Trial-Use Period and before a Draft Standard for Trial Use is submitted to ANSI for approval as an American National Standard. Thereafter, it is expected that this Standard (including any revisions thereto) will be submitted to ANSI for approval as an American National Standard. Suggestions for revision should be directed to the Secretary, Y14.46 Subcommittee using the following form: http://go.asme.org/Y14CommentForm.

The American Society of Mechanical Engineers
Two Park Avenue • New York, NY • 10016 USA

Figure 6: ASME Y14.46 Product Definition for Additive Manufacturing (The American Society of Mechanical Engineers (ASME), 2018)

The creation of these standards and an adherence by industry to a set of processes that include rigorous machine calibration and tensile specimen data collection have allowed early industrialists to partner with academia to quantify these previously unknown technologies.

2.3 Laser Sintering

The laser sintering process uses thermal energy to consolidate powder into a predetermined shape commonly referred to as a part. The first step of the laser sintering process is to preheat a bed of powder, commonly a polyamide (“nylon") material with an average particle size of 50 microns. Once the powder is heated to a sufficient temperature and the slice file is created, a directed energy beam (usually a CO_2 laser) scans the vector field on the prepared bed of powder. The fused layer reproduces the cross-section generated by the vector field (or slice) which can be seen in the system schematic in Figure 7 and the photograph in Figure 8.

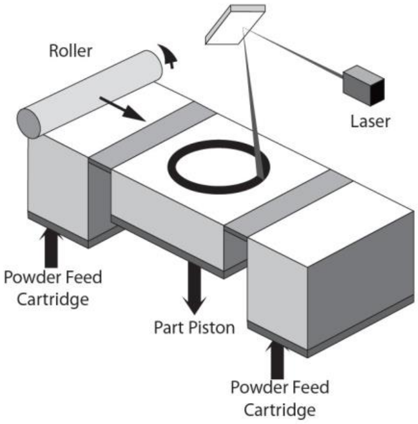

Figure 7: Illustration of Laser Sintering Process (Leigh, Fracture Behavior in Laser Sintering, 2011)

A finished part is created once feedstock powder is added to the process so that subsequent “slices” can be fused together. Each build step, a thin layer of powder equal to the predetermined layer thickness is added, heated, and subsequently fused to prior layers to create a solid physical model, pictured in Figure 8. Darker areas in this photograph have been scanned by the laser while the lighter sections are unsintered powder.

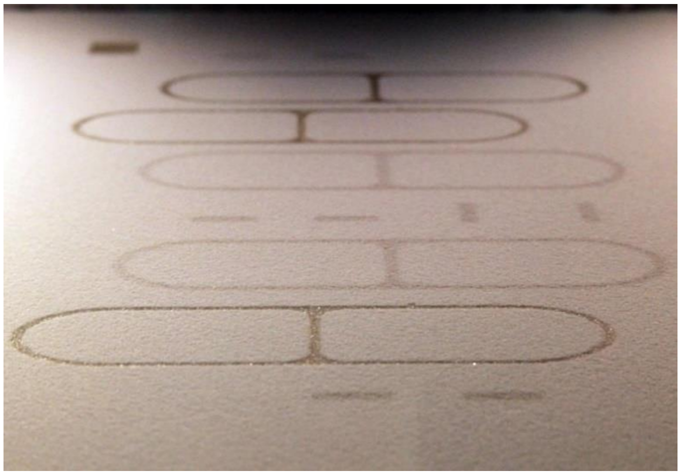

Figure 8: Photograph of a Laser Sintering Powder Bed (Leigh, Fracture Behavior in Laser Sintering, 2011)

The use of additive manufacturing and laser sintering in particular for low and medium volume production has become more important due to the cost savings associated with bypassing expensive tooling. (Ruffo, Tuck, & Hague, 2006) The laser sintering process has become more common in the production of end-use parts in various applications and has allowed for streamlined design, decreased time to market, more efficient engineering changes, and the ability to design for function rather than manufacturability. While there may be many benefits for certain applications, there are significant challenges that must be addressed prior to a broad acceptance of this technology. The key challenge is the limited amount of theoretical or experimental science as well as detailed materials databases specific for the use of laser sintering as a manufacturing process. The use of laser sintered parts for end-use production has increased the scrutiny of the process but has channeled corporate funding towards the end of creating a stronger knowledge-base.

2.4 Formation of Layers in Laser Sintering

Figure 9 is a graphical representation of the raw material powder bed. While the average particle size of the polyamide material is 50 to 80 microns, there is a distribution range of fine and coarse particles in a randomly packed bed. To minimize part distortion, the powder bed is preheated to a point just below the melting temperature. If the feedstock in the powder bed is too hot it will completely melt and there will be no distinction between the scanned area and the powder. If the particles are too cold, they will not have sufficient internal energy to allow for a full melt. A temperature regime where the sintered material solidifies between subsequent layers undergoes dimensional distortion when the processed layer is fused to previous layers that have already undergone shrinkage. This adhesion creates residual stresses as the processed layer shrinks at a different rate than previous layers.

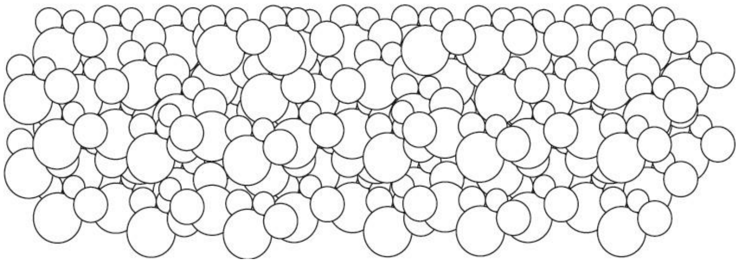

Figure 9: Cross Sectional Illustration of a Laser Sintering Powder Bed (Leigh, Fracture Behavior in Laser Sintering, 2011)

In an ideal build, the powder bed is pre-heated and the laser will scan the subject cross-section using a field of x-y vectors at a prescribed speed, spacing, and laser power. These settings are optimized to yield an ideal melt pool such that there is enough energy to have a full melt without losing precision, seen in Figure 10. If the laser energy applied is too great, detail and precision are lost (analogous to writing on tissue paper with a large permanent marker). If too little laser energy is applied, there will not be enough depth of penetration to melt the exposed layer to the previous layers.

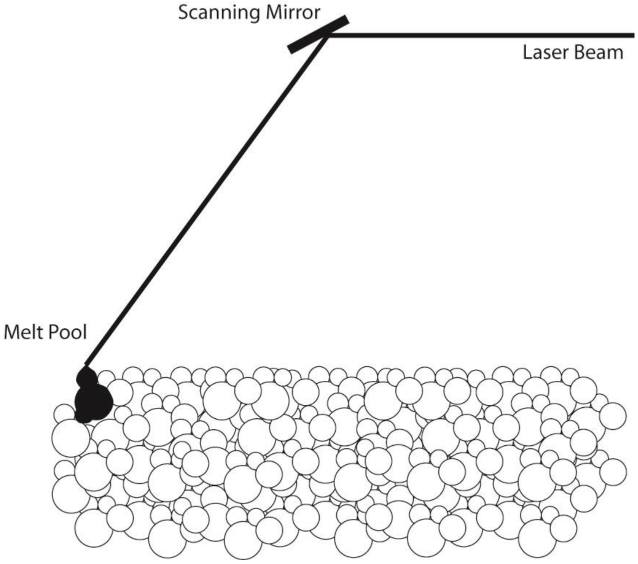

Figure 10: Melt Pool Generated on the Laser Sintered Powder Bed (Leigh, Fracture Behavior in Laser Sintering, 2011)

2.5 Process Variability and Process Limitations

A significant limitation to any layer-based additive manufacturing process is the anisotropic nature of the process. In this case, a single layer (typically 0.004" thick) is fused to the previous layer. The properties within this layer are consistent, but the bond between layers is typically weak. Intralayer bonding is achieved as the laser passes across the pre-heated powder causing particles to melt and flow together in the creation of a molten region defined by the slice. Interlayer bonding is more challenging for three primary reasons: the previous layer that is being adhered to has had time to cool, the thin layer of powder that has been added serves as a thermal insulator and can inhibit laser penetration and laser energy is absorbed and dissipated at a higher rate near the surface.

This is discussed by Caulfield in “Dependence of mechanical properties of polyamide components on build parameters in the SLS process” and illustrated in Figure 11. (Caulfield, McHugh, & Lohfeld, 2006) This work showed that fracture followed the layer lines where the bond was weaker between layers. Layer lines in Z-Axis oriented parts are in the X-Y plane as illustrated in Figure 11.

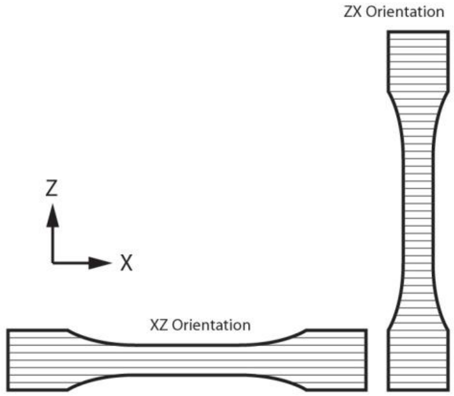

Figure 11: Schematic of Layer Interfaces in Multiple Part-build Orientations (Leigh, Fracture Behavior in Laser Sintering, 2011)

As a quality assurance step during the production of end-use parts, it is common to quantify build performance through the placement of standard ASTM D638 tensile specimens oriented in the x-axis (left to right), y-axis (front to back), and z-axis (vertical build direction). (ASTM Subcommittee D20-10, 2018) It is generally observed that there is little to no variation between the x and y axes specimens but the z-axis specimens exhibit a significantly lower elongation-at-break (EAB) than the x and y axis specimens.

The primary cause of the lower mechanical properties in the z-axis can be attributed to layer-to-layer adhesion (interlayer bonding). Several papers have been dedicated to the characterization and optimization of the laser sintering process in relation to z-axis anisotropy. In a presentation at the Additive Manufacturing User’s Group in 2013, Dr.

Manfred Schmid presented a comprehensive Ishikawa (fishbone) diagram on factors that influence laser sintering part quality, which can be seen in Figure 12. (Schmid M. L., 2013) Several key factors that have been observed to contribute to poor interlayer bonding in the production of laser sintered end-use parts are:

- Large layer size – The powder insulates the thermal energy and prevents the energy of the beam from penetrating to the prior layer.
- Poor powder quality – Used powder will yield a high melt-flow and higher molecular weight. This is primarily caused through thermal aging and cross-linking of the polymer. The result of the high melt-flow is a polymer that is slow to melt and has a high viscosity. This, in turn, results in voids produced between layers.
- Poor thermal control – If the powder bed is processed in a way that the temperature is too low or is cooled at a high rate, it will inhibit the formation of a melt pool that penetrates the previous layer. The result can be weak layer-to-layer adhesion as well as dimensional distortions.
- Low laser energy – High scan speed, low laser power, and large spacing between scan vectors (scan spacing) can lower the overall laser energy delivered to the powder bed. This decreased energy is not sufficient to penetrate the current layer and create strong layer-to-layer adhesion.

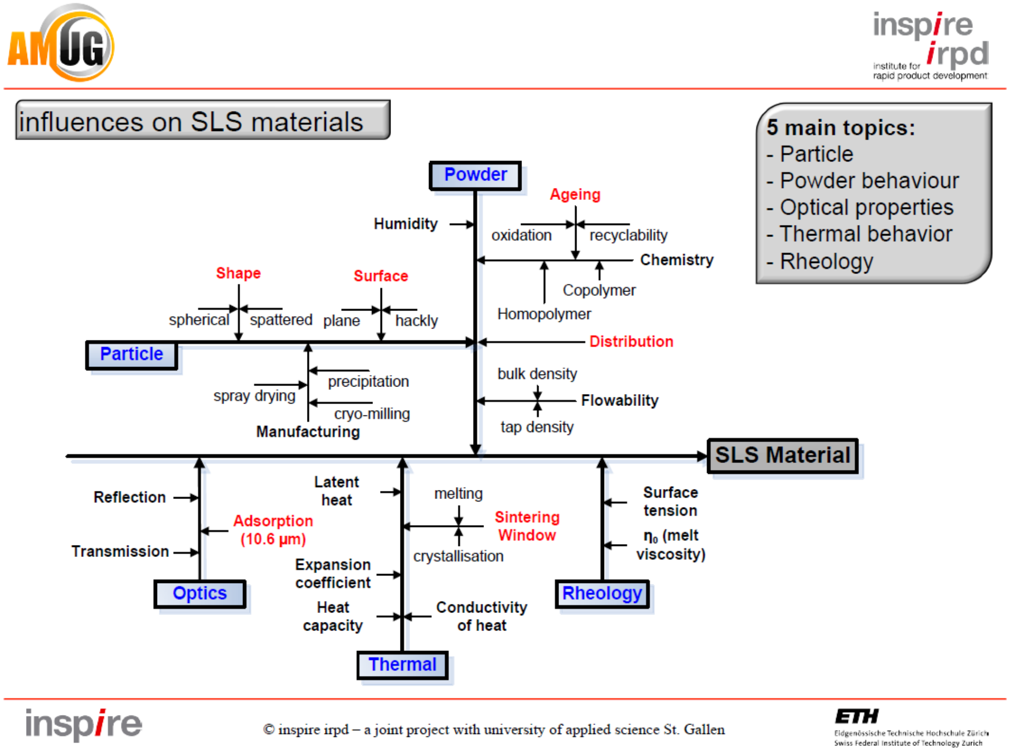

Figure 12: Influences on SLS Part Quality (Schmid M. L., 2013)

2.6 Process Optimization and Characterization

Laser sintering became a broadly used additive manufacturing process in the early 1990s with the introduction of Duraform® PA, a Polyamide 12 material. Christian Nelson published an article in 1995 speaking to the need for process and material optimization to improve part accuracy. (Nelson, McAlea, & Gray, 1995) The primary application of laser sintering in the early stages of development was functional prototypes and concept models with the chief competitor being 3D Systems™ Stereolithography (SL) process. While laser sintering held an edge over the SL process in material properties, the SL process had become the de facto standard in prototyping and held an edge in accuracy. The conclusions that Mr. Nelson made at the time were:

- Use of better galvanometers to control the laser and scanners will increase accuracy and repeatability.
- Optimization of scanning parameters can improve surface finish, accuracy, and repeatability.
- Optimized powder particle distribution can yield surface finish comparable to those made with liquid-based techniques. (Nelson, McAlea, & Gray, 1995)

2.6.1 MATERIAL FEEDSTOCK OPTIMIZATION

With increased utilization of the laser sintering process in the 1990s, there became a focus on process optimization and repeatability regarding the use and re-use of raw material. Poor accuracy, surface finish, and part quality were seen in parts being made with Duraform® PA due in large part to inconsistent material feedstock due to the thermal degradation of the material. There were several schools of thought that were proposed to mitigate this issue:

- David K. Leigh of Harvest Technologies (currently Stratasys Direct Manufacturing) developed a steady-state feedstock blend of used and virgin material based on quantified mechanical properties and visual inspection. (Leigh & Gornet, Laser Sintering Powder Studies)
- Timothy J. Gornet of the University of Louisville developed a way of quantifying the melt flow rate and correlating this measurement to a usable standard. Virgin powder would be added to the powder feedstock to bring it to a specific melt flow reading. (Leigh & Gornet, Laser Sintering Powder Studies)

- John Choren proposed varying manufacturing parameters based on the feedstock powder degradation, increasing the energy applied to aging material feedstock. (Choren, Gervasi, Herman, Kamara, & Mitchell, 2001)

Based on a paper written by Choren in 2001, it was noted that thermal processing parameters were stable but that laser power had to be increased as material continued to be reused. (Choren, Gervasi, Herman, Kamara, & Mitchell, 2001) The mechanical properties achieved are shown in Figure 13 with the elongation-at-break absent from this data. In addition to this work, a 2008 paper by Yusoff showed the effects of powder degradation on surface finish. (Yusoff & Thomas, 2008) These two published reports along with work by Leigh and Gornet illustrate the effect of powder melt flow (molten viscosity) on material properties, machine parameters, and part quality. (Leigh & Gornet, Laser Sintering Powder Studies)

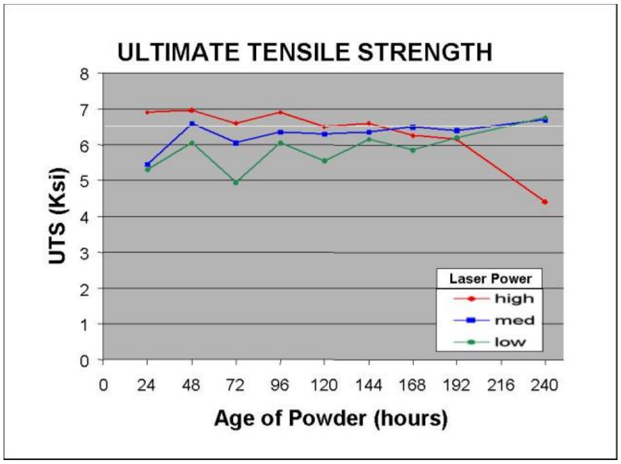

Figure 13: UTS Data from 2001 Choren Powder Life Study (Choren, Gervasi, Herman, Kamara, & Mitchell, 2001)

2.6.1.1 Evaluation of Melt Flow Rate on Specimen Failure Using Injection Molding

Continuous exposure of the unsintered material to the elevated thermal environment causes cross-linking across the polymer chains and contributes to decreased physical and mechanical properties. As the material undergoes thermal aging, the viscosity of the material is seen to increase. This can be evaluated using a melt-flow measurement tool, as shown in Figure 14. (Drummera, 2015)

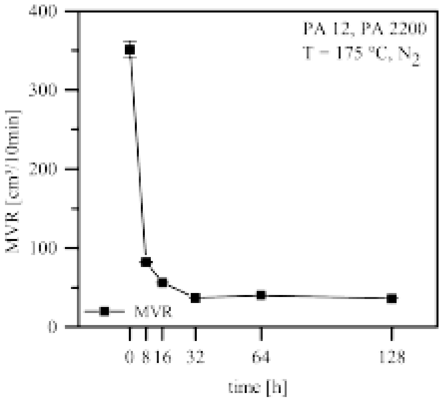

Figure 14: Effect of Thermal Aging on Melt Flow Rate (MVR). (Drummera, 2015)

An unknown is whether thermally degraded material which is unfit for laser sintering is either usable or unusable in other processes such as injection molding. To test this, unusable polyamide powder was segregated from production at Harvest Technologies (currently Stratasys Direct Manufacturing) and its viscosity (melt flow rate) evaluated. This ‘bad’ polyamide powder was then processed in a BOY laboratory injection molding machine at The University of Texas at Austin to produce several tensile specimens.

Standard injection molding parameters from a materials handbook were used to create fully dense ASTM D638 tensile specimens in an attempt to assess the impact of material degradation when processed using injection molding equipment. (ASM

Engineering Materials Handbook) (ASTM Subcommittee D20-10, 2018) The used material feedstock powder was poured directly into the feed hopper of the injection molding machine and processed manually. An image of the tensile bar after testing can be seen in Figure 15 and the results of the tensile tests are presented in Table 2.

Sample	σ_y (psi)	UTS (psi)	EAB %	Fracture Mode
1	3884	5572 psi	>50%	Ductile
2	3937	5530 psi	>200%	Ductile

Table 2: Injection Molded Tensile Results of Previously Used PA-12 (Leigh, Fracture Behavior in Laser Sintering, 2011)

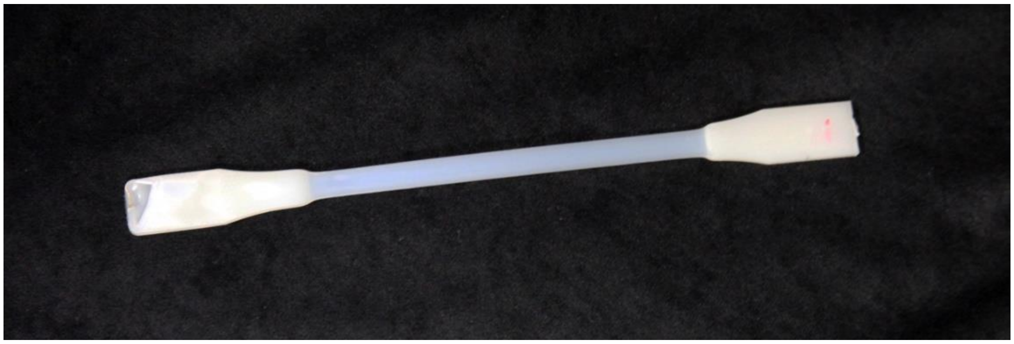

Figure 15: Photograph of Injection Molded Specimen (Leigh, Fracture Behavior in Laser Sintering, 2011)

Both specimens exceeded the range of the extensometer (50%) with one specimen reaching the mechanical limits of the load cell. Based on the tensile data acquired, it is apparent that degraded powder does not yield poor mechanical properties when injection molded. This test provides a good degree of confidence that the degradation of mechanical properties in the laser sintering process is not an intrinsic material property defect but a property that affects the processing of the polyamide material in laser sintering. The melt flow index (MFI) of new powder is generally a value of 30g/10sec which corresponds to a low viscosity and relatively high melt flow rate. The material used in the injection molding of tensile specimens was previously used material with an MFI measurement of 1g/10sec which correlates to a very low flow rate with a high viscosity.

2.6.1.2 Summary of Feedstock Optimization

Summarizing the feedstock optimization with respect to the Ishikawa diagram in Figure 12, three of the five broad influencers on laser sintering part quality are present in the feedstock alone: particle shape, powder, and rheology. While feedstock can vary and will degrade after repeated use, this negative affect can be mitigated by having a rigorous feedstock management protocol. **A stable feedstock serves as the foundation for optimizing and characterizing the laser sintering process.**

2.6.2 OPTICAL PATH OPTIMIZATION

One of the five areas of influence expressed in Figure 12 is related to optics. The optical path of a laser sintering system is standardized and has no direct process variables that can be managed by the end user. While optical issues such as the fouling of optics will affect the part quality, the control over these factors is limited. Production facilities mitigate the issues of optics by having the following quality control steps present:

1. Measurement of the laser power at multiple areas of the part bed.
2. Measurement of the laser power prior to and following a build to quantify laser power loss due to fouled optics.

3. Measurement of the laser spot size and beam shape are illustrated in Figure 16 and Figure 17. The shape of the beam and focal point on these figures are measurements of a fiber laser used in metal laser sintering but illustrate the sharp focus of a gaussian beam in Figure 16 and the "waist" of the beam in Figure 17. The term waist is used to illustrate the region where a converging focal point starts to diverge and represents the smallest focal point achievable for the laser and the given set of optics.

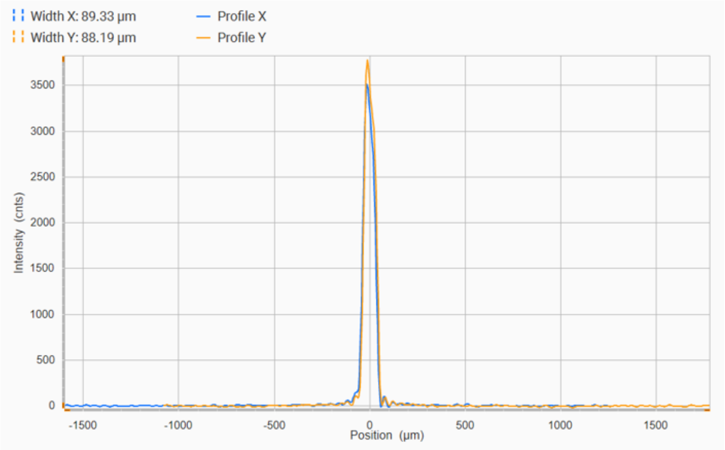

Figure 16: Laser Beam Profile

4. Verification of scanner insures that the theoretical coordinates used by the build software are consistent with the actual results at the build plane. Laser power calibration maps a given system's laser power to a control percentage used by the software. Percentage power is not useful as an operational control parameter, so look-up calibration tables must be maintained on each machine.

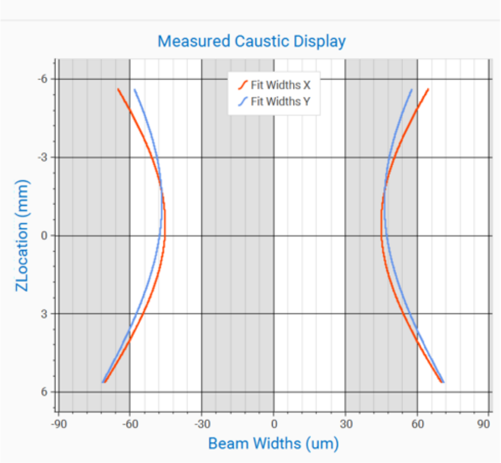

Figure 17: Laser Beam Shape

The laser sintering systems used for this work are manufactured by 3D Systems and utilize a z-focusing optic to maintain a constant focus across the part bed. There is not an active feedback system that allows for closed loop control of the laser, so laser power calibration, verifying optical path clarity, and regular verification of the beam quality and focus are critical in maintaining a multi-platform production environment. When these processes are in place, the thermal effect of the laser energy can be simplified to a measurement such as power density which will be explained in the next section.

2.6.3 THERMAL ENERGY CHARACTERIZATION

The final factor that can influence part quality that is illustrated in Figure 12 is the thermal response of the material and the thermal energy applied to a build region and the subsequent part or parts. Since there is an inextricably linked relationship between how energy is used to melt a material and the response of that material to the energy applied, much of the study of laser sintered materials has centered on the behavior of the material when it melts and then resolidifies. Early materials for laser sintering included both amorphous (polycarbonate) and crystalline materials (wax). In the late 1980s and early 1990s, there was not an understanding of how materials performed in the laser sintering process and there was an attempt to process all available materials in a standard system. Figure 18 is a polymer materials performance chart that divides polymers into amorphous and partially crystalline (semi-crystalline).

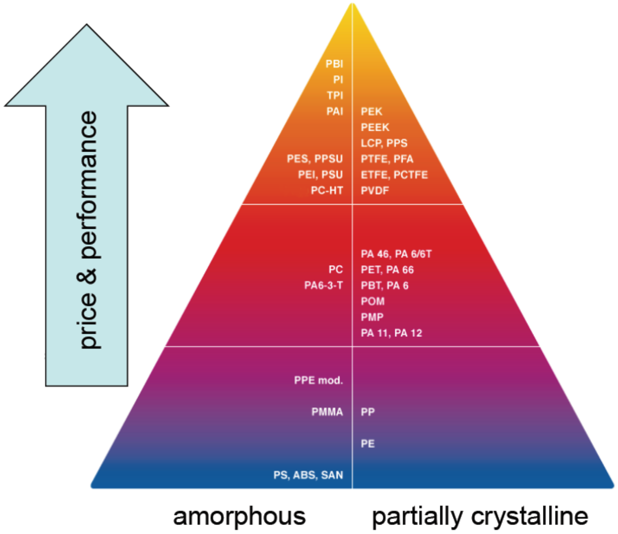

Figure 18: Polymer Performance Pyramid (Schmid M. L., 2013)

2.6.3.1 Material Response to Thermal Energy

The primary issue of supplying the critical energy for any laser sintered polymer is that there is a critical balance between the amount of energy applied by the laser and the energy supplied by the part heater. Amorphous polymers presented a significant challenge in processing because the energy needed to create a dense part would either warp the build geometry or would put so much energy into the part that material outside of the melt region would consolidate and cause part growth. Therefore, it became standard practice to heat the polymer to a temperature just shy of the melting temperature. For amorphous polymers this created a significant issue. As Ian Gibson commented in an article written in 1997:

> *"The part bed temperature must not exceed T_g for amorphous, otherwise all the powder at part bed surface could stick together." (Gibson I. a., 1997)*

Since the melting behavior of feedstock powders under certain thermal conditions affect their ability to be processed in laser sintering, thermal tests were used to identify certain behaviors. As seen in the same article by Gibson in Figure 19, a simple test could be used to identify powder bed temperature process parameters and how the material might behave while being melted. Semi-crystalline material has a more distinct melting point, allowing the processing temperature to be closer to the melting point as seen in Figure 20. A comment at this point is that many papers and figures references use the term recrystallization to define the transition of the polymer to a solid part. Without melt-phase x-ray diffraction results to quantify the level of crystallinity in a semi-viscous solid, the term solidification will be used instead.

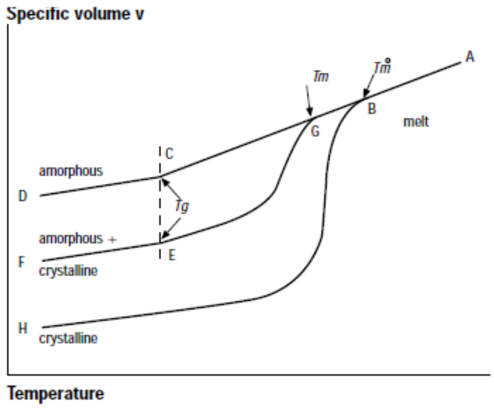

Figure 19: Variation of Specific Volume with Temperature (Gibson I. a., 1997)

It was not initially understood that the unique thermal behavior of semi-crystalline materials lent themselves to being suitable in laser sintering. Because there are distinct melting and solidification points, the thermal processing parameters become quite evident when evaluating the thermogram of a material. When processing a material at a temperature below or too close to the solidification point the melted layer will shrink before a new layer can be fused to it. This premature shrinking will create a tensile stress at the top of the part that will pull the top edges towards the center of mass which will distort or curl the part. If processed above the melting point, all powder in the build region will solidify. Therefore, a processing window between the solidification and melting points is desired.

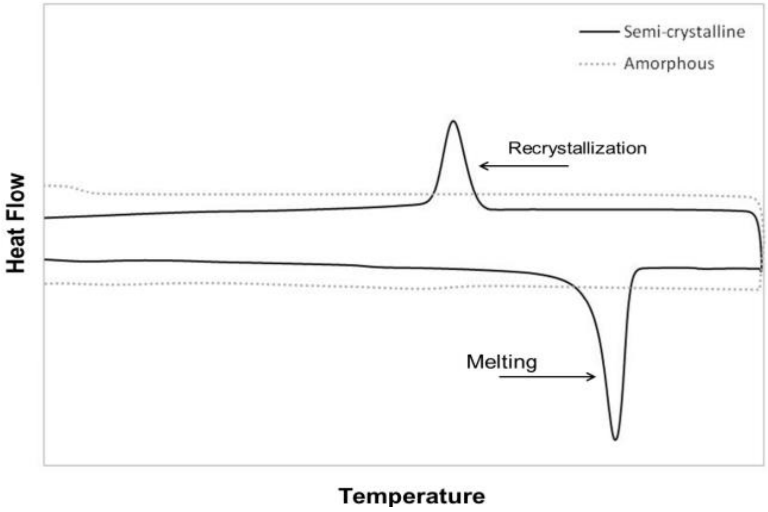

Figure 20: Differential Scanning Calorimetry (DSC) Thermogram of Amorphous and Semi-Crystalline Polymers (Vasquez M. , 2012)

2.6.3.2 Laser Sintering Processing Characterization

In Gibson's 1997 article, he was able to correlate an increase in density and tensile strength of X & Y oriented tensile bars with increased laser power (P) shown in Equation 1. While the equation ascribed the energy needed to melt the part solely to the laser, it was stated in the article that the part bed was heated to a temperature (T_b) such that the laser energy did not create distortion. This equation also considers the slice thickness (h) which represents the depth of penetration required to fuse material to a previously sintered layer.

$$\mathrm{P} = (\mathrm{BS} \times \rho \times D_b \times h \times \frac{[C \times (T_m - T_b) + l_f)}{(1-\mathrm{R})}) \qquad \text{(Gibson I. a., 1997)}$$

Equation 1: Laser Power Calculation

where BS=beam speed, ρ=power density, D_b=diameter of beam, h = slice thickness C=specific heat, T_m = Melting Temperature, T_b = part bed temperature, l_f=latent melting heat, and R=reflectivity.

To better describe the effective energy delivered to the part bed, the scanning parameters must be accounted for. The laser is directed to the part bed through a set of controlled mirrors (scanners) that trace an array of vectors that represent a cross-sectional area of the geometry. The scan spacing, illustrated in Figure 21, allows for an overlap to deliver more energy to the part or a wider spacing when less dense parts are desired.

Figure 21: Illustration of Scan Spacing and Beam Overlap

The resulting Equation 2 combines the power in Equation 1, with scanning parameters and yields an effective energy density. As can be seen in Figure 22, parts were built in several orientations and with a variety of processing parameters. Tensile strength and density were graphed on the Y-axis with varying process parameters on the X-axis to correlate variations in mechanical properties to those parameters. The processing parameters tracked in this study included laser power, scan speed and scan spacing. It can be seen in Figure 23 that there is a strong correlation between increased laser power and increased tensile strength. It can also be noted that the tensile strength in the z-axis as recorded in the VZ-oriented samples have a very tight grouping around 5% elongation-at-break, which is significantly less than the value for the tensile specimens produce in other orientations.

$$\text{Energy Density}\left(\frac{\text{cal}}{cm^2}\right) = \frac{P \times f}{\text{BS} \times \text{SCSP}} \qquad \text{(Gibson I. a., 1997)}$$

Equation 2: Energy Density Calculation (with factor f)

Where SCSP is scan spacing and f is a conversion factor.

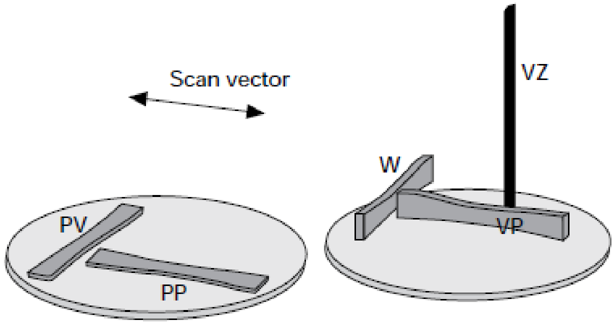

Figure 22: Tensile Specimen Orientation (Gibson I. a., 1997)

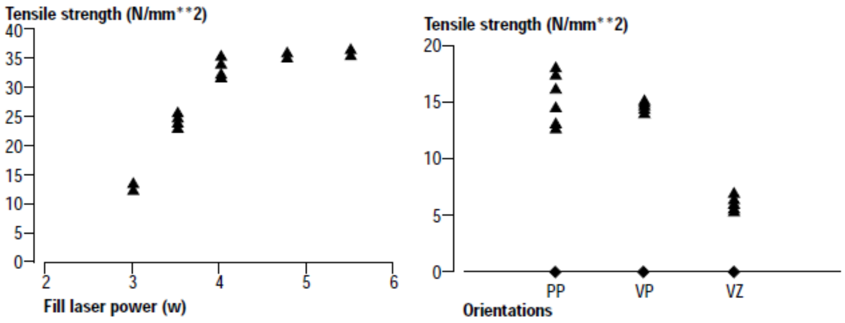

Figure 23: Sensitivity of Tensile Strength to Process Parameters (Gibson I. a., 1997)

In a telling statement, Gibson said "*In SLA, the largest slice thickness is limited by the 'penetration depth* D_p*' of resin.*" The compelling conclusions from this early work and the ease at which parameters can be varied at the build plane made it easy to establish a **paradigm of evaluating the mechanical properties with respect to processing parameters exclusively at the build layer**.

Follow-on research to quantify the effect of powder melt and mechanical properties was performed by Majewski at the University of Loughborough in 2008. (Majewski, Zarringhalam, & Hopkinson, 2008) These authors were able to determine both visually (Figure 24) and with differential scanning calorimetry (DSC) that there were two distinct melt peaks representing areas in the processed part that had not been fully melted. It was proposed that the degree of particle melt (DPM) had an overall impact on mechanical properties. A key conclusion in this research was stated:

> *This work has shown that the percentage crystallinity of a two-phase SLS part, as calculated from a DSC chart, has an appreciable effect on the Tensile Strength and Elongation at Break, whereby a decrease in crystallinity leads to an increase in the mechanical property.* (Majewski, Zarringhalam, & Hopkinson, 2008)

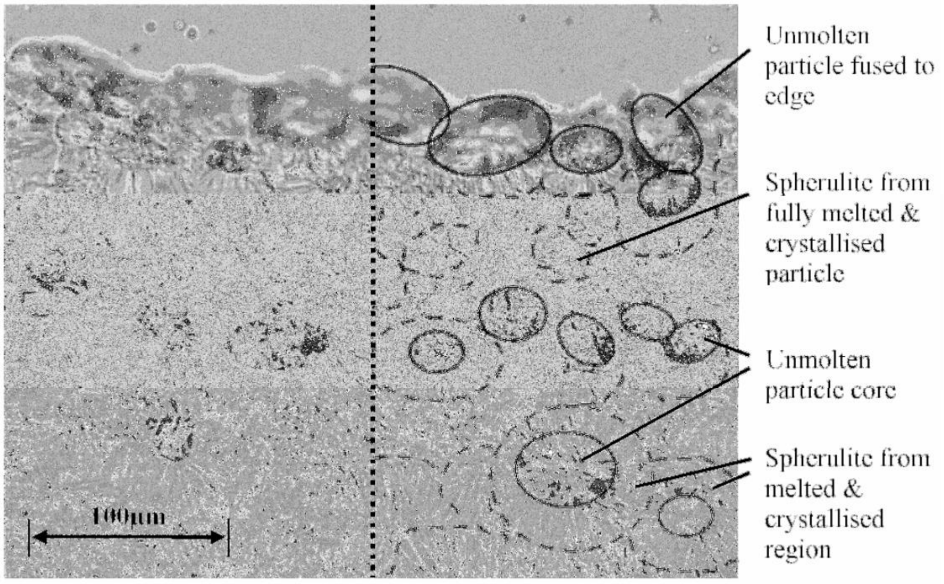

Figure 24: Laser Sintering Morphology from Particle Melt Study (Majewski, Zarringhalam, & Hopkinson, 2008)

In work done at the University of Louisville and published in 2011, Thomas L. Starr and Timothy J. Gornet further characterized the correlation of process settings, material morphology, and resultant mechanical properties. Starr correlated the amount of energy that is delivered to the part bed during laser sintering (Energy Density) to the resultant material properties. The formula for volumetric energy density is shown in Equation 3 and is a variant of the previously referenced Equation 2, substituting a quantifiable variable layer thickness (h) for the generic conversion factor (f). A plot of yield stress and elongation-at-break are in Figure 25 and Figure 26, respectively. (Starr T. , Gornet, Usher, & Sherzer, 2008) The energy-to-melt is shown to be insufficient for optimized material properties and it is proposed that there is an effective energy-to-melt ratio. This excess energy is necessary for stronger layer-to-layer adhesion. In addition, Gornet showed in separate work that the use of microtoming is a practical tool in analyzing laser sintering morphology. (Gornet, 2010) Figure 27 shows a microtomed cross-section of a specimen with layer lines being apparent at both magnifications. Correlating these images with those from Majewski in Figure 24, the particles that are not fully melted are colinear in the photographs, which is a result of the coplanar phenomenon of decreased energy density at the bottom of the sintered layer.

$$\text{Energy Density} = \frac{Laser\ Power}{(SS)(SP)(h)}$$ (Starr, Gornet, & and Usher, 2011)

Equation 3: Energy Density Calculation

where SS is scan spacing, SP is scan speed, and h is layer thickness.

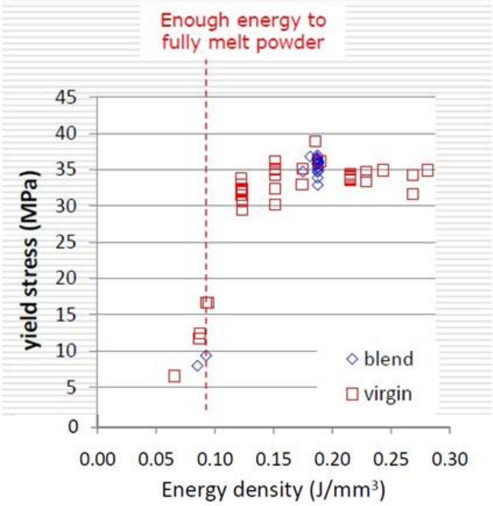

Figure 25: Plot of Yield Stress vs. Energy Density (Starr T. , Gornet, Usher, & Sherzer, 2008).

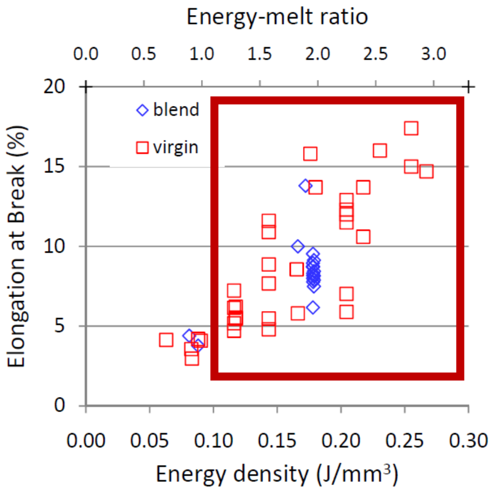

Figure 26: Plot of Elongation-at-Break vs. Energy Density (Starr T. , Gornet, Usher, & Sherzer, 2008).

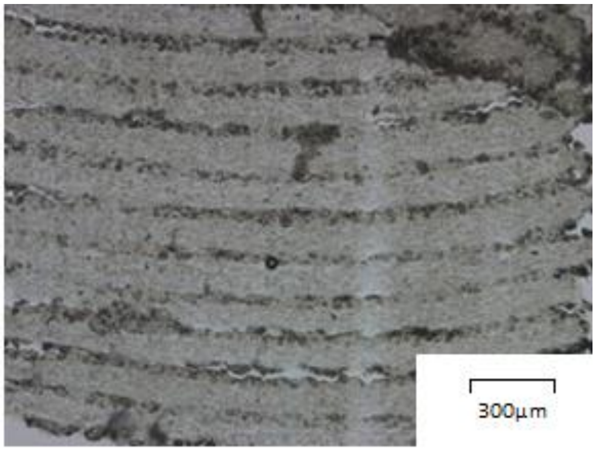

Figure 27: Microtomed Sample in Laser Sintering (Gornet, 2010)

Further work to create a more accurate thermal energy representation was performed by Starr and referenced in a dissertation by Mike Vasquez at Loughborough University. (Vasquez M. , 2012) The resulting Equation 4 accounts for key material, powder bed, and processing parameters to more accurately reflect a model that can be used with a variety of feedstocks in multiple applications.

$$\text{EMR} = \frac{\frac{\text{P} \times V_C}{V_S \times V_B \times z}}{\left[C_p(T_m - T_b) + h_f\right](\delta_s)(\delta_d)}$$ (Vasquez M. , 2012)

Equation 4: Energy-to-Melt Ratio Formula

> *Energy Melt Ratio where P= laser power, V_c=scan count, V_s=scan spacing, V_B=beam speed, z=layer thickness, C_p=specific heat capacity, T_m=melting temperature, T_b=powder bed temperature, h_f=enthalpy of melt, δ_s=material density, and δ_d =packing density.* (Vasquez M. , 2012)

There have been numerous studies done to characterize mechanical properties with respect to material and processing parameters that are referenced in the bibliography, but based on the characterization that has been done previously and discussed in this section, there are several key takeaways: (Kim & Oh, 2008) (Schmid, Amado, & Wegener, Polymers for AM, 2014) (Rietzel, Aquite, Drummer, & Osswald, 2011) (Schmid M. , Amado, Levy, & Wegener, 2013) (Egger, Gygax, Glardon, & Karapatis, 1999) (Russenberg, Schmidt, Hosse, & H.J., 2012) (Vasquez, Haworth, & Hopkinson, 2013)

- Intrinsic raw material properties influence processing in laser sintering.
- The degree of particle melt study and the microtoming specimens indicate that threre is weak layer-to-layer adhesion.
- Correlation of energy density to mechanical properties shows a strong correlation of energy density to tensile strength but with significant variability with respect to elongation-at-break; this is illustrated in the region of the red box in Figure 26.

- Models to correlate mechanical properties to processing parameters focus exclusively on the build layer processing parameters including powder bed temperature and laser settings.

2.7 Fracture Behavior of Laser Sintered Polyamide

Based on the research done on the failure mechanisms in laser sintered polyamide (Starr T. , Gornet, Usher, & Sherzer, 2008), the yield stress and ultimate tensile strength are relatively consistent and comparable to traditional processes like injection molding. The key deficiency in the laser sintering process is a ductility that is significantly lower than traditional manufacturing processes. As energy increases, there is a critical amount of energy required to get consistent tensile strength, as shown in Figure 25. The fact that there is not a similar correlation to the elongation-at-break seen in Figure 26 shows that there is a fracture-driven failure mechanism contributing to the decreased elongation.

2.7.1 FRACTURE MECHANICS

Linear elastic fracture mechanics is a means of characterizing brittle failure. There are three modes of failure with the primary failure mode in tension being Mode I, as shown in Figure 28.

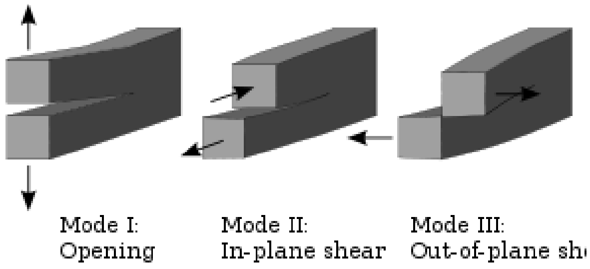

Figure 28: Fracture Mechanics Failure Modes (Twisp, 2008).

The critical yield stress, or fracture stress (σ_f), of polyamide processed using conventional methods is significantly greater than what is observed in laser sintering while the fracture toughness remains the same. The correlation of fracture toughness to critical yield stress is shown in Equation 5. This correlation assumes that there is a crack within a specimen (a) and that the geometry of the crack and specimen can be quantified using a shape factor (Y). This is generally true for cracks and specimens that have a simple geometry. A sampling of shape factors is shown in Figure 29.

$$K_{Ic} = Y\sigma_f\sqrt{\pi a}$$ (Roesler, Harders, & Baeker)

Equation 5: Fracture Toughness

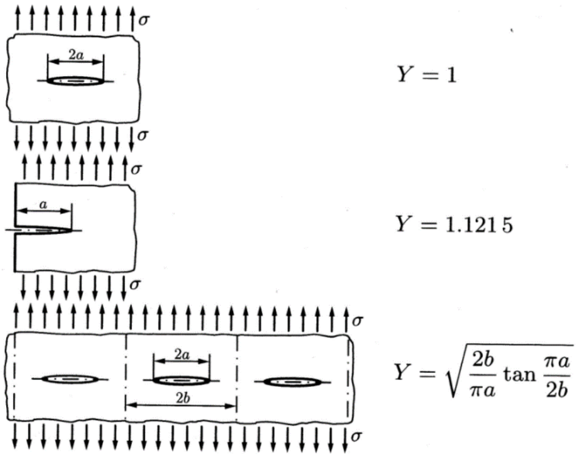

Figure 29: Fracture Mechanic Shape Factors (Y) for Different Crack Geometries (Roesler, Harders, & Baeker)

Equation 5 and Figure 29 illustrate that, even if the fracture toughness of a material remains constant, the strength of the part will be negatively affected by large flaws or arrays of flaws.

2.7.2 FRACTURE BEHAVIOR IN LASER SINTERED POLYAMIDE SAMPLES

The primary failure of laser sintered nylon polyamide specimens has been attributed to a lack of energy to melt the top powder layer and the corresponding poor interlayer adhesion; this in turn leads to anisotropy. The relative porosity of the interface boundary layers shown in Figure 24 and Figure 27 contribute to decreased ductility and the possibility of fast fracture.

In preliminary research, specimens were built and analyzed to establish a correlation of the failure modes of specimens with the amount of energy used to fabricate them. A total of 24 PA-12 specimens were produced and evaluated. Figure 30 shows the locations within the builds for 8 tensile specimens with 4 being oriented primarily in the z-axis, and 4 being oriented primarily in the x-axis. Three builds were used with varying laser powers to illustrate the full range of failure mechanisms typically seen in laser sintering.

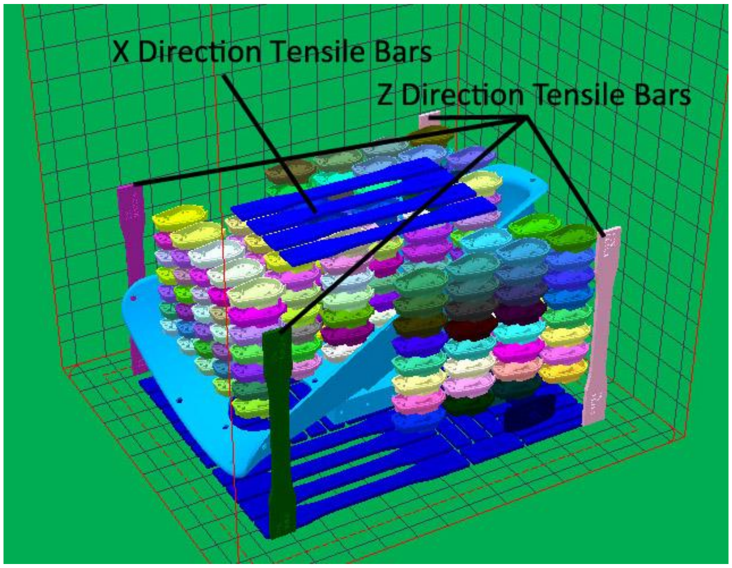

Figure 30: Tensile Specimen Location in Build (Leigh, Fracture Behavior in Laser Sintering, 2011)

2.7.2.1 Tensile Specimen Characterization

Data from 8 tensile specimens are listed in Table 3 and illustrated in the SEM photographs that follow. Tensile specimen nomenclature identifies the geometric location of the sample in the build as well as the build orientation. A “zx” specimen would be oriented with its long axis in the z-axis with the short axis oriented in the x-axis, consistent with ISO/ASTM F2921. (ASTM F42 Committee) An “x” or “y” specimen would be oriented flat in the x-y plane with thelong axis along the x or y-axis, respectively.

The x and y-axis specimens produced better mechanical properties and more consistent results. There were three primary modes of failure that were common among all the specimens which are discussed in 2.7.2.2 Morphology of Tensile Specimen Fracture Surfaces, can be seen in **Error! Reference source not found.** and are enumerated in Table 3.

Sample	Energy Density J/mm^3	(UTS) psi	Elongation %	Fracture Mode
ZX 12.0.3	0.1	494	1	Delamination
ZX 0.0.3	0.1	2969	1	Delamination
ZX 0.12.3	0.1	1278	1	Delamination
ZX 13.11.3	0.2	5164	3	Brittle
X 4.2.8	0.2	5886	7	Brittle
X 4.3.8	0.2	5991	6	Brittle
X 4.4.8	0.2	5763	7	Brittle
+Y 1.4.1	0.3	6099	44	Ductile

[1] *Ductile fracture taken from independently optimized build.*

Table 3: Tensile Properties and Fracture Mode of PA-12 (Leigh, Fracture Behavior in Laser Sintering, 2011)

2.7.2.2 Morphology of Tensile Specimen Fracture Surfaces

When using scanning electron microscopy (SEM) to evaluate the 3 distinct fracture patterns illustrated in **Error! Reference source not found.**, clear patterns arose in each of the three types of failure mechanisms. The fracture surfaces were evaluated using a JEOL JSM 5610 Scanning Electron Microscope (SEM) at The University of Texas at Austin with a tungsten filament.

The SEM images shown in Figure 31 shows an x-y sample with layering in the z-axis shown vertically. When inspected, the photographs show clear patterns for the layers with elongated horizontal voids showing clear inter-layer porosity. Two light blue guides are shown to help define this interface boundary region. Based on the formulas shown in Equation 3 and Equation 4, the approximate energy density is 0.10 J/mm^3 with an energy-to-melt ratio of 1.0. Fully dense regions and areas of porosity are visible in the magnified image.

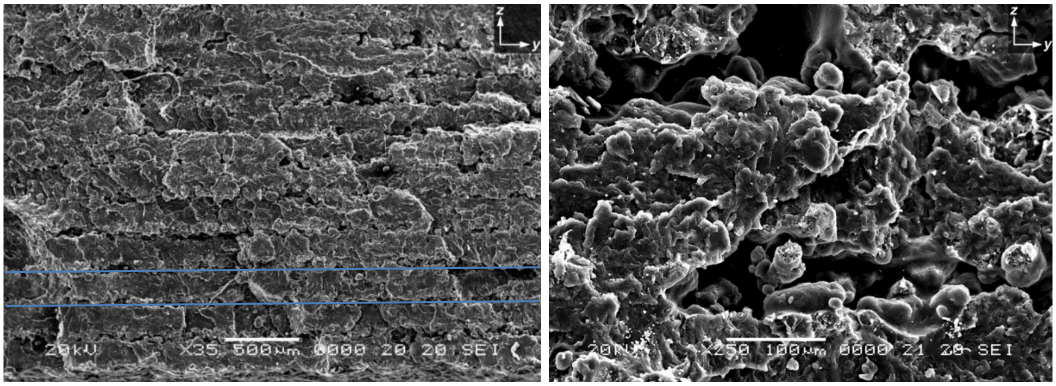

Figure 31: SEM of X Tensile Bar Fracture Surface - PA12 @ 0.1 J/mm^3 (Leigh, Fracture Behavior in Laser Sintering, 2011)

The top surface of a Duraform PA (PA-12) XY tensile specimen is illustrated in Figure 32. This shows the upper facing surface and the surface to which the loose powder must be bonded by the thermal energy of the system heaters and laser. The average particle size is roughly 50 microns and individual melted particles in the magnified image have a lily pad or pancake appearance. Some particles can be seen to have melted with other particles while others appear to be isolated with voids between particles. Of interest is the 250 μm boulder-like particle in the center of the micrograph, which is indicated with a red arrow.

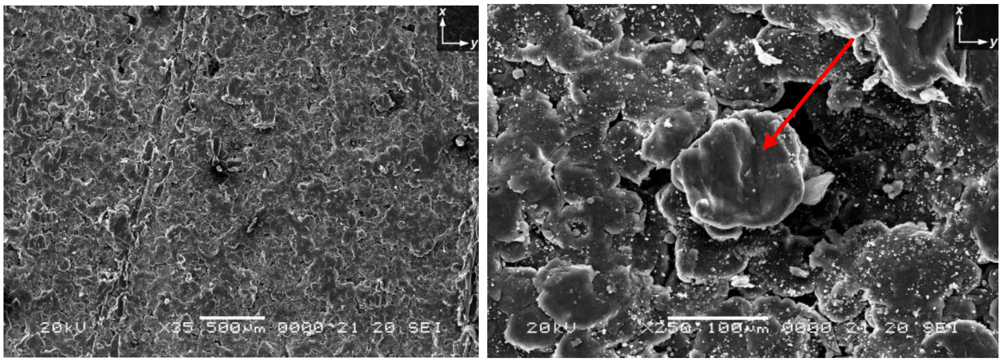

Figure 32: SEM Images of X Tensile Bar Top-Facing Surface - PA-12 @ 0.2 J/mm^3
(Leigh, Fracture Behavior in Laser Sintering, 2011)

The fracture surfaces of Duraform PA (PA-12) Z tensile specimens are shown in Figure 33 through Figure 35. These specimens were evaluated parallel to the z-axis looking at a fracture aurface that lies in the x-y plane. Delamination is apparent in Figure 33, brittle fracture in Figure 34, and ductile fracture in Figure 35. The delamination and ductile fracture surfaces were photographed perpendicular to the z-axis, showing the underside of a layer in the delamination fracture specimen. The brittle-fracture surfaces photographed were evaluated at a 45° shear surface.

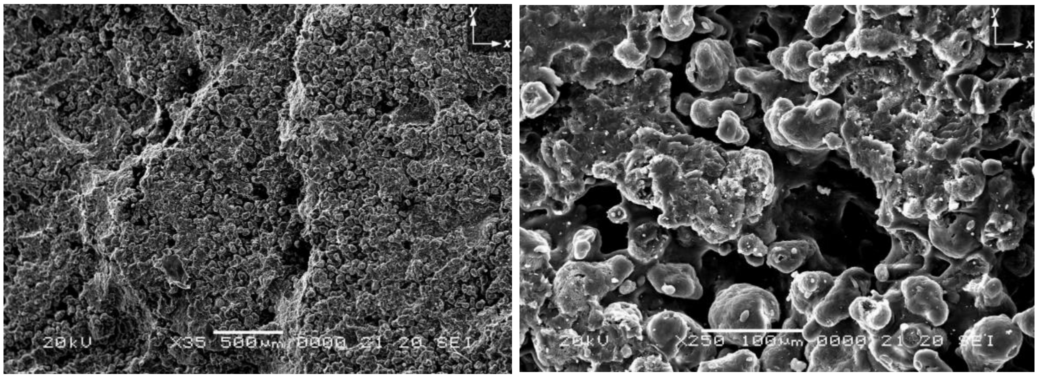

Figure 33: SEM of Z Tensile Bar – Delamination - PA-12 @ 0.1 J/mm^3 (Leigh, Fracture Behavior in Laser Sintering, 2011)

When evaluating the image of the fracture surface shown in Figure 31, a periodicity can be observed. With the understanding that the z-axis is the primary direction for added layers, a pattern of voids between layers is apparent. This stratification contributes to anisotropic material properties and significant weakness if a tensile stress is exerted parallel to the z-axis. In addition, these patterns of voids contribute to a significant reduction in elongation and ultimate tensile strength.

When looking at the upper facing surface of the specimen shown on the right side Figure 33, it appears that the 250 μm particle was formed when several particles melted together but did not fully adhere to the surface. This particle appears to have been created when the surface tension of multiple particles drew them together while under the influence of the laser, creating larger voids which could contribute to interlayer porosity.

It is apparent from the analysis of these samples that the cracks propagate through voids created by a lack of full melt between layers. The general observations for each fracture mode are listed below:

- Delamination fracture surfaces can be seen in Figure 33. These images show a fracture of the Z specimen that is parallel to the x-y plane. Three distinct layers are represented as the crack propagation followed the area between two parallel layers and then migrated to neighboring layers. This pattern, when examined in Figure 27 shows that the particles are roughly 50 µm in diameter, which corresponds to the average particle size of the raw material. When compared to the morphology of the top layer (Figure 33), the bottom layer has very little bonding to the previous layer.

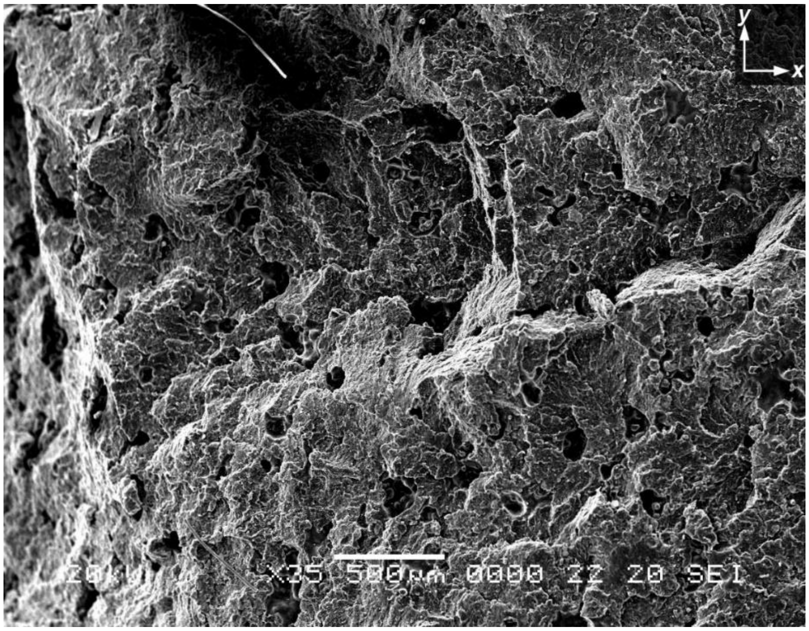

Figure 34: SEM of Z Tensile Bar – Brittle Fracture - PA-12 @ 0.2 J/mm^3 (Leigh, Fracture Behavior in Laser Sintering, 2011)

- Brittle fracture surfaces can be seen in Figure 34 where voids are isolated and somewhat periodic, with similar size and spacing. Fracture surfaces show a ductile tear with transgranular fractures or river marks. These fracture surfaces are like the ductile specimen (Figure 35), but with a higher void fraction on the failure surface.

- Ductile fracture surfaces from a specimen that had an elongation-at-failure of 44% can be seen in Figure 35. There was significantly higher ductility in this sample since voids from processing are not visibly present. It is likely that in this case, void nucleation occurs where the material tore apart from itself. Shards of material from the resultant fracture are also visible.

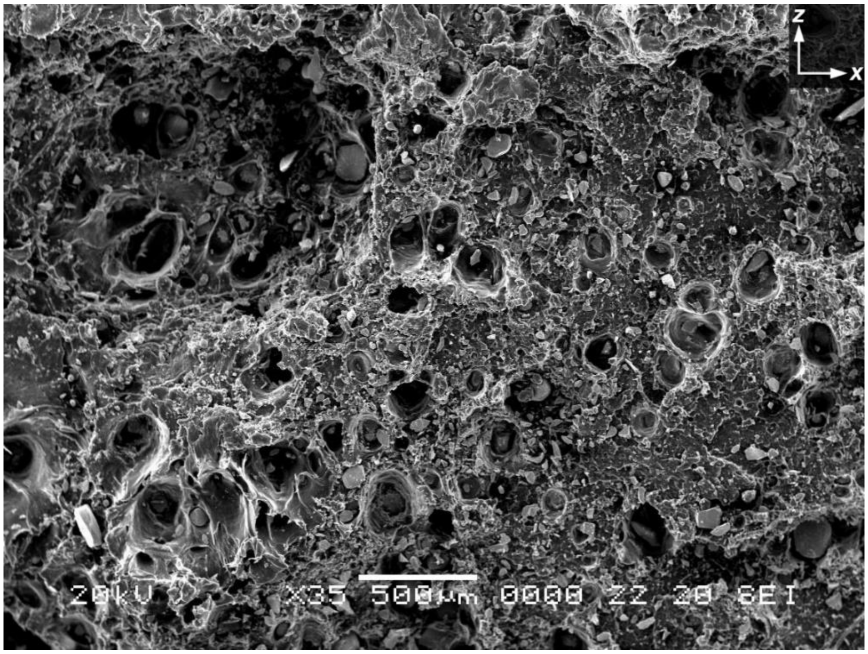

Figure 35: SEM of Y Tensile Bar - Ductile Fracture. PA-11 @ 0.3 J/mm^3 (Leigh, Fracture Behavior in Laser Sintering, 2011)

2.7.2.3 Illustrating the Interface Boundary Layer using Coplanar Porosity

It is apparent that the material properties observed in Table 3 can be correlated to the extent of voids present between sintered layers. Without sufficient energy to melt through the top layer of the build and bond it with the rest of the part, there is such weak bonding that the part will delaminate. With such little adhesion between layers, delamination of the part at an interface boundary layer happens when stress is applied, and the elongation-at-break is near 1%.

With sufficient energy to melt through the target layer into the previous layer, the interface boundary layer is healed and will result in a fully dense part, allowing for elongations-at-break values well above 10%. As the layer has a higher degree of melt, the voids will decrease through the brittle range until the voids from processing no longer contribute to the fracture. As will be discussed later, there are two apparent stages of sintering. The initial phase allows the powder particles to bond together and start forming a larger particle through surface tension as seen in the 250 μm seen in Figure 32. The second stage of sintering, when complete, contributes to the porosity being fully overrun. A lack of visible pores is present once the pores are fully overrun as seen in Figure 35 and tensile specimens exhibit significantly better ductility.

Figure 36 illustratess the effect of the depth of penetration of the laser in a single layer and is consistent with the literature review and SEM images. The surface tension of the fully melted top surface creates a level plane on each processed layer. On the initial layer to be processed, the bottom surface is defined by the pack density and particle shape of the nylon particles affected by the laser energy. While the number of particles affected is proportional to the energy applied to the surface, it is apparent from Figure 33 that the bottom surface has a grainy appearance. This indicates that there was sufficient energy to consolidate a layer of powder, but insufficient energy to penetrate the layer. With the bottom of the particles largely unaffected there is an irregular downward facing surface which is the impetus for void creation.

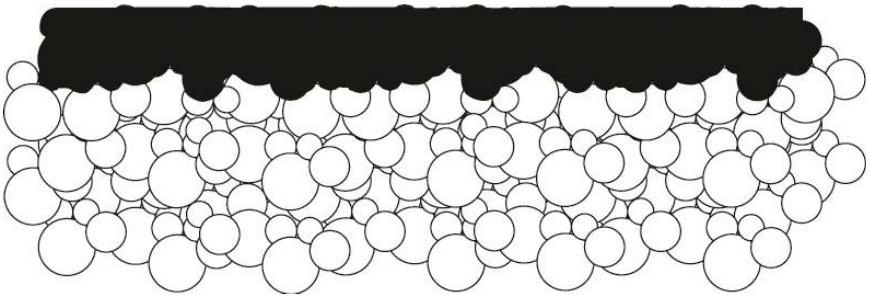

Figure 36: Initial Layer of Sintered Powder (Leigh, Fracture Behavior in Laser Sintering, 2011)

In the case of a delaminated sample, there is insufficient energy applied to the surface to fully melt and adhere to the previously sintered layer. Figure 37 illustrates what is seen in the delamination samples examined by SEM. In this illustration, it can be noted that the interface boundary layer is dominated by porosity and unsintered particles, but that there is enough layer-to-layer adhesion to maintain geometric integrity.

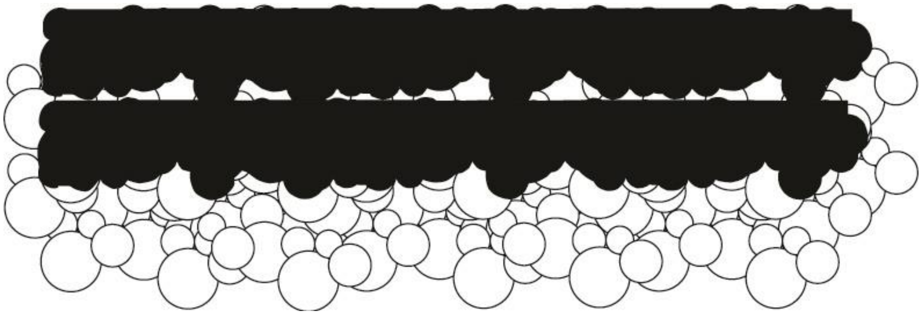

Figure 37: Lightly Adhered Layers Contributing to Delamination. (Leigh, Fracture Behavior in Laser Sintering, 2011)

These coplanar voids found at the interface boundary layer represent pre-existing cracks in the specimen. When the cracks are long enough and spaced close enough, the crack propagation that happens under tensile stress results in crack propagation between the ligaments of in tact material. In this case not only will ductility be impacted, but the onset of yield and ultimate tensile strength will be quite low due to the small percentage of the area of the cross section that consists of sintered particles.

Figure 38 schematically illustrates the brittle fracture sample shown in Figure 34. While voids in these samples are present, they are more isolated and periodic. The crack propagation in this example is much less planar since the voids are no longer exclusively coplanar: meaning that the distance between cracks on one layer may be as close or closer to a crack on another layer than within the same layer. Fracture in this case may originate between layers but will typically travel through voids in neighboring layers since the distribution of voids is much more well distributed.

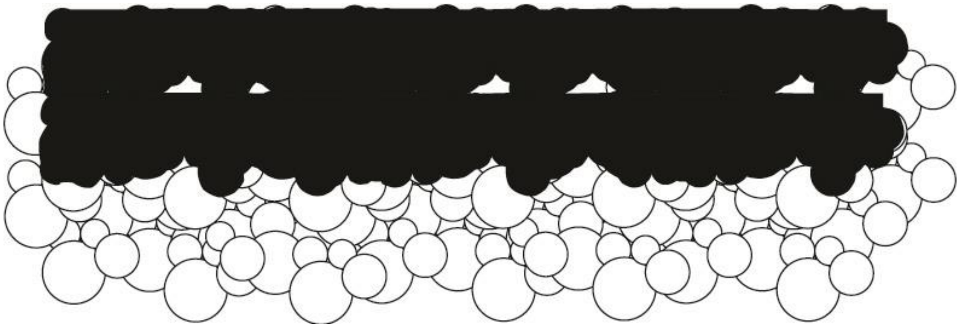

Figure 38: Incomplete Fusion Contributing to Brittle Fracture (Leigh, Fracture Behavior in Laser Sintering, 2011)

2.7.3 SIMULATION OF THE INTERFACE BOUNDARY LAYER

To insure the best properties of a part created though the laser sintering process, layers must be processed in such a way as to minimize or eliminate voids between layers.

It should be clarified that while many voids are visible, as shown in Figure 31, Figure 33 and Figure 34, the term void can also be used to define the space between molecules where there is no reptation. If a 'void' at the interface boundary layer is infinitely thin and not visible, there is still no adhesion between layers. Voided regions between layers define the fracture modes of delamination, brittle fracture, or ductile fracture. When laser sintered specimens are observed optically, there is a visible boundary layer between subsequently fused layers. This boundary layer is exclusively seen in the X-Y plane with the boundary layers stepped in Z. This interface boundary layer has shown to be a primary culprit in decreased mechanical properties and can be characterized as a layer of coplanar voids. Specimens with varying levels of void periodicity were intentionally fabricated to characterize the relationship between fracture behavior and void density.

If the bottom surface of a layer were to be represented by close packed spheres and the top surface can be represented by a plane, it is possible to simulate the interface boundary layer with the geometry described in Figure 39. This geometry is defined by the radius (r) of the close packed spheres and the extent at which they intersect the planar surface (h) of the previously sintered layer.

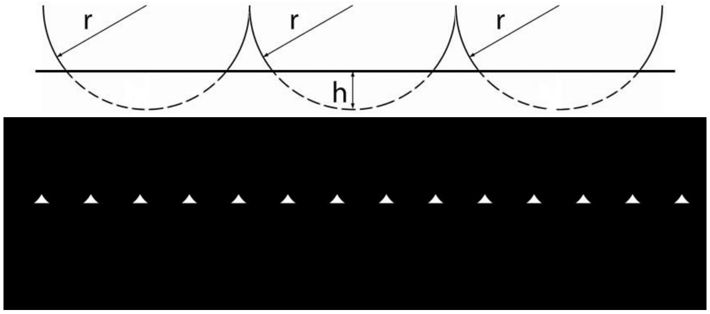

Figure 39: Schematic of h/r Ratio (Leigh, Fracture Behavior in Laser Sintering, 2011)

The interplay of the sphere radius to the interface boundary can be shown as a ratio between h/r. In the example of the delamination specimens, there is practically no adhesion of the bottom of one layer to the top of the other. In the delamination case, h would be 0 and the radius could be normalized as 1. Therefore, in a delamination sample, the h/r ratio=0. In the case of a fully dense part with no visible voids between layers the bottom of the sphere would be totally fused to the previously sintered layer and would yield an h/r ratio=1. The transition of this ratio from 0 to 1 corresponds to the degree of sintering where the pores would be eliminated at h/r ratio=1.

Tensile specimens were designed using CAD to simulate the interface boundary layer with varying degrees of severity. These specimens were then processed in the stronger X-direction to isolate the effect of anisotropy mechanical properties on this experiment. These tensile specimens were modeled with a closed pack array of hemispheres to simulate a layer of powder, seen in Figure 40. The second half of the tensile bar with a flat plane was combined with the specimen having the hemispheres to create a single tensile specimen STL file, seen in Figure 41. This operation was repeated for h/r ratios of 0 to 1 at 10% increments. With the hemispheres measuring 0.050” radius, the interface was moved 0.005” for each incremental sample. A total of eleven (11) specimens were created and labeled with the appropriate h/r ratio on each.

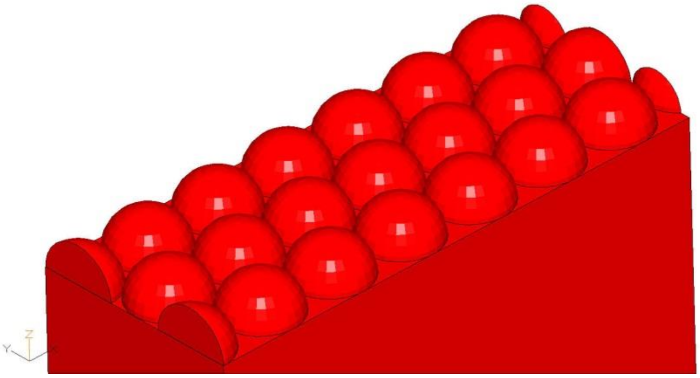

Figure 40: Model of Close Packed Hemispheres on Tension Specimen (Leigh, Fracture Behavior in Laser Sintering, 2011)

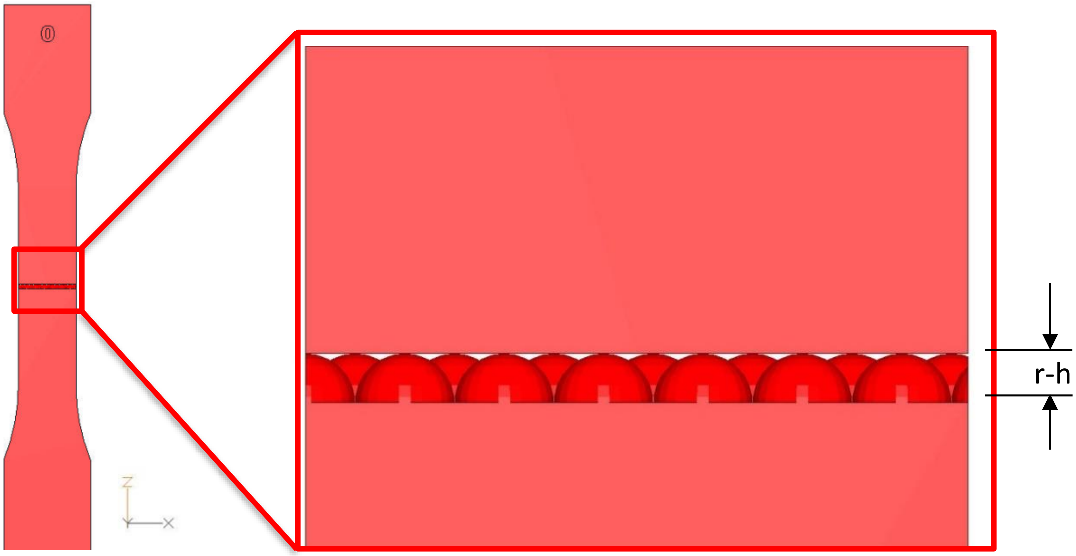

Figure 41: Simulated ASTM D638 Tension Specimen with Visible Interface Boundary (Leigh, Fracture Behavior in Laser Sintering, 2011)

Interface boundary specimens were produced in optimized production builds using the 3D Systems, Inc. laser sintering system. The tensile specimens were produced in an optimized production build with production-grade feedstock and processing parameters. Two builds of eleven (11) samples each were built and evaluated, with one set of samples having a finished surface and the other set having no post finishing done. There was no significant difference in UTS or ductility between these two builds, so a single set of data was recorded. The data presented in Table 4 and Figure 42 are from the unfinished tensile specimens.

All h/r ratio specimens followed the same stress-strain curve seen in Figure 42. The data collected was graphed in Figure 43 to illustrate the patterns observed in three primary regions of fracture. It should also be noted that delamination is a special case of brittle fracture.

Sample	h/r Ratio	σ_y (psi)	UTS (psi)	EAB %
1	0	2772	2954	4
2	0.1	2854	3124	4
3	0.2	3028	4021	6
4	0.3	3056	4976	7
5	0.4	3163	5312	9
6	0.5	3047	5468	9
7	0.6	2824	5882	17
8	0.7	3090	6130	17
9	0.8	3225	5994	16
10	0.9	3214	6133	18
11	1.0	3015	7391	>50*

[*] *Specimen exceeded extensometer limit of 50%.*

Table 4: h/r Ratio Tensile Results (Leigh, Fracture Behavior in Laser Sintering, 2011)

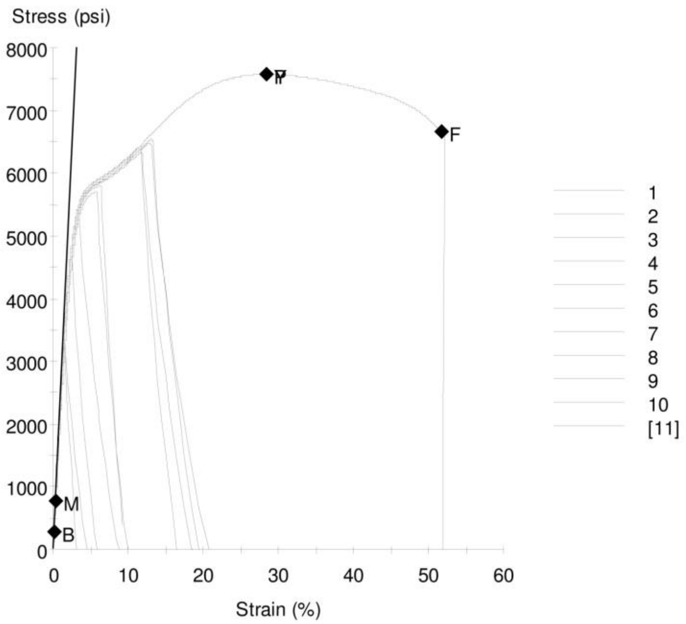

Figure 42: Stress-Strain Curves for h/r Ratio Specimens (Leigh, Fracture Behavior in Laser Sintering, 2011)

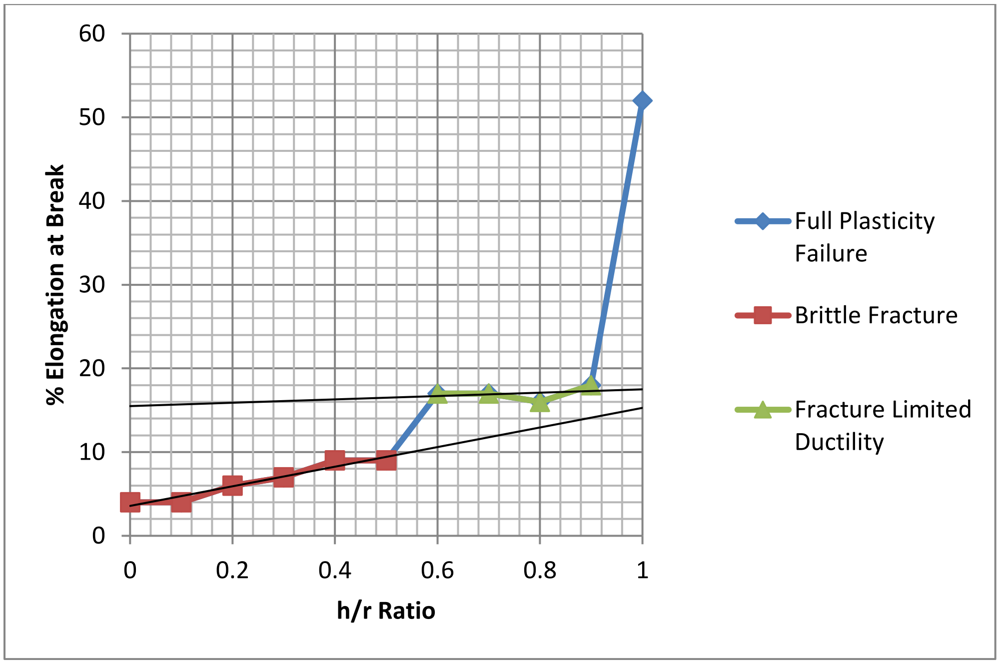

Figure 43: Trends in h/r Ratio Elongation-at-Break (Leigh, Fracture Behavior in Laser Sintering, 2011)

When analyzing the graph in Figure 43, there are two distinct trends present with an outlier at an h/r ratio of 1.0. An h/r ratio of 0 to 0.5 results in samples that fail by brittle fracture with no visible plastic deformation whereas h/r ratios of 0.6-0.9 plastically deform, but still fracture brittly. Only the sample with h/r = 1.0 failured in a completely ductile fashion. The same trend is also apparent from the groupings of samples in the stress-strain curves shown in Figure 42. The use of an h/r ratio helps qualify the failure modes at a macro scale and can help in identifying material process improvements that may help on a micro scale.

2.7.4 CORRELATION OF PHYSICAL AND VISUAL PROPERTIES

To summarize the findings from the fracture behavior of nylon specimens processed using laser sintering, there were three modes of fracture that corresponded to the presence of voids in the interface boundary area:

1. Delamination – A special type of brittle fracture that is characterized by very weak layer-to-layer adhesion. The fracture of a z-axis-oriented specimen will break exclusively in the region between layers. Delaminated Z-direction specimens were processed at standard thermal parameters with laser power at less than 50% of recommended parameters.
2. Brittle Fracture – Failure of a laser sintered specimen in tension within the elastic deformation range of a standard stress-strain curve. Fracture stress is less than yield stress with strains less than 10%. Typical fracture surfaces have a 45^o shear fracture.
3. Ductile Fracture – This is the desired failure mode. A ductile fracture will yield nearly isotropic parameters. Processing parameters have been optimized for build

quality with a sacrifice in efficiency and cost. There are two characterized ductile failure modes:

a. Fracture Limited Ductility -- A fracture that occurs after the onset of strain hardening and typically before UTS and the onset of significant necking. Strains are typically 15-25%.

b. Full Plasticity Failure – Fracture occurring after the onset of necking at UTS. If this level of strain is reached, it is very common that failure will not occur until 40-60% strain.

One metric that is commonly used to evaluate laser sintering parts is the density of the specimen. The boundary layer density was calculated using a slice taken from the CAD file of the periodic layer and interface boundary (r-h). The CAD file volumetric density data is plotted with the corresponding h/r ratio in Figure 44. This figure shows the density of a single layer based on the corresponding h/r ratio. If layers are consistent throughout the build, the resultant part density would be the same as an individual layer. Contrary to this assumption, the mechanical properties do not show the same trend when comparing the elongation data in Figure 43 to the part density in Figure 44. It is likely that the jump in elongation data shown in Figure 43 when going from an h/r ratio of 0.9 to 1.0 is that the effective crack size hits a ***critical value***. **In these samples, the number of voids did not decrease, but the size and shape of these voids approached 0 with only 0.0039% porosity on a coplanar level creating fracture limited ductility. Since this trend on a macro scale follows results seen at the interface boundary layer, we can conclude that the macro-results also apply quantitatively for microscale voids.**

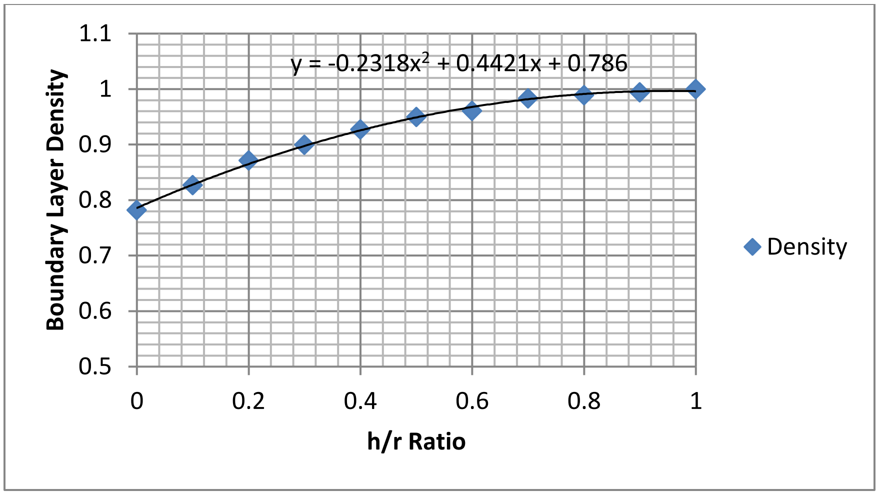

Figure 44: Correlation of Effective Part Density and h/r Ratio (Leigh, Fracture Behavior in Laser Sintering, 2011)

2.8 X-Ray Diffraction Specimens

The elongation-at-break of tensile specimens located at the top of a laser sintered production build is typically less than what is observed in the interior. It has been observed in production builds at Harvest Technologies (currently Stratasys Direct Manufacturing) that the placement of specimens up to 0.5" deeper in a build results in parts with better mechanical properties. It was hypothesized in prior work that the higher rate of cooling of the external samples contributed to a decrease in mechanical properties. The potential of a higher cooling rate, or quenching, was theorized to influence the crystallinity of the specimens or that it was affecting the interface boundary layer. To test this hypothesis, a total of 20 PA-11 samples were built in the orientation illustrated in Figure 45. These tensile specimens were produced using optimized heater setpoints as well as laser and scanning parameters.

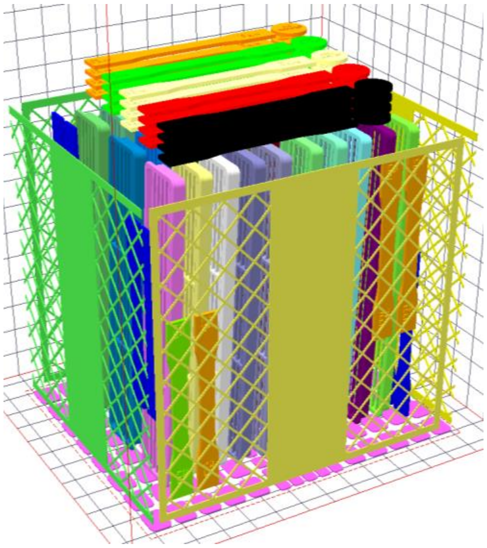

Figure 45: X-Ray Diffraction Specimens and Corresponding Tensile Specimens (Leigh, Fracture Behavior in Laser Sintering, 2011)

Four sets of five tensile and x-ray diffraction specimens were placed in the build at depths of 0.125”, 0.461”, 0.797” and 1.133”. The corresponding ultimate tensile strength and elongation shown in Table 5 illustrates there is a clear improvement of mechanical properties with an increased depth.

Specimen	Depth (in)	σ_y (psi)	UTS (psi)	EAB %
1	-.125	2906	4757	11
2	-.461	2933	4749	12
3	-.797	2872	4876	14
4	-1.133	2891	5007	15

Table 5: Effect of Build Depth on Tensile Properties of XY Oriented PA-11 (Leigh, Fracture Behavior in Laser Sintering, 2011)

It was theorized that the rate of cooling could be correlated to the degree of crystallinity in the resultant specimens. A Scintag X1 theta-theta powder diffractometer fitted with a solid-state detector using a Cu K-alpha radiation source was used for characterizing the amorphous/crystalline nature of the polymers in this study. The diffractometer operated at 40 kV and 30 mA. Figure 46 shows the x-ray diffraction results for four specimens listed in Table 5. The peaks in the x-ray diffraction figure are characteristic of the base material and the peak heights are a measure of the level of crystallinity of the material. ***Based on these results, it is apparent that there are no significant differences between the levels of crystallinity in these samples. Thus it is likely that the differences in the behavior of the samples is related to the processing dwell time above the solidification point, promoting stronger inter-layer adhesion.***

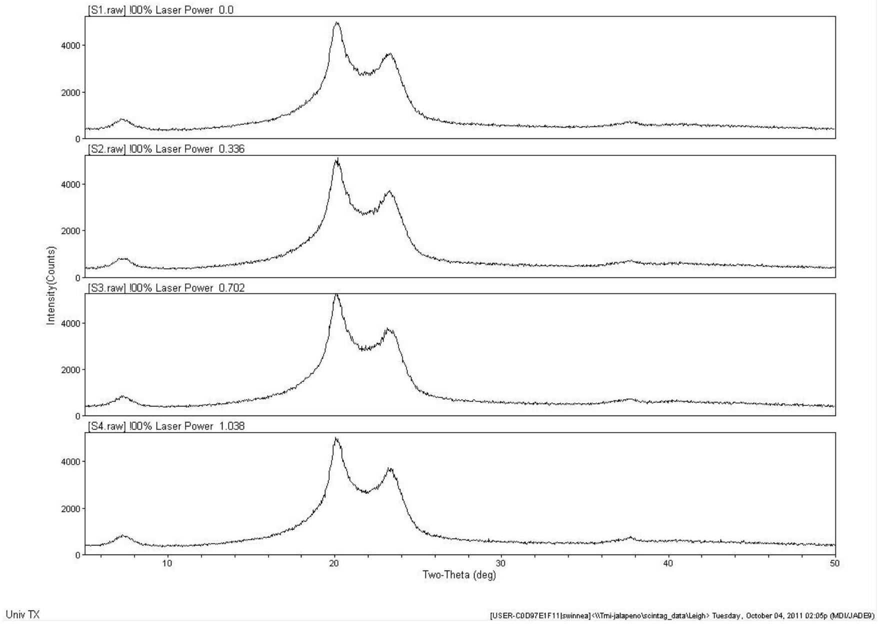

Figure 46: X-ray Diffraction Results

2.9 Production Requirements for Laser Sintered Parts

Independent of the work being done in the academic setting, industry was evaluating the laser sintering technology as a means for producing high value, low volume aerospace components. (Hopkinson, Hague, & Dickens, 2006) This section as well as Section 2.10 Mechanical Behavior in A Multi-Platform Production Environment were included because the statistical information collected during serial production in laser sintering provided significant insight into the pattern of mechanical failure in a production environment. The challenge until recently was that few AM-specific standards were available which meant that: material data reported by companies are not compatible, multiple processing parameters are employed, and few specifications can be referenced by end users to help them achieve product quality. (Gibson, Rosen, & Stucker, 2015)

The use of nylon 11 for low pressure ducting in the F/A-18 was the first serial production application using laser sintering. This program was developed as a collaborative effort between DTM Corporation of Austin, Athena of Austin, Harvest Technologies of Belton, the U.S. Navy Naval Air Systems Command (NAVAIR) and The Boeing Company (Boeing) in the mid-1990s. The full production ecosystem was developed from scratch since there were no material, process, or production standards. At the time, there was limited confidence in the ability of laser sintered parts to perform at the rigorous level required of a carrier-based fighter.

The advantages afforded by laser sintering and additive manufacturing was compelling enough for NAVAIR and Boeing to establish the manufacturing protocol and design standards needed for certified serial part production. There are three major hurdles to overcome in certified production: material specifications, process specifications, and design standards. An additional challenge in additive manufacturing is that the material is being made along with the part during the process. A conventional process such as CNC machining would have a material specification for the raw material that would include inspection reports and material traceability. A process such as investment casting would be more analogous to laser sintering because the material is being formed during the manufacturing process. But the x-ray inspection of cast parts would add a time and cost burden to plastic production that would push the price beyond the price-point for a viable business case.

To take advantage of a new manufacturing process and still maintain a viable price-point, special considerations had to be taken and a new way to qualify parts was created. The history of failure in aerospace production has been dominated by fracture mechanics. Because of the concern of fatigue and fast fracture, an array of tensile specimens in varying orientations were built and analyzed. The material processing, machine setpoints, and resulting tensile specimen mechanical properties became the basis for a new production standard and would serve as the foundation for future production standards in additive manufacturing.

2.9.1 PROCESS-BASED SPECIFICATION

Initial parts were built using Nylon 11 on a DTM Sinterstation 2000, and later the Sinterstation 2500. The constant evolution of hardware and software on the early systems created a challenge for those trying to quantify mechanical properties in a multiple platform environment. This challenge led the team to create a process-based specification. The premise of a process-based specification is that every step of the process is prescribed to secure a predictable outcome. The material specification was relatively simple and called out a single manufacturer's grade of Nylon 11 powder with a defined particle size based on the manufacturer's pre-existing specification sheet. The design standards were also straightforward and were developed based on the statistical analysis of a statistically significant number of tensile bars built and analyzed. The design guidelines outlined the material specification, the process specification, part orientation, part labeling, and minimum wall thickness. The materials and processing engineering efforts created a set of statistically significant laser sintered mechanical properties that could be used in finite element analysis in assisting the design engineers in optimizing part geometry.

The process specification was a bit more challenging and led to a move to a product-based specification. There were multiple stages in qualifying a laser sintered part based solely on process-based methodology:

1. <u>Qualification:</u> To allow parts to be manufactured under the product-based specification, individual part geometries were built with a specified number of tensile specimens to qualify a platform, machine, build, or new geometry.
2. <u>Geometry Qualification</u>: The majority of geometries that were built were low pressure ducting for use in the crew and avionics cooling and circulation. Representative geometries were created and used for destructive testing. The platform, machine, material, and build parameters were used as a baseline to map the processing of the material to the mechanical performance of the geometry as well as mapping these results to tensile specimens that were built near the geometry being tested. The destructive testing done was a burst test to ascertain the maximum pressure a given geometry could sustain under prescribed environmental factors that simulated real-life operations. Other tests conducted included drop and impact tests. Once a geometry performed at a level sufficient for implementation in the field, the resulting parameters, tensile specimen locations, tensile specimen

performance, machine definition, et.al. were used as flow-down engineering requirements for the manufacture of the given geometry. This qualification step was performed by the customer (Boeing and NAVAIR).

3. Platform Qualification: Given the material requirements, a unique platform (DTM Sinterstation 2000 and 2500) was qualified. This qualification had stringent requirements on the manufacturer of the laser, the firmware on the galvanometer scanners, manufacturer of the computer, computer operating system, DTM software version, and a host of other requirements. To allow for any hardware or software changes or upgrades, the platform would have to be re-qualified by the customer's materials and processing engineers. This qualification step, while necessary in the early adoption phase of specification development, proved to be a significant cost and time burden on production operations in a rapid changing environment. Early machines used a UNIX based operating system and migrated to Windows through this program. These simple changes required additional testing, and in some cases, it required the customer and supplier to maintain legacy equipment. This qualification step was performed by the customer (Boeing and NAVAIR) in conjunction with the supplier (DTM).
4. Machine Qualification: Each machine to be used in the production of parts were required to be qualified. There were restrictions on the equipment to be dedicated to the qualified material and solely to the production of the customer's parts. To qualify, the machine would have to run several successful qualification builds. If those builds were successful, the parts could be sold to the customer and enter the supply chain. Builds that did not pass the mechanical testing requirements were quarantined and the parts were disposed as scrap. The following is an abbreviated

list of machine settings: part heater setpoint, layer thickness, scan spacing, scan speed, laser power, part orientation, part location, number of tensile specimens, tensile specimen location, as well as several requirements on software and hardware revision control.

5. <u>Machine Qualification Restrictions</u>: The process-based specification placed most of the requirements on maintaining the quality standards on an individual machine configuration and the setpoints used to build a part. Listed below are several restrictions and where applicable the ability of the user to alleviate issues that arose during the production contract:

   - If the parts in a build do not achieve the minimum standard and subsequent root-cause-analysis found an issue with the laser, the laser would have to be repaired or replaced. Once a machine's laser is repaired or replaced, the machine is no longer qualified. To bring the machine into compliance, machine qualification builds would have to be redone and the data submitted to the customer for validation and recertification. In some cases, the customer would have to dispatch materials and process engineering staff to oversee certification operations.
   - If software upgrades were made through the course of the production contract, new machine configurations would have to be tested and added to the specification. In the event a qualified machine was to encounter a failure or require the need for a software upgrade, it would no longer be qualified. These requirements locked machines into a static configuration without the ability to be upgraded and increased the cost of ownership of legacy equipment.

- If an additional part was added to the statement of work, it would create a scenario where a custom build configuration would have to be qualified. If the additional part was able to be added to a preapproved build, the new build configuration would have to be approved and qualification builds made. This undue burden put financial and timeline restrictions on the customer and did not allow the producer to move parts from one build to another to maintain continuity in the supply chain. It is not uncommon in series production that a build configuration would have two of part X and two of part Y in a pre-approved build, but the production utilization demands might require four of part X to be produced one week and seven of part Y the following week.

2.9.2 PRODUCT-BASED SPECIFICATION

As the production of aerospace parts became more mature and the success of the parts in the field opened the door to new opportunities, the process-based specification became unmanageable because of the amount of bureaucratic support, the inability to maintain production on state-of-the-art equipment, and the inability of the contract manufacturer to make continuous improvements. Boeing as well as new players in the market started switching to product-based specifications to eliminate inefficiencies and allow for improvements in delivery time, part cost, and part quality. This product-based specification focuses more on the results than it does on the prescribed method to make the product. In summary, a product-based specification is one in which ‘the ends justify the means.’

The product-based specification still required material specifications and process specifications. The material specification was largely the same, but the product-based specification gave a broader definition of the process and more detailed definitions on physical testing and quality record. Several examples of the product-based specification follow:

- Parts must be fabricated on a laser-based powder bed fusion machine.
- Production equipment must operate under an audited aerospace ISO quality system: AS9100. (ISO Central Secretariat , 2015)
- Flame strips must be built using the flame strip CAD file and placed in the location and orientation shown in Figure 45. One flame strip from each build is to be tested according to the FAR 25.853 aerospace standard regarding transport category aircraft. (Federal Aviation Administration, 2017)
- A minimum number of tensile specimens are to be placed in every production build in the location and orientation shown in Figure 45. These bars are to be tested using an ASTM standard test method on equipment that is part of the quality system's calibration record. (ASTM Subcommittee D20-10, 2018)

The flow-down of these broader product-based specifications allow companies like Stratasys Direct Manufacturing to apply resources in statistical process control to increase yield, improve product quality, and decrease the production time required. Creating the requirements to operate in a quality system with specific mechanical testing requirements provided the production staff the tools necessary to find ways to understand and quantify a previously unknown process like laser sintering. Procedures such as testing the laser power before and after every build allowed the staff to know when there might be problems with the laser or restrictions in the optical path. Comparing data from multiple machines in respect to material used, date produced, or location yielded a greater understanding of the process on a macro level. The single greatest thing to come out of a product-based production standard was the amount of recorded data.

2.10 Mechanical Behavior in A Multi-Platform Production Environment

In the summer of 2007, Bell Helicopter had the requirement to use the laser sintering process to rapidly deploy a solution to the field. Traditional manufacturing methods could not meet the compressed timeframe and Bell Helicopter had just created and adopted new production specifications for the use of a nylon 11 material produced on 3D Systems equipment. The issue was that the V-22 Osprey had been grounded from operations in Afghanistan and Iraq. The Osprey was able to safely ascend in a green (safe) zone to a height that would minimize the risk of being damaged by small arms fire or shoulder mounted missiles – something the Marine helicopters were unable to do.

Figure 47: Laser Sintered Parts on the Nacelle of a Bell/Boeing V-22 Osprey (Kruse, 2010)

Increased deployment of the Osprey in a challenging environment eventually caused a component in the nacelle to fail. The sand in the region is highly abrasive and damages the rotors of the turbo-prop engine during take-off, landing and when the craft is hovering close to the ground. To mitigate the effect of the sand, a high-speed centrifugal fan is used to displace the sand before the air is pulled into the main engine. When the centrifugal fan bearings fail, the hydraulic system over-pressure and causes a rupture in the line at the air intake. Since the centrifugal fan is in the air intake duct, the leaking hydraulic fluid ignites and is pulled into the engine. This failure resulted in the destruction of several airship nacelles before an investigation and failure analysis pinpointed the root-cause. One of the solutions involved shunting the hydraulic fluid away from the engine intake and towards the tail end of the nacelle. Two sets of exterior mounted tubing on each nacelle were designed, built in laser sintering and tested. These parts, emphasized in the region bounded by a red circle, can be seen in Figure 47. Since a new product-based specification had recently been developed and approved by Bell Helicopter, Harvest was able to have production qualified parts in the field within six (6) weeks from the time of initial order. This rapid ramp-up for qualified aerospace production components was unprecedented, but the existence of a qualified standard for the use of additive manufacturing for end-use parts created a way to deploy the unique production solution in support of global assets.

Bell Helicopter required parts to be produced on a Sinterstation ® *2500plus* in the Duraform EX ® material which is an Arkema Nylon PA-11 variant. (3D Systems Staff, 2018) Parts produced required at least five (5) sacrificial tensile specimens to be built and all specimens were required to meet an Ultimate Tensile Strength (UTS) of at least 6,000 psi. An engineering build followed by first article production parts were built and inspected by Bell Helicopter engineering staff before the production contract was fully executed. A representative tensile specimen location can be seen in Figure 48. An addition to the newer production standards included the labeling of tensile specimens with orientation and location. In Figure 48 the tensile bars can be seen to have a primary axis of orientation aligned with the build direction (z-axis). The secondary axis is along the x-axis and there are three numbers for each of these tensile specimens. These numbers represent the location within the build of the centroid of the tensile specimen. The first number represents the distance in inches from origin of the build, located in the lower left corner with the first number being the distance along the x-axis, the second number represents y, and the third number represents z. Using this nomenclature, the yellow tensile bar in Figure 48 would be labeled “ZX 7.6.3”. The addition of these labels eventually contributes to a better understanding of how part location and build processing parameters affect mechanical properties.

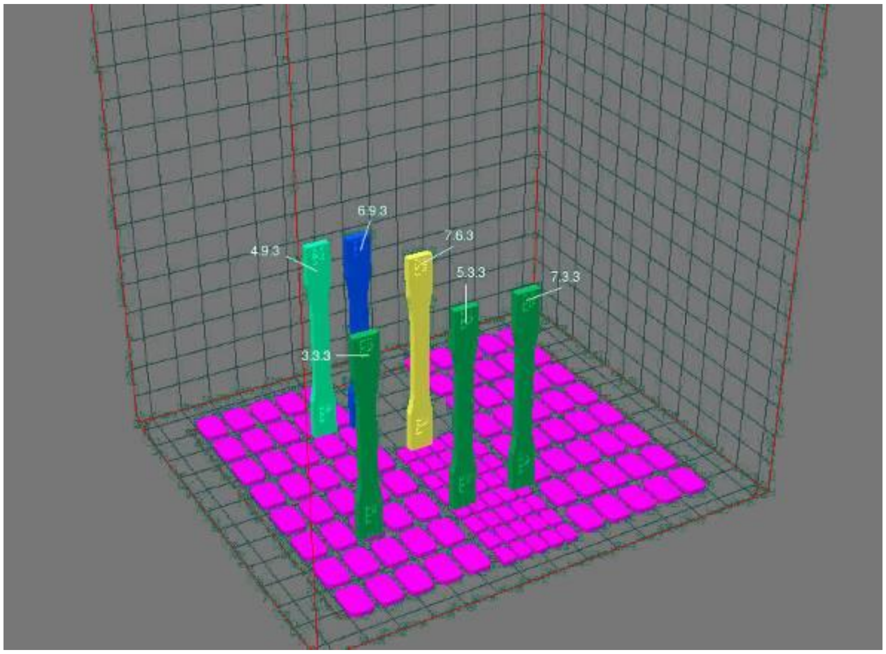

Figure 48: Example of Tensile Specimen Location

While there was initial success in building these parts, the compressed timeline required bringing multiple production platforms into service. It was the general assumption that using the same parameter sets on similar platforms with the same material feedstock would yield similar results. As additional machines were added, scrap rates started to increase. To put the effect of scrap rate into perspective, these parts were long cylindrical parts requiring multiple builds of at least 16". As a rule, laser sintered builds are quoted around $300/inch, putting a price tag of $4,800/build. The margin for production parts do not allow for a high scrap rate and the burden for performance is on the company manufacturing the parts. A 10% scrap rate adds roughly $500/build in additional cost.

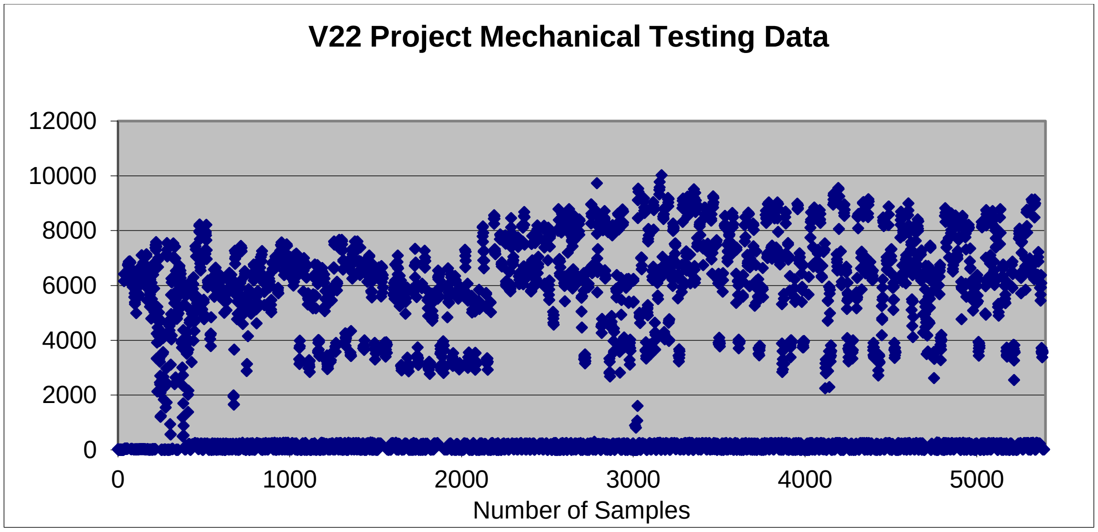

Figure 49: Subset of Data from Production Build Mechanical Testing

The new paradigm of multiple platform production under a compressed timeline required a new approach to process management. Since mechanical properties from tensile specimen data was being collected, a new database was created to capture this data for use in production workflow analytics and statistical process control. A sample of the V-22 project mechanical testing data can be seen in Figure 49. The data shown represents data for builds across multiple platforms and are arranged in no particular order. The scatter of data close to zero is elongation-at-break (EAB) that generally ranges from 0 to 20% and the rest of the data represents UTS which has a 6,000 psi requirement.

The data is segregated into UTS and EAB in Figure 50 and Figure 51 respectively. It can be seen while there are some broad ranges of results, the UTS is grouped generally around 6,000 psi with a maximum of 8,000 psi with a few outliers. The EAB has a grouping primarily in the 10-20% range, but with significant variations. These two charts correlate well with data shown by the University of Louisville in Figure 25 and Figure 26.

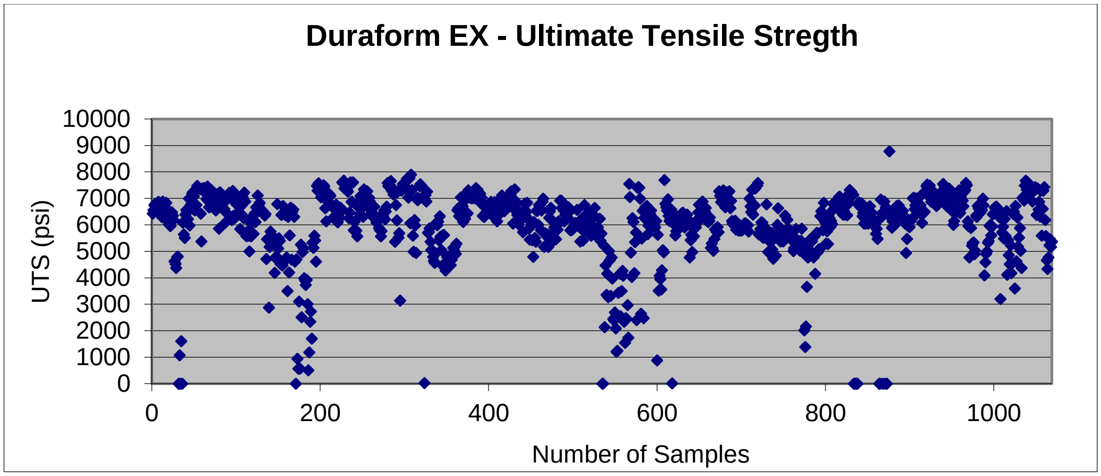

Figure 50: Ultimate Tensile Strength (UTS) Data

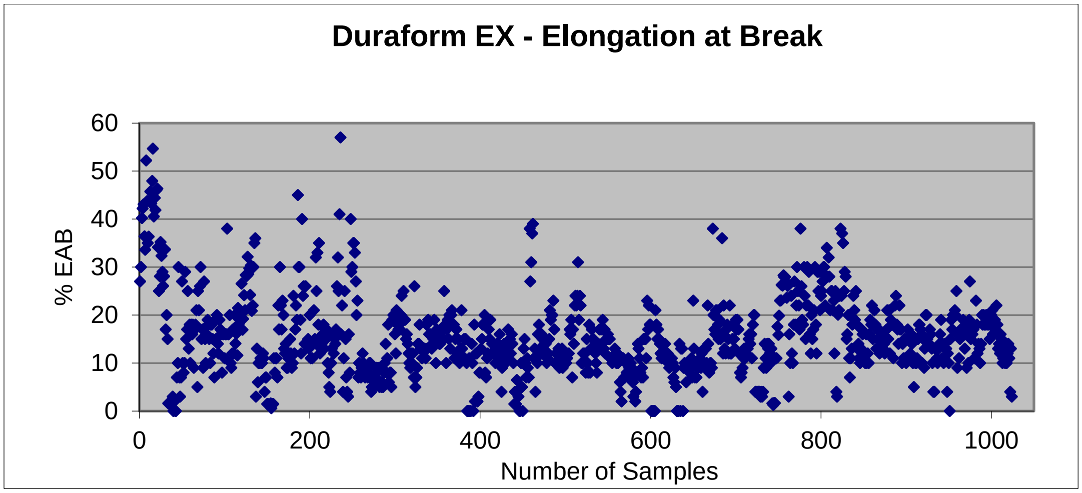

Figure 51: Elongation at Break (EAB) Data

While measuring mechanical properties is useful to determine the disposition of production builds into a "pass" category or a "failed" category, it was necessary to use the available data to help determine what parameters or machine issues might be affecting part quality and build success rate. Data was first segregated by machine serial number and evaluated. A sample size of 80 datapoints from a single machine can be seen in Figure 52. This data has not been grouped and individual data points are represented in no order, with the x-axis of the chart representing the number of datapoints being measured.

Grouping the data provided useful information on the average mechanical properties for a build and the range of that data. In addition, by looking at a set of build data it could be evaluated over time and linked to parameters, feedstock, and machine configuration changes. Each build had five (5) data points which were grouped to create a mean, a range, and a distribution. Three charts used to analyze the data include an X bar chart, an R chart, and a histogram which are shown in Figure 53, Figure 54, and Figure 55 respectively. The X bar chart shows the mean UTS, the R chart shows the range of the UTS, and the histogram aggregates the average UTS for all builds in the dataset.

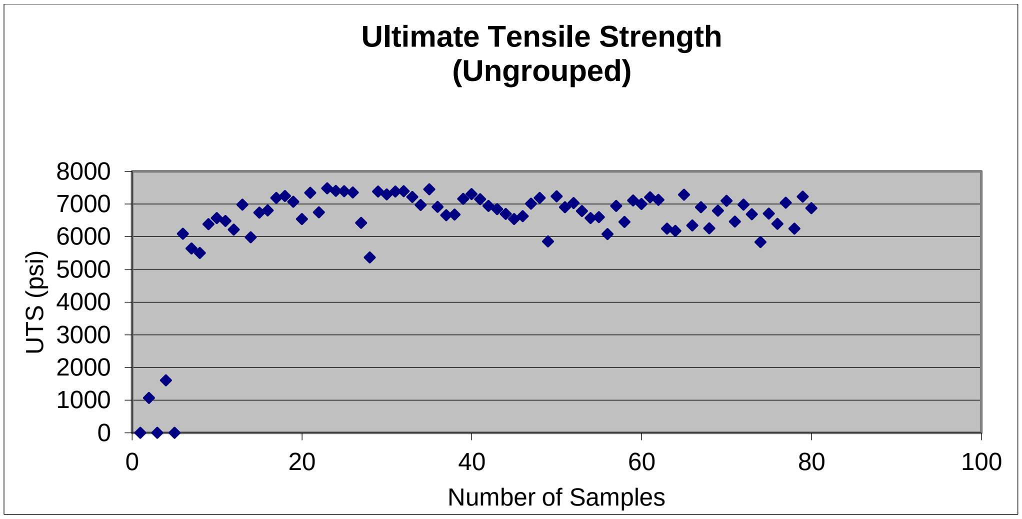

Figure 52: Machine 458 Ungrouped Ultimate Tensile Strength Data

Data was collected in a relational database that allowed mechanical properties to be mapped and analyzed in multiple ways. The data for the V-22 production builds is displayed in Figure 53, Figure 54, Figure 55, and Appendix A: Production Case Study Statistical Data. When analyzing the data in the appendix, mechanical properties improved over time with the mean UTS increasing and the range of UTS decreasing. The knowledge gained from this analysis allowed for a new machine (Serial Number 458) to be brought into production compliance after a single build. Figure 53 shows a failure to reach mechanical properties on the first build, but after evaluation of the system and parameter setpoints the user was able to create a successful build on the second try and continue to improve parameters and machine stability over the subsequent four (4) or five (5) builds.

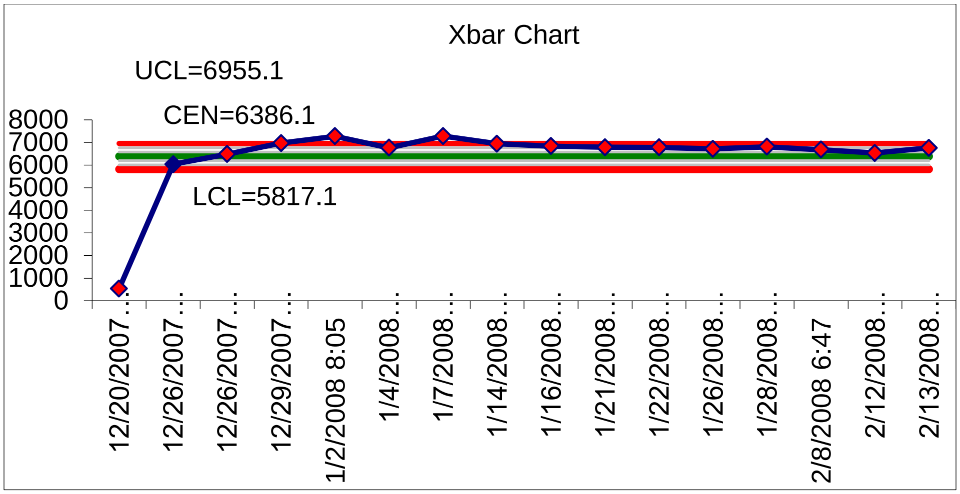

Figure 53: Machine 458 UTS Mean (X bar) Chart

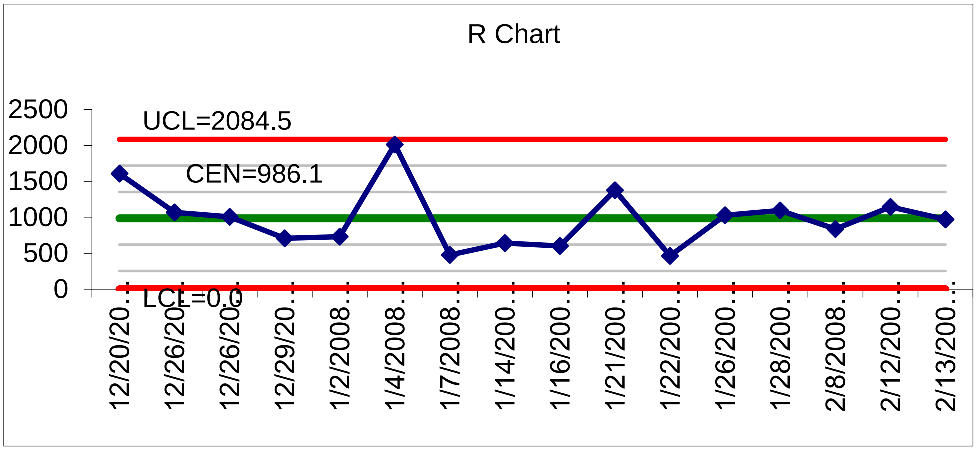

Figure 54: Machine 458 UTS Range Chart

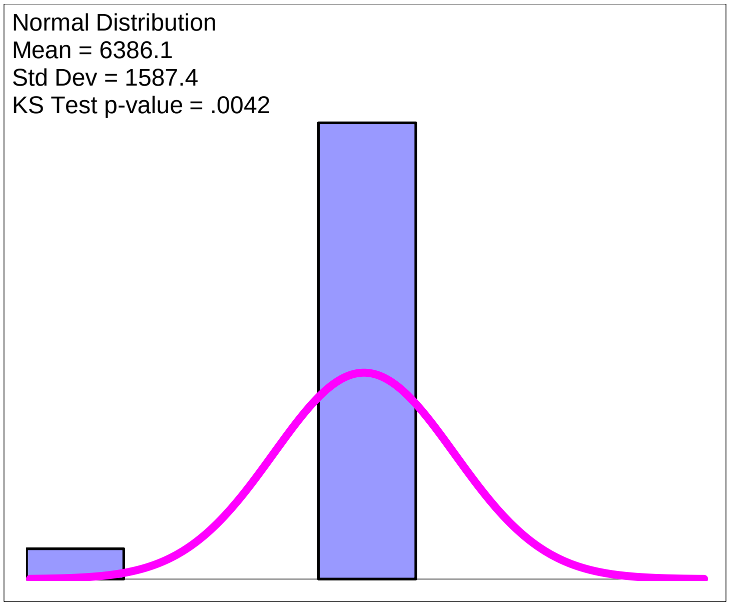

Mean = 6776

Std Dev = 489

1st build excluded

Figure 55: UTS Normal Distribution for Machine 458

There were several takeaways from this production case study that were assisted by the logging of mechanical property data and the circumstances surrounding the production of the parts:

- Having a regimented powder mixing and post processing strategy is critical in maintaining the best mechanical properties achievable.
- Maintaining a machine calibration and preventive maintenance schedule is critical to maintaining consistent build-to-build processing parameters and machine-to-machine performance. Leaking door seals that contribute to increase part bed convection, clouding optics that contribute to a decrease in laser power throughout the build, and IR sensor drift that contribute to unpredictable processing temperatures are several issues that contributed to inadequate part quality.
- Tracking mechanical testing data independently allows for the observation of trends related to machine configuration and parameter changes.

- The link between process settings and mechanical properties can be correlated between platforms.
- A matrix of settings and results help predict behavior on other systems as demonstrated by a new system being qualified in short order.
- An expanding R chart indicates a process that is becoming unstable and is a leading indicator for preventive maintenance.
- Shifts in data typically indicate a physical change in the equipment and settings.
- Duraform EX is particularly sensitive to thermal distribution at the surface and laser tuning. Other material systems are less dependent and require specific tuning and calibration that may be different from the experience with this material.

3.0 HYPOTHESIS

The statistical analysis of the mechanical property performance as it relates to machine configuration and processing parameters have shown that performance predictors such as energy-to-melt shown in Equation 4 are incomplete. As illustrated in Figure 56, the energy density or energy-to-melt ratio is only one aspect of the thermal history of any given laser sintered geometry. ***This study will attempt to derive a more complete thermal model of the laser sintering process that can be used to predict the mechanical performance of polymer laser sintered components.***

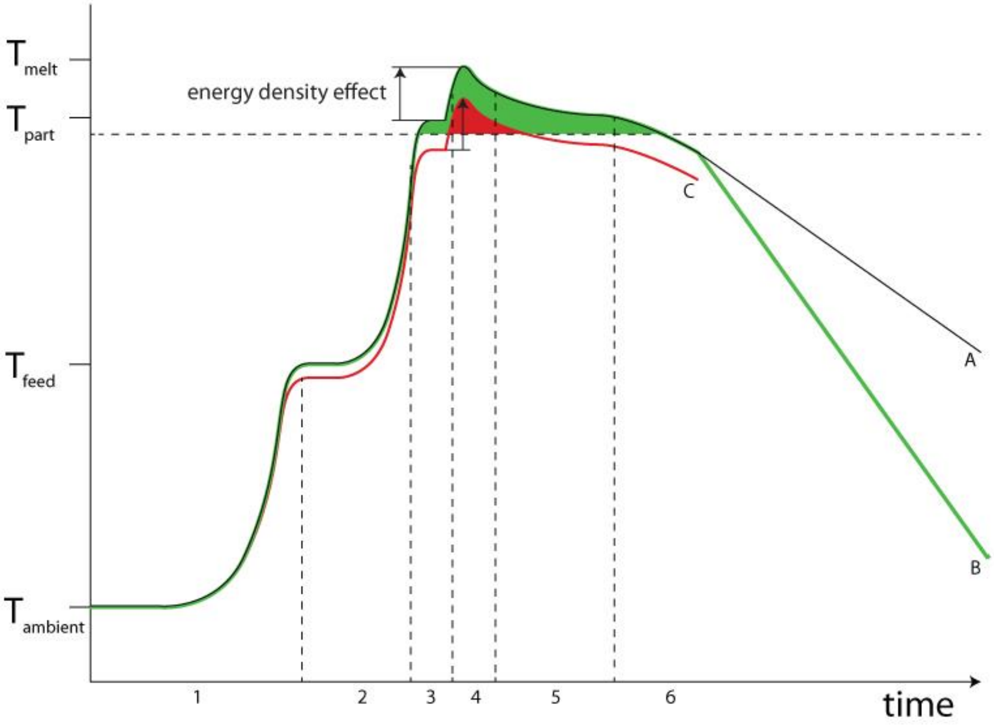

Figure 56: Schematic of the Thermal History Profile in Laser Sintering

4.0 THEORY AND MODELING

4.1 Theory of Sintering

According to Kang in Sintering: Densification, Grain Growth and Microstructure, sintering is one of the oldest technologies dating back to the prehistoric era with the firing of pottery. It wasn't until the 1940s that sintering was studied scientifically. The basic phenomena occurring during the sintering process are densification and grain growth. The sintering process can be divided into two categories: solid-state sintering and liquid-phase sintering. Solid-state sintering occurs when the powder coalesces completely in a solid state. Liquid phase sintering occurs when a liquid phase is present during the process. (Kang, 2005) In both cases the dominating factor for propagation of sintering is the reduction of surface energy. (Waldron, 1978) Neither of these processes require the presence of external pressure. In the case of polymer laser sintering the primary method for consolidation is in liquid or melt-phase sintering. This melt-phase occurs when laser energy elevates a selected region above the melt temperature.

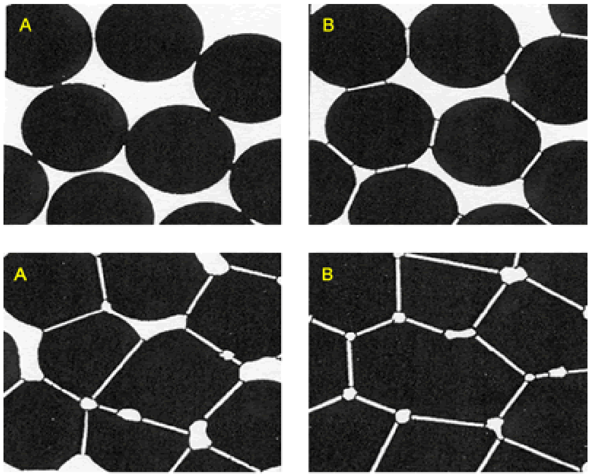

Figure 57: Stages of Sintering (Guzman, 2006)

Figure 57 shows the stages of sintering with the starting point in the top left consisting of contacting particles. With sintering the contacts grow and in the initial stage shown in the top right there is an extensive loss in surface area. As the sintering process progresses, the consolidation of particles starts to be defined more by the pores than the actual particles. (Guzman, 2006) An image of the microstructure of solid-state sintering and liquid state sintering can be seen in Figure 58 with regions showing large gaps between particles and some regions with full consolidation.

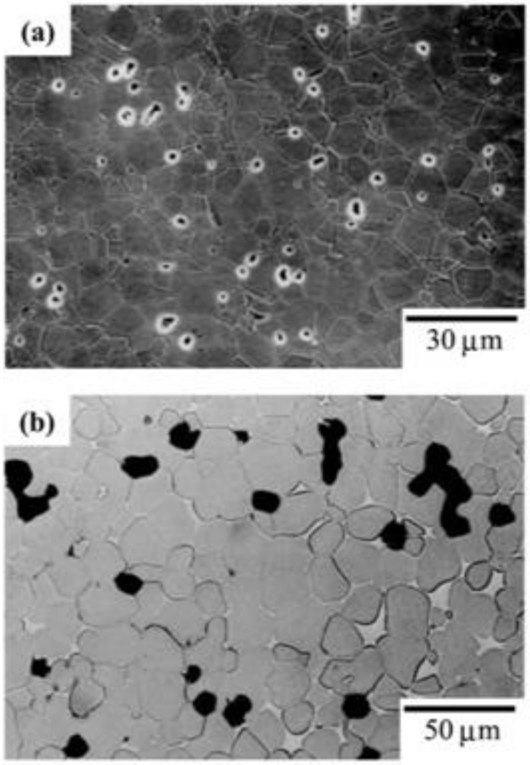

Figure 58: Microstructure in (a) Solid-State and (b) Liquid-State Sintering (Kang, 2005)

The first physical theory of sintering established by Ya. I. Frenkel “Viscous flow of crystalline bodies under action of surface tension” in which the cause of sintering and its transferring force were defined as sufficient of Gibb's surface energy. (Ristic & Milosevic, 2006) The process of flow takes place when there is a pattern of voids that are clearly defined, and which are present when processing powders. The first stage of sintering can be represented as the initial stage of liquid drops that touch each other before they are fully joined as a larger drop, illustrated in Figure 59.

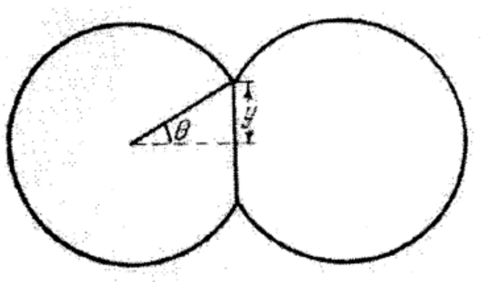

Figure 59: Schematic of Frenkel's First Stage of Sintering (Ristic & Milosevic, 2006)

According to this theory, the second stage of sintering takes place when the pores are completely overrun. As the powder particles coalesce and the pores shrink, they can be defined by their dihedral angle which is illustrated in Figure 60.

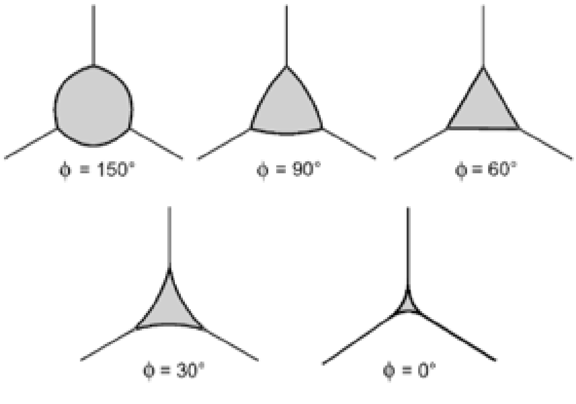

Figure 60: Distribution of a Second Stage of Sintering with Various Dihedral Angles (Kang, 2005)

When the pores are defined initially as the spaces between a number of close packed spheres, the pores described in Figure 60 can be more accurately illustrated like the pores shown in Figure 61. Comparing this schematic draws a strong comparison to the fracture surfaces shown in Figure 33 as well as the interface boundary specimen shown in Figure 40 and Figure 41.

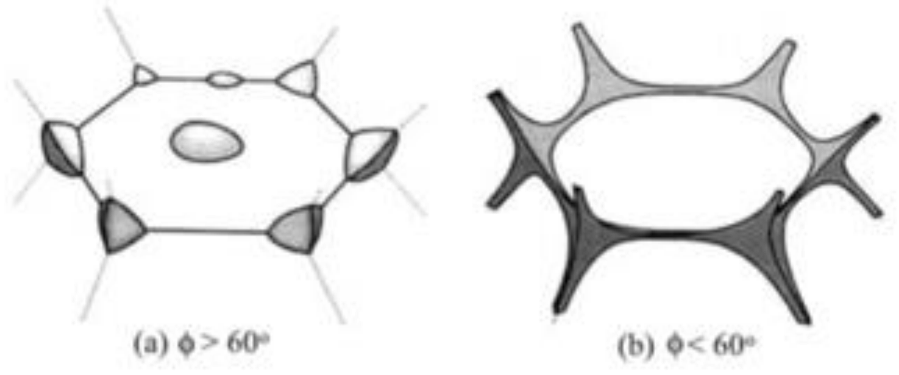

Figure 61: Schematic of Three-Dimensional Distribution of Second Phase Sintering (Kang, 2005)

It is reasonable to equate the shrinking of the dihedral angle during the second stage of sintering to the effective crack described in Section 2.7.4 Correlation of Physical and Visual Properties. It can therefore be assumed that full plasticity failure in laser sintered specimens reach a critical crack size characterized by the rate of the second stage of sintering with sufficient time for the pore sizes to fall below a critical value. The rate of the second stage of sintering is characterized by Equation 6 below:

$$\frac{da}{dt} = -\frac{3}{4}\frac{\sigma}{\eta}$$

Equation 6: Rate of Second Stage of Sintering (Ristic & Milosevic, 2006)

Ristic and Milosevic state in their journal article that while the first stage of sintering is dominated by surface tension, the second stage of sintering is dependent on the gas in the pores to be diffused and therefore subject to capillary pressure. They state through their literature search that Pines concluded that the kinetics of the process can be defined with the relation shown in Equation 7. **The following equation will serve as the basis to find the critical pore size that allows for laser sintered specimens to achieve improved ductility through full plasticity failure.**

$$\frac{da}{dt} = -\frac{2\sigma}{a^2} \times \frac{\delta^3}{kT} D$$

Equation 7: Kinetics of Second Stage of Sintering (Ristic & Milosevic, 2006)

4.2 Thermal Model

A laser sintered part is formed when a heated powder bed is irradiated by laser energy to bring the affected part sufficiently above the melting point to promote particle consolidation. The heaters used to irradiate the surface of the powder in three zones are shown in Figure 62. Each of these zones are controlled using non-contact infrared (IR) sensors. Two radiant heaters preheat the feedstock in the zones labelled below as Left Feed Heater and Right Feed Heater. The third radiant heater maintains the part build area surface temperature. Two heaters used as conduct heaters for the part build area are also found in Figure 62. The piston heater conducts thermal energy to the bottom of the build area and maintains a boundary condition at the Piston Heater Setpoint. The cylinder heater conducts thermal energy through the side-walls of the part build area and maintains a boundary condition at the Cylinder Heater Setpoint.

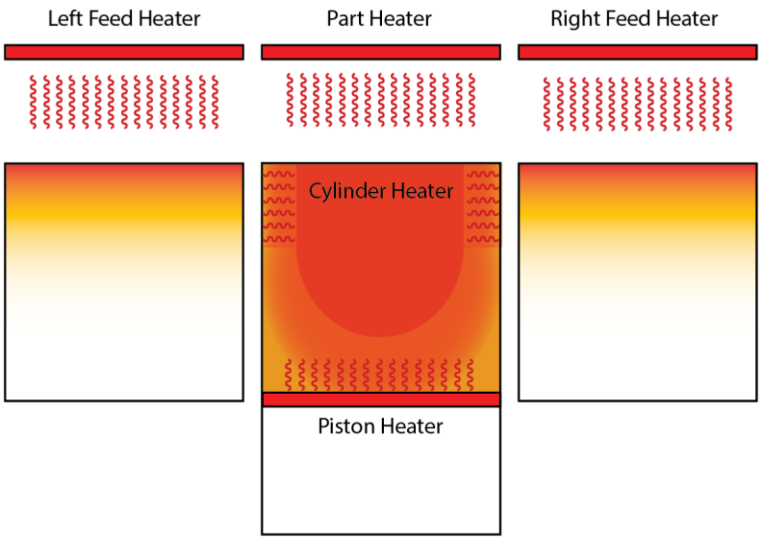

Figure 62: Thermal Schematic of a Laser Sintering System

4.2.1 TEMPERATURE DISTRIBUTION AND THERMAL RESISTANCE

While convection is present at the powder bed surface, it has been assumed in the machine design and in practice that the radiant heaters provide enough heat flux to balance the convective cooling of the top surface and maintain a constant temperature across the left feed zone, right feed zone, and part build zone. It is an objective of this research to create a thermal model of the thermal lifecycle of a laser sintered part so that mechanical properties can be mapped not only to processing parameters but to quantifiable a thermal processing history. It is also an objective to create a thermal model that can be used to predict mechanical properties.

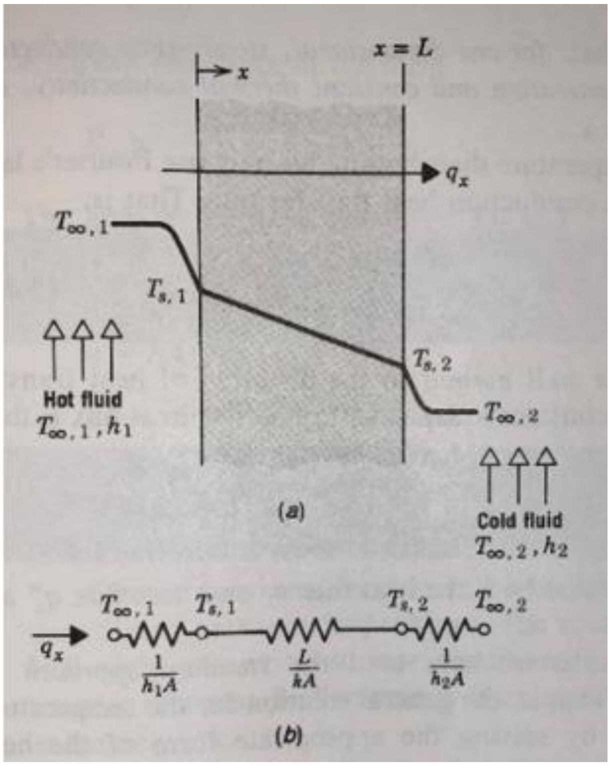

Figure 63: Heat Transfer through a Plane Wall. (a) Temperature Distribution (b) Equivalent Thermal Circuit (Incropera & De Witt, 1990)

The primary region of interest in the laser sintering process is the part build area. The temperature distribution is maintained through a set of boundary conditions and is affected by the thermal conductivity of the powder. Figure 63 illustrates heat transfer through a plane wall with multiple boundary conditions and shows how heat transfer can be represented through equivalent thermal circuits. Furthermore, the conductive thermal resistance formula mirrors Ohm's law of electrical resistance in the form shown in Equation 8.

$$R_{t,cond} \equiv \frac{T_{s,1} - T_{s,2}}{q_x} = \frac{L}{kA}$$

Equation 8: Conductive Thermal Resistance (Incropera & De Witt, 1990)

> *Where* $\boldsymbol{R}_{(\boldsymbol{t,cond})}$ *is the thermal resistance of conduction,* $\boldsymbol{T}_{(\boldsymbol{s},\mathbf{1})}$ *and* $\boldsymbol{T}_{(\boldsymbol{s},\mathbf{2})}$ *are the surface or boundary condition temperatures,* q_x *is the heat transfer rate in a specific direction (x), L is the characteristic length in that direction,* k *is the thermal conductivity, and* A *is area.*

Equivalent thermal circuits may also be used for more complex systems such as composite walls. Such walls may involve any number of series of parallel thermal resistances due to layers of different materials. The heat transfer rate can be related to the temperature difference and resistance associated with each element. (Incropera & De Witt, 1990) In the case of laser sintering bulk powder has a consistent thermal conductivity but will have varying thermal gradients due to the location of a node within the build and its proximity to the boundary conditions. Therefore, it is helpful to divide the thermal solution into a higher fidelity of nodes like the heat transfer rate equation for a composite wall shown in Figure 64 through a multi-dimensional analysis.

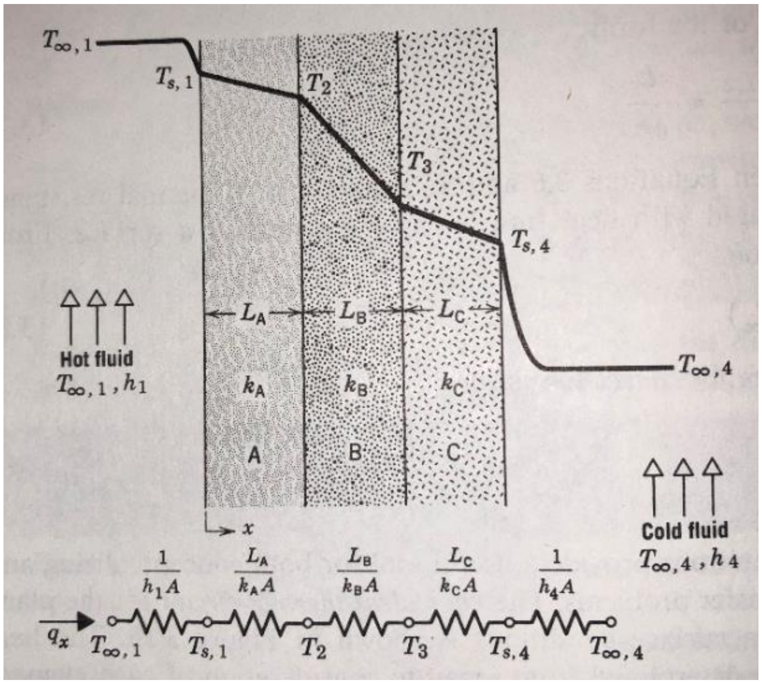

Figure 64: Equivalent Thermal Circuit for a Series Composite Call (Incropera & De Witt, 1990)

4.2.2 TWO-DIMENSIONAL STEADY-STATE CONDUCTION

Most of the time, two-dimensional problems involve geometries and/or boundary conditions that cannot be generalized with the use of shape factors or broad assumptions. In these cases, the best alternative is often one that uses numerical, or finite-difference, techniques. These techniques are often solved in thermal finite-element analysis software with significant computing power. (Incropera & De Witt, 1990)

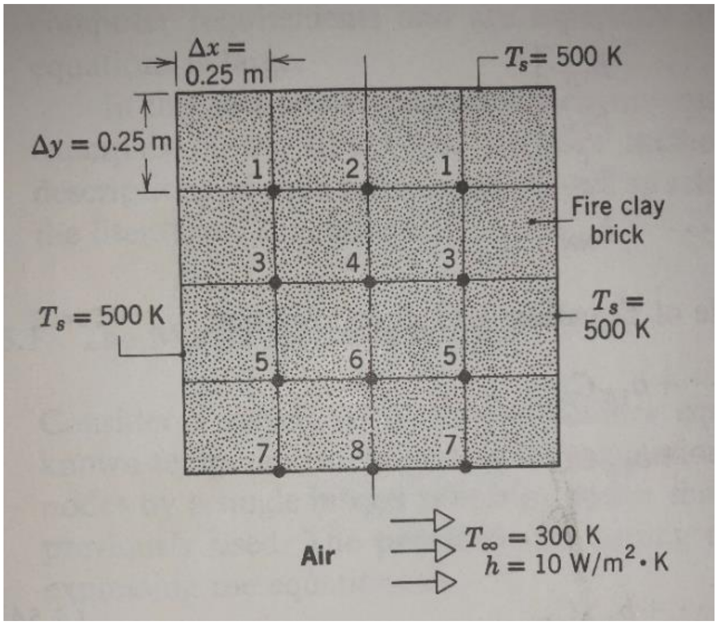

Figure 65: Schematic of a Sample Geometry with Nodes and Boundary Conditions (Incropera & De Witt, 1990)

The use of a nodal network allows for the determination of an average temperature within the region. To have more fidelity of the model, a relatively simple region might have to be divided into many nodes. An example of a thermal model with multiple nodes and symmetry can be seen in Figure 65. Modern software tools allow for higher fidelity regions where there are anticipated gradients and larger nodes in regions that may represent more stable thermal properties. Once the nodal network has been established and appropriate finite-difference equations have been written for each node, the temperature distribution may be determined. Numerous methods are available to determine the temperature distribution, but most require significant preparation and computing power. The most effective method is an iterative method like the matrix inversion method which is expressed in Equation 9 through Equation 11. (Incropera & De Witt, 1990)

$$
\begin{array}{ccccccccccc}
a_{11}T_1 & + & a_{12}T_2 & + & a_{13}T_3 & + & \cdots & + & a_{1N}T_N & = & C_1 \\
a_{21}T_1 & + & a_{22}T_2 & + & a_{23}T_3 & + & \cdots & + & a_{2N}T_N & = & C_2 \\
\vdots & & \vdots & & \vdots & & \vdots & & \vdots & & \vdots \\
a_{N1}T_1 & + & a_{N2}T_2 & + & a_{N3}T_3 & + & \cdots & + & a_{NN}T_N & = & C_N
\end{array}
$$

Equation 9: Numerical Representation of Thermal Nodes (Incropera & De Witt, 1990)

where a and C are known coefficients and constants involving quantities like Δx*, k, h, and* T_∞.

Using matrix notation, these equations can be expressed as:

$$[A]\,[T] = [C]$$

Equation 10: Thermal Nodes in Simple Matrix Form (Incropera & De Witt, 1990)

$$\mathit{Where}\ \ A \equiv \begin{bmatrix} a_{11} & a_{12} & \cdots & a_{1N} \\ a_{21} & a_{22} & \cdots & a_{2N} \\ \vdots & \vdots & \vdots & \vdots \\ a_{N1} & a_{N2} & \cdots & a_{NN} \end{bmatrix} \quad \mathrm{T} \equiv \begin{bmatrix} T_{11} \\ T_{21} \\ \vdots \\ T_{N1} \end{bmatrix} \quad \mathrm{C} \equiv \begin{bmatrix} C_{11} \\ C_{21} \\ \vdots \\ C_{N1} \end{bmatrix}$$

The solution vector may now be expressed as

$$[T] = [A]^{-1}[C]$$

Equation 11: Matrix Inversion Method Solution Vector (Incropera & De Witt, 1990)

Where $[A]^{-1}$ is the inverse of $[A]$ and is defined as:

$$[A]^{-1} = \begin{bmatrix} b_{11} & b_{12} & \cdots & b_{1N} \\ b_{21} & b_{22} & \cdots & b_{2N} \\ \vdots & \vdots & \vdots & \vdots \\ b_{N1} & b_{N2} & \cdots & b_{NN} \end{bmatrix}$$

Using numerical methods to solve problems for complex shapes or three-dimensional geometries is cumbersome and has limited utility considering thermal solvers and finite analysis software packages. But, understanding the basis for the solver packages with respect to nodes, governing equations, and the interaction between multiple components at the boundary conditions assists in getting a more complete thermal solution or simulation.

4.2.3 LASER SINTERING THERMAL MODEL

When considering the thermal energy to build a laser sintered part, one must consider the laser energy component enumerated in Equation 4 along with the build region located at the center of the schematic in Figure 62. These two components require different types of thermal analysis, so for the sake of this study, the energy provided by the laser is assumed to be at an optimal level to initiate the first stage of sintering. Once the powder has been consolidated in order to define the cross-sectional region of the desired geometry, the part and surrounding material will continue to be influenced by the build for an amount of time to complete a production build.

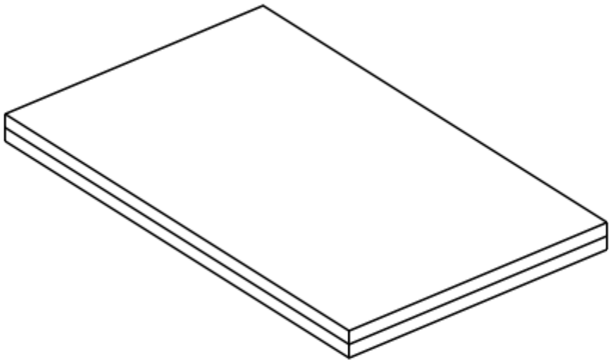

Figure 66: Schematic of a Simple Two-Layer Build Geometry

Since a laser sintered part is built in multiple layers, the thermal model cannot be assumed to be a static mass defined by a geometric bounding box. Parts are created by preheating the powder bed and forming a single layer which will be repeated many times. To develop an accurate thermal model, it needs to be assumed that there will be a dynamic pattern of layers added and heated. A simple illustrated of a rectangular build region divided into two layers is shown in Figure 66. A primitive layer will be used as the foundation of the thermal model and a thermal coupling technique will be employed to create a complete thermal simulation of a laser sintering build.

Once the build region has been defined into a subset of nodes, the thermal history can be used to analyzed at individual nodes over a period or at a point in time. Figure 67 is a schematic of a laser sintering machine with a blue dot representing a voxel of powder. This voxel thermal history prior to being deposited on this point would have transitioned from ambient temperature through the feed heating setpoint and eventually to the part heater setpoint.

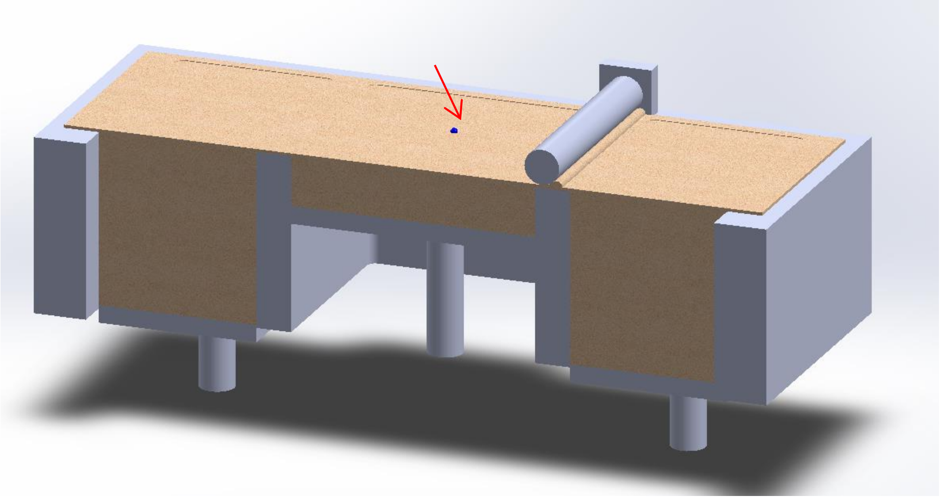

Figure 67: Illustration of a Voxel (Node) at the Top Surface of the Build Region

As a part is built a voxel of material will either be affected by the laser and transition through melt-phase sintering or it will reach a maximum temperature close to the part heater setpoint. Figure 68 shows the voxel in relation to a sample geometry with the surrounding powder being transparent so that the build area boundary can be clearly seen.

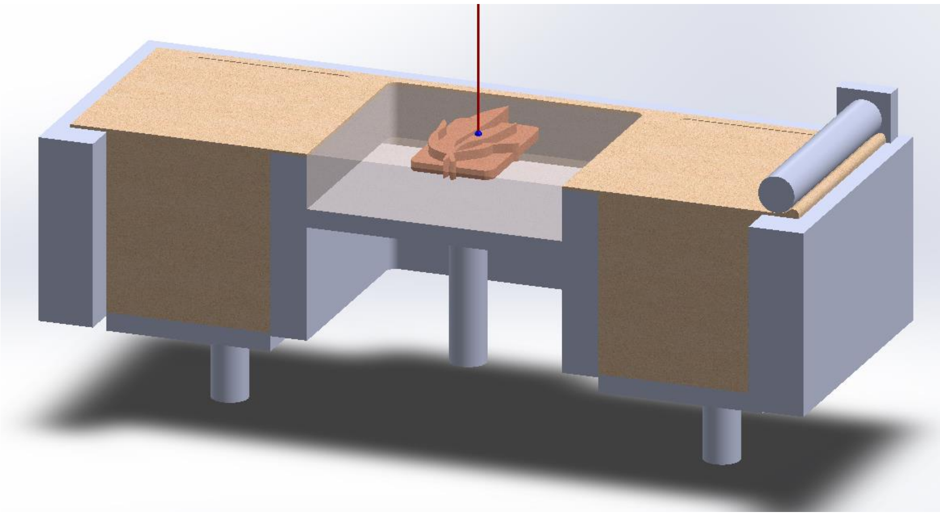

Figure 68: Voxel (Node) in Relation to a Build Geometry

During the build progression new layers are added and the part geometry travels away from the build plane, eventually being buried by feedstock powder. Figure 69 shows the build as it nears the end of the build cycle with the representative voxel being towards the bottom of the build region. It should be noted that if there were no other geometries processed during the build, additional build layers would not be required, and the subject geometry would be at the top of the build. In this illustration, a single geometry is shown without additional geometries obscuring the representative voxel.

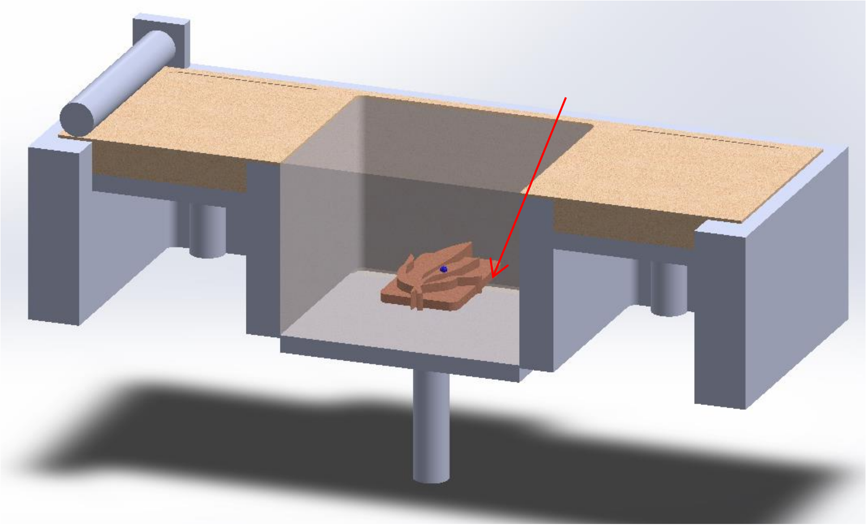

Figure 69: Voxel (Node) after Many Build Layers are Processed

When the temperature for a representative voxel is charted over time, it will progress through six (6) stages and experience temperatures from ambient room temperature to a temperature close to the melt point. Table 6 gives a description of these stages with the temperature range and the stage numbers corresponding to the schematic in Figure 56.

No	**Stage**	**Temperature Range**
1	Feed Piston	Ambient to ~130°C
2	Add Powder Layer	130°C to ~160°C
3	Build Layer	180°C
4	Melt Stage (Laser)	>185°C
5	Post Melt Build Stage	180°C to ~150°C
6	Cooldown	150°C to Ambient

Table 6: Thermal Stages During a Laser Sintering Build Life Cycle

The key machine processing parameters used are marked on the y-axis of Figure 56. These setpoints correspond to key measurements derived from the feedstock DSC shown in Figure 70. If the bulk powder is heated to a temperature close to are above the material's solidification temperature, it will become tacky and will be unable to flow in a way that small layers (0.004"-0.010") can be reliably deposited. Therefore, the feed temperature setpoint (T_{feed}) must be 10°C to 20°C below the solidification temperature. Similarly, if the powder is heated above the onset of melt, particles will start to consolidate in a way that a fused part cannot be separated from the sintered material surrounding it. For this reason, the part bed temperature setpoint (T_{part}) should be in the processing window that is called out in Figure 70. To maximum mechanical properties and minimize distortion, the part bed should be set within a few degrees of the onset of melt but not exceed it. Finally, the energy required to melt the material as discussed and represented by Equation 4 must be enough for the laser melt pool to affect the previously melted layer and that the subject geometry build layer must be fully melted without degrading the polymer chains.

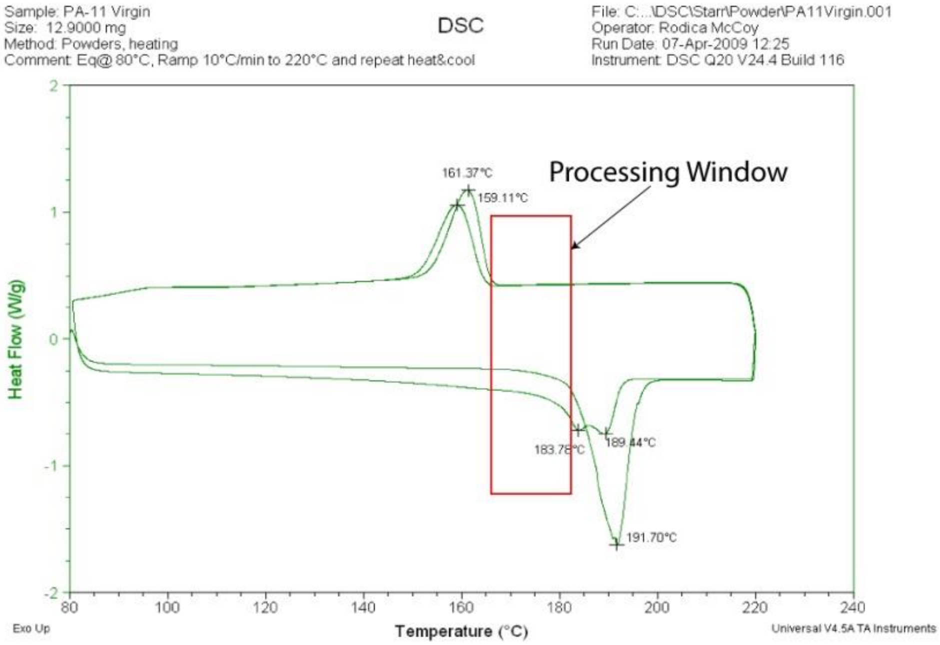

Figure 70: Differential Scanning Calorimetry (DSC) of Nylon Polyamide 11

4.3 Thermal Simulation

ANSYS® version 18.2 is a computational fluid dynamics program that was used for thermal analysis and simulation. (Ansys Staff, 2018) Solidworks® 2018 was used to create the geometry used in the simulation, ANSYS Fluent thermal solver was used for the simulation, and TecPlot 360 EX 2018 R1 was used to display the data and output thermal history. (Solidworks Staff, 2018) (Tecplot Staff, 2018)

4.3.1 Mesh Creation

For the more detailed simulation model used to analyze the interaction between sequential layers, a very fine mesh was applied to all surfaces with an increase of the mesh at the boundary conditions. To create this mesh, the Mesh tool must be selected within the Fluent Project Dialogue box shown in Figure 71 and will bring up the details of the mesh shown in Figure 72. The resultant mesh for the ten (10) layer simulation can be seen in Figure 73 with each layer having a slightly different color to record the contrast between layers. When analyzing the mesh fidelity, there is significant detail to record the interaction at the layer boundary conditions.

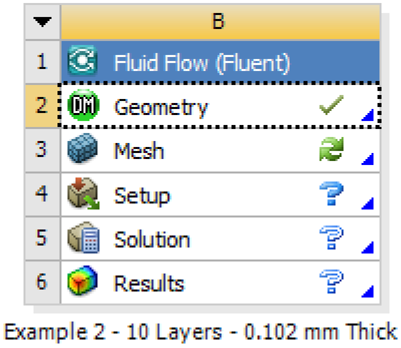

Figure 71: Fluid Flow (Fluent) Project Dialogue Box

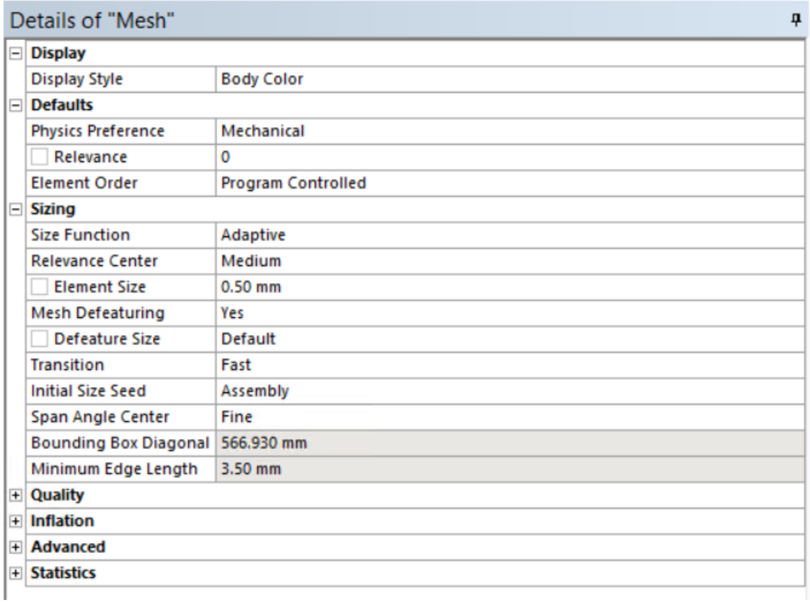

Details of "Mesh"

⊟ **Display**	
Display Style	Body Color
⊟ **Defaults**	
Physics Preference	Mechanical
☐ Relevance	0
Element Order	Program Controlled
⊟ **Sizing**	
Size Function	Adaptive
Relevance Center	Medium
☐ Element Size	0.50 mm
Mesh Defeaturing	Yes
☐ Defeature Size	Default
Transition	Fast
Initial Size Seed	Assembly
Span Angle Center	Fine
Bounding Box Diagonal	566.930 mm
Minimum Edge Length	3.50 mm
⊞ **Quality**	
⊞ **Inflation**	
⊞ **Advanced**	
⊞ **Statistics**	

Figure 72: Fluent Mesh Details

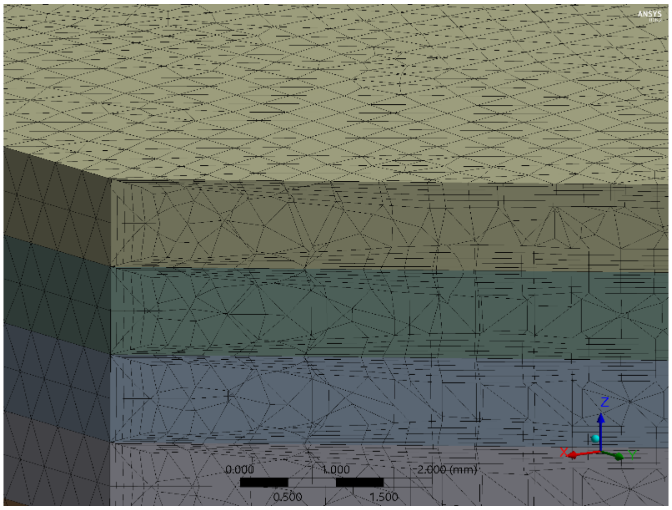

Figure 73: Closeup of Mesh Fidelity

4.3.2 LASER SINTERING POLYAMIDE THERMAL PROPERTIES

The material properties used for this simulation are based on a paper written by Maggie Yuan and are detailedin Figure 74. (Yuan, Bourell, & and Diller, 2011)

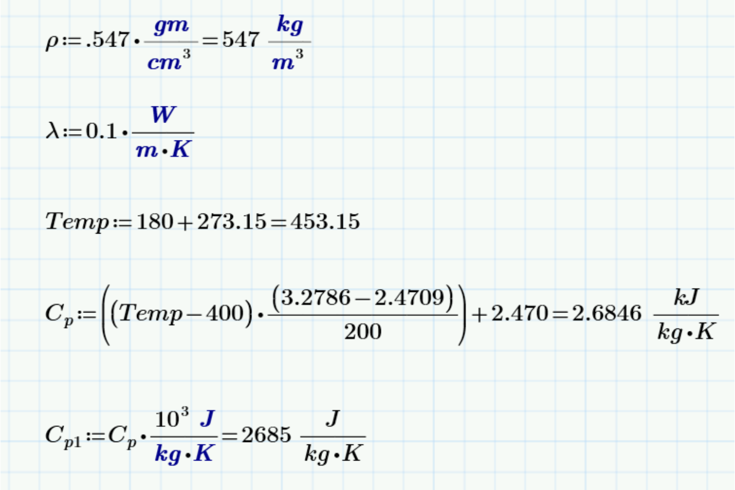

$$\rho := .547 \cdot \frac{gm}{cm^3} = 547\ \frac{kg}{m^3}$$

$$\lambda := 0.1 \cdot \frac{W}{m \cdot K}$$

$$Temp := 180 + 273.15 = 453.15$$

$$C_p := \left((Temp - 400) \cdot \frac{(3.2786 - 2.4709)}{200}\right) + 2.470 = 2.6846\ \frac{kJ}{kg \cdot K}$$

$$C_{p1} := C_p \cdot \frac{10^3\ J}{kg \cdot K} = 2685\ \frac{J}{kg \cdot K}$$

Figure 74: Laser Sintering Polyamide Thermal Properties

4.3.3 SIMULATING A MULTI-LAYER THERMAL PROBLEM

To simulate a full build, boundary conditions for each layer must be manipulated and layers must be activated and deactivated. For example, if there is to be a ten (10) layer build and the first layer is to be simulated, layers 2-10 are deactivated and layer 1 is activated. The initial layer is given a temperature with front, back, bottom, and side boundary conditions that would correspond to the thermal architecture of the laser sintering equipment. A flux of 50 W/m^2·k is applied to the top layer that simulates the radiant heater. The automatic solution and case modification dialogue box used for performing these tasks is shown in Figure 75.

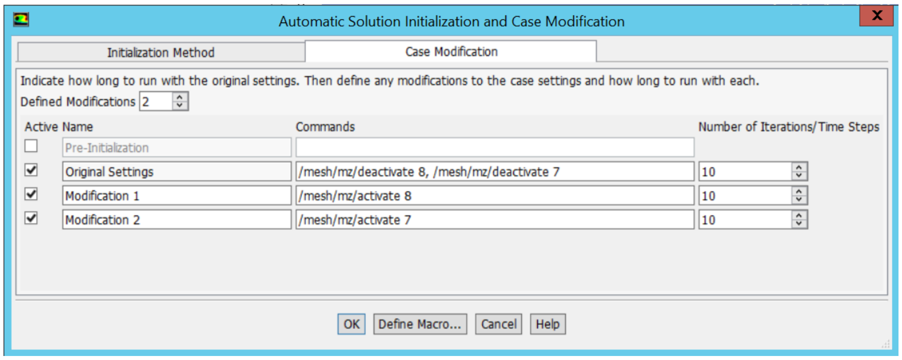

Indicate how long to run with the original settings. Then define any modifications to the case settings and how long to run with each.

Defined Modifications 2

Active	Name	Commands	Number of Iterations/Time Steps
☐	Pre-Initialization		
☑	Original Settings	/mesh/mz/deactivate 8, /mesh/mz/deactivate 7	10
☑	Modification 1	/mesh/mz/activate 8	10
☑	Modification 2	/mesh/mz/activate 7	10

Figure 75: Layer Activation and Editing

The process for activating layers and preparing the geometry for simulation are listed below:

1. Activate/deactivate layers:
   /mesh/modify-zones/deactivate xx (where xx is the layer id)
   /mesh/modify-zones/activate xx (where xx is the layer id)

   Example shown in Figure 75:
   /mesh/modify-zones/deactivate 8, /mesh/mz/deactivate 7
   /mesh/modify-zones/activate 8
   /mesh/modify-zones/activate 7

2. Define Boundary Condition to utilize Heat Flux (50 W/m2-k) on wall called "top1":

   /define/boundary-conditions wall top1 0 no 0 no yes heat-flux no 50 no no 1

3. Define Boundary Condition to be coupled on wall called "top1":

   /define/boundary-conditions wall top1 0 no 0 no yes coupled no no 1

4. Setting up initial temperatures for each layer:
   - Make sure each cell zone is clearly defined
   - Initialize the hybrid case
   - Select the desired cell, click and set desired initial temperature
   - Repeat process for additional cells

4.3.4 SIMULATING A MULTI-LAYER THERMAL PROBLEM AND DISPLAYING RESULTS

Once the construction of the thermal model has been completed, the simulation can run with multiple data export functions. TecPlot 360 (version EX 2018 R1) was chosen to provide a method for viewing the thermal data history, animating the progression of a build, and viewing both 2D and 3D data. (Tecplot Staff, 2018) To use the TecPlot viewing software, the user executes the *Simulate* action within ANSYS, chooses and exports to a TecPlot native data file with a time constant. In this simulation, a time constant of once per second was used for the three (3) layer model and every thirty (30) seconds for the one hundred twenty-five (125) layer model.

The TecPlot post processor was used to enable visualization and export voxel thermal history. A sample case is shown in Figure 76 with the cross-sectional thermal map on the left and the voxel thermal history on the right. A point or node can be selected on the left screen and after some processing time, the thermal history of that node is plotted against time (in seconds). This data can then be exported to an excel file for further analysis.

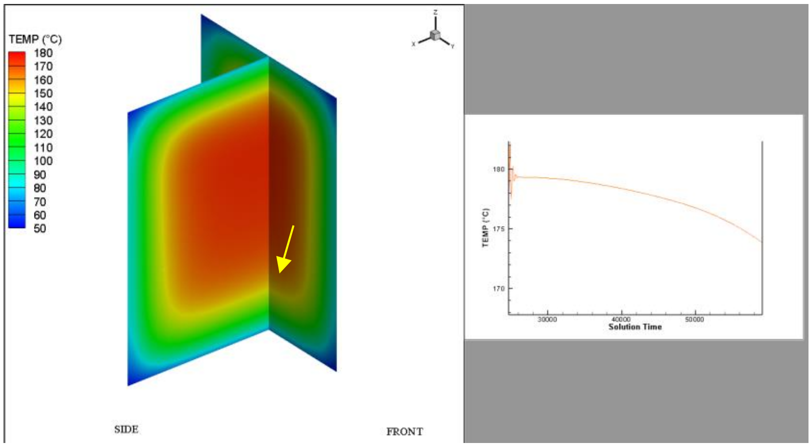

Figure 76: TecPlot 360 Post Processing Data View (Tecplot Staff, 2018)

The initial model was set up and tested with a top layer boundary condition of 180°C with bottom and side boundary condition of 150°C depicted in both Figure 77 and Figure 78. This initial test helped fine tune the mechanics of enabling sequential layers to simulate a laser sintering build. Initially, the fidelity of the model was limited and there were issues with the boundary conditions not coupling correctly in the model. Analyzing these two figures, there is a limited effect of the side boundary conditions in the top layers. As work was done to fine-tune this model, it became a representative model. The details are discussed in greater detail in Section 6.4 ANSYS® Fluent Thermal Model.

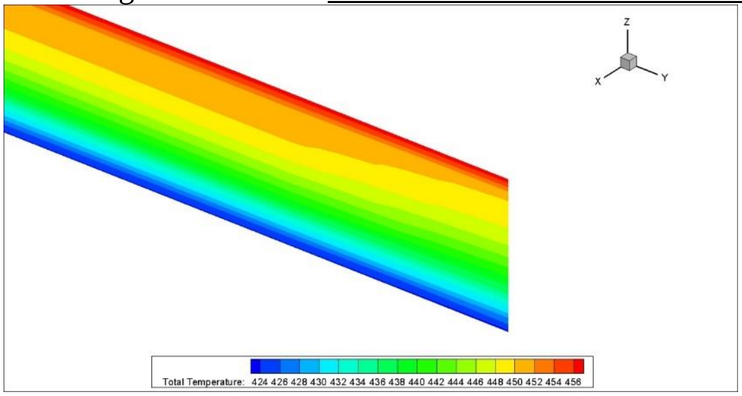

Figure 77: Visualization of a Simple Ten (10) Layer Thermal Model

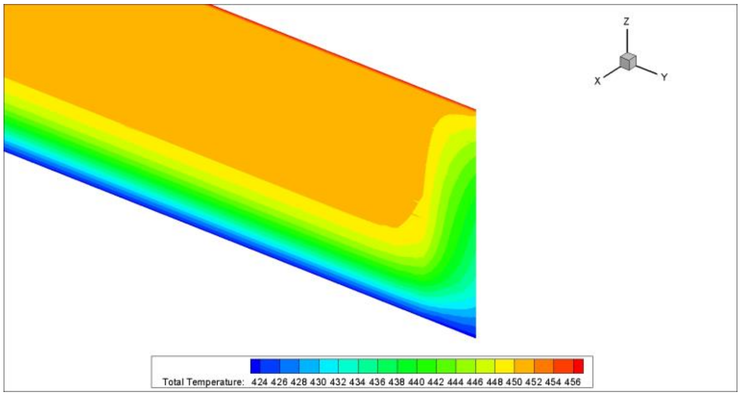

Figure 78: Visualization of a one-hundred (100) layer thermal model.

5.0 EXPERIMENTAL

5.1 Production Dataset

Harvest Technologies, a production service bureau acquired by Stratasys in 2014 and subsequently combined to form the service bureau Stratasys Direct Manufacturing maintains an ISO:AS9100 certified production facility located in Belton, TX. The AS9100 standard is an aerospace quality standard that insures the production systems and data are managed to a standard that allows for certification of customer quality specifications and traceability of components used in commercial aerospace applications. (International Standards Organization, 2016) As part of the quality system, tensile data is collected and becomes a part of the company's quality record.

5.1.1 NYLON POLYAMIDE 11 AEROSPACE PRODUCTION

Stratasys Direct Manufacturing has produced a significant number of laser sintered components for end use parts since 2007. In addition to work done for Bell Helicopter on their V-22 Osprey, work has included long-term production support for the Boeing 787 Dreamliner, pictured in Figure 79. In an article written in 2010 about the Society of Manufacturing Engineers honoring Rethia Williams of Boeing for her contribution to the Rapid Technologies and Additive Manufacturing industry, there is specific mention of the material being used in laser sintering for commercial aerospace applications:

> *The Dreamliner is best known for its groundbreaking use of carbon composites in 50 per cent of its structure, including the fuselage and the wings. It has not been well known that the aircraft also breaks new ground in widespread use of parts created by the direct digital manufacturing process. The 787 features more than 30 air ducts manufactured by laser sintering using specially developed FR-106 flame-retardant nylon from Advanced Laser Materials of Belton, TX.* (Design News Staff, 2010)

As discussed in the background, ASTM D638 tensile specimens are produced in each build for quality verification. (ASTM Subcommittee D20-10, 2018) This data becomes part of the quality record for all commercial aerospace customers. Due to the sensitive nature of material and process specifications, any specific mention of program requirements or actual material and processing parameters are not disclosed. The FR-106 material is a flame-retardant nylon PA-11 produced by Advanced Laser Materials, an EOS subsidiary. The preponderance of the production parts has been done on 3D Systems' sPro 60 laser sintering platform. (3D Systems Staff, 2018)

Figure 79: Boeing 787 Fuselage Assembly (Milberg, 2017)

5.1.2 RELATIONAL DATABASE

More than 80,000 data points measuring the tensile properties of laser sintered polyamide nylon 11 were used for this study. This tensile data is saved in a SQL database that allows a user to analyze the measured tensile properties with respect to build location, orientation, feedstock material, production platform, user and other pertinent data that can be used for statistical process control and part traceability. This data is part of an ISO AS9100 quality system that provides a strong ecosystem of policies and procedures related to data integrity with requirements for calibration procedures.

The SQL database is a relational database that allows for key data to be linked to related datasets within the database which is represented in Figure 80. (Codd, 1970) These relationships maintain referential integrity through a one-to-many relationship illustrated with '$1 - \infty$.' In practical terms, a single machine can have many builds and a single build can have many tensile bars. These relationships allow a user to create a query illustrated in Figure 81 to reduce the number of data points and focus the query results.

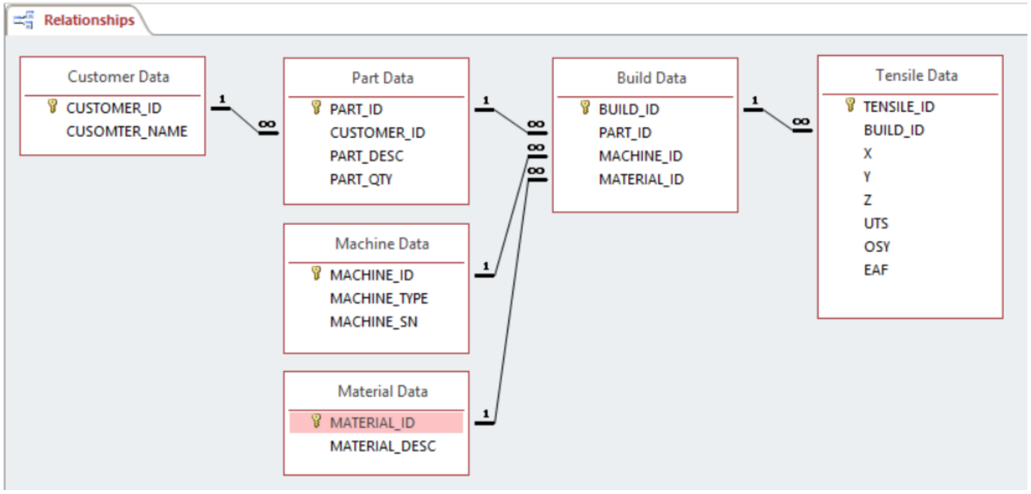

Figure 80: Representative Model of Relational Database

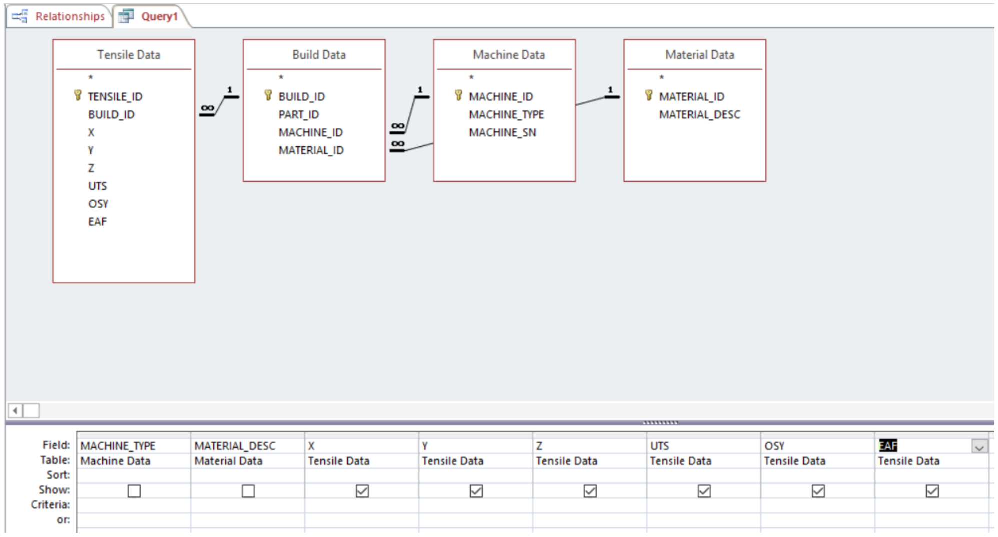

Field:	MACHINE_TYPE	MATERIAL_DESC	X	Y	Z	UTS	OSY	EAF
Table:	Machine Data	Material Data	Tensile Data	Tensile Data	Tensile Data	Tensile Data	Tensile Data	Tensile Data
Sort:								
Show:	☐	☐	☑	☑	☑	☑	☑	☑
Criteria:								
or:								

Figure 81: Query Design View

The query created for this data created a criterion for machine type and material type. The 80,000 datapoints analyzed produced test results from 59,503 individual tensile data points. The reduction in data was a result of restricting the data to only include results for the FR-106 material produced on the 3D Systems™ sPro 60 or equivalent platform. Data collected from different blends of nylon 11 or varying platforms contaminate the results. This data can be analyzed in a variety of software packages and a subset of the data is seen in Figure 82. The tools available in Microsoft Excel work well for getting statistical information like averages and standard deviation but is limited in its ability to represent the data visually.

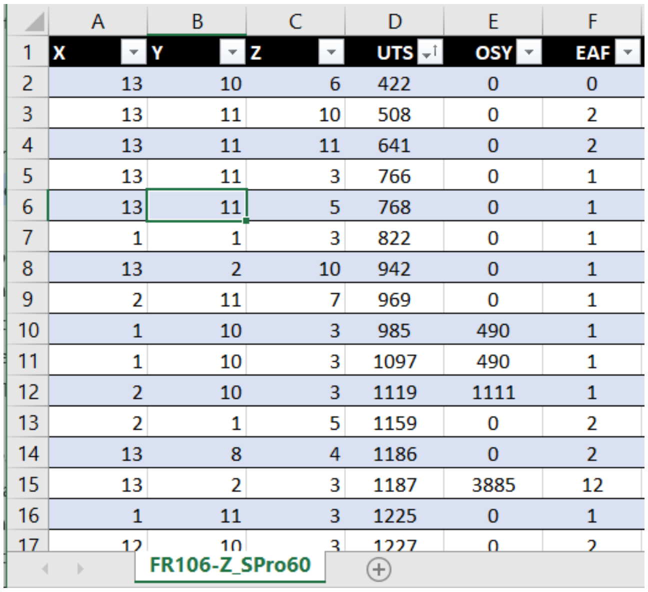

	A	B	C	D	E	F
1	X	Y	Z	UTS	OSY	EAF
2	13	10	6	422	0	0
3	13	11	10	508	0	2
4	13	11	11	641	0	2
5	13	11	3	766	0	1
6	13	11	5	768	0	1
7	1	1	3	822	0	1
8	13	2	10	942	0	1
9	2	11	7	969	0	1
10	1	10	3	985	490	1
11	1	10	3	1097	490	1
12	2	10	3	1119	1111	1
13	2	1	5	1159	0	2
14	13	8	4	1186	0	2
15	13	2	3	1187	3885	12
16	1	11	3	1225	0	1
17	12	10	3	1227	0	2

Figure 82: Exported Data in Microsoft Excel

5.1.3 EVALUATING MECHANICAL PROPERTIES FROM PRODUCTION OPERATIONS

MATLAB 7.12.0 (Student Version) was used as the analytical tool to represent the production data graphically. The data that was exported from the database query to an excel data file is imported into MATLAB. The procedure that was used in conjunction with the MATLAB program (bins.m) is found in Appendix B: MATLAB Program Source Code. (MathWorks Staff, 2018)

5.1.3.1 Importing the Data

Before the data can be plotted, the user must divide the data into individual files by orientation, machine model, material, and tensile bar orientation. This can be accomplished by using the query and segregating the excel data files. If the data is in a single worksheet, the user can copy and paste relevant data into related files. A variable called MachineMnfg must be set to either “3DS” or “EOS.” The MATLAB program (bins.m) uses this to determine XY bounding box dimensions for plotting the resultant mechanical test data. The EOS platform has a build plane constrained by the XY bounding box (27” X 15”). The 3D Systems effective build area is 14” X 12”. The following numbered steps are taken to create the mechanical testing results seen in Section 6.0 Results:

1. Save excel data in the format shown in Figure 98.

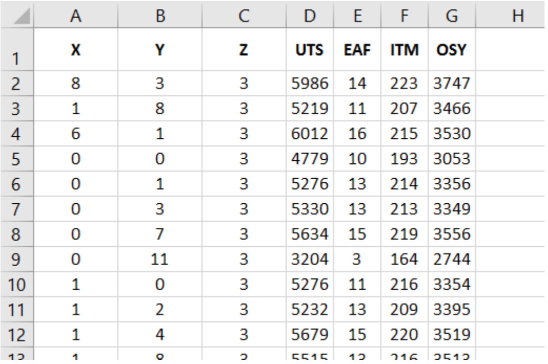

	A	B	C	D	E	F	G	H
1	X	Y	Z	UTS	EAF	ITM	OSY	
2	8	3	3	5986	14	223	3747	
3	1	8	3	5219	11	207	3466	
4	6	1	3	6012	16	215	3530	
5	0	0	3	4779	10	193	3053	
6	0	1	3	5276	13	214	3356	
7	0	3	3	5330	13	213	3349	
8	0	7	3	5634	15	219	3556	
9	0	11	3	3204	3	164	2744	
10	1	0	3	5276	11	216	3354	
11	1	2	3	5232	13	209	3395	
12	1	4	3	5679	15	220	3519	

Figure 83: MATLAB Data Format

2. Import the data into MATLAB using the *Import Data…* function found in the *File* dropdown menu tree shown in Figure 99.

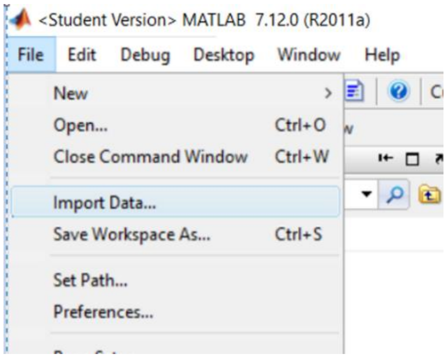

Figure 84: MATLAB Data Import

3. Once the data is displayed, the user must click *Next >* as seen in Figure 100. If the data does not appear to be accurate, repeat the first few steps after the data is cleaned up.

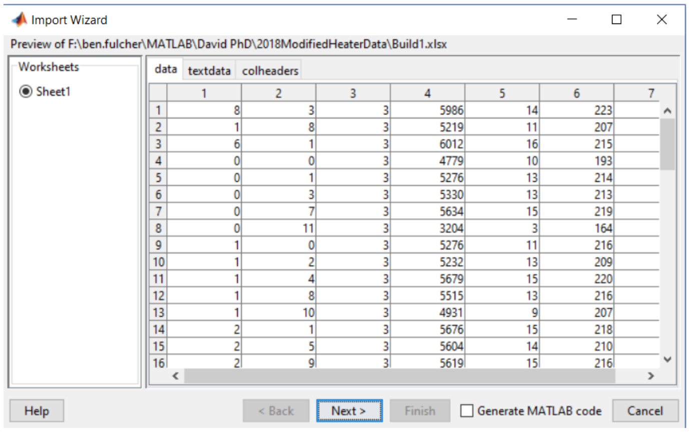

Preview of F:\ben.fulcher\MATLAB\David PhD\2018ModifiedHeaterData\Build1.xlsx

	1	2	3	4	5	6	7
1	8	3	3	5986	14	223	
2	1	8	3	5219	11	207	
3	6	1	3	6012	16	215	
4	0	0	3	4779	10	193	
5	0	1	3	5276	13	214	
6	0	3	3	5330	13	213	
7	0	7	3	5634	15	219	
8	0	11	3	3204	3	164	
9	1	0	3	5276	11	216	
10	1	2	3	5232	13	209	
11	1	4	3	5679	15	220	
12	1	8	3	5515	13	216	
13	1	10	3	4931	9	207	
14	2	1	3	5676	15	218	
15	2	5	3	5604	14	210	
16	2	9	3	5619	15	216	

Figure 85: MATLAB Data View

4. Once the data is imported, the user must select the variables by using the dialogue box shown in Figure 101. Select the second radio button so that the vectors are created using column names. Once the radio button is selected, the user must select *Finish*.

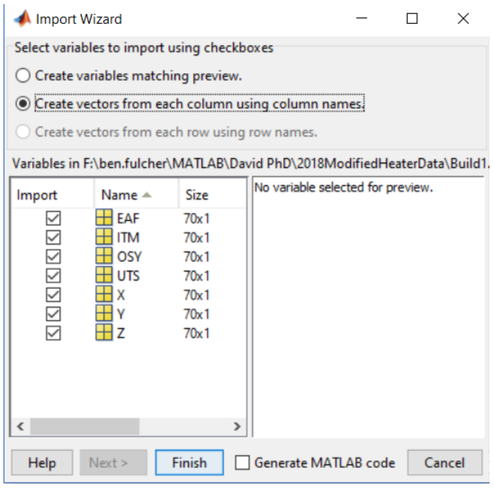

Select variables to import using checkboxes

○ Create variables matching preview.

● Create vectors from each column using column names.

○ Create vectors from each row using row names.

Variables in F:\ben.fulcher\MATLAB\David PhD\2018ModifiedHeaterData\Build1.

Import	Name	Size
☑	EAF	70x1
☑	ITM	70x1
☑	OSY	70x1
☑	UTS	70x1
☑	X	70x1
☑	Y	70x1
☑	Z	70x1

No variable selected for preview.

Figure 86: MATLAB Variable Selection

5. The following variables are entered into the command window so that the resultant data file will have program specific data required for the plot:
    a. MachineMnfg = ‘3DS’
    b. MachineModel = ‘SPro60’
    c. Material = ‘FR-106’ and ‘D80’
    d. Orientation = ‘Z’ and ‘XY’
6. The workspace is saved as a .MAT file so that the data can be accessed by the plotting program in a compatible format. To do so, select the *File* dropdown dialogue menu and choose *Save Workspace As...* which is shown in Figure 87. Ensure that the .MAT file is descriptive enough to avoid confusion from plotting the data.

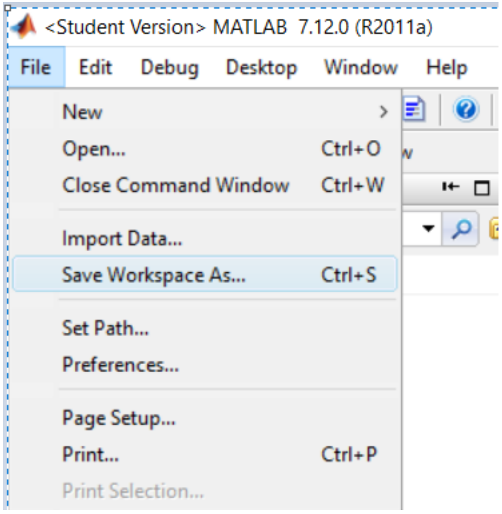

Figure 87: .MAT File Creation

5.1.3.2 Plotting the Data

The MATLAB program file *Bins.m* will be used to create the plotted data shown in the mechanical testing results seen in Section 6.0 Results. The following steps are used to plot the imported and converted data file (.MAT) previously discussed:

1. Ensure that the *Bins.m* file is in MATLAB's Current Folder.
2. Within MATLAB, enter 'Bins' into the command window without using the quotation marks.
3. Choose one of the .MAT files previously created and described in the previous section.
4. Following the prompts, variables must be entered to direct the program to plot the needed data. One of the variable setting is the minimum bin quantity. For example, setting the minimum bin quantity to zero (0) will plot all data in that region. But setting the minimum bin quantity to 30 will prevent data plots with lower sample sizes that could skew the results.
5. Multiple plot types may be output as part of this program, but the selection of the plots must be done within the code. To choose which plot types are to be used, a user must edit the initialization section of the *Bins.m* file and set different plot types to a value of true or false.

5.2 Evaluation of Production Platform

All specimens in the study were built on machines owned and operated by Harvest Technologies (currently Stratasys Direct Manufacturing) in Belton, TX. The specific machines used were 3D Systems™ sPro 60® or equivalent seen in Figure 88. (3D Systems Staff, 2018) These machines are the same as the base Sinterstation® *2500plus* with a 70 W CO_2 laser, the addition of digital scanning, and active thermal control using a black-body reference heat source. During the preliminary investigation tensile specimens were made in both PA 12 (Duraform® PA) and PA 11 (Duraform® EX and ALM FR-106). (ALM Staff, 2018) (3D Systems Staff, 2018) During the primary investigation, production tensile specimens made on multiple 3D Systems sPro60 platforms in ALM FR-106 were compared to discrete builds in FR-106 on an sPro60 equivalent unit with serial number G112. (3D Systems Staff, 2018) (3D Systems Staff, 2018) (ALM Staff, 2018) This machine was selected because it had been removed from production operations due to poor mechanical properties. Parts and tensile specimens at the rear of the build area were producing parts with properties that were below acceptable limits and the efforts of maintenance staff were inadequate to bring the machine to the required service level. Analyzing a machine that is producing specimens with poor mechanical properties affords the opportunity to evaluate root cause and the ability to test the theory of the thermal effect on mechanical properties.

Figure 88: 3D Systems™ (a) sPro 60® Laser Sintering Machine and equivalent (b) Sinterstation *2500plus*

Four (4) builds were run using the 3D Systems™ build setup software. The tensile specimen build setup screen is shown in Figure 89 with seventy (70) vertical tensile specimens arrayed across the build plane.

Build 1: A six-inch build with part scanning disabled to allow for the use of a thermal camera to map the surface temperature. The settings used were obtained from the production specifications so that the results would be comparable to the production data that was analyzed.

Build 2: A duplicate of Build 1 was performed with no parts being built so that thermocouple data could be performed.

Build 3: A build of seventy (70) vertical tensile specimens placed throughout the build to create an x-y map of mechanical testing data. The settings used were obtained from the production specifications so that the results would be comparable to the production data that was analyzed.

Build 4: A duplicate of the Build 3 described above was performed. For this build, additional heaters were installed and used to increase elevated thermal boundary conditions on the front and right build piston walls.

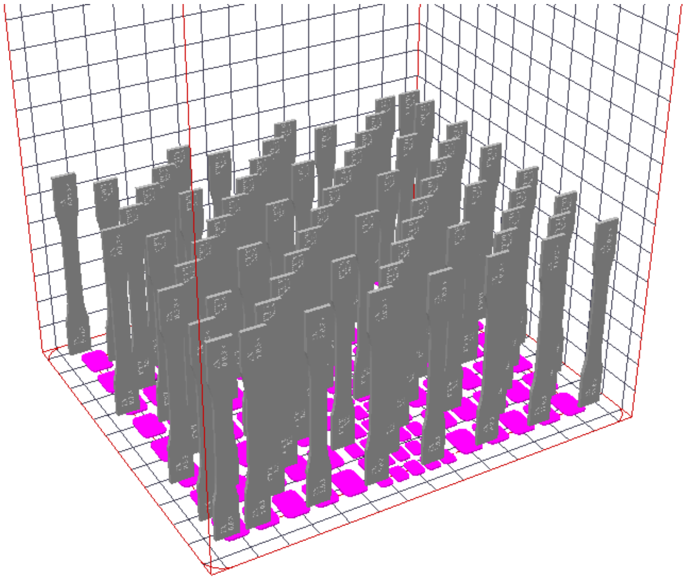

Figure 89: Sinterstation Build with Multiple Tensile Bars

5.2.1 PART BED SURFACE THERMAL CHARACTERIZATION (THERMAL CAMERA)

Surface temperatures in a laser sintering production build are monitored by IR pyrometers located in the build chamber with the data being used to control radiant heaters. This data is also recorded during a build and stored in a build log. The build region, IR sensor location, and IR focal point can be seen in Figure 90. A thermal camera was used to independently verify the accuracy of the machine IR sensor data and provides additional information on thermal gradients that exist in the build chamber. The camera used to evaluate the surface temperature of the build region during a production build was mounted on a 3D Systems Sinterstation *2500plus* pictured in Figure 88.

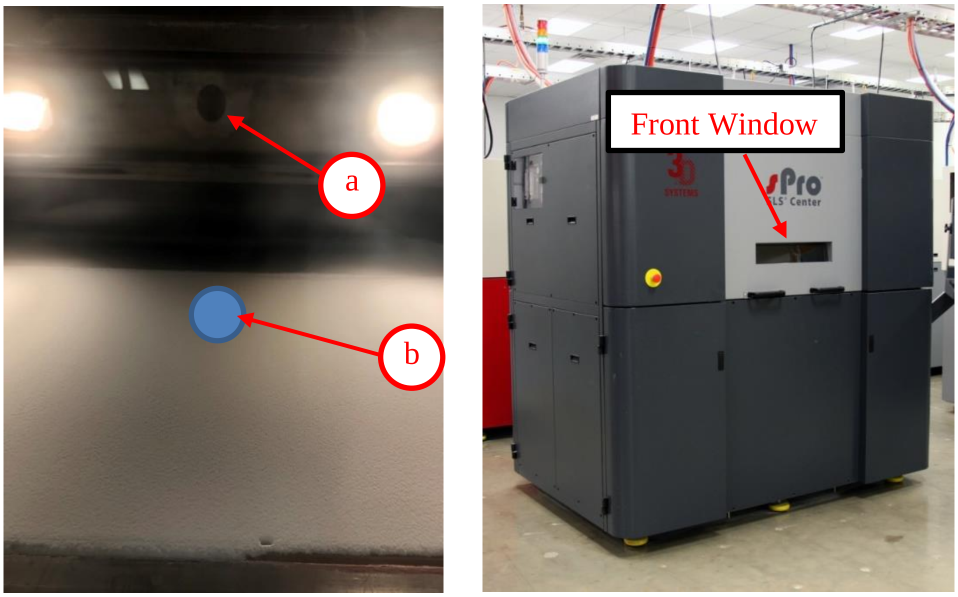

Figure 90: View of Part Bed from Front Window Showing (a) Part Bed IR Sensor and (b) IR Sensor Focal Point

The front glass on the systems cannot be used for IR analysis because it is designed for safety purposes to filter any reflected laser energy which is emitted in the to block IR spectrum radiation. There being no dedicated viewport for an IR camera, the zinc-selenide laser window can be used as a viewport for the thermal camera. The drawback to using this window is that the laser must be disabled, and the scanners removed. Since the objective of this research is to establish a quantified thermal profile of a production build, the analysis and build data can be achieved from the use of multiple and identical builds. To install the IR camera the laser module is opened, the laser controller is disabled, and the X-Y galvanometer scanner assembly is removed. The scanner module is pictured in Figure 91 with the scanner assembly emphasized with the left image showing the scanner and mount in place and the right image showing the scanner being removed and placed out of the way.

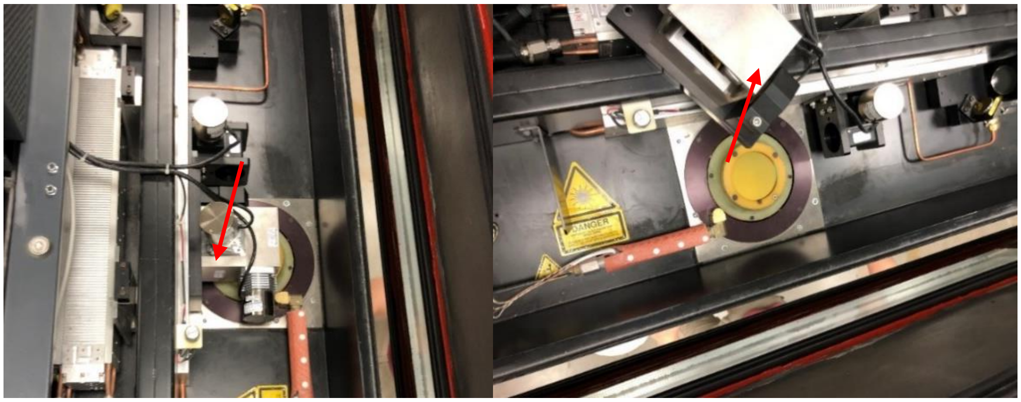

Figure 91: Laser-Scanner-Optics Module

Once the scanner is out of the way, the IR camera has an unobstructed view of the top surface of the build region, generally referred to as the part bed. A view of the part bed through the zinc-selenide laser window is shown in Figure 92 with the top of the image showing the back of the build chamber. The image appears yellow but is transparent when viewed with the IR camera.

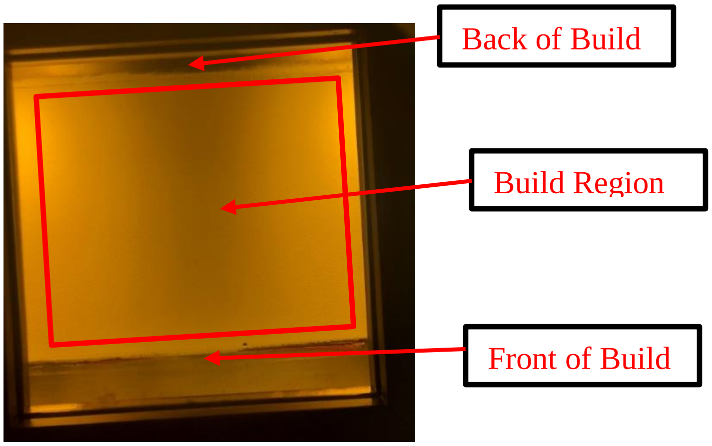

Figure 92: View of Part Bed from Laser Window

A FLIR R&D thermal camera model A325sc was used to capture surface temperatures dynamically during a simulated production build. The thermal camera delivers thermal imaging and temperature readings which capture more than 76,000 temperature measurements in every image. This uncooled thermal imaging camera offers digital input directly to FLIR ResearchIR for start-and-stop recording. The A325sc provides 14-bit, 320 × 240 data-streaming over Ethernet at 60 Hz. The A325sc is connected to a Dell laptop (model #) over ethernet and is controlled with FLIR ResearchIR Max software for viewing during the build and recording for offline analysis. Camera specifications are listed in Table 7.

Figure 93: FLIR A325sc Camera (FLIR Product Website, 2018)

Serial Number and Mfg. Date	48012580 – June 26, 2015
Detector Type	Uncooled Microbolometer
Dynamic Range	16-bit
Packaging Size	495 x 370 x 192 mm (19.5 x 14.6 x 7.6 in.)
Power	12/24 VDC, 24 W Absolute Max.
Spectral Range	7.5 – 13.0 µm
Integrated Lens	18 mm (25°)
Size [L x W x H] w Lens	170 × 70 × 70 mm (6.7 × 2.8 × 2.8 in)

Table 7: Specifications for FLIR Model A325sc Thermal Camera (FLIR Product Website, 2018)

FLIR ResearchIR Max 4 Software is a thermal analysis software package for FLIR Research & Development / Science cameras. It provides camera control, highspeed data recording, image analysis, and data sharing. The ResearchIR software connects directly to FLIR Research and Science cameras via USB, Firewire, gigabit ethernet, and camera link to acquire thermal snapshots or movie files. Users can customize recording options including start times, end times, and the number of frames to acquire. (FLIR Product Website, 2018) The user interface is shown in Figure 94.

Figure 94: FLIR ResearchIR Thermal Imaging Software (FLIR Product Website, 2018)

5.2.2 PART BED IN-SITU THERMAL CHARACTERIZATION (THERMOCOUPLES)

Mapping the temperature within the build region, commonly referred to as the part cake, is difficult to achieve without making system modifications. Since layers are continuously added, the region to be monitored is constantly moving. Wireless thermocouples that could be used to remotely monitor the part cake are not rated to operate at laser sintering build temperatures. For this reason, the system was modified to remove the heated part piston and install thermocouples that are manually adjusted during the build. Figure 95 shows the build chamber of the Sinterstation with powder removed from the build piston and the bolts removed to facilitate removal as seen in the left image. There is a piston seal marked with the red arrow that will be reused once the OEM piston is removed. After the bolts are removed and the top plate is lifted, the piston heater is disconnected so that the lower piston can be removed as seen in the right image.

Figure 95: Production Piston Plate Disassembly

The OEM piston assembly was reverse-engineered, and two aluminum plates were manufactured. The plates measure 12.5” X 14.5” with one of them having a 0.75” notch to allow for the donor piston seal to be installed. The bottom plate was machined to match the piston mechanism anchor bolt pattern as well as multiple holes for use to feed thermocouples into the part cake. A MakerBot was used to build brackets to be used to anchor the thermocouples during a production build as shown in Figure 96. (Makerbot Staff, 2018)

Figure 96: Modified Lower Piston Plate with Thermocouple Supports

Omega k-type thermocouples were inserted into 1 mm diameter hollow bronze tubes as shown in Figure 97. Initial tests of the small diameter thermocouples specified in Table 8 were unsuccessful and one was broken. To measure the temperature during the build, thermocouples must be extended through the lower piston plate and into the part cake. The thin thermocouples did not have enough strength to push through the powder without deforming, so the bronze tubes were used to help locate the thermocouples within the part cake during an active build. The small thermocouples were chosen after several test builds were attempted with larger diameter sheathing. Large diameter thermocouples present two issues when being used with laser sintering:

- the thermal conductivity of the metal in the sheath acts as a heat-sink and does not accurately measure the powder while drawing heat out of the surrounding part cake;
- and the larger diameter thermocouples have a very slow response time in comparison to the thermodynamics of the system.

Figure 97: Thermocouple Inserted in Bronze Tube

TJ36-CASS-101G-12
36” lead wire
CA for Type K
SS for 304 Stainless Steel
010 for 0.010” (.25mm)
G for grounded
12 for 12” thermocouple wire length

Table 8: Omega K-Type Thermocouple Specifications (Omega Staff, 2018)

Three thermocouples were used to measure the thermal history of a layer from the initial (top) build layer and track that temperature until it reached the middle of a full build which measures roughly six (6) inches from the top surface of the build plane. The whisker sized thermocouple protruding from the machined passthrough is highlighted on the left image of Figure 98. The location of the three thermocouples used to measure a production build can be seen in Figure 98 with colored labels that correspond to the experimental results discussed later. The flow rate of the powder was such that the thermocouple passthroughs had to be covered with tape so that it did not create the holes seen in Figure 98.

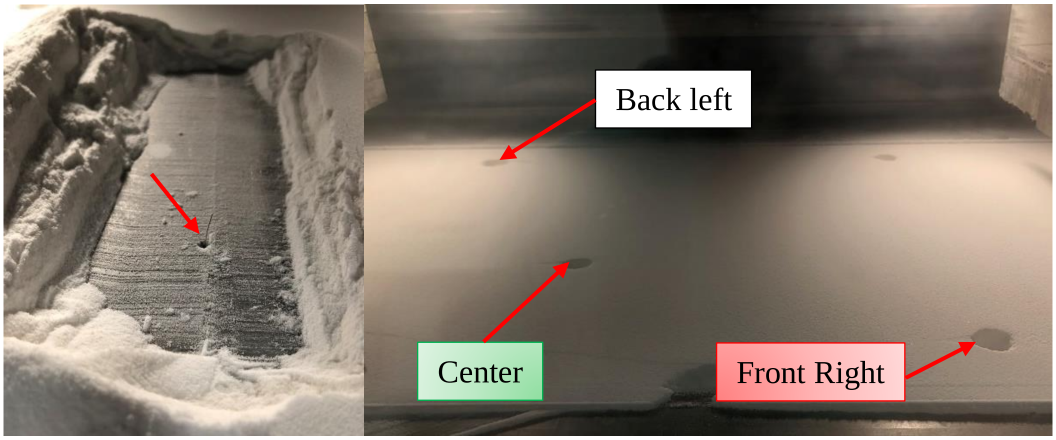

Figure 98: Upper Plate with Thermocouples Protruding through Plate

After the configuration was tested, several test runs were conducted so that the location of the thermocouples could be perfected. Thermocouples were then connected to a data acquisition module which was connected to a Dell Laptop via USB. The configuration of the laptop, DAQ, and machine can be seen in Figure 99.

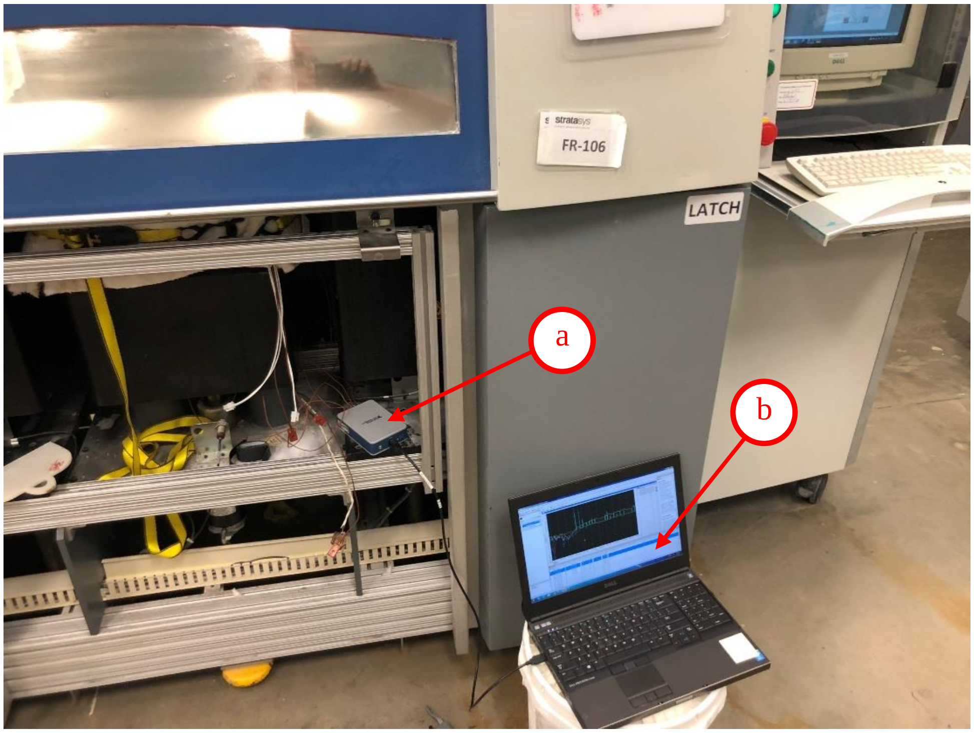

Figure 99: G112 Configured with Thermocouples, (a) DAQ, and (b) Laptop

A 1-slot, USB CompactDAQ chassis from National Instruments (cDAQ-9171) was used for data acquisition. It is a bus-powered, CompactDAQ USB chassis designed for small, portable sensor measurement systems. (NI Staff, 2018) The chassis provides the plug-and-play simplicity of USB for sensor measurements. It also controls the timing, synchronization, and data transfer between C Series I/O modules and the host laptop computer. NI Signal Express 2015 Version 15.0.0 was used to acquire the data and record the thermal build history. The software interface can be seen on the laptop in Figure 99, but is better seen in Figure 100. To capture the data, the software was installed on a laptop and once installed the Data Acquisition Wizard was followed. The data acquisition corresponded to the labels on the I/O module, so the initial four k-type thermocouples could be isolated, given a color scheme, and unused I/O ports could be ignored. Figure 100 shows four colored graphs with the y-axis representing temperature and the x-axis representing time. A beat pattern that corresponds with moving the thermocouple through the gradient temperate in the part cake and exposing it to the radiant heater can be observed on the left side of the graph. The right-side beat pattern corresponded to warm powder being deposited on the surface in a repeating pattern. These tests were done to fine-tune thermocouple location, fixturing, and response time.

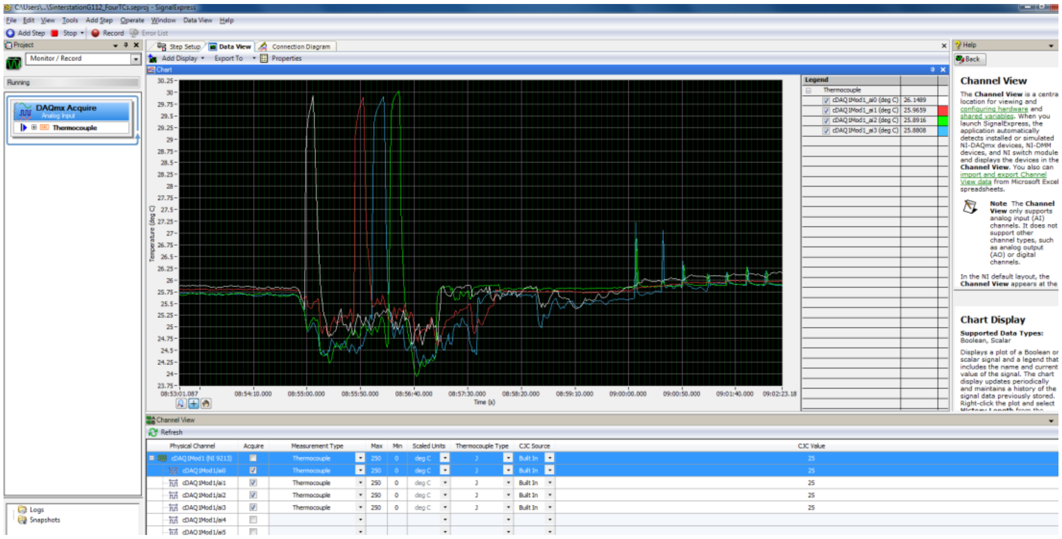

Legend		
⊟ Thermocouple		
☑ cDAQ1Mod1_ai0 (deg C)	26.1489	⬜
☑ cDAQ1Mod1_ai1 (deg C)	25.9659	🟥
☑ cDAQ1Mod1_ai2 (deg C)	25.8916	🟩
☑ cDAQ1Mod1_ai3 (deg C)	25.8808	🟦

Channel View

The **Channel View** is a centra location for viewing and configuring hardware and shared variables. When you launch SignalExpress, the application automatically detects installed or simulated NI-DAQmx devices, NI-DMM devices, and NI switch module and displays the devices in the **Channel View**. You also can import and export Channel View data from Microsoft Excel spreadsheets.

Note The **Channel View** only supports analog input (AI) channels. It does not support other channel types, such as analog output (AO) or digital channels.

In the NI default layout, the **Channel View** appears at the

Chart Display

Supported Data Types: Boolean, Scalar

Displays a plot of a Boolean or scalar signal and a legend that includes the name and current value of the signal. The chart display updates periodically and maintains a history of the signal data previously stored. Right-click the plot and select

Physical Channel	Acquire	Measurement Type	Max	Min	Scaled Units	Thermocouple Type	CJC Source	CJC Value
⊟ cDAQ1Mod1 (NI 9213)	☐	Thermocouple	250	0	deg C	J	Built In	25
cDAQ1Mod1/ai0	☑	Thermocouple	250	0	deg C	J	Built In	25
cDAQ1Mod1/ai1	☑	Thermocouple	250	0	deg C	J	Built In	25
cDAQ1Mod1/ai2	☑	Thermocouple	250	0	deg C	J	Built In	25
cDAQ1Mod1/ai3	☑	Thermocouple	250	0	deg C	J	Built In	25
cDAQ1Mod1/ai4	☐							
cDAQ1Mod1/ai5	☐							

Figure 100: National Instruments SignalExpress 2015 (NI Staff, 2018)

5.2.3 MECHANICAL PROPERTY CHARACTERIZATION

Tensile properties were measured using an MTS Insight 10 at Stratasys Direct Manufacturing, shown in Figure 101. (MTS Staff, 2018) The specimens produced were ASTM D638 specimens with a cross-sectional area at fracture of roughly 0.125” × 0.500”. (ASTM Subcommittee D20-10, 2018) The procedure for pulling the specimens was to use a 0.20 inch/minute rate with an extensometer that conforms to ASTM E83 class B2 with a range of at least 50%. (ASTM Subcommittee E28-01, 2018) The extensometer is limited to 50%; thus, no quantifiable measurements exceeding that limit are recorded.

Figure 101: MTS Insight 10, Extensometer, and Specimen (MTS Staff, 2018)

5.2.4 ELEVATING PART BED THERMAL BOUNDARY CONDITIONS

Three heaters, relays, switches, power supplies, and controllers were purchased to be used to modify the build conditions of an experimental build. The 28 V, 360 W flexible heaters measuring 10” × 4” were installed on the front and right sides of the part piston. They were designed to be able to maintain a 200°C operating temperature. Omron E5DC DIN Track mounted controllers were used to control the heaters and Mean Well 24V and 48V power supplies were used to power the heaters. The configuration can be seen in Figure 102. (Omron Staff, 2018)

Figure 102: Custom ‘Heater in a Box’ used for Piston Wall Heat

5.3 Differential Scanning Calorimetry of FR-106

A TA Instruments Q10 Series Thermal Analyzer, pictured in Figure 103, was used to characterize the heat flow, melting temperatures, and solidification temperatures of ALM FR-106. (TA Instruments Staff, 2018)   A 6.6 mg FR-106 sample was placed on an aluminum pan, purged with nitrogen at a rate of 50 ml/min and processed according to the thermal cycle described in Table 9.

Step	Procedure
1	Equilibrate at 50.00 °C
2	Ramp 10.00 °C/min to 250.00 °C
3	Mark end of cycle 1
4	Isothermal for 1.00 min
5	Ramp 10.00 °C/min to 50.00 °C
6	Mark end of cycle 2
7	Isothermal for 1.00 min
8	Ramp 10.00 °C/min to 250.00 °C
9	Mark end of cycle 3
10	Isothermal for 1.00 min

Table 9: DSC Thermal Programming Cycle

Figure 103: TA Instruments Q Series Thermal Analyzer (TA Instruments Staff, 2018)

6.0 RESULTS

6.1 Historical Production Data

6.1.1 INITIAL DATA ANALYSIS

Historical production data was analyzed in three categories: UTS, Yield Strength, and EAM. The first analysis technique was to look at a snapshot of roughly two (2) years of data and plot the data through time. Data was taken from production builds as described in Section 5.1 Production Dataset and charted using Excel. Figure 104 shows UTS and yield strength while Figure 105 shows elongation-at-break data. This data when compared to University of Louisville test data in Figure 25 and Figure 26 show similar patterns with a tighter grouping for tensile strength and a broader scatter of results when evaluating elongation at break.

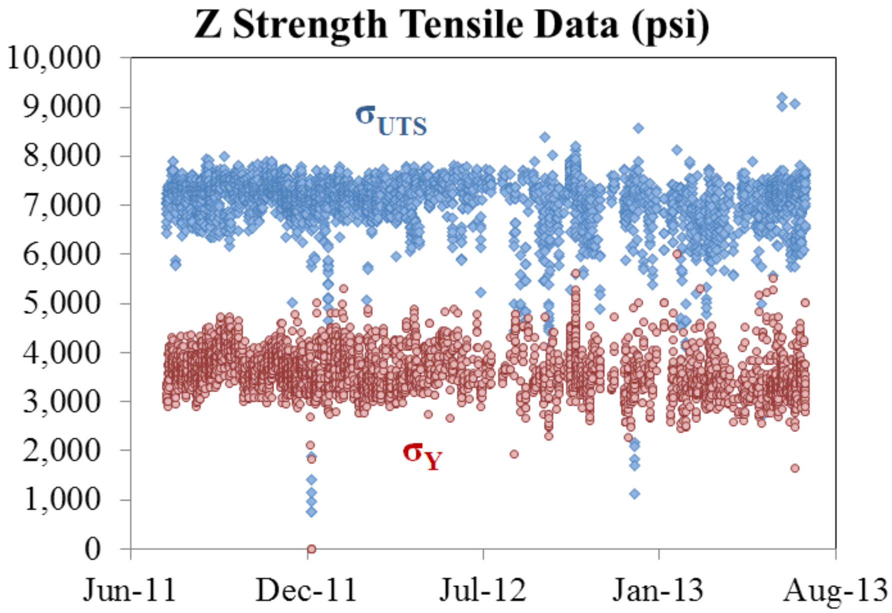

Figure 104: Z-Specimen UTS and Onset of Yield Data by Date

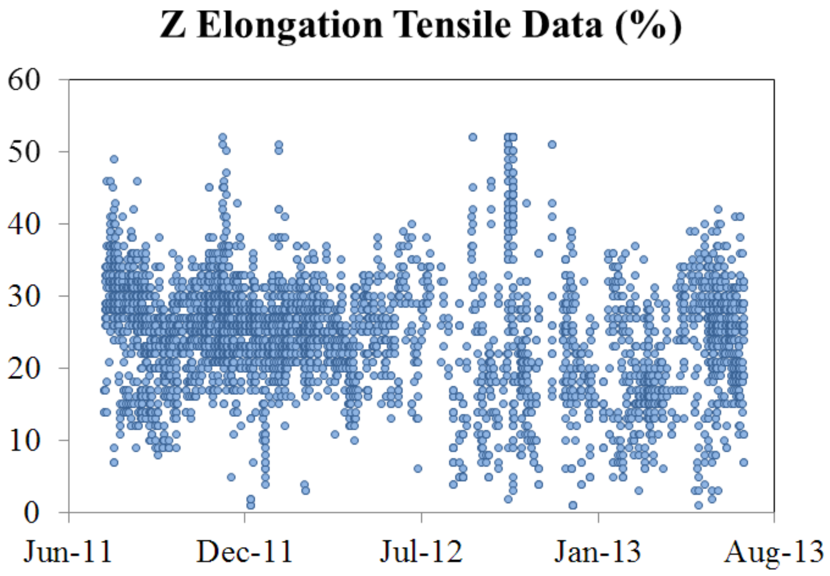

Figure 105: Z-Specimen Elongation-at-Break by Date

When evaluating the elongation data by location instead of by date, a different pattern emerges. Figure 106 shows the number of specimens based on the location of the build as recorded based on the tensile specimen label and Figure 107 shows the average elongation-at-break for those same specimens. While there is not a clear pattern shown in Figure 105, once plotted by location a pattern starts to emerge. This initial dataset had more tensile specimens built throughout the build area while the FR-106 dataset analyzed in the next section relied primarily on data recorded at the edges of the build with few specimens built in the interior.

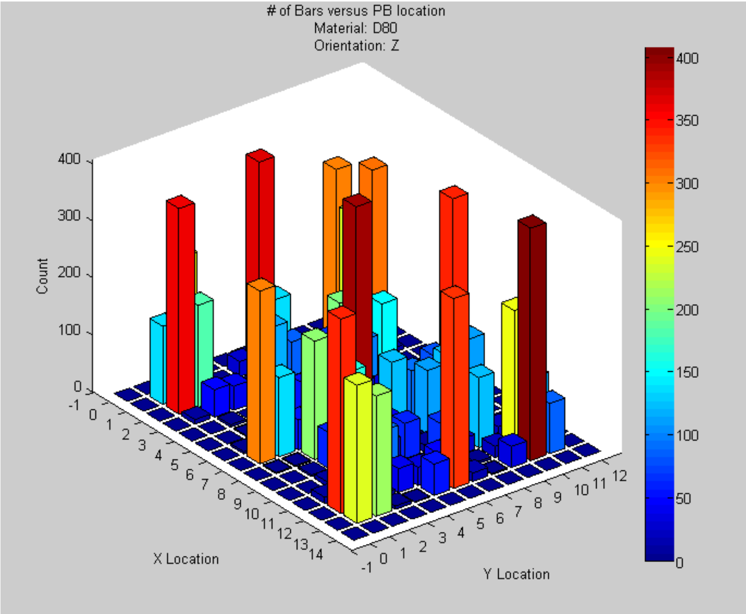

Figure 106: Number of Specimens verses Powder Bed Location

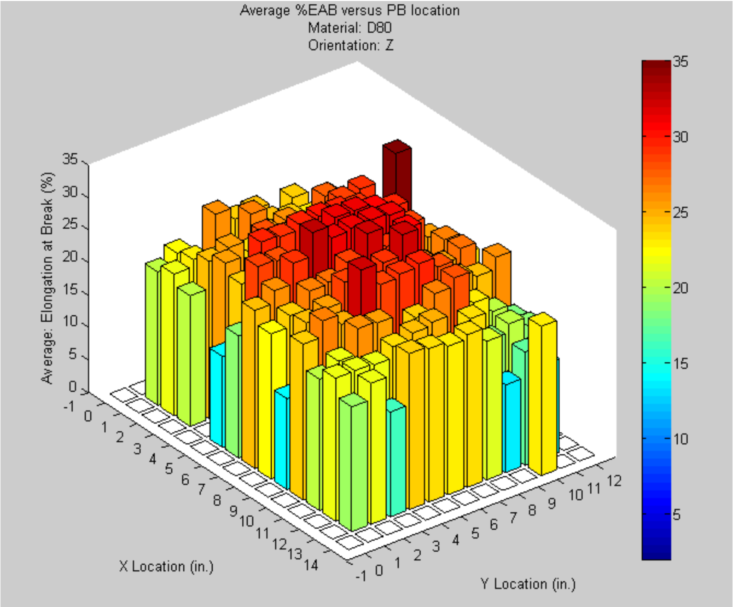

Figure 107: Average Elongation-at-Break (EAB) versus Powder Bed Location

6.1.2 FR-106 PRODUCTION DATASET

There were roughly 50,000 data points used to compile the following figures. When looking at the three graphs shown in Figure 108, Figure 109, and Figure 110 the data follows a similar pattern that has been discussed with the yield strength and UTS reaching a relatively stable average across time and powder bed location but that the elongation-at-break shows a definite pattern of higher elongation-at-break towards the center and the lowest averages generally at the edges and corners of the build.

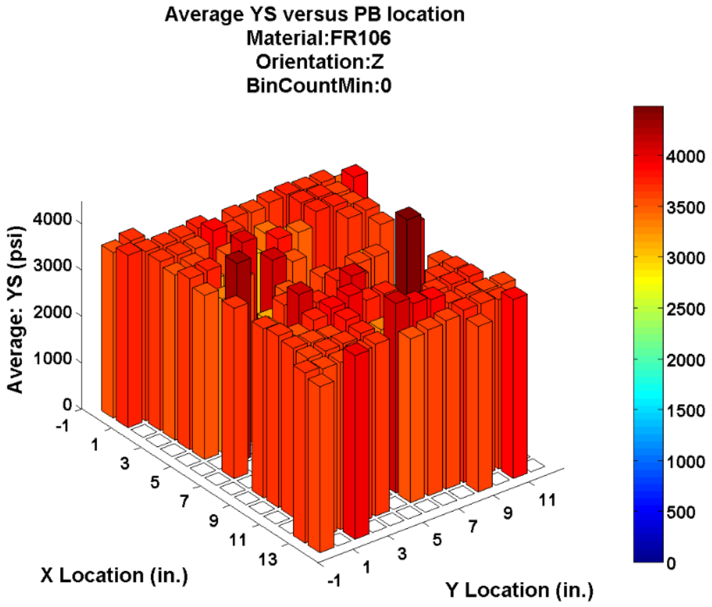

Figure 108: FR-106 Yield Strength versus Powder Bed Location

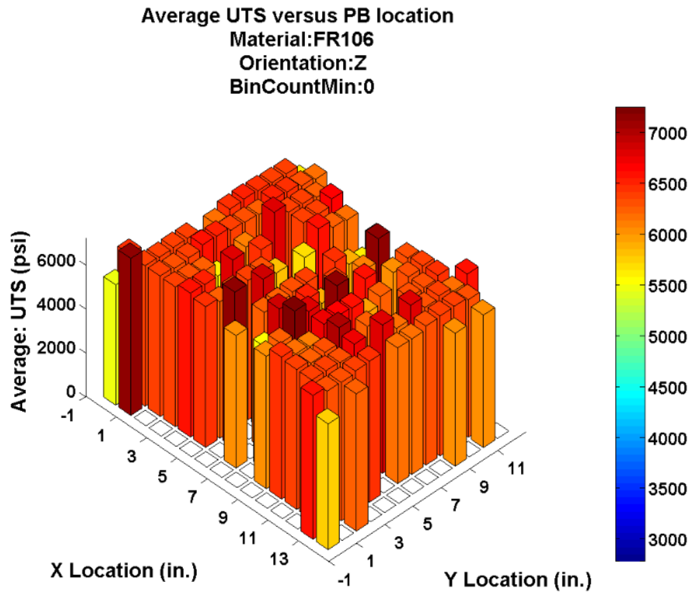

Figure 109: FR-106 UTS versus Powder Bed Location

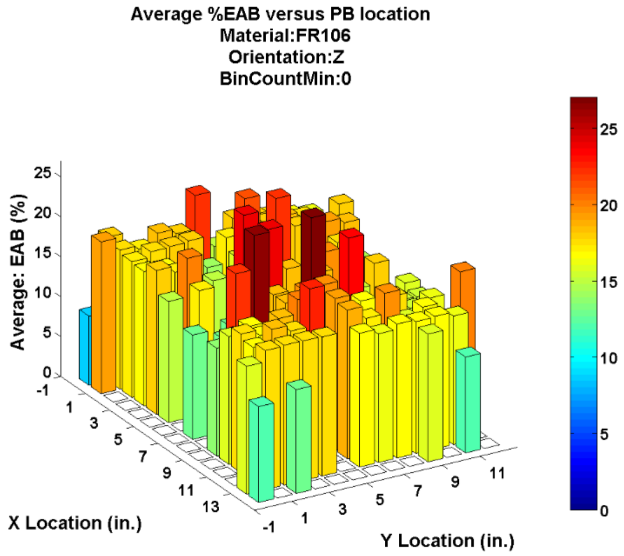

Figure 110: FR-106 Elongation-at-Break (EAB) versus Powder Bed Location

6.2 Production Platform Evaluation Results

Four builds were run, and the thermal data was collected and compared in this section. A subset of the build parameters are shown in Appendix C: Production Processing Parameters and the resultant build log is represented in Appendix D: Production Build Log Data (Sample).

6.2.1 PART BED SURFACE THERMAL CHARACTERIZATION (THERMAL CAMERA)

A six (6) inch build was run and the FLIR thermal camera was employed to record the surface temperature of the part build region. The thermal cameral data is combined with the build log and *in situ* thermocouple measurements to develop a detailed thermal model of the laser sintering production build region. Data was recorded several hours into the build region to allow the machine to reach a thermal steady-state. Layer dwell time during this build was 30 s which corresponds to a process parameter setting that sets the minimum time between layers. The image in Figure 111 was captured after the surface temperate came up to the setpoint and had been maintained for several seconds. A gradient can be observed with the red region maintaining a temperature close to the setpoint of 179.5°C. The minimum temperature of the gradient represented by the gray to green regions is 150°C. It should be noted that the sharpest gradient is generally in the front and left side of the build region. The largest gradient is observed at the back of the build which corresponds to the location where specimens with poor mechanical properties were observed.

Figure 112 shows the build region while the feedstock material is deposited on the part bed. It takes about 15-18 seconds to add a layer of powder. The feedstock powder is being maintained at a 135°C setpoint. It reaches a temperature of 162°C as it is moved by a roller to the part bed and then reaches the part bed setpoint in 10 seconds.

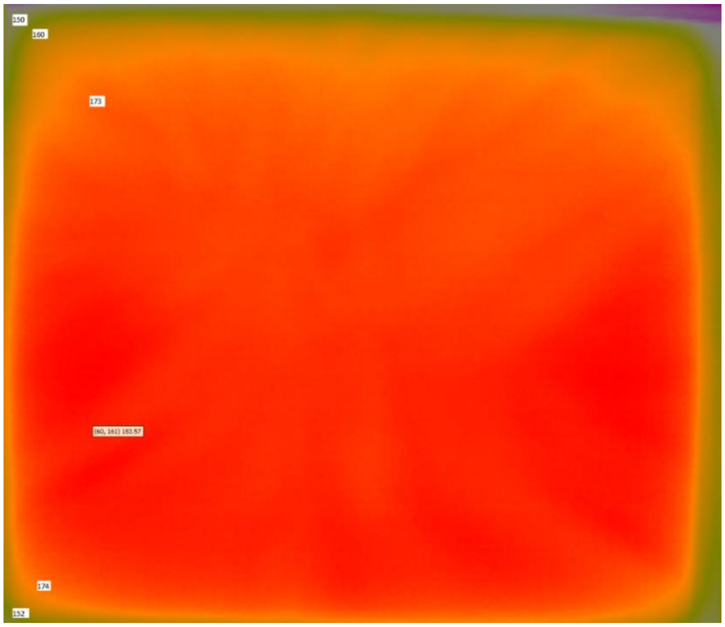

Figure 111: Steady-State Build Condition on Machine G112

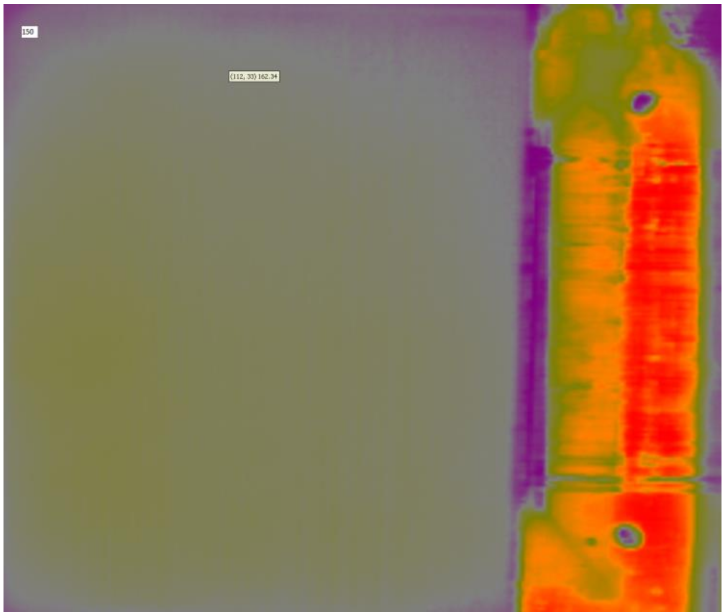

Figure 112: Part Bed Surface Temperature as Roller Applies Feedstock on G112

The surface of the build region represents one of six boundary conditions used to create a dynamic thermal model. Data was analyzed using the Research IR Max software and dimensions were extracted from the machine geometry to create four (4) distinct zones to be used for a more precise thermal model. The zones, illustrated in Figure 113, create a set of boundary conditions emanating from the center of the build going from 180°C in Zone 1, 180°C-175°C in Zone 2, 175°C-162°C in Zone 3, and 162°C-150°C in Zone 4. Each of the zones also have coordinates (x,y) to approximate isothermal boundaries between them. Zone 1 is the only constant temperature zone and the external three (3) zones have a gradient modeled in the software to emulate the observed thermal profile of machine G112.

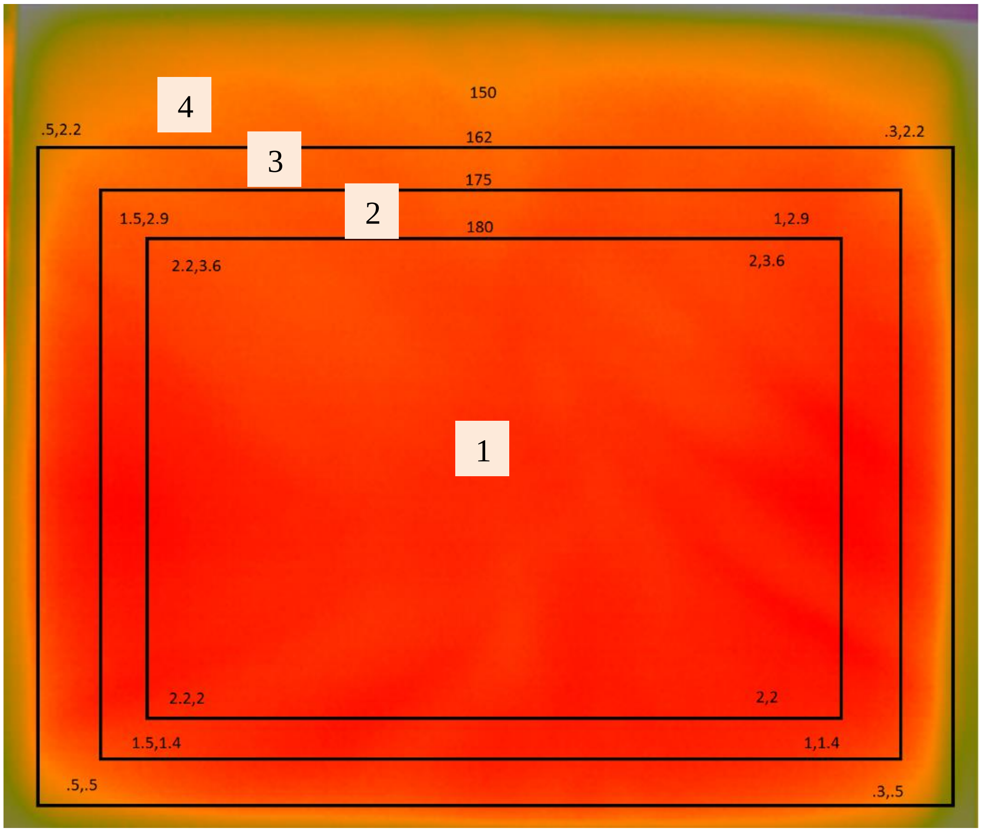

Figure 113: Gradient Analysis of Part Bed for Machine G112

6.2.2 BUILD LOG THERMAL DATA

There are three pyrometers used to manage the part bed and feed heaters. The pyrometers (IR Sensors) are used in conjunction with PID parameters in the control architecture to maintain the heating of distinct feed and part zones within a build chamber. The temperature feedback data is recorded along with a host of other monitoring points such as heater duty cycle. This captured data is recorded every second and saved in a build log file that can be exported and analyzed in a spreadsheet. Build processing setpoints are recorded in Appendix C: Production Processing Parameters.

Figure 114 shows the part bed surface temperature from startup to cooldown. There is an initial wait for temperature that allows the temperature to reach 100°C before the warmup starts and the build runs an initial warmup of 0.5” of build height. The build then maintains a temperature at the 179.5°C setpoint until it is complete. There is an addition 0.1” cooldown at the end of the build. The subject build had a long cool-down until the surface temperature approached room temperature.

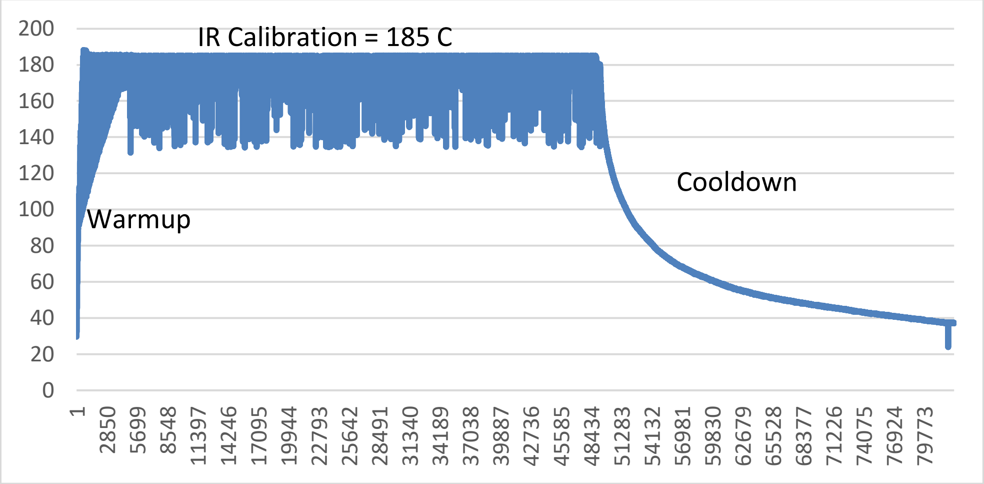

Figure 114: Part Bed Temperature Data Retrieved from Build Log Data

When looking at the build region in Figure 114, there is a jagged region at the lower temperature and a flat region at 185°C. A pattern in this variation can be seen when the data is analyzed closer as seen in Figure 115 and Figure 116. The part bed temperature in Figure 115 has a beat pattern that corresponds with an *add powder layer* sequence. The part heater duty cycle which is a parameter that limits the flux of the energy emitting from the radiant heaters can be seen in the same figure and the time sequence is synchronized.

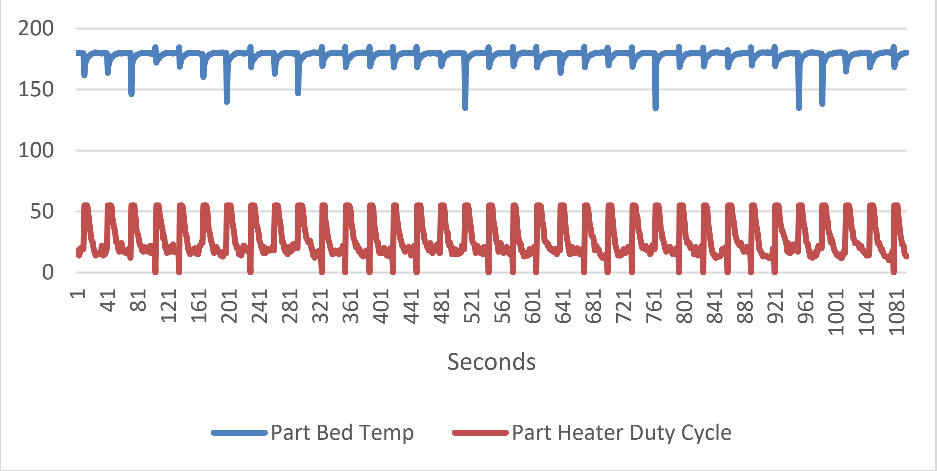

Figure 115: 30 min Section of Part Bed Temperature Data

The data was evaluated in more detail in a shorter time sequence shown in Figure 116. The following observations can be taken from the part bed temperature data:

- The periodicity is 29-31 seconds which corresponds to the 30 seconds setpoint for the minimum time between layers.
- The peak in the temperature is 185°C which corresponds to a black body calibration device. This spike in temperature allows the software to make slight adjustments in the drift of the part bed IR sensor. This device is mounted on the system roller and is visible to the part bed IR sensor as it traverses across the part bed.

- The decrease in temperature that immediately follows the black body spike is a measurement of the recently deposited feedstock powder.
- The part bed heater duty cycle has a maximum setpoint of 55% to limit the thermal flux from the radiant heaters so that the temperature does not overshoot the setpoint.
- The duty cycle is at the maximum level for 2-4 seconds at which point the powder bed is within 2°C degrees of the setpoint. The duty cycle then decreases based on the control algorithms so that the part bed temperature can be maintained.
- The part bed temperature drops initially as new feedstock powder is added. The surface temperature starts at around 168°C and rises to the setpoint of 179.5°C within 5 seconds and maintains a temperature within +/- 1°C until the next add powder layer sequence is executed.
- The temperatures observed here are supported by the IR thermal camera data.

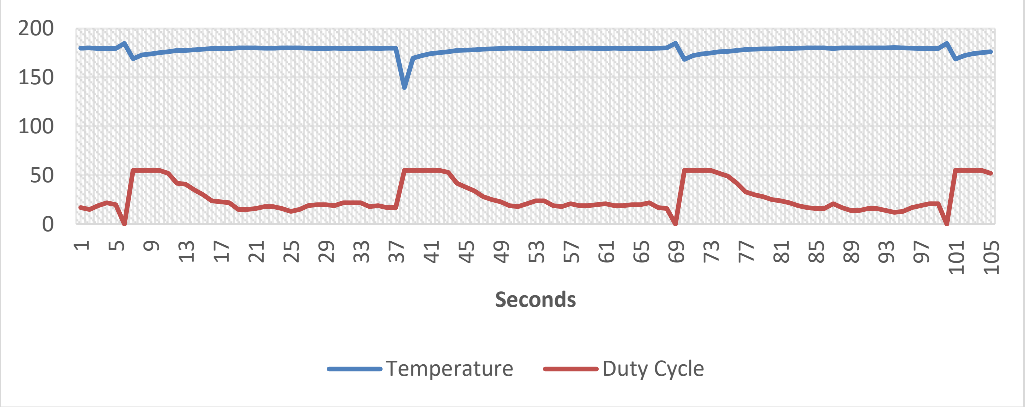

Figure 116: 2 min Section of Part Bed Temperature Data

Figure 117 and Figure 118 show similar data from both feed heaters that preheat the feedstock material prior to material being deposited on the part bed. As previously stated, the spike in temperature corresponds to the black body traversing in front of the sensors. When compared, the build thermal profiles of the part bed and feed beds are very similar.

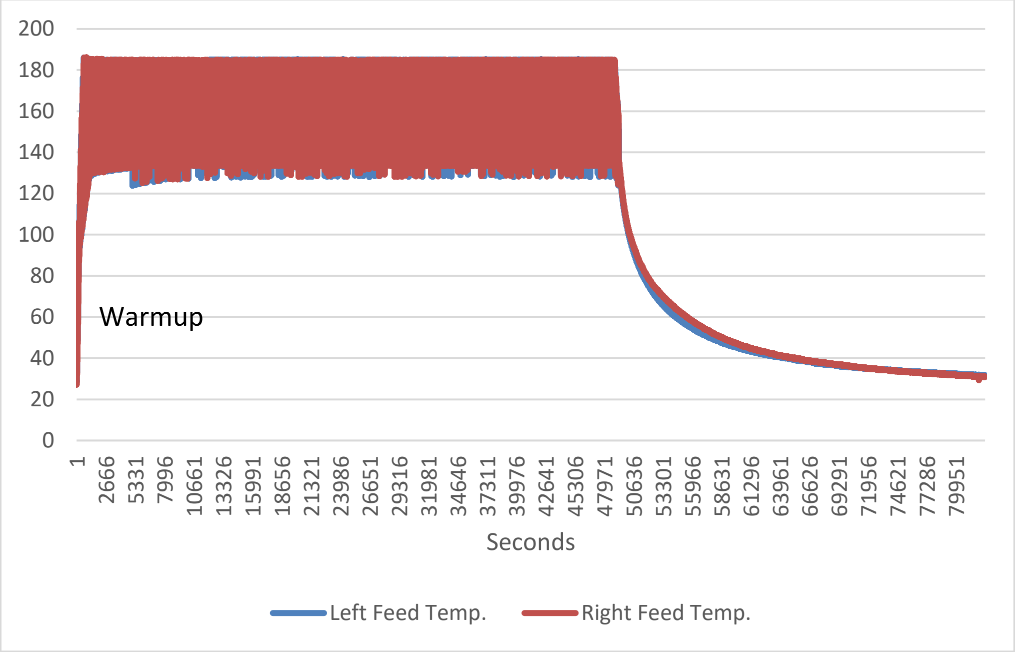

Figure 117: Feed Temperature Data Retrieved from Build Log

When evaluating the feed temperatures shown in Figure 118 in greater detail, the following observations can be made:

- The beat pattern caused by the black body calibration is removed from the first four cycles.
- The maximum duty cycle for the feed heaters is at 80% because they are lower wattage heaters than the part bed heater.
- The temperature cycles between 131°C for a low to the 135°C control temperature during the add powder layer sequence.

- Correlating what is seen between the feed and the part bed area, the feedstock powder increases from an average of 135°C to 164°C in about 5 seconds.

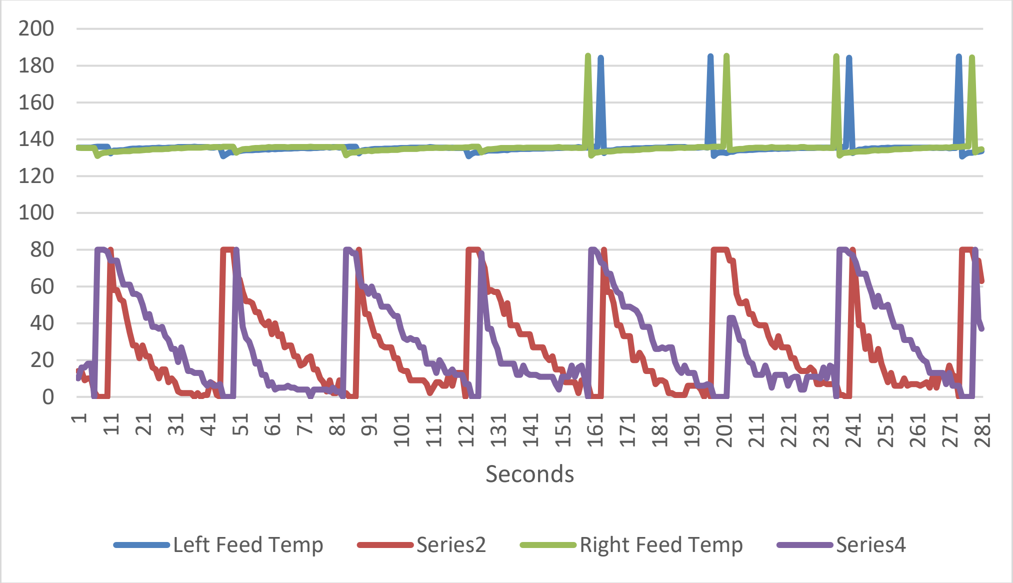

Figure 118: 10 min Section of Feed Temperature Data

6.2.3 PART BED IN-SITU THERMAL CHARACTERIZATION (THERMOCOUPLES)

Four thermocouples were used initially to chart the thermal history of a build plane as it progressed through the life cycle of a laser sintering build. Figure 119 shows the initial setup as each thermocouple were labeled and the colors mapped to the corresponding sensor. It takes about five (5) seconds for the thermocouple to respond to a user touching the tip and approximately one (1) to two (2) seconds to reach ambient after the user releases the sensor.

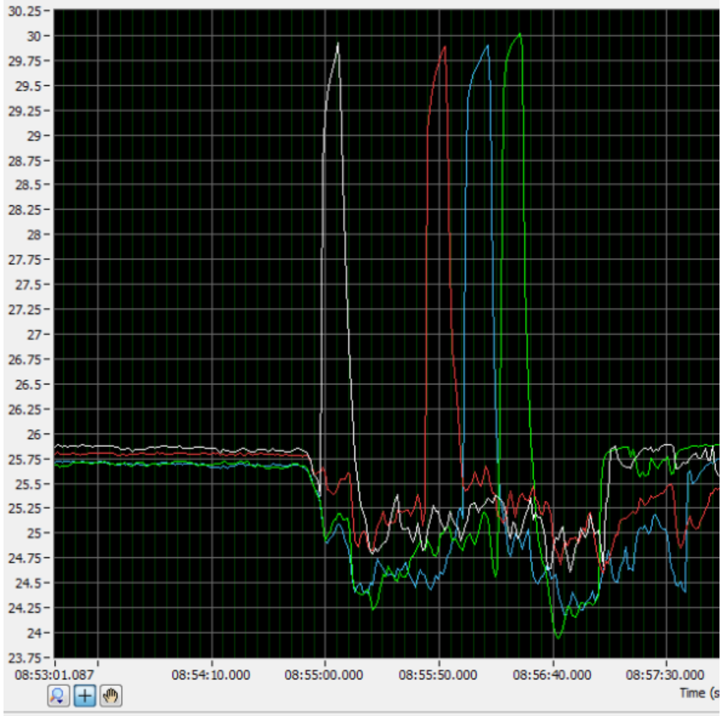

Figure 119: Thermocouple Response Time

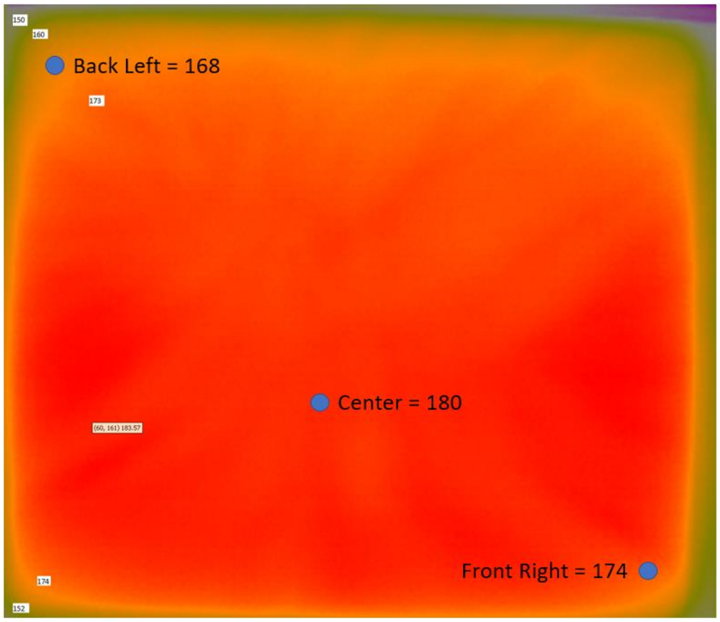

Figure 120: Location of Thermocouples and Corresponding Surface Temperature

The location of the three thermocouples pictured in Figure 98 is overlaid on the thermal image captured by the infrared camera in Figure 120. This data is used to correlate the thermocouple data, the IR camera data, and the build log data. The three thermocouples were inserted through the piston plate and extended to the part bed surface once the machine reached steady state thermal conditions. Figure 121 shows that there is an unstable region on the left side of the graph as the thermocouples are inserted through the build and manually adjusted to extend to the part bed surface.

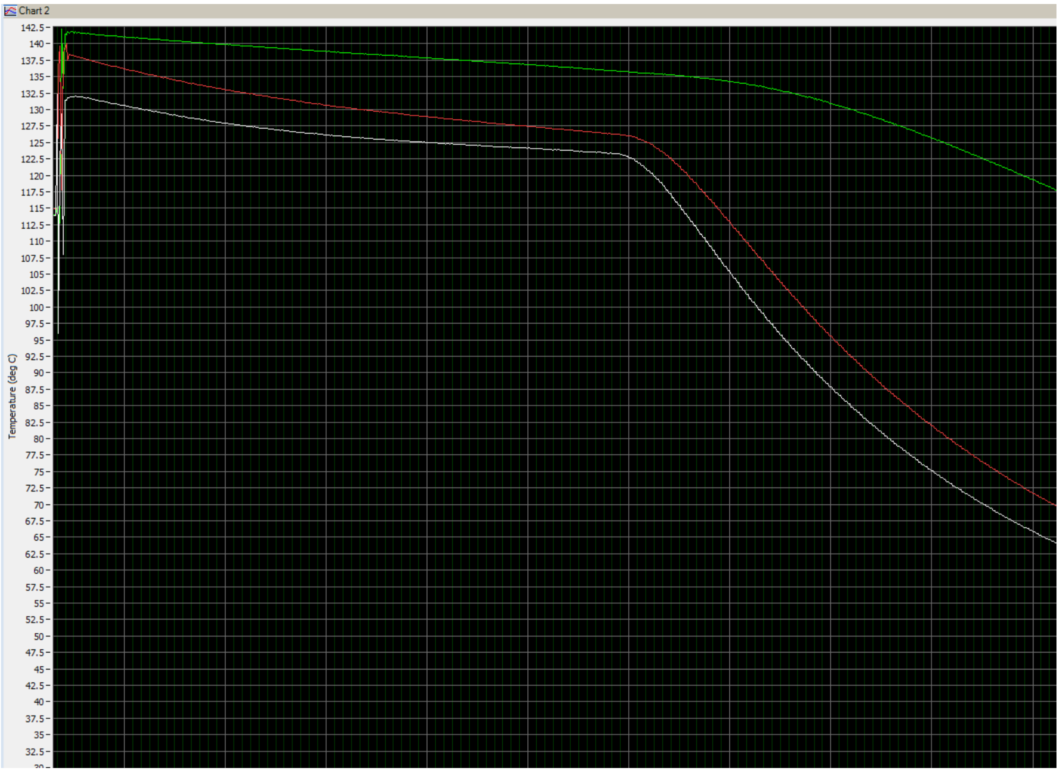

Figure 121: Build Temperature Data Recorded by Thermocouples

When the data is analyzed in more detail as was done in Figure 122, it can be seen that it takes a few minutes for the temperature to stabilize and then it starts to slowly drop.

The green line, representing the center thermocouple has an oscillation in the thermal profile corresponding to the add-powder layer. This graph shows a thermal rise and fall equating to twenty (20) add-powder layers which is equivalent to ten (10) minutes and 0.080” depth of penetration at 30sec/layer and 0.004”/layer.

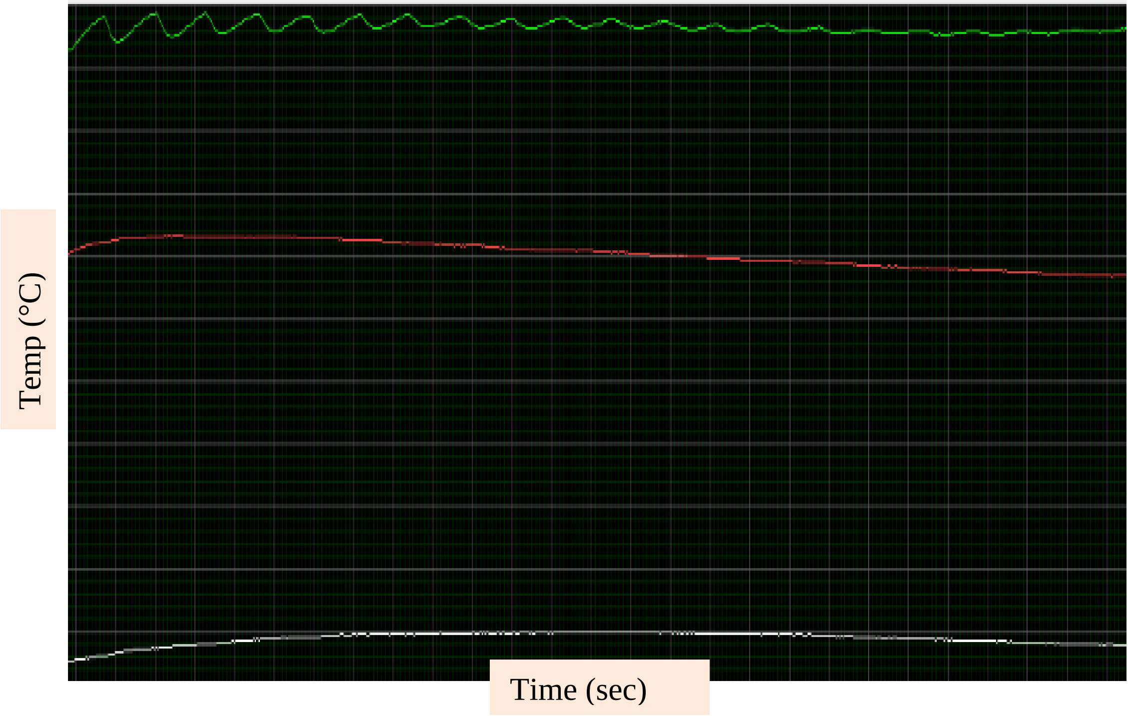

Figure 122: Initial 10 min Section of Thermocouple Dataset with Green Peak Representing 30 sec

6.2.4 STANDARD BUILD CONDITIONS

Seventy (70) tensile specimens were placed in a production build shown in Figure 89 using standard laser sintering production build and part profiles which are provided in Appendix C: Production Processing Parameters. The resulting elongation at break data can be seen in Table 10 and graphed using MATLAB in Figure 123. It should be noted that the table displays the data with an origin (x,y)=(0,0) at the top left but that the graph and machine have an origin located in the front left.

X	0	1	2	3	4	5	6	7	8	9	10	11	12	13
Y														
0	10	11		7		10		14		14		16		10
1	11		15				16				16		17	
2	13	13		14		20		18		14		14		17
3	13				18				14				14	
4		15		18		12		19		19		15		15
5			14				16	15			19			
6				14		18		14		17		13		6
7	15				13				18				13	
8		11		17		11		18		19		15		14
9		13	15				15				14		2	10
10		9		8		13		15		12		13		20
11	3				10				8					3

Table 10: Standard Build Tensile Specimens Elongation-at-Break by Location

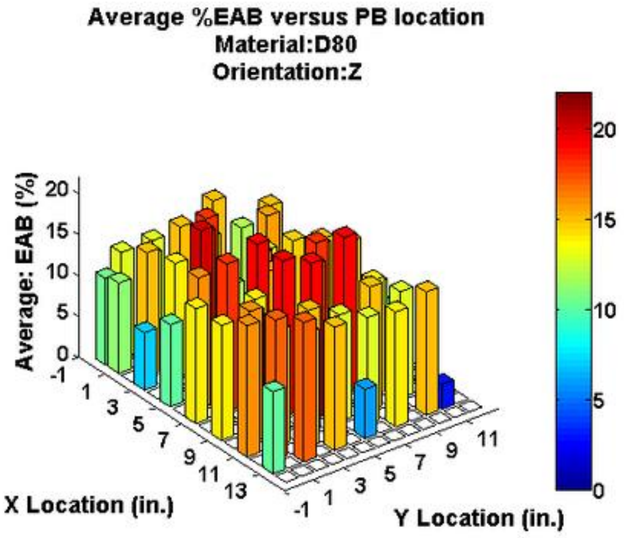

Figure 123: Plot of Standard Build Tensile Specimens Elongation-at-Break by Location

6.2.5 ELEVATED CYLINDER WALL THERMAL BOUNDARY CONDITIONS

The same build comprising seventy (70) tensile specimens shown in Figure 89 using the same build and part profiles listed in Section 6.2.4 Standard Build Conditions. The results of the second experimental build can be seen in Table 11 and graphed using MATLAB in Figure 124. As in the previous section, the origin (0,0) is different between the table and the plot.

X	0	1	2	3	4	5	6	7	8	9	10	11	12	13
Y														
0	12	12		17		16		18	15			16		9
1	13		18				22	20			15		13	
2	15	15		17		21		20		15		13		17
3	13			19	19			18	18				15	
4		21		21		17		18		18		14		16
5			15				13				19			
6		15		18		19		19		18		13		15
7					15				19				16	
8		18		15		10		15		16				17
9			15						16		15			
10		7		7		13		13		13		8		12
11	2				9				5				7	7

Table 11: Elevated Thermal Boundary Condition Build Tensile Specimens Elongation-at-Break by Location

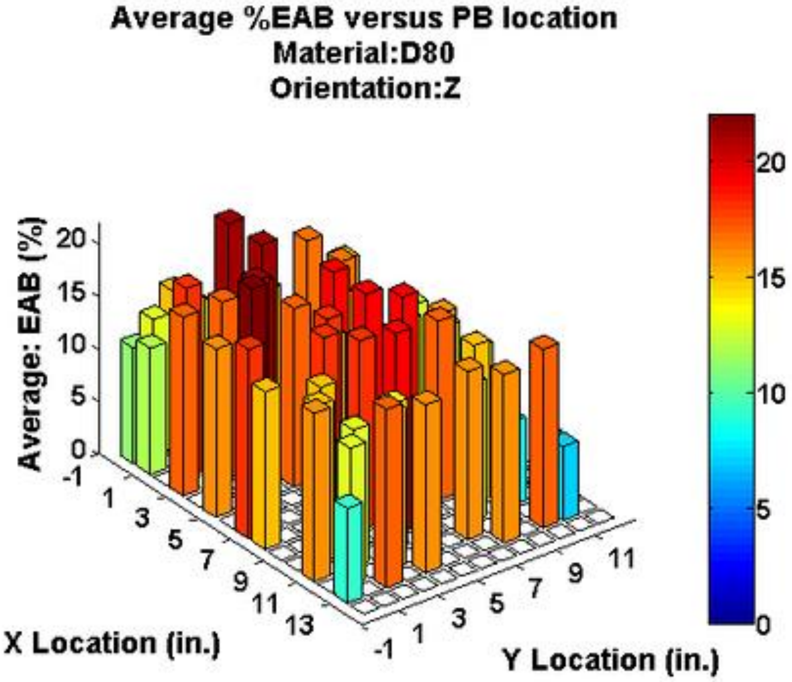

Figure 124: Plot of Elevated Thermal Boundary Condition Build Tensile Specimens Elongation-at-Break by Location

The data in Figure 124 shows that there is a significant increase in elongation-at-break when compared to Figure 123.

6.3 DSC Results of FR-106

Additional DSC data was collected to determine the enthalpy of melt of FR-106. The results of ramp rate from running the FR-106 DSC sample can be seen in Figure 125 and are consistent with the setpoints from Table 9.

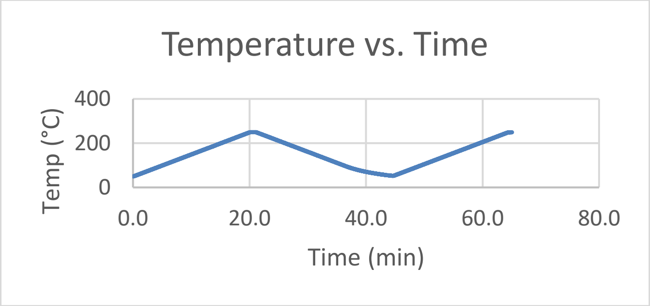

Figure 125: Thermal Cycle during DSC of FR-106

Plotting the heat flow from the FR-106 as seen in Figure 126 with heat flow mapped in relationship to temperature yields a chart like those previously described.

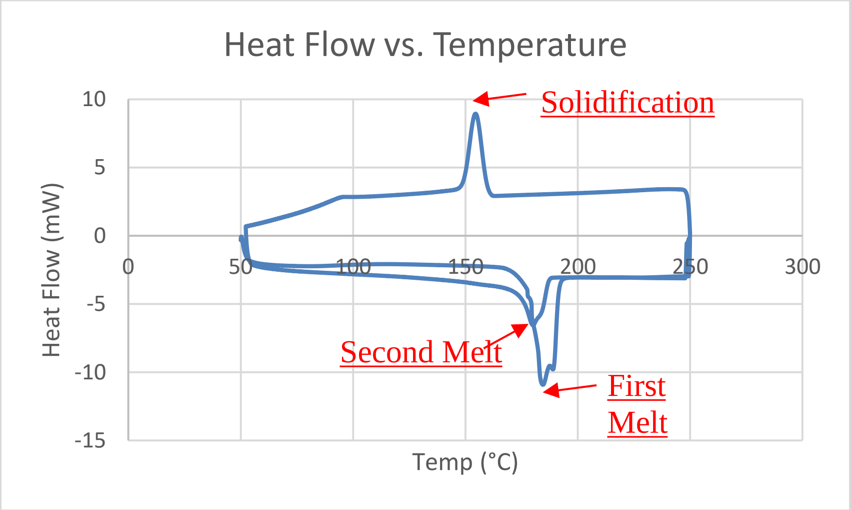

Figure 126: DSC Results of FR-106 Plotted over Temperature Range

Plotting the same data of the FR-106 DSC heat flow over time is used to calculate the activation energy or enthalpy of melt. This value (W) is needed for calculations in Section 7.5 Degree of Sintering Calculation. The second melt peak is marked in Figure 126, Figure 127 and Figure 128 with the key indexes used for the enthalpy calculation in an exploded view shown in Figure 128.

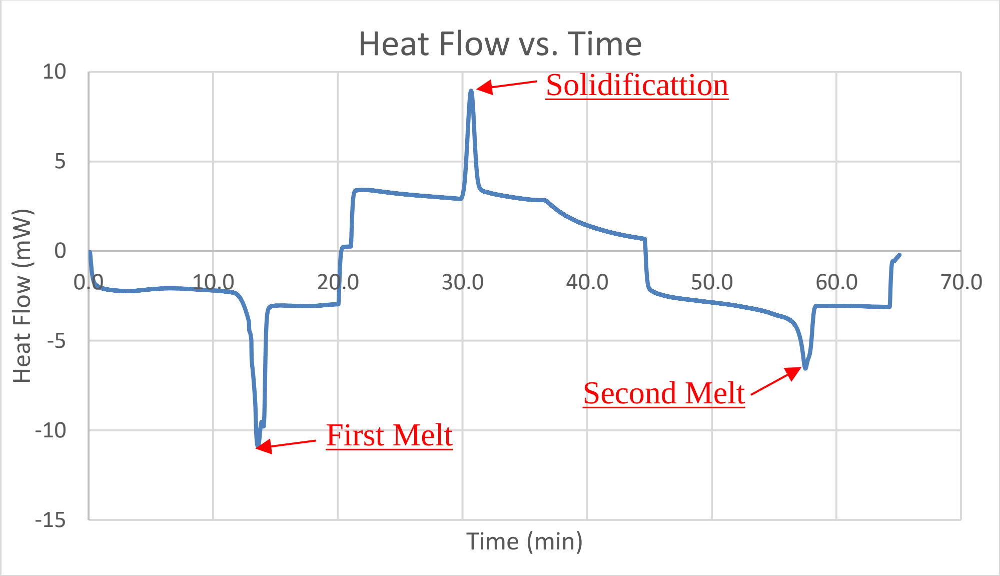

Figure 127: DSC Results of FR-106 Plotted over Time

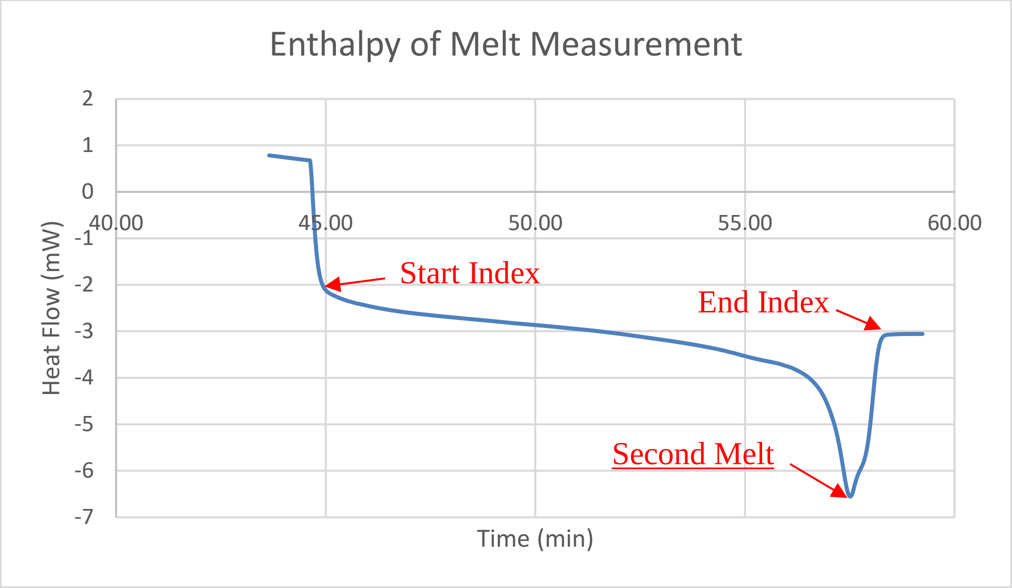

Figure 128: DSC Results of FR-106 which are used in Measurement of W.

There are key processing parameters that can be derived from the DSC tests, shown in Table 12. The processing window of laser sintering is generally between the solidification temperature and the melt peak. Both the melt temperature and the energy required to melt is greater at the first melt and less for the second melt. This second melt is of interest when evaluating the energy required to bond successive layers in the laser sintering process.

Key Information	Temp
Onset of solidification:	161.1°C
Peak solidification:	155.3°C
Onset of First Melt:	174.1°C
First Melt Peak:	184.8°C
Onset of Second Melt:	170.2°C
Second Melt Peak:	180.3°C

Table 12: Laser Sintering Processing Information Derived from DSC

The information obtained through the DSC test was also used to calculate the activation energy or enthalpy of melt (W) and is shown in Table 13 and the calculation of W is shown in Equation 12. The enthalpy shown in Table 13 was calculated by integrating the test data results of heat flow over time as shown in Figure 128. The value of W will be used to determine the degree of sintering in Section 7.5 Degree of Sintering Calculation.

Values for W Calculation	Value	
Sample Size	6.6 mg	
Molecular Weight	183.3g/mol	(Polymerdatabase, 2018)
Start Index	45.0 min	
End Index	58.4 min	
Enthalpy	2616.74 mJ	

Table 13: Enthalpy of Melt Data

$$W_{FR106} = \frac{2.61674\,J}{.0066\,g} \times \frac{183.3\,g}{mol} = 72{,}674\,\frac{J}{mol} = 72.67\,kJ/mol$$

Equation 12: Calculation of Enthalpy of Melt (W)

6.4 ANSYS® Fluent Thermal Model Results

Once the thermal model was established with appropriate nodes and boundary conditions, simulations of three (3), ten (10), and one hundred twenty-five (125) layers were performed. A detailed explanation of sequencing the simulation is available in Appendix E: ANSYS Fluent with the following sequence offering a summary:

- The macro reads thermal parameters into the simulation from a material database.
- Each layer is turned on sequentially with an initial temperature of 150°C which corresponds to an initial powder layer temperature observed during thermal camera measurements.

- The boundary conditions for the first layer is set to 150°C.
- As new layers are activated, the top of the previous layer and the bottom of the new layer become coupled. The top of the new layer has gradients applied that mimic the thermal data taken from the FLIR camera shown in Figure 129.
- When all layers have been simulated, a cool down sequence applies a convection coefficient to all boundaries of 5 W/m-K @ 40°C.

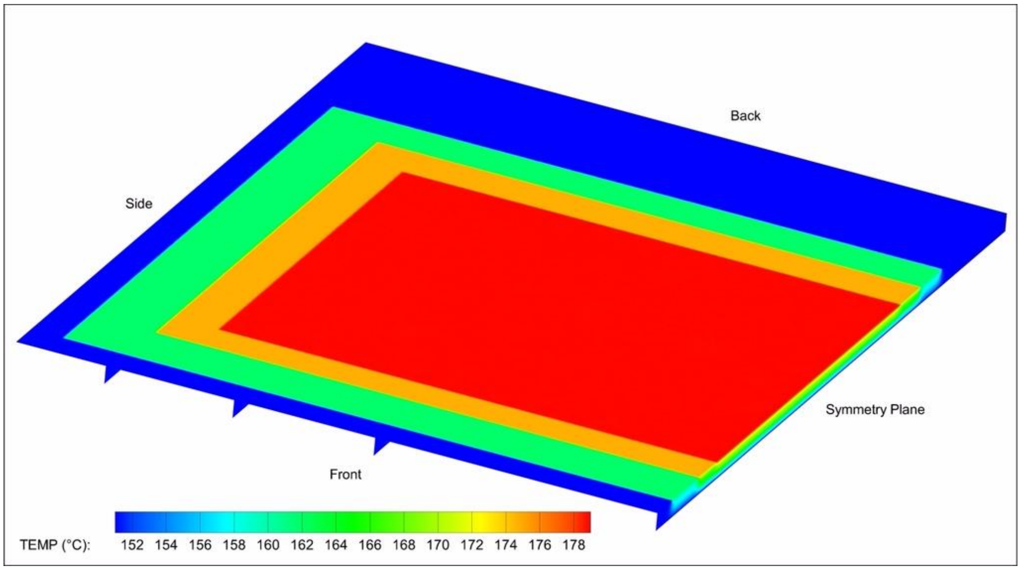

Figure 129: FLIR Camera Data Applied to ANSYS Simulation

Figure 130 and Figure 131 show the first two layers of a three-layer simulation with the same conditions as described in the modeling session and shown in Figure 74. Figure 130 shows the gradient of the top layer as it approaches a boundary conditions like what is expected in a laser sintering build. This also shows that during the initial layer, the 150°C boundary conditions on the bottom and sides has a significant effect on the thermal gradient within the layer.

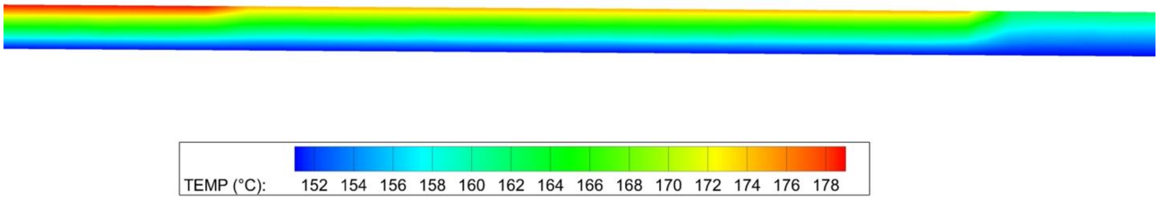

Figure 130: First Layer of a Three (3) Layer Simulation

As the three-layer simulation is allowed to progress through the animation, screen captures were taken at critical points and are displayed in Figure 131 with the add-powder-layer initial interaction at the top and the transition of the lower two images over the 30 second dwell time. The coupling of the joint bottom/top surfaces allow for the new layer to be heated from below as well as by the heater flux applied from above. After a few seconds, the two layers behave as a single layer.

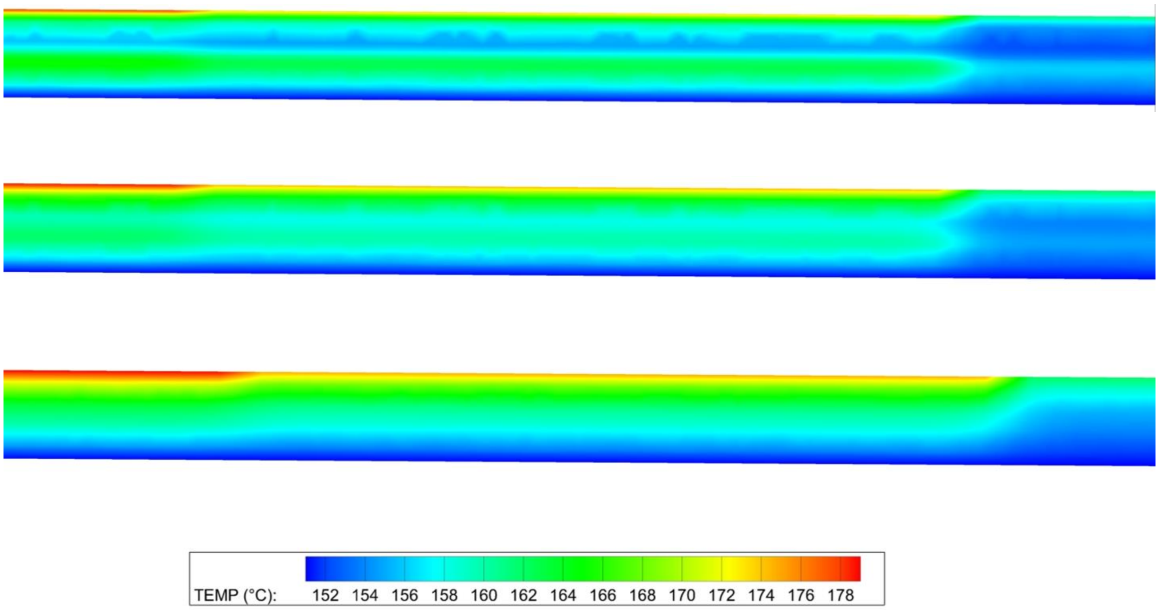

Figure 131: Thermal Dynamics of Add-Powder-Layer in a Two-Layer Simulation

When the simulation is fully complete, the detailed layer-to-layer thermal history is captured, and the full build thermal history can be observed and analyzed in greater detail from both a micro and macro points-of-view. This model, illustrated in Figure 132 and Figure 133, shows the results in three dimensions by displaying a ZX and a ZY plane cross section with the first image portraying the thermal profile for a build on its final layer and the second image portraying the same build after a cool-down process. TecPlot allows the user to select a node that can be displayed in a two-dimensional time-temperature graph shown in Figure 133 with the data available for export to Excel.

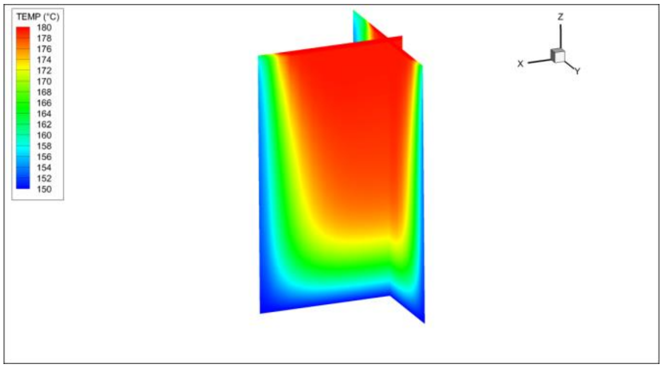

Figure 132: Thermal Map of a Laser Sintered Build on the Last Layer

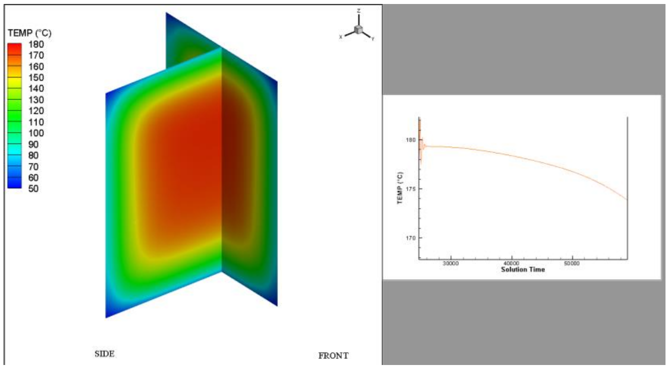

Figure 133: Thermal Map of a Laser Sintered Build During Cool-Down

7.0 DISCUSSION

7.1 Production Dataset

Obtaining production capable mechanical properties in a multi-platform environment over several years has proven that the most difficult parameter to maintain is the elongation-at-break value for tensile specimens oriented in the z-direction. As shown in the background and confirmed from the production dataset shown in Figure 134, the yield strength and ultimate tensile strength (UTS) are stable when sufficient energy is applied to the melt region. It is also observed that yield strength and UTS are consistent across the complete build region.

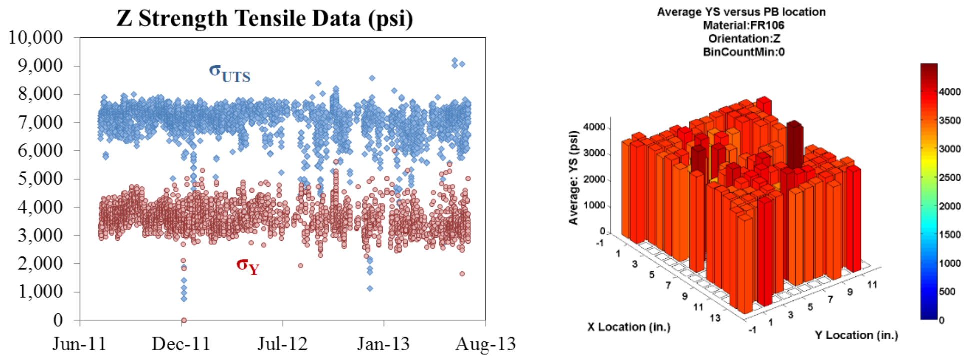

Figure 134: UTS and Yield Strength by Date and Yield Strength by Location

When elongation-at-break is evaluated by date there is significant scatter in the data but a pattern is observed when evaluating the same data based on tensile specimen build location as shown in Figure 135. While there is some contribution of the lower mechanical properties to a decreased part bed temperature at the edges of the build chamber, the gradient observed at the build plane does not fully align with the observed data. It is therefore reasonable to assume that there are additional factors that may explain the decreased elongation-at-break in this region.

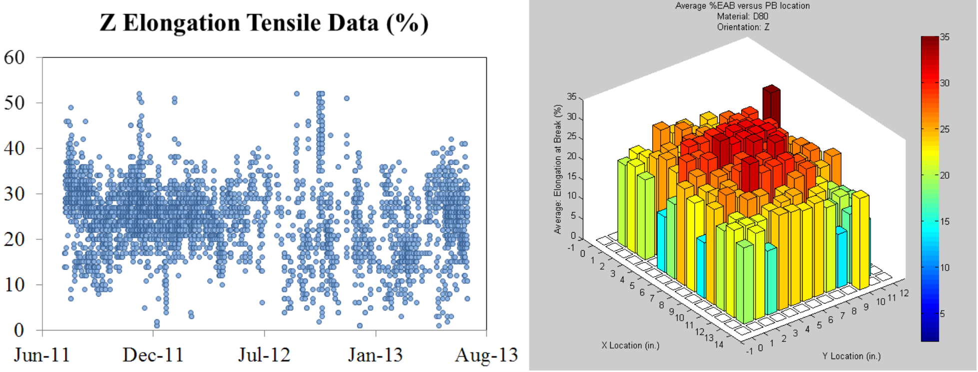

Figure 135: Elongation-at-Break by Date and Location

Coupling what was observed in the production dataset with observations of the elongation-at-break pattern observed in relation build depth shown in Figure 136 and Table 14, it can be shown that elongation-at-break is lower towards the extremity of the build envelope irrespective of direction. This is further confirmed based on the practice of having a longer warm-up height and the addition of a thermal boundary layer at the beginning of builds which is shown in Figure 137.

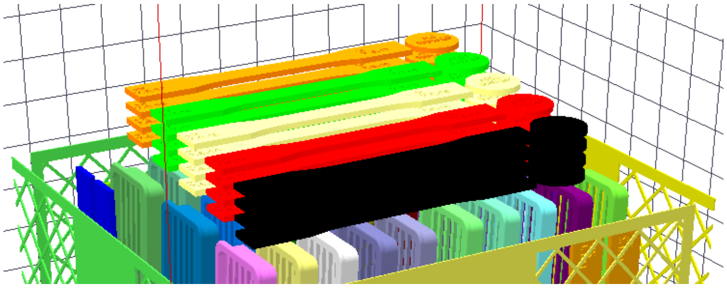

Figure 136: X-Ray Diffraction Specimens and Tensile Specimens (Leigh, Fracture Behavior in Laser Sintering, 2011)

Specimen	Depth (in)	σ_y (psi)	UTS (psi)	EAB %
1	-.125	2906	4757	11
2	-.461	2933	4749	12
3	-.797	2872	4876	14
4	-1.133	2891	5007	15

Table 14: Effect of Build Depth on Tensile Properties of XY Oriented PA-11 (Leigh, Fracture Behavior in Laser Sintering, 2011)

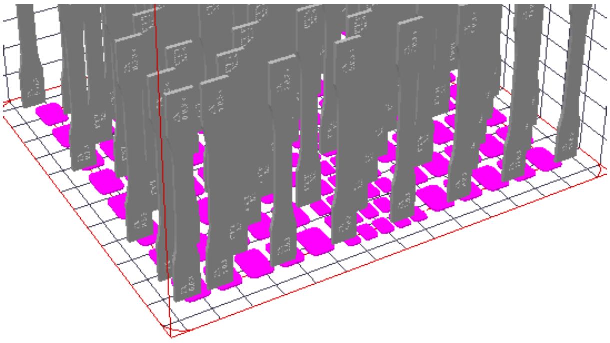

Figure 137: Initial Thermal Boundary Layer Geometry

Since the surface temperature observed was being maintained at a consistent value during a build, it would be reasonable to assume if mechanical properties were attributable to laser and surface temperature that there would be consistency at a given X-Y coordinate regardless of build depth or layer built. Since this is not the case, it is more reasonable to hypothesize that ***there is greater ductility observed in the regions that have critical time at temperature exposure***. Figure 138 shows a schematic of a build region that highlights the region of greatest ductility. Region 1 has sufficient surface temperature and laser power, but the dwell time is insufficient due to the cool-down effect at the end of the build. Region 2 shares the same surface temperature and laser power as region 1, but the dwell time is impacted by a bottom boundary condition insufficient to reach optimal healing of the interface boundary layer. Regions 3 and 4 are like region 2 in that they have side boundary conditions that are insufficient. In addition, the outermost edges of the build region may be impacted by thermal gradients and convection that are not present in the center region.

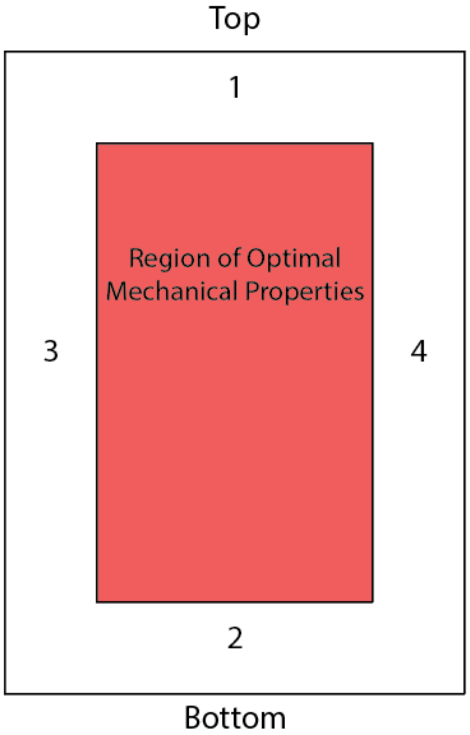

Figure 138: Cross-Sectional Schematic of Laser Sintering Build Region

7.2 Production Platform Evaluation

The part bed temperature observed on machine G112 showed a larger thermal gradient at the back of the machine and is shown in Figure 139. This large gradient creates a region of the part bed that has insufficient temperature for optimal mechanical properties.

It can also be observed that there are regions of striations in the back of the build chamber that are indicative of convection currents. The rest of the build region shows to be stable with a reasonable gradient at the extents of the build region. The lower side of these gradients corresponds with the boundary conditions of 150°C set by the cylinder heater processing parameter.

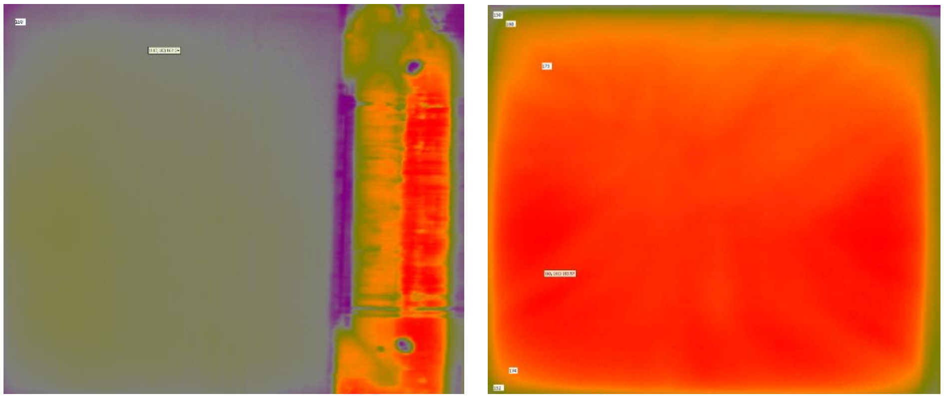

Figure 139: Part Bed Surface Temperature (Right image 10 seconds after left)

Figure 140 helps illustrate the add-powder-layer sequence and how the fluctuation in surface temperate is affected by the feedstock moving from the feed piston to the part piston region. The description of the callouts in the figure are provided below:

A. Left feed surface at setpoint of 135°C
B. Part piston previous layer surface at 180°C
C. Newly deposited layer at 150°C-165°C
D. Right feed surface drops to 131°C when powder is removed.

During this add-powder layer the left side of Figure 139 illustrates the drop in the surface temperature followed by a return to the setpoint in the right image after approximately ten (10) seconds. For simulation, the gradient observed on the right image is applied to the top surface and a temperature of 150°C is used to define the powder initial condition when layers are activated.

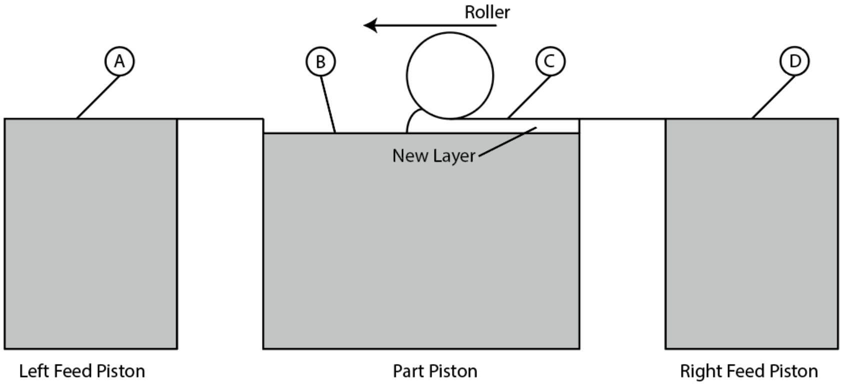

Figure 140: Add-Powder-Layer Schematic

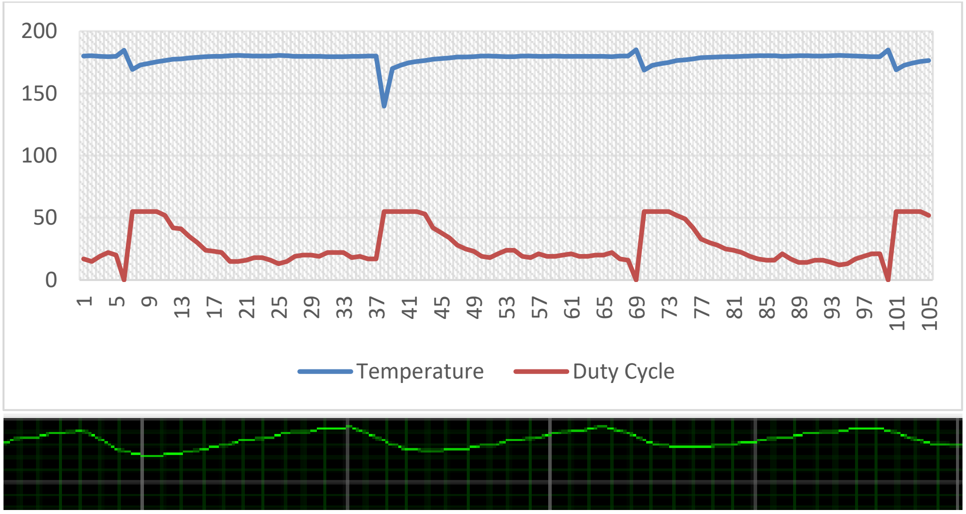

Figure 141: Comparison of In Situ Thermocouple to Surface Temperature Data

When evaluating the thermocouple data shown in Figure 121 and Figure 122 it was observed that the thermocouple continued to see a rise and fall in temperature at a period that matched the add-powder layer, which is shown in Figure 141. This oscillation in temperature is either caused by the cooler feedstock being deposited or is a result of the thermal energy from the radiant heater penetrating multiple layers. Since the polymer powder does not absorb 100% of IR radiation, it is reasonable to assume that the thermal energy produced by the radiant heater penetrates multiple layers and that there is additional heating of each layer not only contributable to the heater, but the laser as well. Using the data in Figure 122, there is an observable thermal effect for up to 20 layers over 10 minutes which represents a build depth of 0.080”.

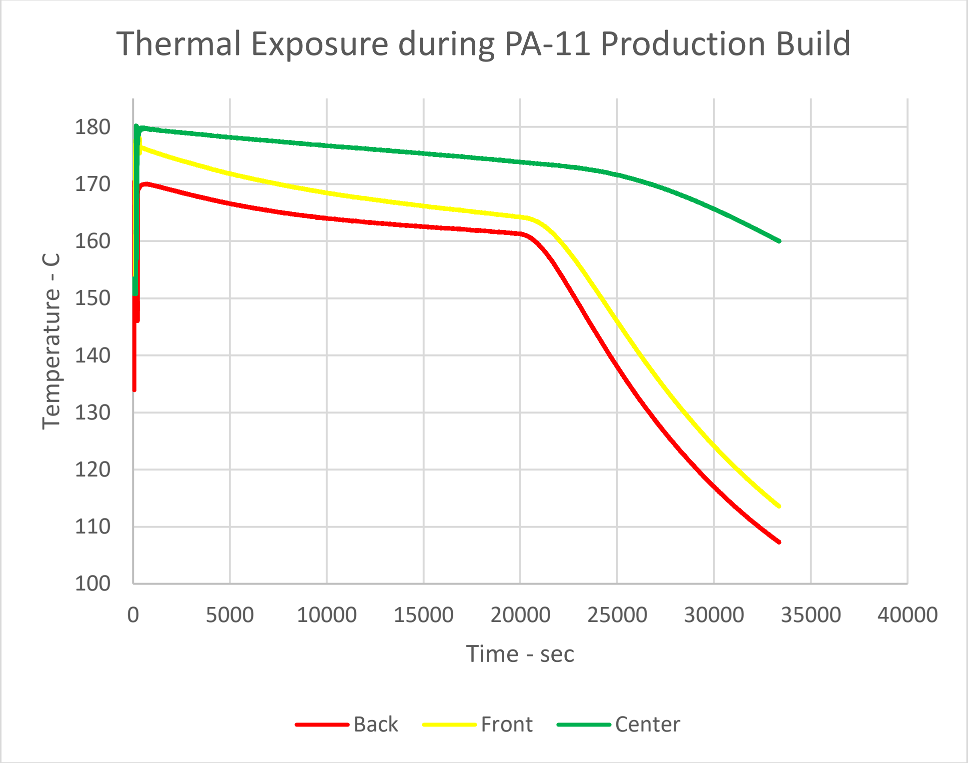

Figure 142: Adjusted Thermocouple Data exported to Excel

Thermocouple data was exported to an excel spreadsheet and is shown in Figure 142. When comparing the thermocouple data at the surface to the observed temperature from the IR camera and the equipment pyrometer, the thermocouple data is approximately

38°C below the value for all three probes. Prior builds with larger thermocouples were performed, but the thermal conductivity of the larger metal probes had a greater effect on the temperature than was desirable. While going to a small gauge thermocouple wire allowed for greater sensitivity and response, it was still sheathed by a bronze tube that is highly thermally conductive. This thermal conductivity likely contributed to the decreased temperature measurements. Instead of doing a detailed analysis, an offset of 38°C was applied to the data so that the temperature measurements are more accurate. This offset shows to be reasonable in that the final temperature of the red line is close to the 100°C termination point. In addition, the slope of the red line approaching a value of 160°C is consistent when compared to the results of the thermal model displayed in Figure 148.

The initial data captured on this graph was not filtered out and represents fluctuations in temperature as the probes were adjusted to the build surface. A significant deviation at 20,000 seconds can be observed which represents the point at which the build finished, and the cool-down cycle began.

7.3 ANSYS Fluent Thermal Model Discussion

The color scheme chosen to display the ANSYS thermal model using TecPlot ranges from blue to red and can be seen in Figure 143 and Figure 144. The blue regions (<154°C) represent a value at or below the solidification point of the material. Parts in this region will have crystallized and become solid. The burnt orange to red area (>175°C) represents a region at or very close to the melt temperature. Parts in this region are still a semi-viscous solid and very soft. This region will have undergone no solidification or shrinkage. The region ranging from green to yellow are the region that the material starts to change in flow behavior. The upper band is closer to the semi-viscous solid and the lower band is closer to the fully crystallized and solid part. This color scheme helps identify areas that are in an optimal flow condition for improving interface boundary healing.

Figure 143 compares the thermal profile during a build with a partial build shown on the left with the completed build on its last layer on the right. It can be observed that the initial layers and the region towards the edge see a transition to the solidification temperature. These regions also show decreased ductility as measured by elongation-at-break.

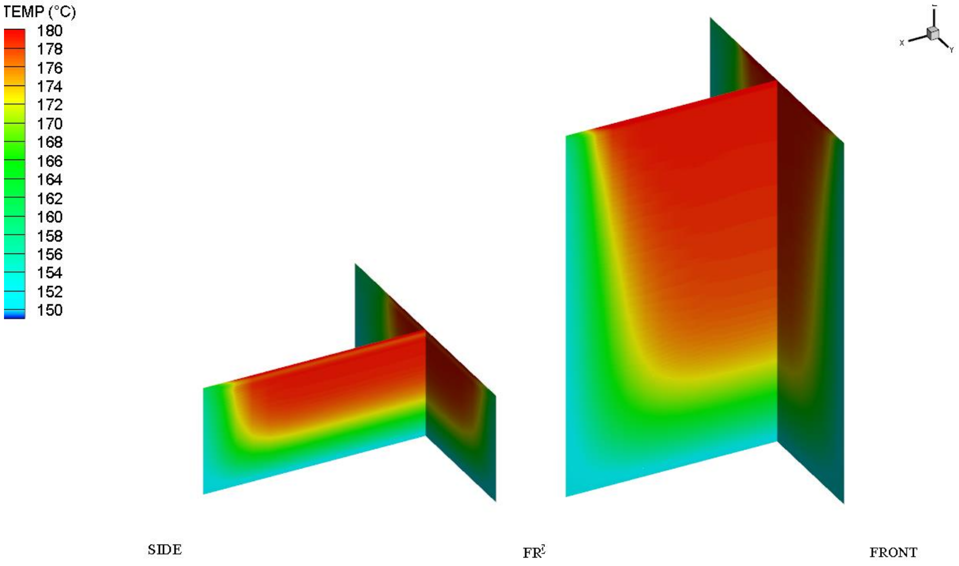

Figure 143: ANSYS Thermal Model – Partial and Complete Build

Figure 144 shows the same build illustrated in Figure 143 after a cool-down cycle of 30 and 40 min respectively. There is a significant change between 30 and 40 minutes as the top of the build transitions rapidly from a semi-viscous solid to a solid part. This upper region has the same XY plane thermal profile as previous layers, but the rapid transition to solidification can explain the decreased elongation of specimens built at the top of a production build.

TecPlot allows the user to probe a specific node that will allow for the extraction of the full thermal history of the selected voxel. When comparing the thermal model in the three regions representing locations similar to those where the thermocouples were located (Figure 145), the resultant thermal history is very close to what was observed in Figure 142.

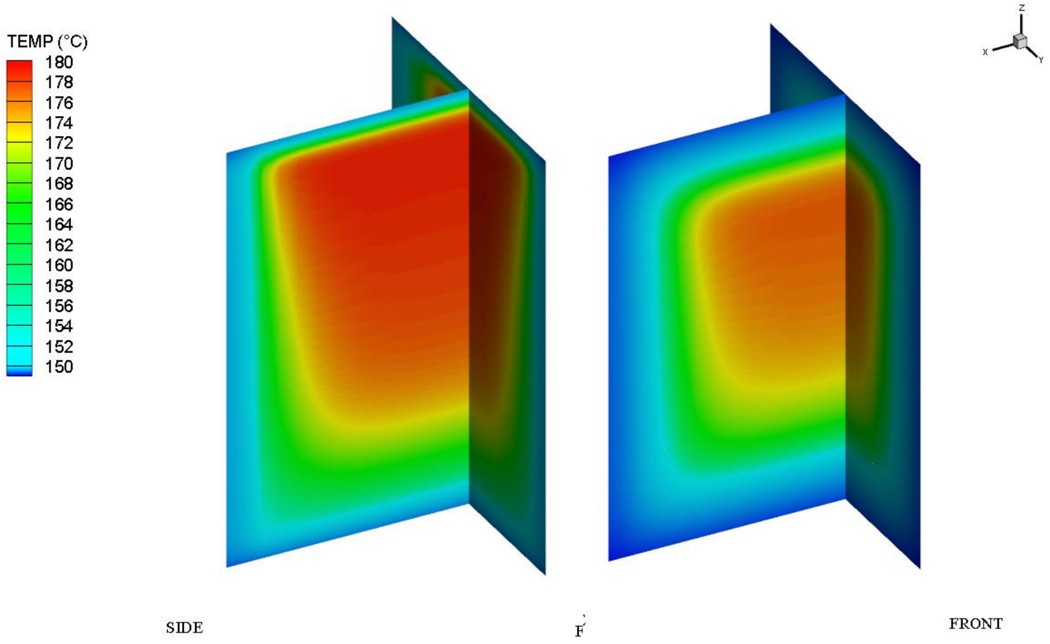

Figure 144: ANSYS Thermal Model – Cooldown at 30 min and 40 min

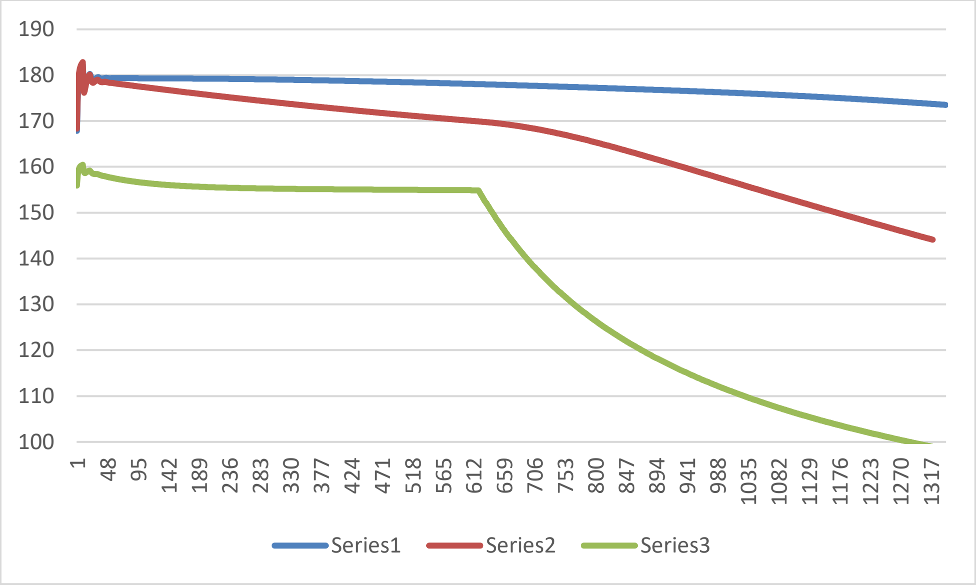

Figure 145: Time-Temperature output from TecPlot

There are three regions that experience consistently poor ductility during polymer laser sintering builds as described previously and illustrated in Figure 138. These three regions include the initial layers at the bottom of the build, the final build layers at the top of the build, and the regions on the extremities of the part bed. Using the ANSYS simulation and the TecPlot probe tool, Figure 146 through Figure 148 show that these regions have a minimal time at or near the melting temperature of 180°C. In contrast, the regions closest to the interior build region maintains a temperature above 175°C until the cool-down sequence is started. This compares to approximately 173°C which was captured by the thermocouple data.

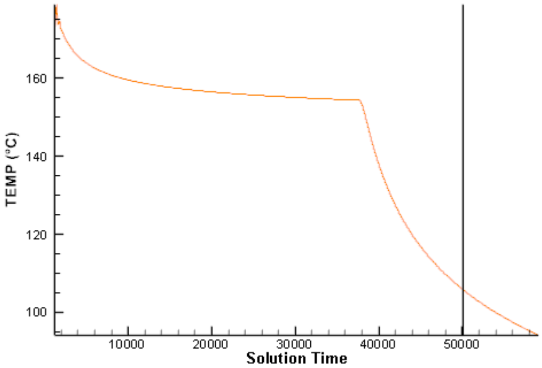

Figure 146: ANSYS Simulation - Initial Layer Build Conditions

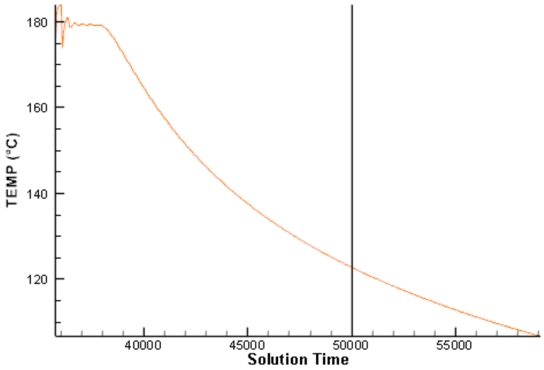

Figure 147: ANSYS Simulation – Late Layer Build Conditions

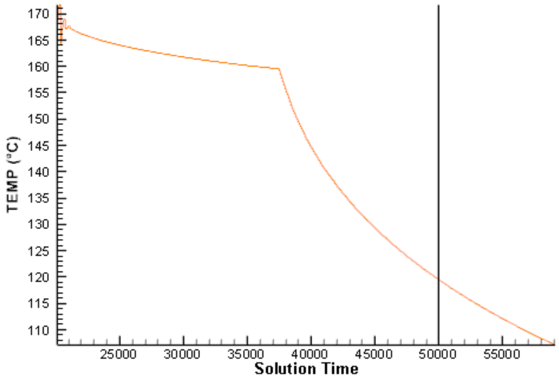

Figure 148: ANSYS Simulation – Exterior Boundary (edge) Build Conditions

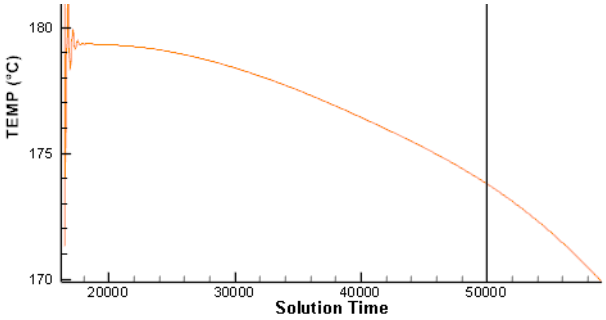

Figure 149: ANSYS Simulation – Interior Layer Build Conditions

7.4 Manipulated Boundary Condition Results

The builds described in Sections 6.2.4 Standard Build Conditions and 6.2.5 Elevated Cylinder Wall Thermal Boundary Conditions are compared below. The number of parts built were limited due to machine constraints and there were several tensile specimens that were broken or lost before the data could be collected. This gap in the data affected the ability of excel to plot a comparison map between the two builds. To create a more effective graphic, regions in the table were filled in by extrapolating the surrounding data to fill in an approximate value. These extrapolated datapoints can be seen highlighted in yellow in Table 15.

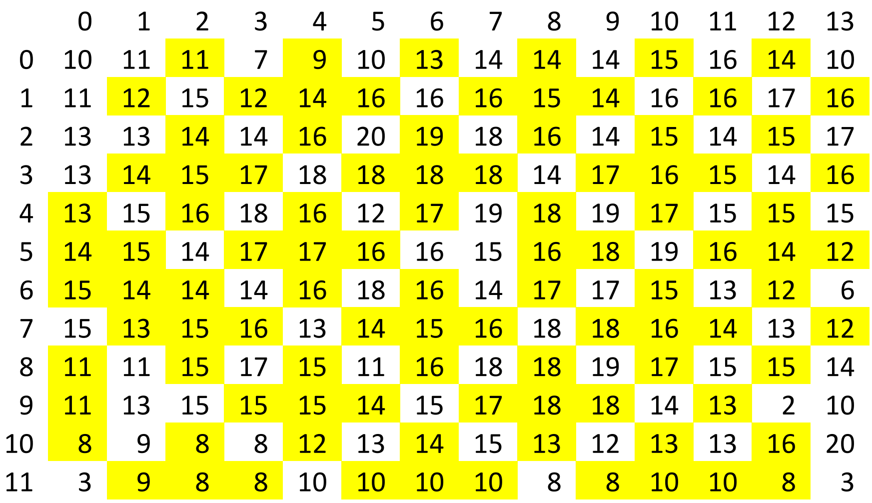

	0	1	2	3	4	5	6	7	8	9	10	11	12	13
0	10	11	11	7	9	10	13	14	14	14	15	16	14	10
1	11	12	15	12	14	16	16	16	15	14	16	16	17	16
2	13	13	14	14	16	20	19	18	16	14	15	14	15	17
3	13	14	15	17	18	18	18	18	14	17	16	15	14	16
4	13	15	16	18	16	12	17	19	18	19	17	15	15	15
5	14	15	14	17	17	16	16	15	16	18	19	16	14	12
6	15	14	14	14	16	18	16	14	17	17	15	13	12	6
7	15	13	15	16	13	14	15	16	18	18	16	14	13	12
8	11	11	15	17	15	11	16	18	18	19	17	15	15	14
9	11	13	15	15	15	14	15	17	18	18	14	13	2	10
10	8	9	8	8	12	13	14	15	13	12	13	13	16	20
11	3	9	8	8	10	10	10	10	8	8	10	10	8	3

Table 15: Standard Build Tensile Specimens Elongation-at-Break by Location with Extrapolated Gaps

The second build was built with additional heaters elevating the boundary conditions at the front and right cylinder walls to 175°C. This temperature was chosen for several reasons: the nylon powder will start to consolidate if it maintains a temperature of

178°C to 182°C and the interior region of the build that exhibit the greatest ductility maintained a temperature of at least 175°C during the build.

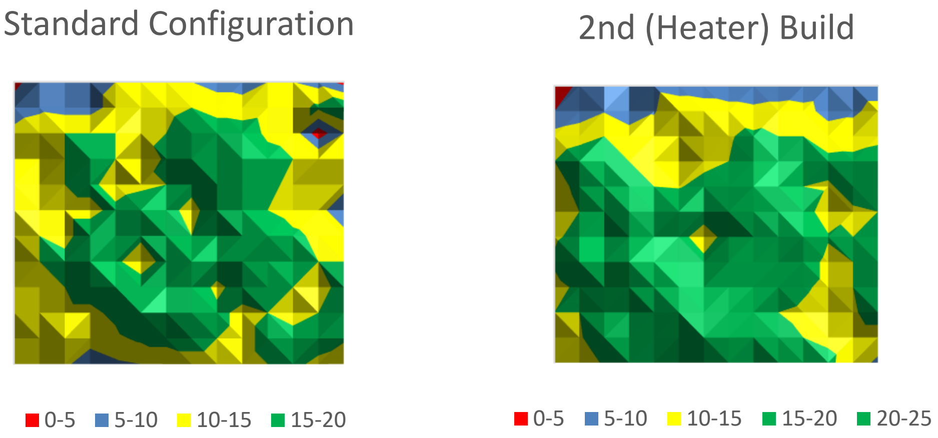

Figure 150: Comparison of Elongation at Break (%) in the Standard and Elevated Thermal Build using Excel

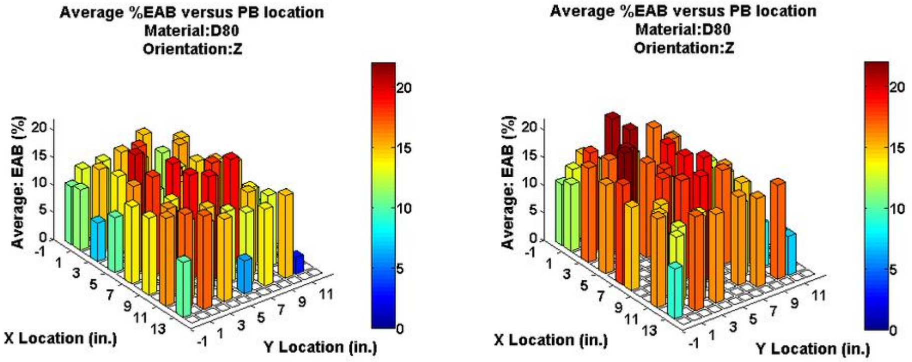

Figure 151: Comparison of Elongation-at-Break (%) in the Standard and Elevated Thermal Build using MATLAB

It can be seen in Figure 150 and Figure 151 that the second build saw a significant increase in ductility by increasing the temperature at the part cylinder boundary conditions. This increase had the result of increasing the dwell time of the affected geometries at a temperature of at least 175°C. There were sixty-two (62) tensile specimens that had data captured in corresponding builds at the same build location. Of these sixty-two (62) datapoints, thirty-two (32) had an increase in ductility, eleven (11) had no change, and nineteen (19) had a decrease in ductility. The rear of the build chamber with the higher thermal gradient and a boundary condition of 150°C did not have an increase in ductility. The green region that represents acceptable ductility by many customers increased significantly towards the front of the build chamber which had a boundary condition of 175°C. Ultimately, only two (2) of the five (5) boundary conditions were increased (40%) and positively impacted the ductility in thirty-two (32) of the sixty-two (62) or 52% tensile specimens. These results demonstrate that elevating the boundary conditions to 175°C can significantly improve part ductility and machine reliability.

7.5 Degree of Sintering Calculation

A variation of the sintering equations discussed in Section 4.1 Theory of Sintering should prove useful in quantifying the Degree of Sintering at the interface boundary layer. It has been shown that increased time at temperature allows for greater ductility. While the energy equations discussed in Section 2.6.3 Thermal Energy Characterization are adequate in the general case, an equation governing the second stage of sintering in polymer laser sintering applications needs to be defined. The second stage of sintering is a description of the aspect of sintering when the pores are overrun. The fracture surfaces of tensile specimens described in Section 2.7 Fracture Behavior of Laser Sintered Polyamide show the contribution of voids (or visible pores) to fracture limited ductility.

Equation 13 will be used as the basis to find the critical pore size that relates to a degree of sintering at which optimal ductility is achieved.

$$\frac{da}{dt} = -\frac{2\sigma}{a^2} \times \frac{\delta^3}{kT} D$$

Equation 13: Kinetics of Second Sage of Sintering (Ristic & Milosevic, 2006)

Where $D = Ae^{-\frac{W}{kT}}$

$A = \delta^2/6\tau_o$

$W = U + \Delta U$

$p = capillary\ pressure = \frac{2\sigma}{a}$

$\sigma = interfacial\ tension$

$a = radius\ of\ the\ critical\ size$

$\delta = constant\ of\ the\ crystal\ lattice$

$D = Constant\ of\ Diffusion$ (Fick's Law)

$k = Bolzmann's\ Constant$

$\tau_0 = period\ of\ oscillation\ of\ atoms\ at\ equillibrium$

$U = Energy\ of\ Forming\ Vacancies$

$\Delta U = Activation\ Energy$

$$\frac{da}{dt} = -\frac{2\sigma}{a^2} \times \frac{\delta^3}{kT} D$$

$$da = -\frac{2\sigma}{a^2} \times \frac{\delta^3}{kT} D\, dt \;\; where\; D = Ae^{-\frac{W}{kT}}$$

$$da = -\frac{2\sigma}{a^2} \times \frac{\delta^3}{kT}\, Ae^{-\frac{W}{kT}}\, dt\; where\;\; A = \delta^2/6\tau_o$$

$$da = -\frac{\sigma\delta^5}{3a^2\tau_o k} \times \frac{1}{T}\; e^{-\frac{W}{kT}}\, dt$$

rewritten

$$\Delta a = \left(-\frac{\sigma\delta^5}{3a^2\tau_o k}\right)\left(\frac{1}{T}\; e^{-\frac{W}{kT}}\right)\Delta t = \left(-\frac{\sigma\delta^5}{3a^2\tau_o k}\right) f_c(t,T)$$

Note the first term in parentheses contains constants, and the second term is the function of temperature (T) and time (t). Based on similarity in the general densification of a powder mass in laser sintering to the "densification" in the two-sphere model defined by the decrease in pore size represented by Δa, we can assume that, for the former, the amount of densification is proportional to the second term, defined to be $f_c(t,T)$. And since this equation will be used as a relative comparison within a given material system, a laser sintered nylon normalization factor can be used (N_{ls}).

At a point in the powder bed, we assume that a critical temperature must be maintained as a threshold upon initial heating at which point the sintering mechanism "kicks in" and the porosity is being diffused. Likewise, on cooling, at this same threshold temperature, the sintering mechanism halts.

The “front”, “back” and “center” thermocouple measurements were numerically integrated using the summation form of the part associated with $f_c(t,T)$:

$$Degree\ of\ Sintering = DoS = \left[f_c(t,T) = N_{ls} \sum_{i=1}^{n} \frac{1}{T_i} \left(e^{-\frac{W}{kT_i}} \right) \Delta t_i \right]$$

Equation 14: Degree of Sintering Calculation

$$Where\ \ W = \frac{72.67\ kJ}{mol} and\ R\ was\ substituted\ for\ k. \quad R = .008314 \frac{kJ}{mol\ K}.$$

One might assume that the activation energy takes care of the thermal impact on the sintering mechanism and that a threshold temperature is not needed. The value of the activation energy was mentioned in literature, but no specific value was given for the laser sintering process. (Parrini & Romanini, 1976) (Perkins & Porter, 1981) Therefore, it was necessary to derive W from experimental results with the result being calculated in Equation 12.

Integrating the $f_c(t,T)$ function over all temperatures in the excel spreadsheet, the values are obtained and shown in Table 16. In this case of the thermal exposure of the front thermocouple, a “marginally acceptable” result is 1.44x10^{-7} s/K.

Location	Fc(t,T), s/K
Back	1.17x10^{-7}
Front	1.44x10^{-7}
Center	2.40x10^{-7}

Table 16: Results of $f_c(t,T)$.

Converting this number to an intuitive number can be used by creating a normalization factor where $N_{ls} = 7 \times 10^6 K/s$. Doing so provides a *degree of sintering* shown in Table 17 where the front thermocouple results which were equated to the breakover between acceptable and unacceptable have a value of 1. With this baseline established, the front thermocouple and center have values greater than or equal to one (1) which represents an acceptable level.

Location	*Degree of Sintering*
Back	.816
Front	1.008
Center	1.677

Table 17: Degree of Sintering Results

7.6 Build Analysis using ANSYS and Degree of Sintering Model

Thermocouple data, ANSYS simulation, and the Degree of Sintering model are compared in the different regions to show the similarity between the actual vs. modeled thermal results. The thermal results are also plotted with $f_c(t, T)$ or Degree of Sintering to show the time at which a selected region has (or has not) met the ideal sintering conditions. Figure 152 through Figure 154 compare the actual thermocouple data presented in Section 6.2 Production Platform Evaluation Results with the ANSYS model presented in Section 6.4 ANSYS® Fluent Thermal Model Results.

The degree of sintering value was multiplied by one hundred (100) so that it is visible on the same scale the temperature data (°C). A red line is used to mark when the degree of sintering crosses the ideal threshold. The modeled results are similar to the actual recorded temperature. The slight difference can likely be attributed either to the metal sheath around the thermocouple acting as a heat sink or the material feedstock thermal conductivity used.

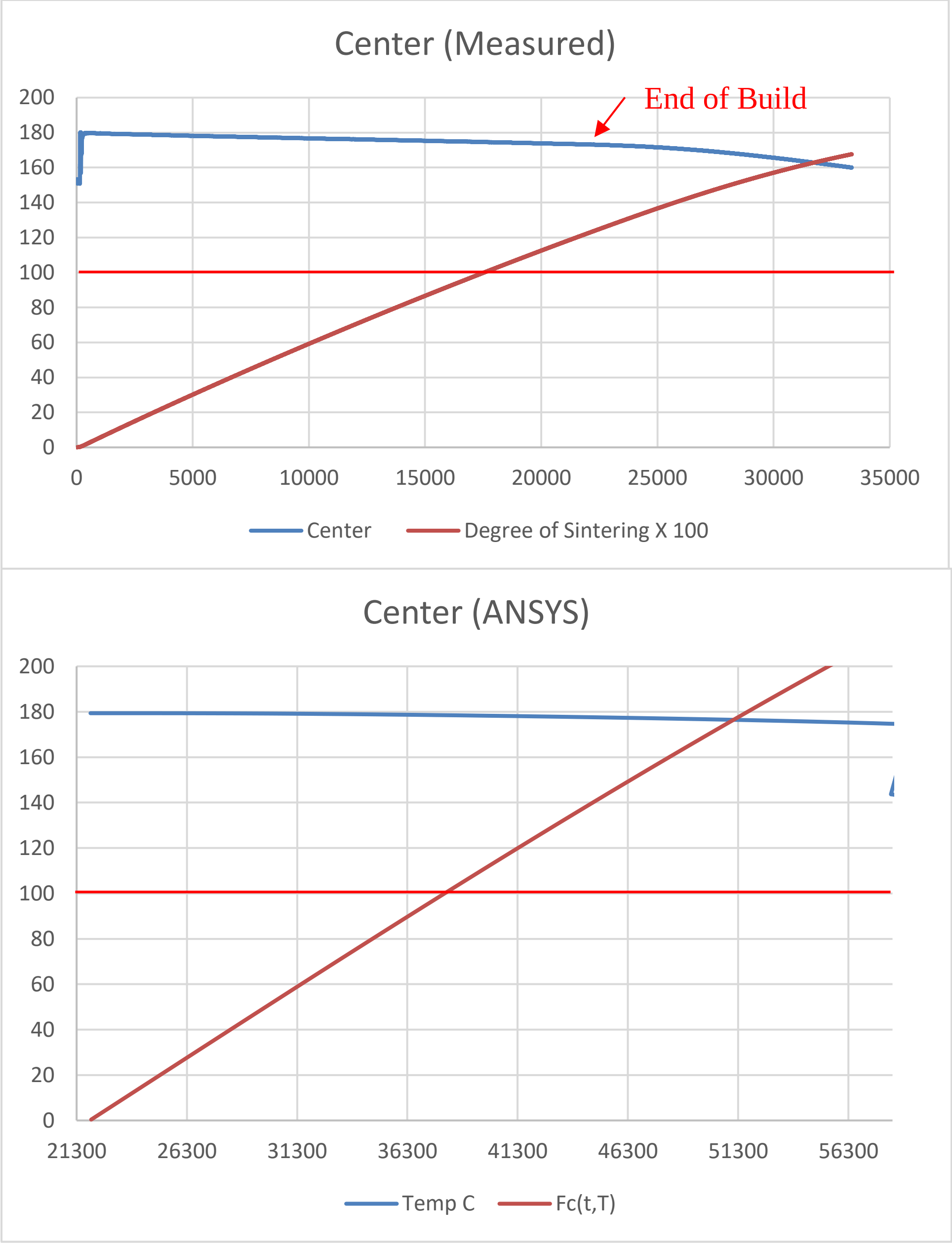

Figure 152: Temperature Profile of Center Thermocouple Location and Resultant Degree of Sintering Value

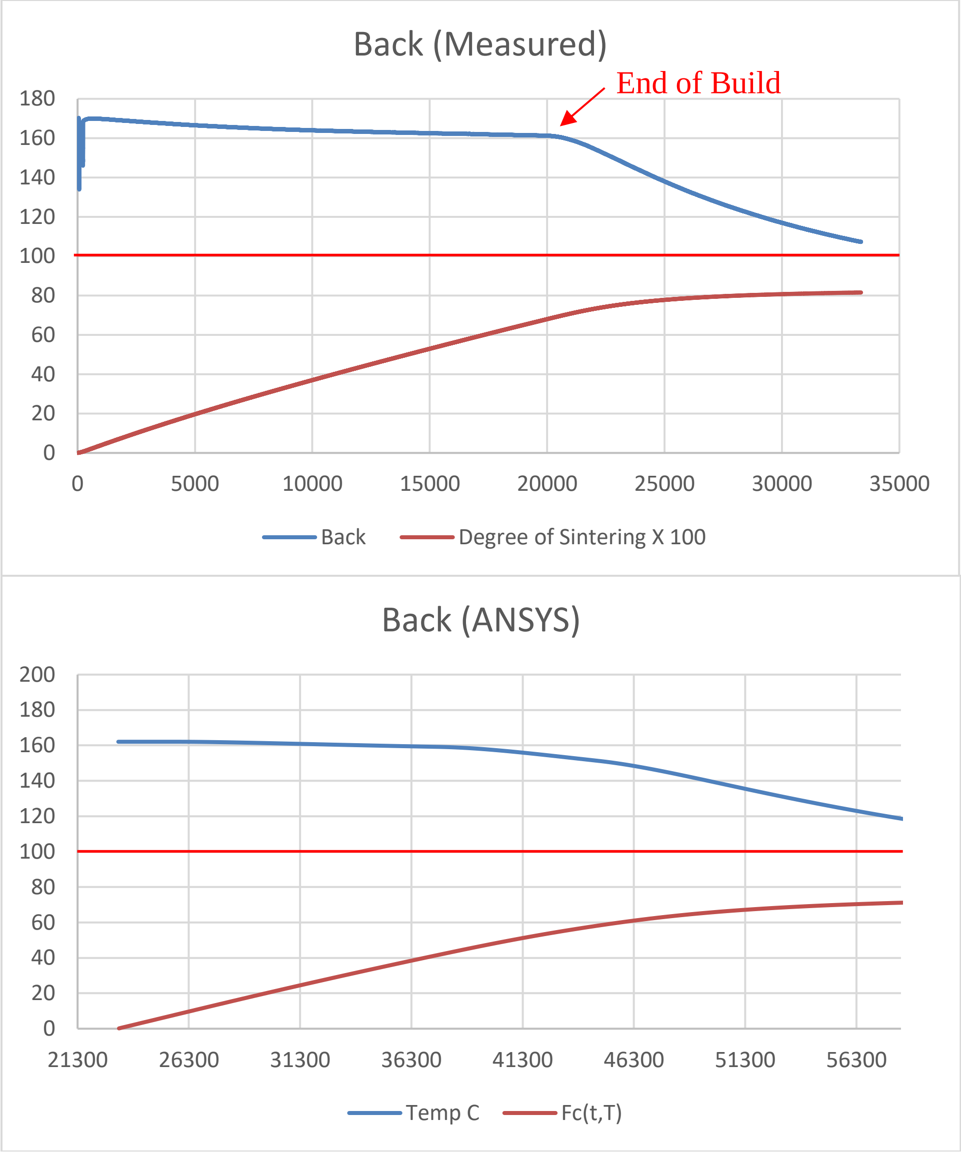
Back (Measured)

Back (ANSYS)

Figure 153: Temperature Profile of Back Thermocouple Location and Resultant Degree of Sintering Value

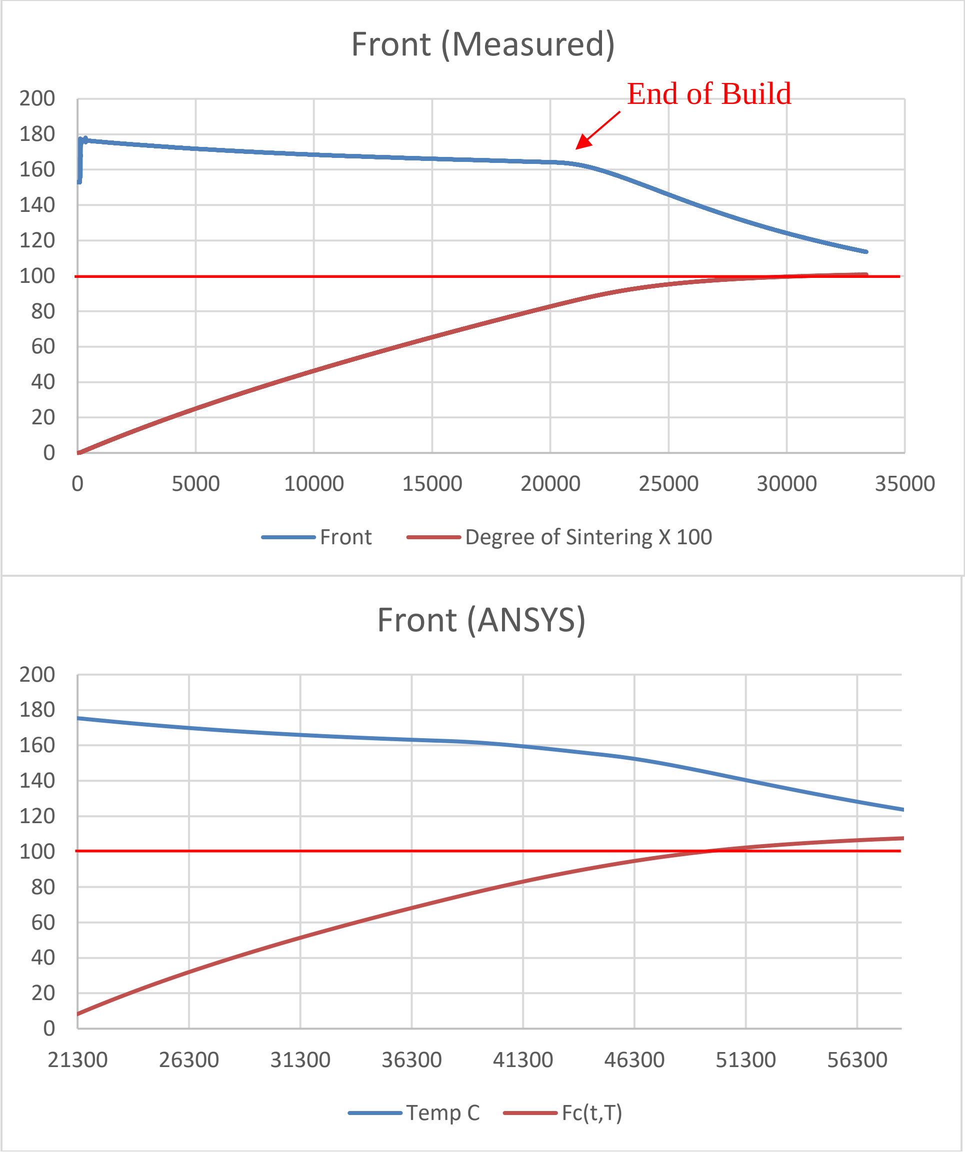

Figure 154: Temperature Profile of Front Thermocouple Location and Resultant Degree of Sintering Value

There were two builds discussed previously in which one set of tensile specimens were built under normal conditions and the second set of specimens were produced using elevated boundary conditions. The parameters from both builds were used to create a standard build simulation and an elevated build simulation. The results from these two simulations and the corresponding increase in the profile temperatures can be seen in Figure 155 and Figure 156. The Degree of Sintering increased significantly in the front right quadrant where the node would have been influenced by the elevated front and right boundary conditions as illustrated in the lower graph in Figure 155. The back thermocouple in this model is in the region of the lower thermal gradient experiences in the back of the build with proximity to only the elevated right boundary condition which can be seen in Figure 156. This slight elevation does not increase the thermal exposure enough to cross the Degree of Sintering threshold. Based on these results, it would be expected that the ideal sintering region would be minimally affected in the back and should see an increase in the front and side of the build.

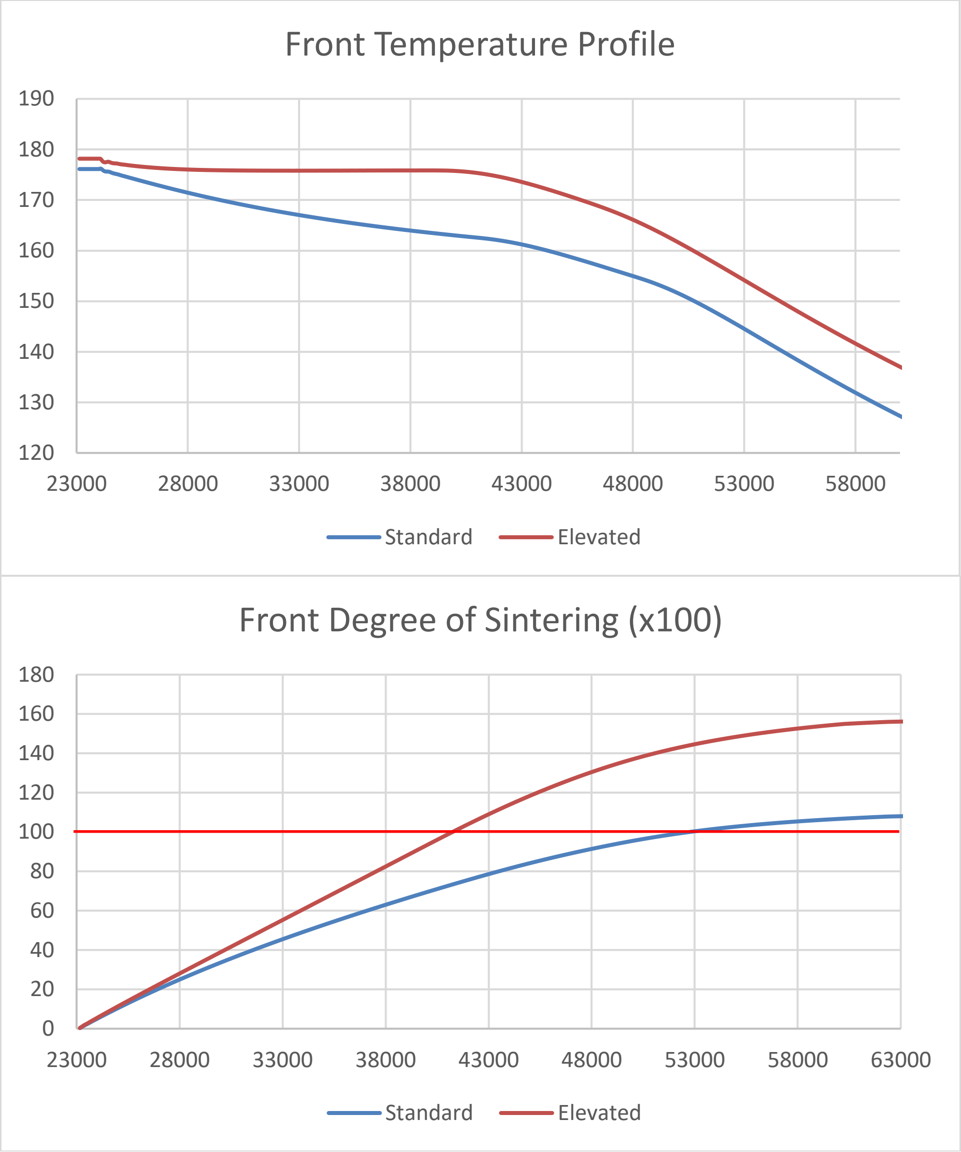

Figure 155: Thermal Data from Finite Element Model Comparing the Front Thermocouple Location in the Standard and Elevated Thermal Builds

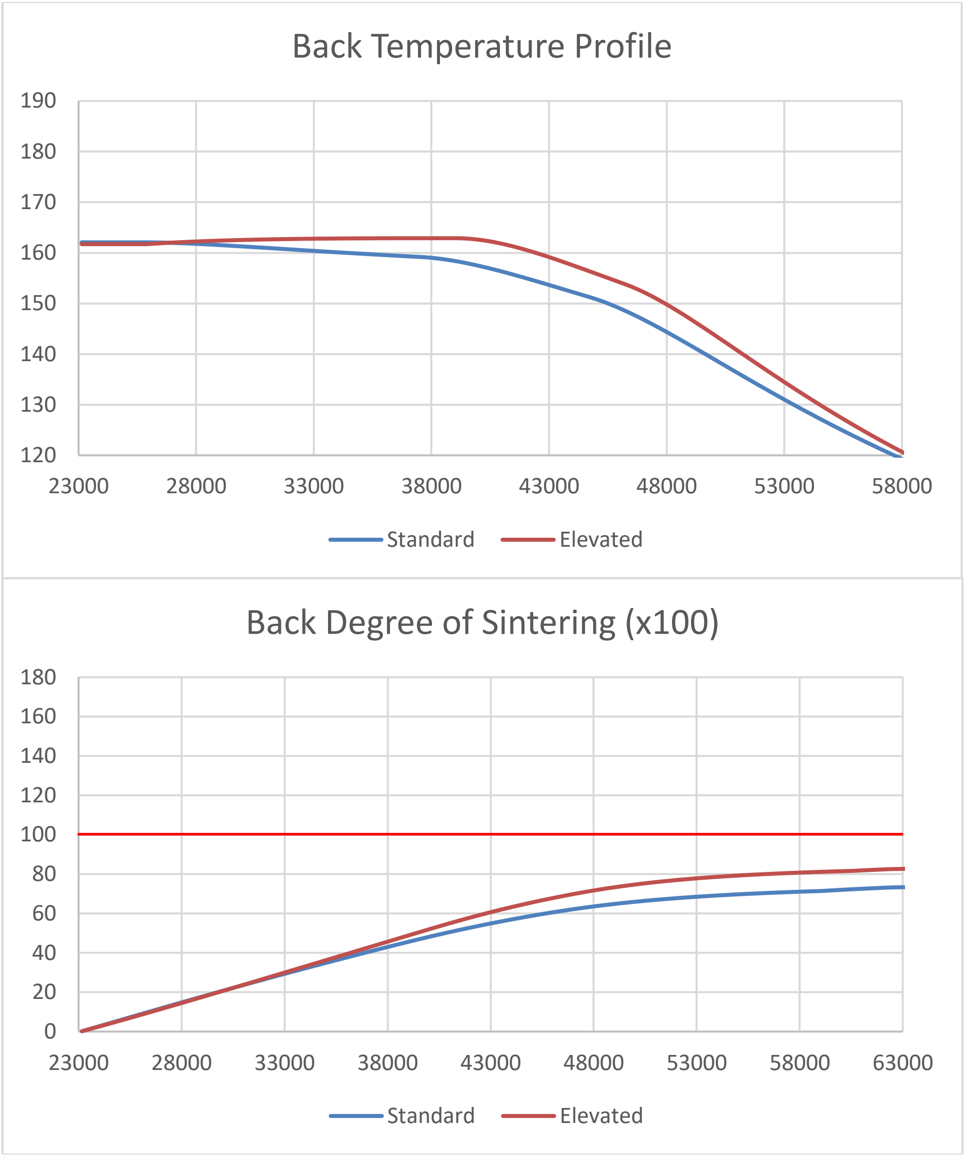

Figure 156: Thermal Data from Finite Element Model Comparing the Back Thermocouple in the Standard and Elevated Thermal Builds

Symmetry was used, and several cross-sectional planes were defined in TecPlot so that nodes could be selected to create a map of the temperature profiles and corresponding Degree of Sintering. The objective was to create a map of the ideal sintering region: that region in which the degree of sintering would be greater than or equal to one (1). This map could then be compared to the phenomenological results from the standard and elevated build, the x-ray diffraction samples that were built at the top of a build, and the experience in production of creating sacrificial geometry at the beginning of the build. Many nodes were selected, and the data was exported to Excel for use in calculating the degree of sintering. When a node was found to have a value of one (1), the coordinates of that node were recorded and plotted. Figure 157 shows the symmetry and the cross-sectional planes. This simulation represents one-half of the build (right half) with the symmetry plane along the y-axis, another plane extending along the x-axes to the build extent, and two planes placed at 45°. The results of mapping the extents of the ideal sintering region can be seen in Figure 158 and Figure 159 with the planes marked as lines extending from the center. The x-y coordinates that produced degree of sintering value of one (1) are circled.

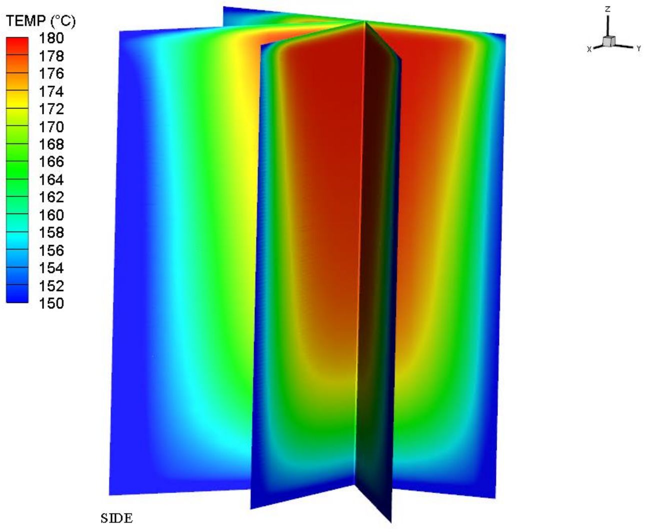

Figure 157: Symmetry Planes in ANSYS – TecPlot

Figure 158 shows a top view of the laser sintering build area with three marked regions. Region 1 represents the area of ideal sintering for the standard build and Region 2 represents an expanded region of increased material properties as predicted by the Degree of Sintering while Region 3 is the area predicted to have the poorest mechanical properties. There is a reasonable correlation when comparing the predicted results in Figure 158 with the actual results shown in Figure 150 and Figure 151.

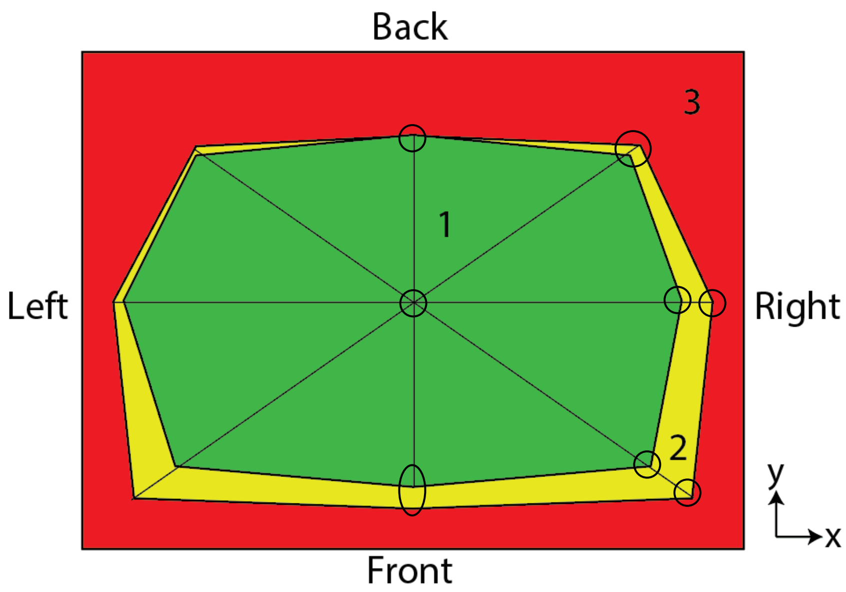

Figure 158: Comparison of Standard and Elevated Thermal Builds Using Degree of Sintering Values

The bottom and top extents were determined by probing the Y-plane of symmetry in the TecPlot model for a standard build at the top and bottom along the central axis. The results are illustrated in Figure 159 with the highest vertical node to achieve a Degree of Sintering of one (1) was 1.60” from the top and the lowest was 0.44” from the bottom. Figure 160 and Figure 161 show the top and bottom temperature profiles and Degree of

Sintering values. The bottom extent is more sensitive to the cool-down boundary conditions due to the proximity to the boundary.

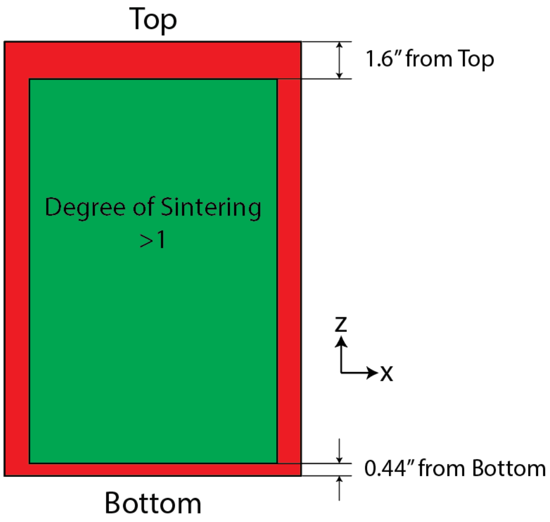

Figure 159: Top and Bottom Extents of Ideal Sintering Region in Green with Degree of Sintering >1.

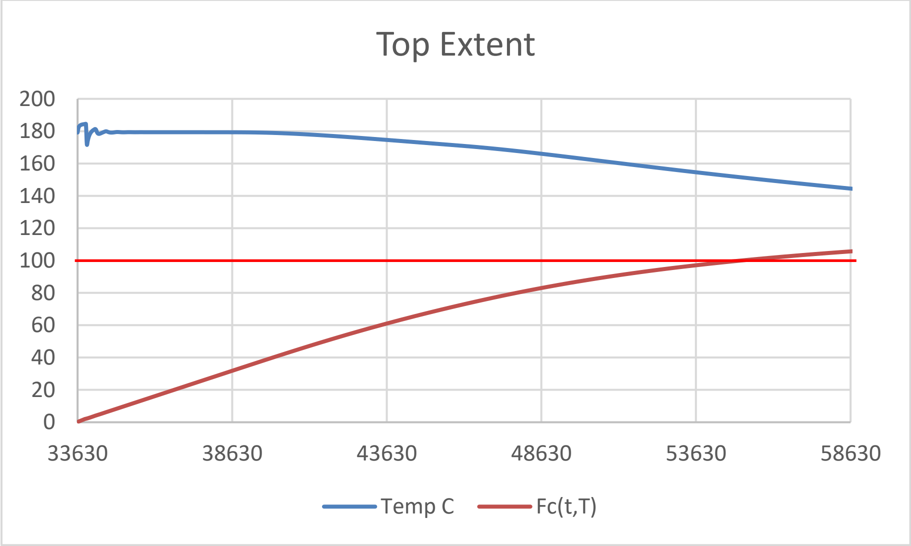

Figure 160: Top Extent Thermal Profile and Degree of Sintering

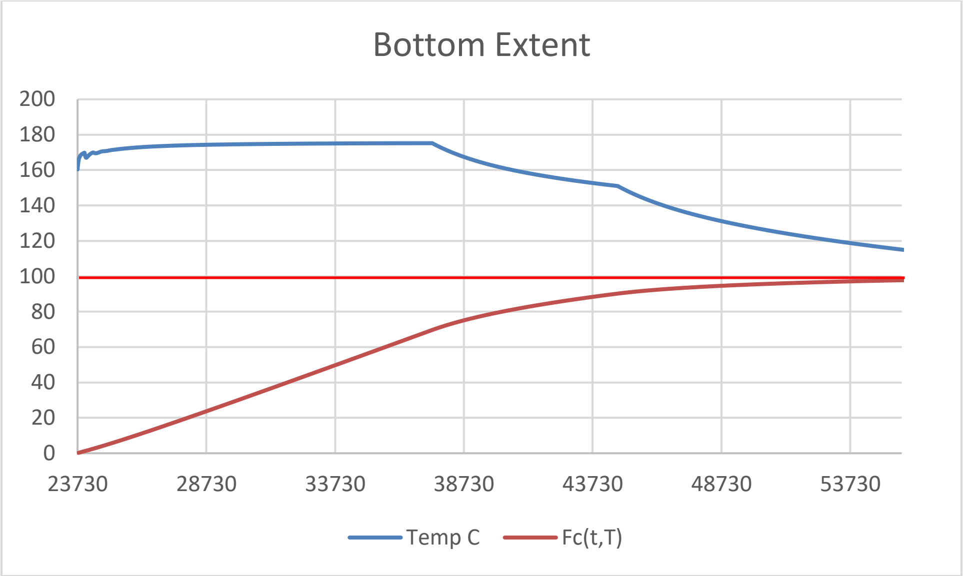

Figure 161: Bottom Extent Thermal Profile and Degree of Sintering

8.0 CONCLUSIONS

The most sensitive measure of the quality of parts built in the laser sintering process is the elongation-at-break of tensile specimens built in the z-direction. These values are lowest at the extremities of the build region in all directions: edges, bottom, and top. The lower ductility of specimens located at the edges, top, and bottom of the build cannot be an issue exclusively of initial laser energy and local part bed temperature. Therefore, mechanical properties are also be tied to a critical thermal exposure.

An accurate full-scale thermal model was developed to reflect the machine architecture and this model was correlated to mechanical properties through the following *degree of sintering* equation:

$$Degree\ of\ Sintering = \left[f_c(t,T) = N_{ls}\ \sum_{i=1}^{n} \frac{1}{T_i}\left(e^{-\frac{W}{kT_i}}\right)\Delta t_i\right] > 1$$

Where $W = \frac{72.67kJ}{mol}$ $and\ R$ was substituted for k. $R = .008314\,\frac{\mathrm{kJ}}{\mathrm{mol}}$

$N_{ls} = 7 \times 10^6 K/s.$

In addition, results from this study can be used to develop processing parameters and develop a more robust machine architecture and can contribute to improved build performance. Two key improvements are a decrease in scrap rate and an improvement in build efficiency:

- Regarding scrap rate, roughly 10% of all production volume is scrapped almost exclusively due to failed mechanical properties. Production contracts of \$2 million to \$7 million per year would see annual cost savings of \$200k to \$700k.

- Regarding efficiency – machines could see an increase in the productive build region from an area of 13”X11” to 15”X13” or 36%. In addition, improved thermal control within the build region can lead to a decreased warm-up time and contribute to 5% material savings which is equivalent to 1 to 2 kg per build.

9.0 RECOMMENDATIONS FOR FURTHER STUDY

There are two primary contributors to improved mechanical properties discussed in this study: the laser energy needed to sufficiently melt the powder layer to the preceding layer and the critical time at temperature for the interface boundary to sufficiently heal. There are other contributors that can either negatively affect the interface boundary layer or other mechanisms that may promote stronger interface boundary layers that may not have been appropriately addressed. Areas for further study are described below.

9.1 Development of Degree of Sintering Constant

The normalization factor that was used in the degree of sintering calculation should be further explored. The melt-flow of the material, the reptation of the polymer molecules, and the ability to diffuse has much to do with minimizing the pores at the interface boundary layer. There are also other energy sources in addition to point laser heating that may affect the ability to bond between layers. Developing material and process specific constants and coefficients would allow for this degree of sintering formula to be used to compare between material systems and processes.

9.2 Layer Thickness

As layer thickness increases, there is a critical thickness for a given material feedstock and particle size that will exceed the laser penetration. The thermal coupling of the laser to the material feedstock, the melt pool size, and the melt pool overlap with previously sintered layers need to have better characterization. The resultant characterization should provide guidelines for maximum layer thickness but may also yield insight into the formation of the interface boundary layer.

9.3 Part Bed Surface Convection

The most critical boundary condition in polymer laser sintering is the top boundary which is impacted by a radiant heater and natural convection at the surface. While this study observed and characterized a surface temperature gradient for an individual machine, the cause of this gradient is a balance between the radiant heater input and the convection coefficient across the surface of the part bed. It has been observed in production operations that leaking door seals, improper nitrogen gas inlet temperatures, or other leaks in the system contribute to poor mechanical properties which are evident in the large thermal gradients observed at the part bed surface. A method for measuring and characterizing convection coefficients across a part bed surface would greatly assist in developing solutions to inadequate surface temperatures.

9.4 Feedstock Temperature

The feedstock temperature is a variable that is controlled by the build processing parameters and is dictated by the material DSC. It has been observed that material feedstock at low temperatures negatively impact mechanical properties. It is reasonable to assume that if the feedstock is applied to the part bed surface at a temperature below the solidification point, it may cause the surface of the previous layer to start to solidify. This solidification likely causes something analogous to a cold-joint in concrete and there may be no remedy to a weak interface boundary caused in this manner. A better characterization of the effect of material feedstock on a layer may contribute to a better understanding of the interaction of the unsintered layer to the previously sintered layer. It may be possible that solid-state sintering or even melt phase sintering is taking place even before the laser energy is applied and that this process could be critical to reaching optimal mechanical properties.

9.5 Reptation Time and Temperature

There is similar work being done in polymer films and the adhesion of these films through thermal energy. Creating multiple layers in the polymer laser sintering process may be comparable to the work done with polymer films. One article that was reviewed titled *Reptation Time, Temperature, and Cosurfactant Effects on the Molecular Interdiffusion Rate during Polystyrene Latex Film Formation* provided other ways to characterize the time and temperature response of polymers through reputation and diffusion. (Kim, Sperling, & and Klein, 1994) While fracture mechanics and the elimination of pores at the interface boundary were discussed, a better understanding of how the laser sintering polymers reptate and diffuse at the interface boundary layer may assist polymer chemists in designing laser sintering material systems. Polymer chemistry has many polymers primarily designed for processes with high heat, pressure, and mixing. The study with polymer films are more analogous to laser sintering. According to this paper on reputation and interdiffusion rate, the temperature dependence of the diffusion coefficient, D, can be described by the Arrhenius activation energy, the WLF equation, or the Vogel relationship. This approach provides a formula very similar to the Frenkel Theory of Sintering equations used in this study.

APPENDIX A: PRODUCTION CASE STUDY STATISTICAL DATA

The data presented in Section 2.10 Mechanical Behavior in A Multi-Platform Production Environment included only the data from a single machine. The follow XBarR charts and histograms comprise the data from the other machines in the multi-platform environment that produced the laser sintered production parts. For more detail on this study, please refer to the background chapter referenced.

Machine G128

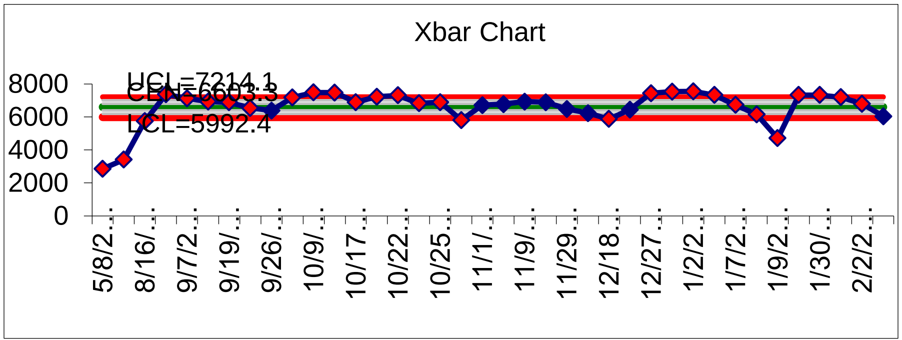

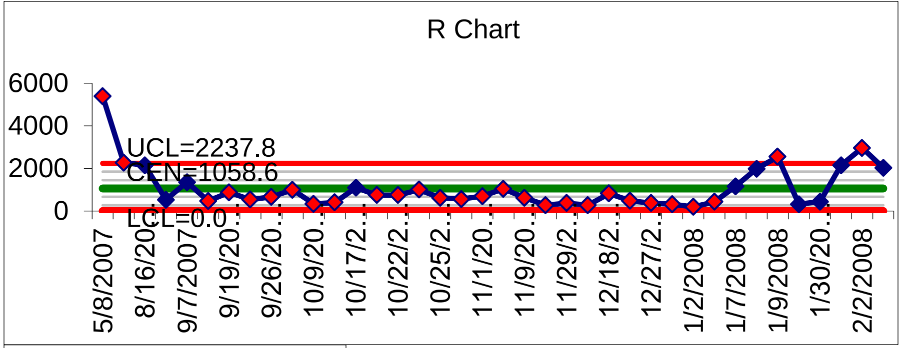

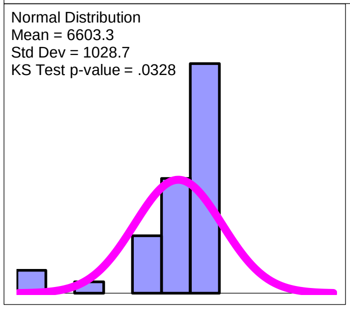

Machine G82

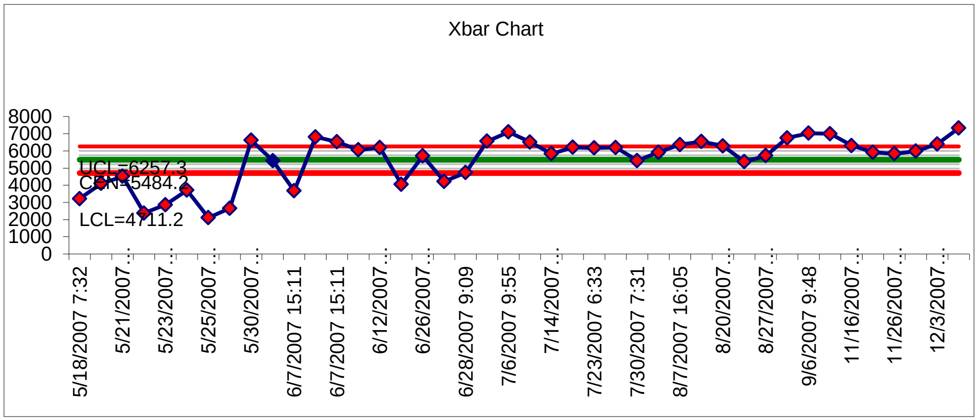
Xbar Chart
8000
7000
6000
5000
4000
3000
2000
1000
0
UCL=6257.3
CEN=5484.2
LCL=4711.2
5/18/2007 7:32
5/21/2007...
5/23/2007...
5/25/2007...
5/30/2007...
6/7/2007 15:11
6/7/2007 15:11
6/12/2007...
6/26/2007...
6/28/2007 9:09
7/6/2007 9:55
7/14/2007...
7/23/2007 6:33
7/30/2007 7:31
8/7/2007 16:05
8/20/2007...
8/27/2007...
9/6/2007 9:48
11/16/2007...
11/26/2007...
12/3/2007...

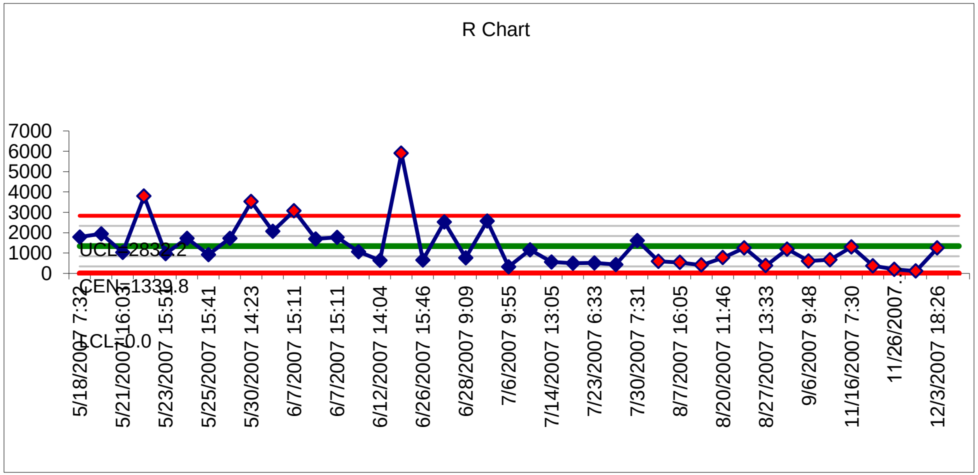
R Chart
7000
6000
5000
4000
3000
2000
1000
0
UCL=2832.2
CEN=1339.8
LCL=0.0
5/18/2007 7:32
5/21/2007 16:03
5/23/2007 15:51
5/25/2007 15:41
5/30/2007 14:23
6/7/2007 15:11
6/7/2007 15:11
6/12/2007 14:04
6/26/2007 15:46
6/28/2007 9:09
7/6/2007 9:55
7/14/2007 13:05
7/23/2007 6:33
7/30/2007 7:31
8/7/2007 16:05
8/20/2007 11:46
8/27/2007 13:33
9/6/2007 9:48
11/16/2007 7:30
11/26/2007...
12/3/2007 18:26

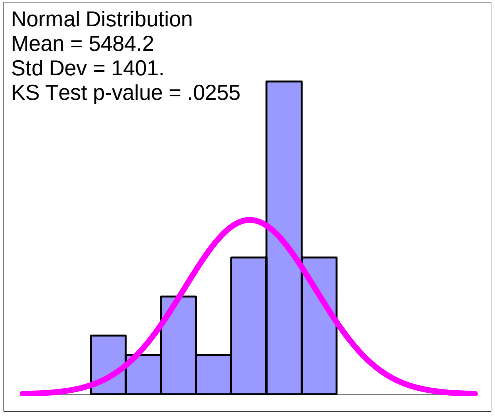
Normal Distribution
Mean = 5484.2
Std Dev = 1401.
KS Test p-value = .0255

Machine G223

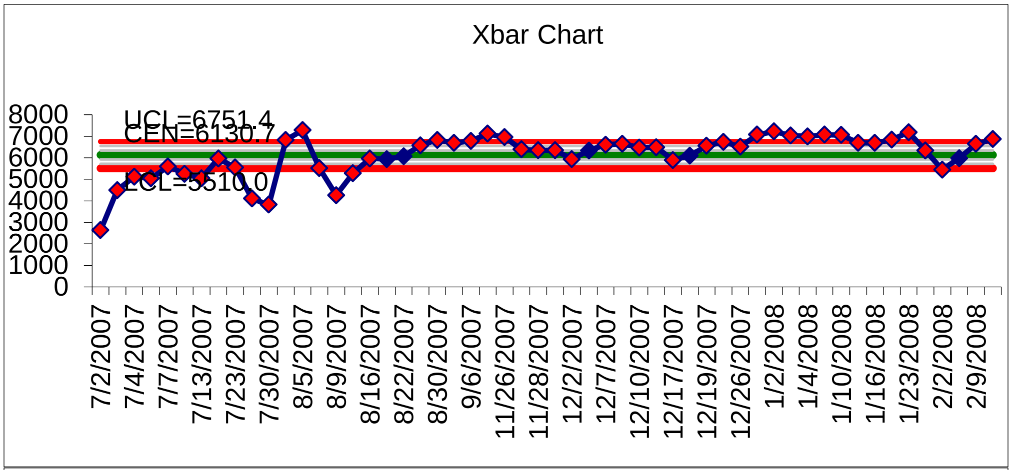

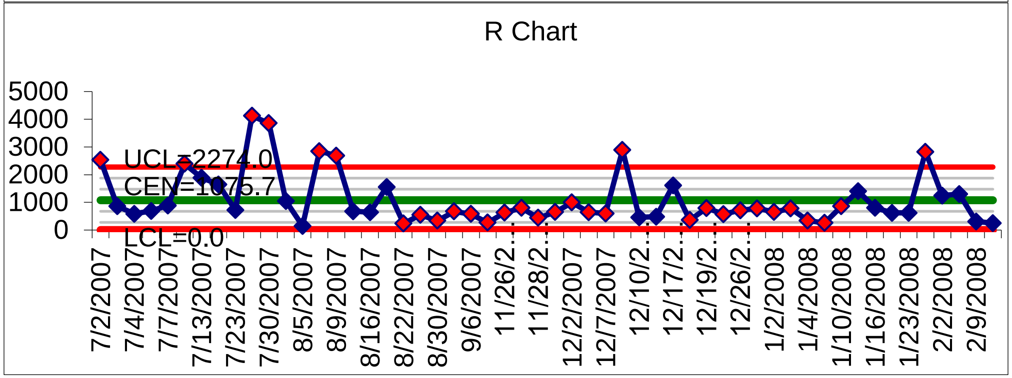

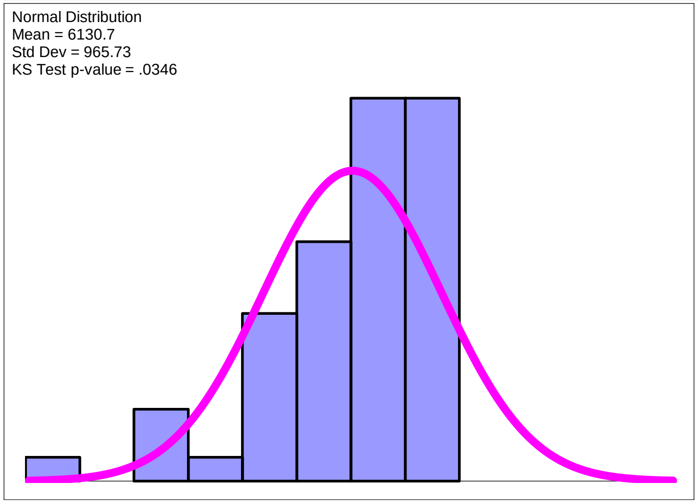

APPENDIX B: MATLAB PROGRAM SOURCE CODE

The source code used in this chapter is for use with MatLab in the creation of a program for visualization of an array of data taken from a relational database query. For details on how this analysis was done or how to create the database and/or query, please refer to Section 5.1 Production Dataset.

```
%Bins.m

%*.mat file must have material, machine mnfg, machine model, and
%orientation defined (manually define after importing data). Save
workspace
%to *.mat file after importing data and defining these inputs.

%Import data as an X vector, Y vector, and Z vector of equal
lengths.
%Choose plot types, X and Y limits, and the code will spit out plots
of
%average, StDev, and Count Z data versus XY locations.
clear all;
close all;
%N.B.:For some reason, I had to use Y labels to refer to the X axis,
and
%vice versa
%% Initialization

%Select data file to be analyzed
filename=uigetfile;
load(filename);

%Inputs: Variable and MinBins
Variable=input('Enter the variable of interest (1-EAB,2-UTS,3-YS,4-
Modulus): ');
switch Variable,
    case 1,
        Variable=EAF;
    case 2,
        Variable=UTS;
    case 3,
        Variable=OSY;
    case 4,
        Variable=ITM;
end
%PB locations with less than BinMin datapoints will be excluded
```

```
BinMin=input('Enter the minimum bin qty: ');

%Choose plots to create
%true or false
SCATTER=true;
STEM=false;
AVG=true;
STDEV=true;
STDEV_Norm=false;
COUNT=true;

%Define Boundaries
if MachineMnfg=='EOS';
    [Lims]=[0 27 0 15];
elseif MachineMnfg=='3DS';
    [Lims]=[0 14 0 12];
end
MinX=Lims(1); MaxX=Lims(2); MinY=Lims(3); MaxY=Lims(4);

%Initialize indices
i=1;j=1;k=1;a=1;z=1;

%Initialize Vectors
sizeBin=(MaxX+1)*(MaxY+1);
AvgBin=zeros(1,sizeBin);
StDevBin=zeros(1,sizeBin);
ZBin=zeros(1, sizeBin);


%% Loops
for i=1:1:MaxX+1;
    for j=1:1:MaxY+1;
        z=1;
        SumBin=0;
        ZBin=0;
        tstart=tic;
        for k=1:1:length(X)
            if (i-1)<=X(k)&&X(k)<i && (j-1)<=Y(k)&&Y(k)<j
                ZBin(z)=Variable(k);
                SumBin=SumBin+Variable(k);
                z=z+1;
            end
        end
        CountBin(a)=length(ZBin)-1;
        if CountBin(a)<BinMin;
            ZBin=0;
            SumBin=0;
            z=1;
        end
```

```
        AvgBin(a)=SumBin/(z-1);
        MaxBin(a)=max(ZBin);
        StDevBin(a)=std(ZBin);
        elapsed(i,j)=toc(tstart);
        YBin(a)=j;
        XBin(a)=i;
        a=a+1;
        %h=bar3(i,j,AvgBin(i,j),'o');
        %hold on;
    end
end
%KloopTime=sum(sum(elapsed))


%Plot labels
if Variable==UTS;
    Label1='UTS'; Label2='UTS (psi)';
elseif Variable==OSY;
    Label1='YS'; Label2='YS (psi)';
elseif Variable==EAF;
    Label1='%EAB'; Label2='EAB (%)';
elseif Variable==ITM;
    Label1='Modulus'; Label2='Modulus (ksi)';
end
TSize=14; %Title Font Size
LSize=14; %Label Font Size
NumSize=12; %Number Font Size

%Scatter Plot
if SCATTER==true;
    figure(1);
    h(1)=scatter3(XBin,YBin,AvgBin,100,AvgBin,'filled'); colorbar;
    grid on;
    axis([MinX MaxX+2 MinY MaxY+2 0 max(AvgBin)]);
    xlabel('X Location (in.)')
    ylabel('Y Location (in.)')
    zlabel(sprintf('%s',Label2))
    t=sprintf('Average %s versus PB
location\nMaterial:%s\nOrientation:%s\nBinCountMin:%d',Label1,Materi
al,Orientation,BinMin);
    title(t,'FontSize',TSize);
    alltext=findall(gcf,'Type','text');

set(alltext,'FontName','Arial','FontWeight','Bold','FontSize',LSize)
;
    allaxes=findall(gca,'Type','axes');

set(allaxes,'FontName','Arial','FontWeight','Bold','FontSize',NumSiz
e);
```

```
end

%Stem Plot
if STEM==true;
    figure(2);
    stem3(XBin,YBin,AvgBin);
    grid on;
    axis([MinX MaxX+2 MinY MaxY+2 0 max(AvgBin)]);
    xlabel('X Location (in.)')
    ylabel('Y Location (in.)')
    zlabel(sprintf('%s',Label2))
    t=sprintf('Average %s versus PB
location\nMaterial:%s\nOrientation:%s\nBinCountMin:%d',Label1,Materi
al,Orientation,BinMin);
    title(t,'FontSize',TSize);
    alltext=findall(gcf,'Type','text');

set(alltext,'FontName','Arial','FontWeight','Bold','FontSize',LSize)
;
    allaxes=findall(gca,'Type','axes');

set(allaxes,'FontName','Arial','FontWeight','Bold','FontSize',NumSiz
e);
end

%% Avg Bar Plot
if AVG==true;
    figure(3);
    A = zeros(MaxX,MaxY);
    for i = 1:length(XBin)
    A(XBin(i),YBin(i)) = AvgBin(i);
    end
    h=bar3(A);
    colorbar;
    grid off;
    axis([MinY (MaxY+2) MinX (MaxX+2) 0 max(max(A))]);
    set(gca,'xtick',[MinY:2:MaxY+1])
    set(gca,'ytick',[MinX:2:MaxX+1])
    set(gca,'XTickLabel',[MinY-1:2:MaxY]);
    set(gca,'YTickLabel',[MinX-1:2:MaxX]);
    xlabel('Y Location (in.)')
    ylabel('X Location (in.)')
    zlabel(sprintf('Average: %s',Label2))
    t=sprintf('Average %s versus PB
location\nMaterial:%s\nOrientation:%s\nBinCountMin:%d',Label1,Materi
al,Orientation,BinMin);
    title(t,'FontSize',TSize);
    alltext=findall(gcf,'Type','text');
```

```
set(alltext,'FontName','Arial','FontWeight','Bold','FontSize',LSize)
;
    allaxes=findall(gca,'Type','axes');

set(allaxes,'FontName','Arial','FontWeight','Bold','FontSize',NumSiz
e);
    %Found this code online for coloring Bar3 chart according to z-
height.
    %http://www.mathworks.com/matlabcentral/answers/98236-how-can-i-
color-b
    %ars-to-correspond-to-their-heights-when-using-bar3
    numBars = size(A,1);
    numSets = size(A,2);
    for i = 1:numSets
        adata = ones(6*numBars,4);
        k = 1;
        for j = 0:6:(6*numBars-6)
          adata(j+1:j+6,:) = A(k,i);
          k = k+1;
        end
        set(h(i),'Cdata',adata)
    end
end

%% StDev Bar Plot
if STDEV==true;
    figure(4);
    A = zeros(MaxX,MaxY);
    for i = 1:length(XBin)
    A(XBin(i),YBin(i)) = StDevBin(i);
    end
    A(A==0)=NaN;%This makes it where colorbar starts at min value
    h=bar3(A);
    grid off;
    colorbar;
    axis([MinY MaxY+2 MinX MaxX+2 0 max(max(A))]);
    set(gca,'xtick',[MinY:2:MaxY+1])
    set(gca,'ytick',[MinX:2:MaxX+1])
    set(gca,'XTickLabel',[MinY-1:2:MaxY]);
    set(gca,'YTickLabel',[MinX-1:2:MaxX]);
    xlabel('Y Location')
    ylabel('X Location')
    zlabel(sprintf('StDev: %s',Label2))
    t=sprintf('%s Standard Deviation versus PB
location\nMaterial:%s\nOrientation:%s\nBinCountMin:%d',Label1,Materi
al,Orientation,BinMin);
    title(t,'FontSize',TSize);
    alltext=findall(gcf,'Type','text');
```

```
set(alltext,'FontName','Arial','FontWeight','Bold','FontSize',LSize)
;
    allaxes=findall(gca,'Type','axes');

set(allaxes,'FontName','Arial','FontWeight','Bold','FontSize',NumSiz
e);
    %Found this code online for coloring Bar3 chart according to z-
height.
    %http://www.mathworks.com/matlabcentral/answers/98236-how-can-i-
color-b
    %ars-to-correspond-to-their-heights-when-using-bar3
    numBars = size(A,1);
    numSets = size(A,2);
    for i = 1:numSets
        adata = ones(6*numBars,4);
        k = 1;
        for j = 0:6:(6*numBars-6)
          adata(j+1:j+6,:) = A(k,i);
          k = k+1;
        end
        set(h(i),'Cdata',adata)
    end
end

%Norm Stdev Bar Plot
if STDEV_Norm==true;
    figure(5);
    A = zeros(MaxX,MaxY);
    for i = 1:length(XBin)
    A(XBin(i),YBin(i)) = StDevBin(i)./AvgBin(i);
    end
    h=bar3(A);
    colorbar;
    grid off;
    axis([MinY MaxY+2 MinX MaxX+2 0 max(max(A))]);
    set(gca,'xtick',[MinY:2:MaxY+1])
    set(gca,'ytick',[MinX:2:MaxX+1])
    set(gca,'XTickLabel',[MinY-1:2:MaxY]);
    set(gca,'YTickLabel',[MinX-1:2:MaxX]);
    xlabel('Y Location')
    ylabel('X Location')
    zlabel(sprintf('Normalized StDev: %s',Label2))
    t=sprintf('Normalized %s Standard Deviation versus PB
location\nMaterial:%s\nOrientation:%s\nBinCountMin:%d',Label1,Materi
al,Orientation,BinMin);
    title(t,'FontSize',TSize);
    alltext=findall(gcf,'Type','text');
```

```
set(alltext,'FontName','Arial','FontWeight','Bold','FontSize',LSize)
;
    allaxes=findall(gca,'Type','axes');

set(allaxes,'FontName','Arial','FontWeight','Bold','FontSize',NumSiz
e);
    %Found this code online for coloring Bar3 chart according to z-
height.
    %http://www.mathworks.com/matlabcentral/answers/98236-how-can-i-
color-b
    %ars-to-correspond-to-their-heights-when-using-bar3
    numBars = size(A,1);
    numSets = size(A,2);
    for i = 1:numSets
        adata = ones(6*numBars,4);
        k = 1;
        for j = 0:6:(6*numBars-6)
          adata(j+1:j+6,:) = A(k,i);
          k = k+1;
        end
        set(h(i),'Cdata',adata)
    end
end

%Count Bar Plot
if COUNT==true;
    figure(6);
    A = zeros(MaxX,MaxY);
    for i = 1:length(XBin)
    A(XBin(i),YBin(i)) = CountBin(i);
    end
    A(A==0)=NaN; %This makes it where colorbar starts at min value
    h=bar3(A);
    colorbar;
    grid off;
    axis([MinY MaxY+2 MinX MaxX+2 0 max(max(A))]);
    set(gca,'xtick',[MinY:2:MaxY+1])
    set(gca,'ytick',[MinX:2:MaxX+1])
    set(gca,'XTickLabel',[MinY-1:2:MaxY]);
    set(gca,'YTickLabel',[MinX-1:2:MaxX]);
    xlabel('Y Location')
    ylabel('X Location')
    zlabel('Count')
    t=sprintf('# of Bars versus PB
location\nMaterial:%s\nOrientation:%s',Material,Orientation);
    title(t,'FontSize',TSize);
    alltext=findall(gcf,'Type','text');
```

```
set(alltext,'FontName','Arial','FontWeight','Bold','FontSize',LSize)
;
    allaxes=findall(gca,'Type','axes');

set(allaxes,'FontName','Arial','FontWeight','Bold','FontSize',NumSiz
e);
    %Found this code online for coloring Bar3 chart according to z-
height.
    %http://www.mathworks.com/matlabcentral/answers/98236-how-can-i-
color-b
    %ars-to-correspond-to-their-heights-when-using-bar3
    numBars = size(A,1);
    numSets = size(A,2);
    for i = 1:numSets
        adata = ones(6*numBars,4);
        k = 1;
        for j = 0:6:(6*numBars-6)
          adata(j+1:j+6,:) = A(k,i);
          k = k+1;
        end
        set(h(i),'Cdata',adata)
    end
end
```

APPENDIX C: PRODUCTION PROCESSING PARAMETERS

There are two subsets of paramters used on a 3D Systems Sinterstation: Part Parameters and Build Parameters. Part parameters can be varied on each individual part within a given build and include processing instructions such as laser power during during a fill operation (fill_laser_power), laser power during an outline operation (outine_laser_parameter), beam offset, and a host of other parameters. The build parameters are global processing parameters that affect all parts and include things such as layer thickness, part bed temperature, feed bed temperature, minimum time between layers, as well as a number of other thermal setpoints and operating parameters. The following parameter sets are typical production parameters that were used for the control builds discussed in Section 5.2 Evaluation of Production Platform.

C1: Part Parameters

```
STRUCTURE build_stage_default_part_profile
 PARAM beam_offset_max_gap
  Category_mask = 1
  GUIName = "Maximum Gap Distance"
  Order = 0
  Type = 3
  Units = 1 # Inches
  ZUnits = 1
  profile_z= 0.000000 profile_value = 0.100000
 ENDPARAM
 PARAM beam_offset_x_fill
  Category_mask = 65537
  GUIName = "Fill Beam Offset X"
  Order = 3
  Type = 3
  Units = 1 # Inches
  ZUnits = 1
  profile_z= 0.000000 profile_value = 0.015000
 ENDPARAM
 PARAM beam_offset_x_outline
  Category_mask = 65537
  GUIName = "Outline Beam Offset X"
  Order = 13
  Type = 3
  Units = 1 # Inches
  ZUnits = 1
  profile_z= 0.000000 profile_value = 0.014000
 ENDPARAM
 PARAM beam_offset_y_fill
  Category_mask = 65537
  GUIName = "Fill Beam Offset Y"
  Order = 4
  Type = 3
  Units = 1 # Inches
  ZUnits = 1
  profile_z= 0.000000 profile_value = 0.015000
 ENDPARAM
 PARAM beam_offset_y_outline
  Category_mask = 65537
  GUIName = "Outline Beam Offset Y"
  Order = 14
  Type = 3
  Units = 1 # Inches
  ZUnits = 1
  profile_z= 0.000000 profile_value = 0.014000
 ENDPARAM
 PARAM cross_fill_scan
  Category_mask = 65537
  GUIName = "SinterScan (License Required)"
  Order = 26
  Type = 0
  ZUnits = 1
  profile_z= 0.000000 profile_value = 1
 ENDPARAM
 PARAM fill_laser_power
  Category_mask = 65537
  GUIName = "Fill Laser Power"
  Order = 2
  Type = 3
  ZUnits = 1
  profile_z= 0.000000 profile_value = 46.000000
 ENDPARAM
```

```
PARAM fill_scan_count
  Category_mask = 65537
  GUIName = "Fill Scan Count"
  Order = 3
  Type = 0
  ZUnits = 1
  profile_z= 0.000000 profile_value = 2
ENDPARAM
PARAM fill_scanner_jd
  Category_mask = 1
  GUIName = "Fill Jump Delay"
  Order = 5
  Type = 0
  ZUnits = 1
  profile_z= 0.000000 profile_value = 900
ENDPARAM
PARAM fill_scanner_js
  Category_mask = 1
  GUIName = "Fill Jump Speed"
  Order = 6
  Type = 3
  Units = 1 # Inches
  ZUnits = 1
  profile_z= 0.000000 profile_value = 400.000000
ENDPARAM
PARAM fill_scanner_lf
  Category_mask = 1
  GUIName = "Fill Laser Off"
  Order = 7
  Type = 0
  ZUnits = 1
  profile_z= 0.000000 profile_value = 1100
ENDPARAM
PARAM fill_scanner_lo
  Category_mask = 1
  GUIName = "Fill Laser On"
  Order = 8
  Type = 0
  ZUnits = 1
  profile_z= 0.000000 profile_value = 350
ENDPARAM
PARAM fill_scanner_sd
  Category_mask = 1
  GUIName = "Fill Stroke Delay"
  Order = 9
  Type = 0
  ZUnits = 1
  profile_z= 0.000000 profile_value = 1200
ENDPARAM
PARAM fill_scanner_ss
  Category_mask = 1
  GUIName = "Fill Scan Speed"
  Order = 10
  Type = 3
  Units = 1 # Inches
  ZUnits = 1
  profile_z= 0.000000 profile_value = 400.000000
ENDPARAM
PARAM optimized_fill_samples
  Category_mask = 65537
  GUIName = "Optimized Fill Samples"
  Order = 26
  Type = 0
```

```
  ZUnits = 1
  profile_z= 0.000000 profile_value = 1
ENDPARAM
PARAM outline_laser_power
  Category_mask = 65537
  GUIName = "Outline Laser Power"
  Order = 12
  Type = 3
  ZUnits = 1
  profile_z= 0.000000 profile_value = 12.000000
ENDPARAM
PARAM outline_outside_only
  Category_mask = 64
  GUIName = "Outline Outside Contour Only"
  Order = 0
  Type = 0
  ZUnits = 1
  profile_z= 0.000000 profile_value = 0
ENDPARAM
PARAM outline_scan_count
  Category_mask = 65537
  GUIName = "Outline Scan Count"
  Order = 13
  Type = 0
  ZUnits = 1
  profile_z= 0.000000 profile_value = 1
ENDPARAM
PARAM outline_scanner_jd
  Category_mask = 1
  GUIName = "Outline Jump Delay"
  Order = 15
  Type = 0
  ZUnits = 1
  profile_z= 0.000000 profile_value = 1200
ENDPARAM
PARAM outline_scanner_js
  Category_mask = 1
  GUIName = "Outline Jump Speed"
  Order = 16
  Type = 3
  Units = 1 # Inches
  ZUnits = 1
  profile_z= 0.000000 profile_value = 70.000000
ENDPARAM
PARAM outline_scanner_lf
  Category_mask = 1
  GUIName = "Outline Laser Off"
  Order = 17
  Type = 0
  ZUnits = 1
  profile_z= 0.000000 profile_value = 800
ENDPARAM
PARAM outline_scanner_lo
  Category_mask = 1
  GUIName = "Outline Laser On"
  Order = 18
  Type = 0
  ZUnits = 1
  profile_z= 0.000000 profile_value = 400
ENDPARAM
PARAM outline_scanner_sd
  Category_mask = 1
  GUIName = "Outline Stroke Delay"
```

```
   Order = 19
   Type = 0
   ZUnits = 1
   profile_z= 0.000000 profile_value = 900
  ENDPARAM
  PARAM outline_scanner_ss
   Category_mask = 1
   GUIName = "Outline Scan Speed"
   Order = 20
   Type = 3
   Units = 1 # Inches
   ZUnits = 1
   profile_z= 0.000000 profile_value = 70.000000
  ENDPARAM
  PARAM slicer_fill_first
   Category_mask = 1
   GUIName = "Slicer Fill First"
   Order = 21
   Type = 0
   ZUnits = 1
   profile_z= 0.000000 profile_value = 1
  ENDPARAM
  PARAM slicer_scan_spacing
   Category_mask = 65537
   GUIName = "Slicer Fill Scan Spacing"
   Order = 23
   Type = 3
   Units = 1 # Inches
   ZUnits = 1
   profile_z= 0.000000 profile_value = 0.010000
  ENDPARAM
  PARAM sorted_fill_enabled
   Category_mask = 65537
   GUIName = "Sorted Fill Enabled"
   Order = 24
   Type = 0
   ZUnits = 1
   profile_z= 0.000000 profile_value = 1
  ENDPARAM
  PARAM sorted_fill_max_jump
   Category_mask = 64
   GUIName = "Sorted Fill Max Jump"
   Order = 25
   Type = 3
   Units = 1 # Inches
   ZUnits = 1
   profile_z= 0.000000 profile_value = 0.500000
  ENDPARAM
  PARAM up_down_enabled
   Category_mask = 64
   GUIName = "Upward/Downward Fill Compensation"
   Order = 1
   Type = 0
   ZUnits = 1
   profile_z= 0.000000 profile_value = 0
  ENDPARAM
 ENDSTRUCTURE
ENDPACKET
checksum 0xe721
```

C2: Build Parameters

```
STRUCTURE BuildInfo
  PARAM First_Create_Version
   Value = 3602
  ENDPARAM
  PARAM Need_Check_Collision
   Value = 1
  ENDPARAM
  PARAM Powder_Needed
   Unit = 1
   Units = 1 # Inches
   Value = 8.091521
  ENDPARAM
  PARAM Version
   Value = 3602
  ENDPARAM
  PARAM build_height
   Units = 1 # Inches
   Value = 6.942799
  ENDPARAM
  PARAM cooldown_height
   Units = 1 # Inches
   Value = 0.100000
  ENDPARAM
  PARAM exslice_flag
   Value = 0
  ENDPARAM
  PARAM hal_config_flag
   Value = 17658
  ENDPARAM
  PARAM laser_scan_done
   Value = 11854
  ENDPARAM
  PARAM laser_units
   Value = ""
  ENDPARAM
  PARAM last_build_date
   Value = 1525790744
  ENDPARAM
  PARAM last_saved
   Value = "5/7/2018 5:18:06 PM"
  ENDPARAM
  PARAM last_verified
   Value = "9/16/2014 3:11:53 PM"
  ENDPARAM
  PARAM layer_file_directory
   Value = "\dtm\layer\build"
  ENDPARAM
  PARAM layer_file_units
   Value = 1
  ENDPARAM
  PARAM locked
   Value = 0
  ENDPARAM
  PARAM material_date
   Value = "dummy"
  ENDPARAM
  PARAM material_name
```

```
      Value = "\dtm\config\material\DuraFormEX-MP-Natural.cfg"
    ENDPARAM
    PARAM part_count
      Value = 68
    ENDPARAM
    PARAM scan_file_directory
      Value = "\dtm\scan\build"
    ENDPARAM
    PARAM unlock_password
      Value = ""
    ENDPARAM
    PARAM warmup_height
      Units = 1 # Inches
      Value = 0.500000
    ENDPARAM
  ENDSTRUCTURE

  STRUCTURE build_stage_profile
    PARAM OptiScan
      Category_mask = 65537
      GUIName = "OptiScan (License Required)"
      Order = 0
      Type = 0
      ZUnits = 1
      profile_z= 0.000000 profile_value = 0
    ENDPARAM
    PARAM chamber_airflow_damper_position
      Category_mask = 1
      GUIName = "Blower Speed"
      Order = 0
      Type = 0
      ZUnits = 1
      profile_z= 0.000000 profile_value = 20
    ENDPARAM
    PARAM fast_add_powder_layer
      Category_mask = 32
      GUIName = "Fast Add Powder Layer"
      Order = 4
      Type = 0
      ZUnits = 1
      profile_z= 0.000000 profile_value = 0
    ENDPARAM
    PARAM left_feed_distance
      Category_mask = 1
      GUIName = "Left Feed Distance"
      Order = 5
      Roundoff = 4
      Type = 3
      Units = 1 # Inches
      ZUnits = 1
      profile_z= 0.000000 profile_value = 0.010000
    ENDPARAM
    PARAM left_feed_heater_output_limit
      Category_mask = 1
      GUIName = "Left Feed Heater Output Limit"
      Order = 6
      Type = 0
      ZUnits = 1
      profile_z= 0.000000 profile_value = 60
    ENDPARAM
    PARAM left_feed_heater_set_point
      Category_mask = 65537
      GUIName = "Left Feed Heater Set Point"
      Order = 7
      Type = 4
      ZUnits = 1
      profile_z= 0.000000 profile_value = 135.000000
    ENDPARAM
    PARAM left_feed_heater_wait_for_temp
      Category_mask = 65537
      GUIName = "Left Feed Heater Wait for Temp"
      Order = 8
      Type = 0
      ZUnits = 1
      profile_z= 0.000000 profile_value = 0
    ENDPARAM
    PARAM minimum_time_between_layers
      Category_mask = 65537
      GUIName = "Minimum Layer Time "
      Order = 9
      Type = 0
      ZUnits = 1
      profile_z= 0.000000 profile_value = 20
    ENDPARAM
    PARAM part_cylinder_heater_enable
      Category_mask = 65540
      GUIName = "Part Cylinder Heater Enable"
      Order = 10
      Type = 0
      ZUnits = 1
      profile_z= 0.000000 profile_value = 1
    ENDPARAM
    PARAM part_cylinder_heater_pid_output_limit
      Category_mask = 4
      GUIName = "Part Cylinder Heater Output Limit"
      Order = 11
      Type = 0
      ZUnits = 1
      profile_z= 0.000000 profile_value = 80
    ENDPARAM
    PARAM part_cylinder_heater_pid_set_point
      Category_mask = 65540
      GUIName = "Part Cylinder Heater Set Point"
      Order = 12
      Type = 4
      ZUnits = 1
      profile_z= 0.000000 profile_value = 150.000000
    ENDPARAM
    PARAM part_heater_pid_output_limit
      Category_mask = 1
      GUIName = "Part Heater PID Output Limit"
      Order = 13
      Type = 0
      ZUnits = 1
      profile_z= 0.000000 profile_value = 55
    ENDPARAM
    PARAM part_heater_pid_set_point
      Category_mask = 65537
      GUIName = "Part Heater Set Point"
      Order = 14
      Type = 4
      ZUnits = 1
      profile_z= 0.000000 profile_value = 180.000000
    ENDPARAM
    PARAM part_heater_wait_for_temp
      Category_mask = 65537
      GUIName = "Part Heater Wait for Temp"
      Order = 15
      Type = 0
```

```
 ZUnits = 1
 profile_z= 0.000000 profile_value = 0
ENDPARAM
PARAM part_heater_zone_2_ratio
 Category_mask = 65540
 GUIName = "Part Heater Inner/Outer Ratio"
 Order = 16
 Type = 4
 ZUnits = 1
 profile_z= 0.000000 profile_value = 0.750000
ENDPARAM
PARAM piston_heater_enable
 Category_mask = 32
 GUIName = "Piston Heater Enable"
 Order = 17
 Type = 0
 ZUnits = 1
 profile_z= 0.000000 profile_value = 1
ENDPARAM
PARAM piston_heater_output_limit
 Category_mask = 32
 GUIName = "Piston Heater Output Limit"
 Order = 18
 Type = 0
 ZUnits = 1
 profile_z= 0.000000 profile_value = 50
ENDPARAM
PARAM piston_heater_pid_set_point
 Category_mask = 32
 GUIName = "Piston Heater Set Point"
 Order = 19
 Type = 4
 ZUnits = 1
 profile_z= 0.000000 profile_value = 150.000000
ENDPARAM
PARAM post_add_powder_delay
 Category_mask = 1
 GUIName = "Post Add Powder Layer Delay"
 Order = 21
 Type = 0
 ZUnits = 1
 profile_z= 0.000000 profile_value = 0
ENDPARAM
PARAM powder_layer_delay
 Category_mask = 1
 GUIName = "Pre Add Powder Layer Delay"
 Order = 20
 Type = 0
 ZUnits = 1
 profile_z= 0.000000 profile_value = 3
ENDPARAM
PARAM powder_layer_thickness
 Category_mask = 65537
 GUIName = "Powder Layer Thickness"
 Order = 21
 Roundoff = 4
 Type = 3
 Units = 1 # Inches
 ZUnits = 1
 profile_z= 0.000000 profile_value = 0.004000
ENDPARAM
PARAM right_feed_distance
 Category_mask = 1
 GUIName = "Right Feed Distance"
 Order = 22
 Roundoff = 4
 Type = 3
 Units = 1 # Inches
 ZUnits = 1
 profile_z= 0.000000 profile_value = 0.010000
ENDPARAM
PARAM right_feed_heater_output_limit
 Category_mask = 1
 GUIName = "Right Feed Heater Output Limit"
 Order = 23
 Type = 0
 ZUnits = 1
 profile_z= 0.000000 profile_value = 60
ENDPARAM
PARAM right_feed_heater_set_point
 Category_mask = 65537
 GUIName = "Right Feed Heater Set Point"
 Order = 24
 Type = 4
 ZUnits = 1
 profile_z= 0.000000 profile_value = 135.000000
ENDPARAM
PARAM right_feed_heater_wait_for_temp
 Category_mask = 65537
 GUIName = "Right Feed Heater Wait for Temp"
 Order = 25
 Type = 0
 ZUnits = 1
 profile_z= 0.000000 profile_value = 0
ENDPARAM
PARAM roller_traverse_speed
 Category_mask = 1
 GUIName = "Roller Speed"
 Order = 26
 Type = 3
 Units = 1 # Inches
 ZUnits = 1
 profile_z= 0.000000 profile_value = 9.000000
ENDPARAM
PARAM rotate_scan_order
 Category_mask = 1
 GUIName = "Rotate Scan Order"
 Order = 27
 Type = 0
 ZUnits = 1
 profile_z= 0.000000 profile_value = 0
ENDPARAM
PARAM smart_feed
 Category_mask = 65537
 GUIName = "Smart Feed Enable"
 Order = 0
 Type = 0
 ZUnits = 1
 profile_z= 0.000000 profile_value = 1
ENDPARAM
PARAM smart_feed_gain
 Category_mask = 1
 GUIName = "Smart Feed Gain"
 Order = 0
 Type = 3.000000
 ZUnits = 1
 profile_z= 0.000000 profile_value = 1.100000
ENDPARAM
PARAM vector_bloom_control
 Category_mask = 32
```

```
    GUIName = "Vector Bloom Elimination"
    Order = 28
    Type = 0
    ZUnits = 1
    profile_z= 0.000000 profile_value = 1
  ENDPARAM
  PARAM wait_for_temp_duration
    Category_mask = 1
    GUIName = "Wait for Temp Duration"
    Order = 30
    Type = 3
    ZUnits = 1
    profile_z= 0.000000 profile_value = 0
  ENDPARAM
ENDSTRUCTURE

STRUCTURE cooldown_stage_profile
  PARAM OptiScan
    Category_mask = 65537
    GUIName = "OptiScan (License Required)"
    Order = 0
    Type = 0
    ZUnits = 1
    profile_z= 0.000000 profile_value = 0
  ENDPARAM
  PARAM chamber_airflow_damper_position
    Category_mask = 1
    GUIName = "Blower Speed"
    Order = 0
    Type = 0
    ZUnits = 1
    profile_z= 0.000000 profile_value = 20
  ENDPARAM
  PARAM fast_add_powder_layer
    Category_mask = 32
    GUIName = "Fast Add Powder Layer"
    Order = 4
    Type = 0
    ZUnits = 1
    profile_z= 0.000000 profile_value = 0
  ENDPARAM
  PARAM left_feed_distance
    Category_mask = 1
    GUIName = "Left Feed Distance"
    Order = 5
    Roundoff = 4
    Type = 3
    Units = 1 # Inches
    ZUnits = 1
    profile_z= 0.000000 profile_value = 0.008000
  ENDPARAM
  PARAM left_feed_heater_output_limit
    Category_mask = 1
    GUIName = "Left Feed Heater Output Limit"
    Order = 6
    Type = 0
    ZUnits = 1
    profile_z= 0.000000 profile_value = 60
    profile_z= 0.095000 profile_value = 0
  ENDPARAM
  PARAM left_feed_heater_set_point
    Category_mask = 65537
    GUIName = "Left Feed Heater Set Point"
    Order = 7
    Type = 4
    ZUnits = 1
    profile_z= 0.000000 profile_value = 135.000000
    profile_z= 0.090000 profile_value = 135.000000
    profile_z= 0.095000 profile_value = 45.000000
  ENDPARAM
  PARAM left_feed_heater_wait_for_temp
    Category_mask = 65537
    GUIName = "Left Feed Heater Wait for Temp"
    Order = 8
    Type = 0
    ZUnits = 1
    profile_z= 0.000000 profile_value = 0
  ENDPARAM
  PARAM minimum_time_between_layers
    Category_mask = 65537
    GUIName = "Minimum Layer Time "
    Order = 9
    Type = 0
    ZUnits = 1
    profile_z= 0.000000 profile_value = 7
  ENDPARAM
  PARAM part_cylinder_heater_enable
    Category_mask = 65540
    GUIName = "Part Cylinder Heater Enable"
    Order = 10
    Type = 0
    ZUnits = 1
    profile_z= 0.000000 profile_value = 1
    profile_z= 0.095000 profile_value = 0
  ENDPARAM
  PARAM part_cylinder_heater_pid_output_limit
    Category_mask = 4
    GUIName = "Part Cylinder Heater Output Limit"
    Order = 11
    Type = 0
    ZUnits = 1
    profile_z= 0.000000 profile_value = 80
  ENDPARAM
  PARAM part_cylinder_heater_pid_set_point
    Category_mask = 65540
    GUIName = "Part Cylinder Heater Set Point"
    Order = 12
    Type = 4
    ZUnits = 1
    profile_z= 0.000000 profile_value = 150.000000
    profile_z= 0.090000 profile_value = 100.000000
  ENDPARAM
  PARAM part_heater_pid_output_limit
    Category_mask = 1
    GUIName = "Part Heater PID Output Limit"
    Order = 13
    Type = 0
    ZUnits = 1
    profile_z= 0.000000 profile_value = 55
    profile_z= 0.095000 profile_value = 0
  ENDPARAM
  PARAM part_heater_pid_set_point
    Category_mask = 65537
    GUIName = "Part Heater Set Point"
    Order = 14
    Type = 4
    ZUnits = 1
    profile_z= 0.000000 profile_value = 180.000000
    profile_z= 0.090000 profile_value = 177.000000
    profile_z= 0.095000 profile_value = 35.000000
```

```
ENDPARAM
PARAM part_heater_wait_for_temp
  Category_mask = 65537
  GUIName = "Part Heater Wait for Temp"
  Order = 15
  Type = 0
  ZUnits = 1
  profile_z= 0.000000 profile_value = 0
  profile_z= 0.095000 profile_value = 1
ENDPARAM
PARAM part_heater_zone_2_ratio
  Category_mask = 65540
  GUIName = "Part Heater Inner/Outer Ratio"
  Order = 16
  Type = 4
  ZUnits = 1
  profile_z= 0.000000 profile_value = 0.750000
ENDPARAM
PARAM piston_heater_enable
  Category_mask = 32
  GUIName = "Piston Heater Enable"
  Order = 17
  Type = 0
  ZUnits = 1
  profile_z= 0.000000 profile_value = 1
  profile_z= 0.095000 profile_value = 0
ENDPARAM
PARAM piston_heater_output_limit
  Category_mask = 32
  GUIName = "Piston Heater PID Output Limit"
  Order = 18
  Type = 0
  ZUnits = 1
  profile_z= 0.000000 profile_value = 50
ENDPARAM
PARAM piston_heater_pid_set_point
  Category_mask = 32
  GUIName = "Piston Heater Set Point"
  Order = 19
  Type = 4
  ZUnits = 1
  profile_z= 0.000000 profile_value = 150.000000
  profile_z= 0.090000 profile_value = 150.000000
  profile_z= 0.095000 profile_value = 30.000000
ENDPARAM
PARAM post_add_powder_delay
  Category_mask = 1
  GUIName = "Post Add Powder Layer Delay"
  Order = 21
  Type = 0
  ZUnits = 1
  profile_z= 0.000000 profile_value = 0
ENDPARAM
PARAM powder_layer_delay
  Category_mask = 1
  GUIName = "Pre Add Powder Layer Delay"
  Order = 20
  Type = 0
  ZUnits = 1
  profile_z= 0.000000 profile_value = 0
ENDPARAM
PARAM powder_layer_thickness
  Category_mask = 65537
  GUIName = "Powder Layer Thickness"
  Order = 21
  Roundoff = 4
  Type = 3
  Units = 1 # Inches
  ZUnits = 1
  profile_z= 0.000000 profile_value = 0.004000
ENDPARAM
PARAM right_feed_distance
  Category_mask = 1
  GUIName = "Right Feed Distance"
  Order = 22
  Roundoff = 4
  Type = 3
  Units = 1 # Inches
  ZUnits = 1
  profile_z= 0.000000 profile_value = 0.008000
ENDPARAM
PARAM right_feed_heater_output_limit
  Category_mask = 1
  GUIName = "Right Feed Heater Output Limit"
  Order = 23
  Type = 0
  ZUnits = 1
  profile_z= 0.000000 profile_value = 60
  profile_z= 0.095000 profile_value = 0
ENDPARAM
PARAM right_feed_heater_set_point
  Category_mask = 65537
  GUIName = "Right Feed Heater Set Point"
  Order = 24
  Type = 4
  ZUnits = 1
  profile_z= 0.000000 profile_value = 135.000000
  profile_z= 0.090000 profile_value = 135.000000
  profile_z= 0.095000 profile_value = 45.000000
ENDPARAM
PARAM right_feed_heater_wait_for_temp
  Category_mask = 65537
  GUIName = "Right Feed Heater Wait for Temp"
  Order = 25
  Type = 0
  ZUnits = 1
  profile_z= 0.000000 profile_value = 0
ENDPARAM
PARAM roller_traverse_speed
  Category_mask = 1
  GUIName = "Roller Speed"
  Order = 26
  Type = 3
  Units = 1 # Inches
  ZUnits = 1
  profile_z= 0.000000 profile_value = 9.000000
ENDPARAM
PARAM rotate_scan_order
  Category_mask = 1
  GUIName = "Rotate Scan Order"
  Order = 27
  Type = 0
  ZUnits = 1
  profile_z= 0.000000 profile_value = 0
ENDPARAM
PARAM smart_feed
  Category_mask = 65537
  GUIName = "Smart Feed Enable"
  Order = 0
  Type = 0
```

```
    ZUnits = 1
    profile_z= 0.000000 profile_value = 1
  ENDPARAM
  PARAM smart_feed_gain
    Category_mask = 1
    GUIName = "Smart Feed Gain"
    Order = 0
    Type = 3.000000
    ZUnits = 1
    profile_z= 0.000000 profile_value = 1.000000
  ENDPARAM
  PARAM vector_bloom_control
    Category_mask = 32
    GUIName = "Vector Bloom Elimination"
    Order = 28
    Type = 0
    ZUnits = 1
    profile_z= 0.000000 profile_value = 1
  ENDPARAM
  PARAM wait_for_temp_duration
    Category_mask = 1
    GUIName = "Wait for Temp Duration"
    Order = 30
    Type = 3
    ZUnits = 1
    profile_z= 0.000000 profile_value = 0
  ENDPARAM
ENDSTRUCTURE

STRUCTURE warmup_stage_profile
  PARAM OptiScan
    Category_mask = 65537
    GUIName = "OptiScan (License Required)"
    Order = 0
    Type = 0
    ZUnits = 1
    profile_z= 0.000000 profile_value = 0
  ENDPARAM
  PARAM chamber_airflow_damper_position
    Category_mask = 1
    GUIName = "Blower Speed"
    Order = 0
    Type = 0
    ZUnits = 1
    profile_z= 0.000000 profile_value = 100
  ENDPARAM
  PARAM fast_add_powder_layer
    Category_mask = 32
    GUIName = "Fast Add Powder Layer"
    Order = 4
    Type = 0
    ZUnits = 1
    profile_z= 0.000000 profile_value = 0
  ENDPARAM
  PARAM left_feed_distance
    Category_mask = 1
    GUIName = "Left Feed Distance"
    Order = 7
    Roundoff = 4
    Type = 3
    Units = 1 # Inches
    ZUnits = 1
    profile_z= 0.000000 profile_value = 0.009500
  ENDPARAM
  PARAM left_feed_heater_output_limit
    Category_mask = 1
    GUIName = "Left Feed Heater Output Limit"
    Order = 8
    Type = 0
    ZUnits = 1
    profile_z= 0.000000 profile_value = 80
  ENDPARAM
  PARAM left_feed_heater_set_point
    Category_mask = 65537
    GUIName = "Left Feed Heater Set Point"
    Order = 9
    Type = 4
    ZUnits = 1
    profile_z= 0.000000 profile_value = 100.000000
    profile_z= 0.100000 profile_value = 135.000000
  ENDPARAM
  PARAM left_feed_heater_wait_for_temp
    Category_mask = 65537
    GUIName = "Left Feed Heater Wait for Temp"
    Order = 10
    Type = 0
    ZUnits = 1
    profile_z= 0.000000 profile_value = 1
    profile_z= 0.004000 profile_value = 0
  ENDPARAM
  PARAM minimum_time_between_layers
    Category_mask = 65537
    GUIName = "Minimum Layer Time "
    Order = 11
    Type = 0
    ZUnits = 1
    profile_z= 0.000000 profile_value = 30
  ENDPARAM
  PARAM part_cylinder_heater_enable
    Category_mask = 65540
    GUIName = "Part Cylinder Heater Enable"
    Order = 12
    Type = 0
    ZUnits = 1
    profile_z= 0.000000 profile_value = 1
  ENDPARAM
  PARAM part_cylinder_heater_pid_output_limit
    Category_mask = 4
    GUIName = "Part Cylinder Heater Output Limit"
    Order = 13
    Type = 0
    ZUnits = 1
    profile_z= 0.000000 profile_value = 80
  ENDPARAM
  PARAM part_cylinder_heater_pid_set_point
    Category_mask = 65540
    GUIName = "Part Cylinder Heater Set Point"
    Order = 14
    Type = 4
    ZUnits = 1
    profile_z= 0.000000 profile_value = 150.000000
  ENDPARAM
  PARAM part_heater_pid_output_limit
    Category_mask = 1
    GUIName = "Part Heater PID Output Limit"
    Order = 15
    Type = 0
    ZUnits = 1
    profile_z= 0.000000 profile_value = 55
  ENDPARAM
```

```
PARAM part_heater_pid_set_point
  Category_mask = 65537
  GUIName = "Part Heater Set Point"
  Order = 16
  Type = 4
  ZUnits = 1
  profile_z= 0.000000 profile_value = 100.000000
  profile_z= 0.200000 profile_value = 180.000000
ENDPARAM
PARAM part_heater_wait_for_temp
  Category_mask = 65537
  GUIName = "Part Heater Wait for Temp"
  Order = 17
  Type = 0
  ZUnits = 1
  profile_z= 0.000000 profile_value = 0
ENDPARAM
PARAM part_heater_zone_2_ratio
  Category_mask = 65540
  GUIName = "Part Heater Inner/Outer Ratio"
  Order = 18
  Type = 4
  ZUnits = 1
  profile_z= 0.000000 profile_value = 0.750000
ENDPARAM
PARAM piston_heater_enable
  Category_mask = 32
  GUIName = "Piston Heater Enable"
  Order = 19
  Type = 0
  ZUnits = 1
  profile_z= 0.000000 profile_value = 1
ENDPARAM
PARAM piston_heater_output_limit
  Category_mask = 32
  GUIName = "Piston Heater Output Limit"
  Order = 20
  Type = 0
  ZUnits = 1
  profile_z= 0.000000 profile_value = 50
ENDPARAM
PARAM piston_heater_pid_set_point
  Category_mask = 32
  GUIName = "Piston Heater Set Point"
  Order = 21
  Type = 4
  ZUnits = 1
  profile_z= 0.000000 profile_value = 130.000000
  profile_z= 0.004000 profile_value = 150.000000
ENDPARAM
PARAM post_add_powder_delay
  Category_mask = 1
  GUIName = "Post Add Powder Layer Delay"
  Order = 23
  Type = 0
  ZUnits = 1
  profile_z= 0.000000 profile_value = 0
ENDPARAM
PARAM powder_layer_delay
  Category_mask = 1
  GUIName = "Pre Add Powder Layer Delay"
  Order = 22
  Type = 0
  ZUnits = 1
  profile_z= 0.000000 profile_value = 0
ENDPARAM
PARAM powder_layer_thickness
  Category_mask = 65537
  GUIName = "Powder Layer Thickness"
  Order = 24
  Roundoff = 4
  Type = 3
  Units = 1 # Inches
  ZUnits = 1
  profile_z= 0.000000 profile_value = 0.004000
ENDPARAM
PARAM right_feed_distance
  Category_mask = 1
  GUIName = "Right Feed Distance"
  Order = 25
  Roundoff = 4
  Type = 3
  Units = 1 # Inches
  ZUnits = 1
  profile_z= 0.000000 profile_value = 0.009500
ENDPARAM
PARAM right_feed_heater_output_limit
  Category_mask = 1
  GUIName = "Right Feed Heater Output Limit"
  Order = 26
  Type = 0
  ZUnits = 1
  profile_z= 0.000000 profile_value = 80
ENDPARAM
PARAM right_feed_heater_set_point
  Category_mask = 65537
  GUIName = "Right Feed Heater Set Point"
  Order = 27
  Type = 4
  ZUnits = 1
  profile_z= 0.000000 profile_value = 100.000000
  profile_z= 0.100000 profile_value = 135.000000
ENDPARAM
PARAM right_feed_heater_wait_for_temp
  Category_mask = 65537
  GUIName = "Right Feed Heater Wait for Temp"
  Order = 28
  Type = 0
  ZUnits = 1
  profile_z= 0.000000 profile_value = 1
  profile_z= 0.004000 profile_value = 0
ENDPARAM
PARAM roller_traverse_speed
  Category_mask = 1
  GUIName = "Roller Speed"
  Order = 29
  Type = 3
  Units = 1 # Inches
  ZUnits = 1
  profile_z= 0.000000 profile_value = 9.000000
ENDPARAM
PARAM rotate_scan_order
  Category_mask = 1
  GUIName = "Rotate Scan Order"
  Order = 27
  Type = 0
  ZUnits = 1
  profile_z= 0.000000 profile_value = 0
ENDPARAM
PARAM smart_feed
```

```
   Category_mask = 65537
   GUIName = "Smart Feed Enable"
   Order = 2
   Type = 0
   ZUnits = 1
   profile_z= 0.000000 profile_value = 1
  ENDPARAM
  PARAM smart_feed_gain
   Category_mask = 1
   GUIName = "Smart Feed Gain"
   Order = 1
   Type = 3.000000
   ZUnits = 1
   profile_z= 0.000000 profile_value = 1.100000
   profile_z= 0.050000 profile_value = 1.000000
  ENDPARAM
  PARAM vector_bloom_control
   Category_mask = 32
   GUIName = "Vector Bloom Elimination"
   Order = 28
   Type = 0
   ZUnits = 1
   profile_z= 0.000000 profile_value = 1
  ENDPARAM
  PARAM wait_for_temp_duration
   Category_mask = 1
   GUIName = "Wait for Temp Duration"
   Order = 33
   Type = 3
   ZUnits = 1
   profile_z= 0.000000 profile_value = 0
  ENDPARAM
 ENDSTRUCTURE
ENDPACKET
```

APPENDIX D: PRODUCTION BUILD LOG DATA (SAMPLE)

The 3D Systems Sinterstation has a States.Log that records key setpoints and resultant parameter data collected during a production build. A subset of the data collected from the builds described in Section 5.2 Evaluation of Production Platform and shown and graphed in Section 6.2 Production Platform Evaluation Results is shown below. This is not a full set of measurements that were taken and does not represent the full build height or time.

Time Stamp	Time Elapsed	Stage Height Z	Part Bed Temp.	Part Bed Duty Cycle	Left Feed Temp.	Left Feed Duty Cycle	Right Feed Temp.	Right Feed Duty Cycle	Cylinder Heat Temp.	Cylinder Heat Duty Cycle	Piston Heat Temp.	Piston Heat Duty Cycle
6/29/2018 13:57	0:00:00	0	29.6	55	28.4	80	27.1	80	25.8	100	399.9	0
6/29/2018 13:57	0:00:00	0	29.9	55	28.5	80	27.3	80	25.9	100	399.9	0
6/29/2018 13:57	0:00:01	0	30.2	55	28.7	80	27.1	80	26	100	399.9	0
6/29/2018 13:57	0:00:02	0	30.6	55	28.6	80	27.3	80	26.1	100	399.9	0
6/29/2018 13:57	0:00:03	0	30.8	55	28.6	80	27.5	80	26.1	100	399.9	0
6/29/2018 13:57	0:00:04	0	31.2	55	28.7	80	27.3	80	26.2	100	399.9	0
6/29/2018 13:57	0:00:05	0	31.5	55	28.7	80	27.4	80	26.4	100	399.9	0
6/29/2018 13:57	0:00:06	0	32	55	28.7	80	27.5	80	26.5	100	399.9	0
6/29/2018 13:57	0:00:07	0	32.4	55	28.9	80	27.5	80	26.7	100	399.9	0
6/29/2018 13:57	0:00:08	0	32.7	55	28.7	80	27.8	80	26.9	100	399.9	0
6/29/2018 13:57	0:00:09	0	33.1	55	28.9	80	27.8	80	26.9	100	399.9	0
6/29/2018 13:57	0:00:10	0	33.3	55	28.9	80	28	80	27.1	100	399.9	0
6/29/2018 13:57	0:00:11	0	33.8	55	29.1	80	28	80	27.4	100	399.9	0
6/29/2018 13:57	0:00:12	0	34.1	55	29.2	80	28	80	27.6	100	399.9	0
6/29/2018 13:57	0:00:13	0	34.5	55	29.2	80	28.3	80	27.9	100	399.9	0

6/29/2018 13:57	0:00:14	0	35.1	55	29.4	80	28.5	80	28.1	100	399.9	0
6/29/2018 13:57	0:00:15	0	35.6	55	29.4	80	28.7	80	28.1	100	399.9	0
6/29/2018 13:57	0:00:16	0	36	55	29.6	80	28.8	80	28.4	100	399.9	0
6/29/2018 13:57	0:00:17	0	36.4	55	29.7	80	28.8	80	28.7	100	399.9	0
6/29/2018 13:57	0:00:18	0	36.7	55	29.9	80	29	80	29	100	399.9	0
6/29/2018 13:57	0:00:19	0	37.1	55	29.9	80	29.3	80	29.3	100	399.9	0
6/29/2018 13:57	0:00:20	0	37.5	55	30.1	80	29.3	80	29.7	100	399.9	0
6/29/2018 13:57	0:00:21	0	38	55	30.3	80	29.5	80	29.7	100	399.9	0
6/29/2018 13:57	0:00:22	0	38.4	55	30.4	80	29.6	80	30	100	399.9	0
6/29/2018 13:57	0:00:23	0	38.9	55	30.6	80	29.8	80	30.3	100	399.9	0
6/29/2018 13:57	0:00:24	0	39.3	55	30.6	80	30.1	80	30.7	100	399.9	0
6/29/2018 13:57	0:00:25	0	39.7	55	31	80	30.1	80	31.1	100	399.9	0
6/29/2018 13:58	0:00:26	0	40.1	55	31	80	30.3	80	31.5	100	399.9	0
6/29/2018 13:58	0:00:27	0	40.6	55	31.3	80	30.6	80	31.8	100	399.9	0
6/29/2018 13:58	0:00:29	0	41	55	31.5	80	30.7	80	31.8	100	399.9	0
6/29/2018 13:58	0:00:30	0	41.6	55	31.6	80	30.8	80	32.2	100	399.9	0
6/29/2018 13:58	0:00:31	0	42	55	31.7	80	30.8	80	32.6	100	399.9	0
6/29/2018 13:58	0:00:32	0	42.5	55	32	80	31.1	80	33	100	399.9	0
6/29/2018 13:58	0:00:33	0	42.9	55	32.2	80	31.3	80	33.4	100	399.9	0
6/29/2018 13:58	0:00:34	0	43.5	55	32.4	80	31.6	80	33.8	100	399.9	0
6/29/2018 13:58	0:00:35	0	44	55	32.5	80	31.5	80	33.8	100	399.9	0
6/29/2018 13:58	0:00:36	0	44.5	55	32.6	80	31.8	80	34.2	100	399.9	0
6/29/2018 13:58	0:00:37	0	45.1	55	32.9	80	32.1	80	34.6	100	399.9	0
6/29/2018 13:58	0:00:38	0	45.6	55	33	80	32.4	80	35	100	399.9	0
6/29/2018 13:58	0:00:39	0	46.2	55	33.3	80	32.6	80	35.4	100	399.9	0
6/29/2018 13:58	0:00:40	0	46.7	55	33.6	80	32.9	80	35.8	100	399.9	0
6/29/2018 13:58	0:00:41	0	47.1	55	33.8	80	32.9	80	35.8	100	399.9	0
6/29/2018 13:58	0:00:42	0	47.5	55	34	80	33.2	80	36.3	100	399.9	0

6/29/2018 13:58	0:00:43	0	48	55	34.2	80	33.3	80	36.7	100	399.9	0
6/29/2018 13:58	0:00:44	0	48.5	55	34.5	80	33.6	80	37.1	100	399.9	0
6/29/2018 13:58	0:00:45	0	49	55	34.7	80	33.8	80	37.5	100	399.9	0
6/29/2018 13:58	0:00:46	0	49.5	55	34.9	80	33.8	80	38	100	399.9	0
6/29/2018 13:58	0:00:47	0	49.9	55	35.1	80	34.1	80	38	100	399.9	0
6/29/2018 13:58	0:00:48	0	50.3	55	35.4	80	34.4	80	38.4	100	399.9	0
6/29/2018 13:58	0:00:49	0	51	55	35.6	80	34.6	80	38.8	100	399.9	0
6/29/2018 13:58	0:00:50	0	51.4	55	36	80	35	80	39.2	100	399.9	0
6/29/2018 13:58	0:00:51	0	51.8	55	36.1	80	35.1	80	39.7	100	399.9	0
6/29/2018 13:58	0:00:52	0	52.5	55	36.3	80	35.4	80	40.1	100	399.9	0
6/29/2018 13:58	0:00:53	0	53	55	36.6	80	35.6	80	40.1	100	399.9	0
6/29/2018 13:58	0:00:54	0	53.3	55	36.8	80	35.9	80	40.6	100	399.9	0
6/29/2018 13:58	0:00:55	0	53.7	55	37	80	36.1	80	41	100	399.9	0
6/29/2018 13:58	0:00:56	0	54.1	55	37.3	80	36.1	80	41.4	100	399.9	0
6/29/2018 13:58	0:00:57	0	54.4	55	37.7	80	36.5	80	41.8	100	399.9	0
6/29/2018 13:58	0:00:58	0	54.8	55	37.9	80	36.7	80	42.3	100	399.9	0
6/29/2018 13:58	0:00:59	0	55.3	55	38.2	80	37.1	80	42.3	100	399.9	0
6/29/2018 13:58	0:01:00	0	55.7	55	38.5	80	37.4	80	42.8	100	399.9	0
6/29/2018 13:58	0:01:01	0	56.2	55	38.6	80	37.6	80	43.2	100	399.9	0
6/29/2018 13:58	0:01:02	0	56.6	55	39.1	80	37.9	80	43.6	100	399.9	0
6/29/2018 13:58	0:01:03	0	57.2	55	39.1	80	38.1	80	44	100	399.9	0
6/29/2018 13:58	0:01:04	0	57.5	55	39.6	80	38.4	80	44.5	100	399.9	0
6/29/2018 13:58	0:01:05	0	58	55	39.8	80	38.7	80	44.5	100	399.9	0
6/29/2018 13:58	0:01:06	0	58.4	55	40.1	80	38.9	80	44.9	100	399.9	0

APPENDIX E: ANSYS FLUENT

E1: Layer Creation

A 12” build with a layer thickness of 0.004”/layer results in a total of 3000 layers. To build the most accurate thermal model in a reasonable amount of time created the need to simulate stages of a build before doing a full build simulation. Builds comprising three (3) layers, twenty (20) layers, and one hundred twenty-five (125) layers were programmed and evaluated.

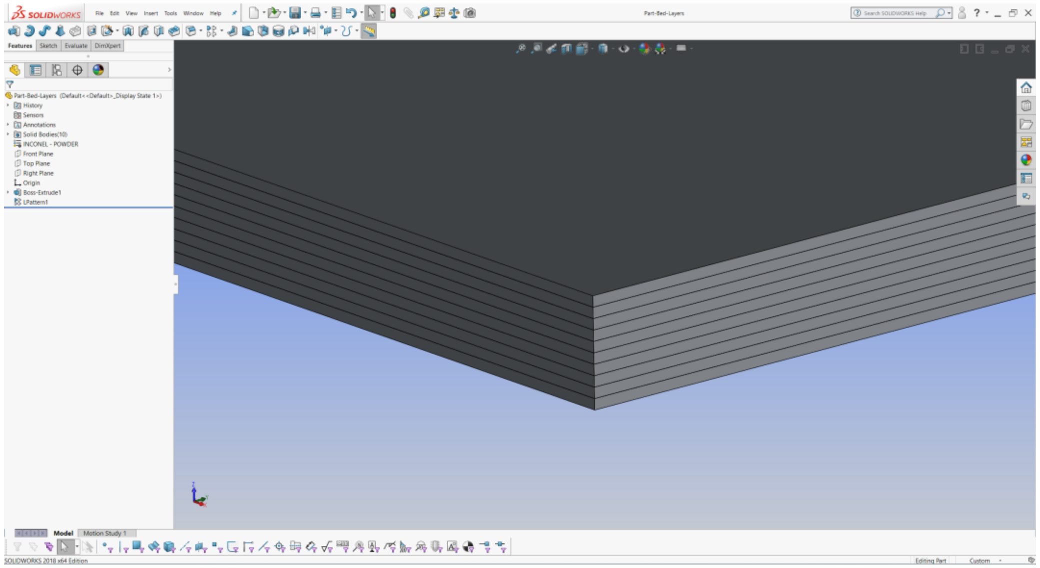

Figure 162: Multi-Layer Solidworks® Solid Model

Fluent can import solid models and apply nodes and boundary conditions to the completed geometries for use in thermal simulation. A solid model representing a single layer was created in Solidworks® by creating an x-y rectangle measuring 400mm X 300mm and extruding a single layer (initially 0.004"), shown in Figure 162. The pattern tool was used to stack the number of desired layers which allows for easier setup between layers within ANSYS. It is critical that the layers share a boundary and that there is no gap between layers.

Once ANSYS has been opened, the following numbered steps will walk through the creation of the layers for the simulation:

1. Drag 'Fluid Flow' (Fluent) to the workspace to create a new project as illustrated in Figure 163.

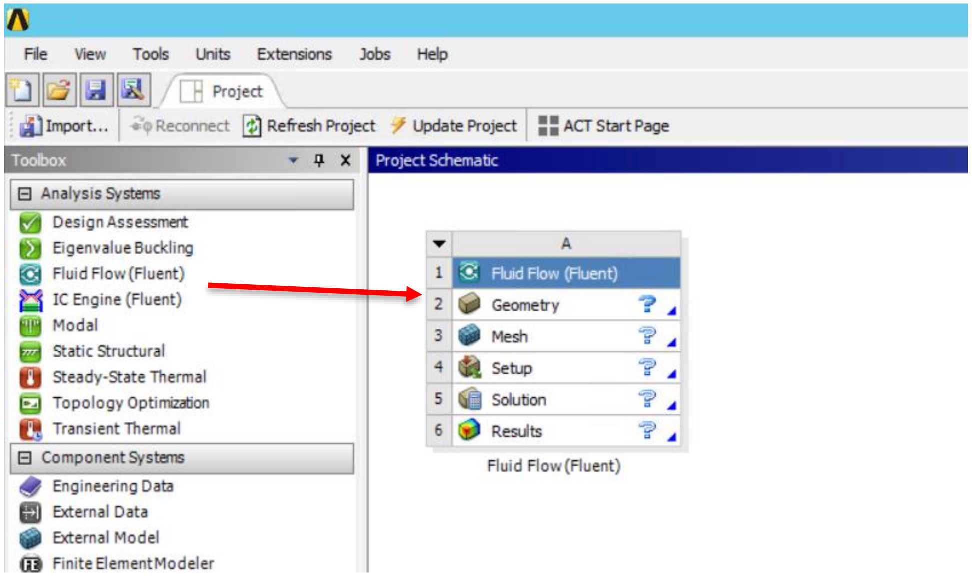

Figure 163: Setting up Fluid Flow (Fluent) Project

2. Right mouse-click on the *Geometry* icon and select *New DesignModeler Geometry* from the selection dialogue box shown in Figure 164.

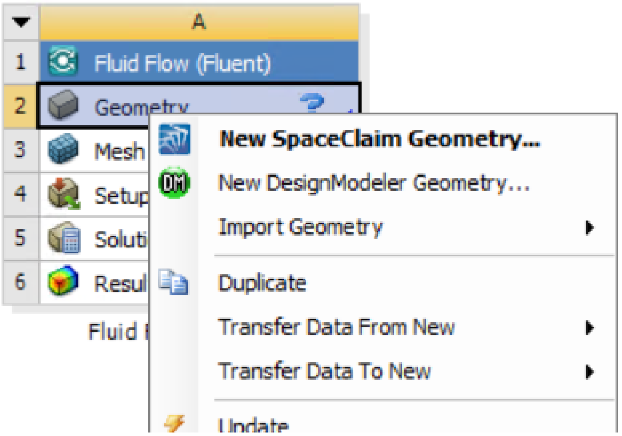

Figure 164: Importing a geometry

3. Once inside **DesignModeler**, click *File* & *Import External Geometry File*, shown in Figure 165, where the Solidworks® part file can be selected.

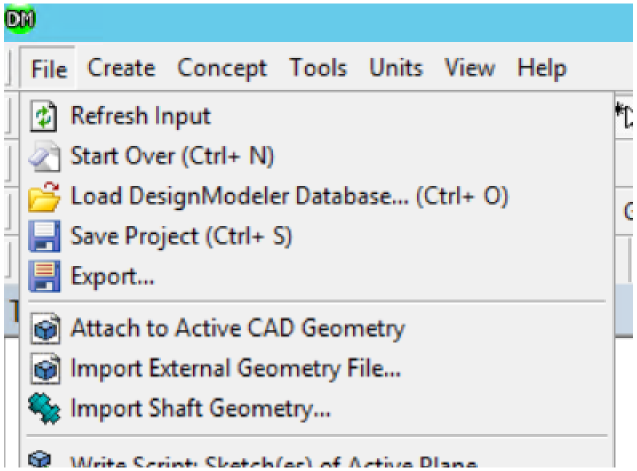

Figure 165: Importing CAD model

4. When the file has been imported, the ***Import*** node is visible in the Fluid Flow (Fluent) history tree. The Generate icon must be selected for the full geometry to be imported. Both the Import node and the Generate icon are circled Figure 166.

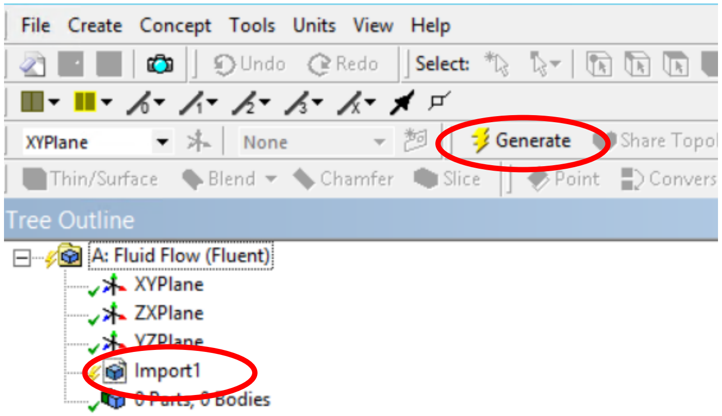

Figure 166: Generating the imported geometry.

5. The part will import with each layer as a body. This structure is important and helps to automatically create a relationship within the mesh between the layers. Rename each body as layer1, layer2, etc. as shown Figure 167. This is important for programming which layer is enabled/disabled within the simulation.

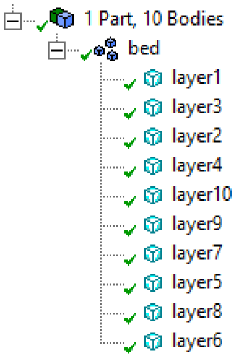

- 1 Part, 10 Bodies
  - bed
    - layer1
    - layer3
    - layer2
    - layer4
    - layer10
    - layer9
    - layer7
    - layer5
    - layer8
    - layer6

Figure 167: Imported geometry with ten layers.

6. Cut the part along any symmetry planes to reduce the mesh and solve time. Go to *Tool* > *Symmetry* and pick the appropriate plane. Click the generate icon to enable.

7. When symmetry is used, all surfaces are labelled with “front, side, or back” and ordered so that the programming can be managed without confusion. Similarly, any surfaces that lie on the symmetry planes should be labeled with “sym”. The simulation will key in on this label and automatically apply the appropriate boundary conditions. See the ten (10) layer example below in Figure 168.

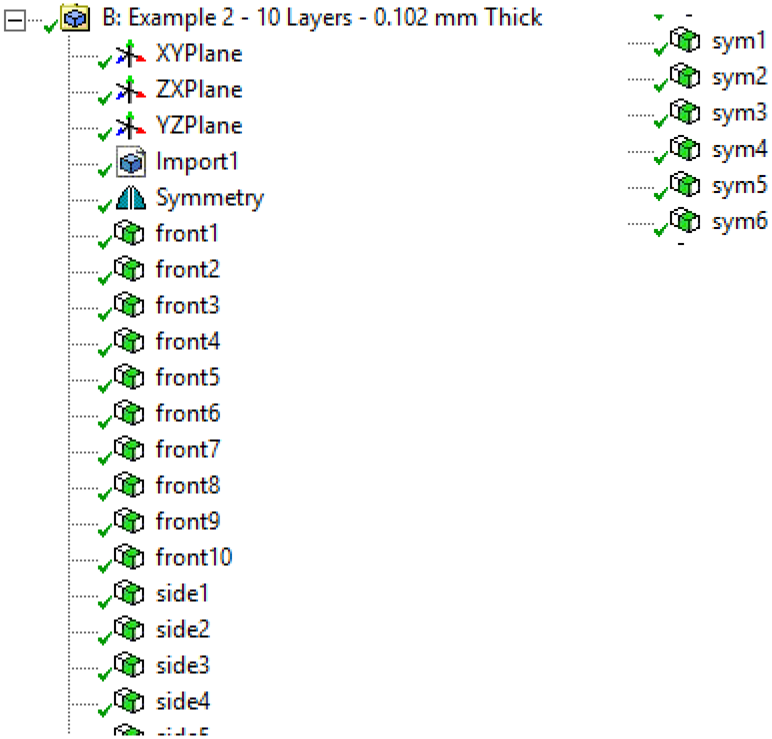

B: Example 2 - 10 Layers - 0.102 mm Thick
XYPlane
ZXPlane
YZPlane
Import1
Symmetry
front1
front2
front3
front4
front5
front6
front7
front8
front9
front10
side1
side2
side3
side4

sym1
sym2
sym3
sym4
sym5
sym6

Figure 168: ANSYS Thermal Model Symmetry Labels

8. The final step in creating the geometry to be used for mesh creation and assembly is to label the top and bottom of the layers. Since this simulation is a series of sequential layers, this aspect is very critical. The first layer will be critical and will have a bottom (bottom1) label and a top (top1) label. All other layers will have a bottom layer defined by the previous layer's top. Therefore, all other layers will only have the top layer labeled in sequential order as seen in Figure

169. Fluent will generate the bottom layer that will be bonded to the previous top layer as a shadow surface for the mesh. Changing the name will confuse the program. Once labeling is completed, save and exit the design modeler.

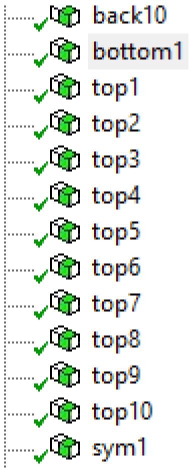

back10
bottom1
top1
top2
top3
top4
top5
top6
top7
top8
top9
top10
sym1

Figure 169: ANSYS Thermal labeling consideration for layers.

E2: ANSYS Fluent Thermal Settings

This section with details of the sequencing required within ANSYS is explained in Section 6.4 ANSYS® Fluent Thermal Model. A user that is proficient in ANSYS Fluent can use this detail along with the information in the previous chapters to replicate the thermal model.

The macro reads these parameters into the simulation from the material database:

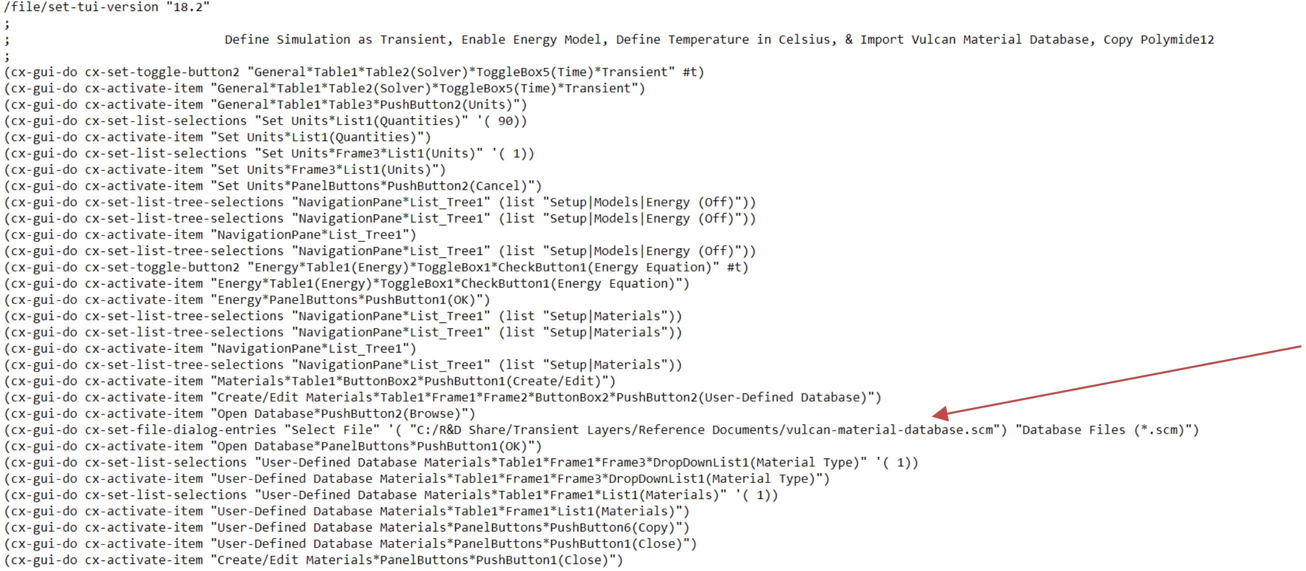

```
/file/set-tui-version "18.2"
;
;                              Define Simulation as Transient, Enable Energy Model, Define Temperature in Celsius, & Import Vulcan Material Database, Copy Polymide12
;
(cx-gui-do cx-set-toggle-button2 "General*Table1*Table2(Solver)*ToggleBox5(Time)*Transient" #t)
(cx-gui-do cx-activate-item "General*Table1*Table2(Solver)*ToggleBox5(Time)*Transient")
(cx-gui-do cx-activate-item "General*Table1*Table3*PushButton2(Units)")
(cx-gui-do cx-set-list-selections "Set Units*List1(Quantities)" '( 90))
(cx-gui-do cx-activate-item "Set Units*List1(Quantities)")
(cx-gui-do cx-set-list-selections "Set Units*Frame3*List1(Units)" '( 1))
(cx-gui-do cx-activate-item "Set Units*Frame3*List1(Units)")
(cx-gui-do cx-activate-item "Set Units*PanelButtons*PushButton2(Cancel)")
(cx-gui-do cx-set-list-tree-selections "NavigationPane*List_Tree1" (list "Setup|Models|Energy (Off)"))
(cx-gui-do cx-set-list-tree-selections "NavigationPane*List_Tree1" (list "Setup|Models|Energy (Off)"))
(cx-gui-do cx-activate-item "NavigationPane*List_Tree1")
(cx-gui-do cx-set-list-tree-selections "NavigationPane*List_Tree1" (list "Setup|Models|Energy (Off)"))
(cx-gui-do cx-set-toggle-button2 "Energy*Table1(Energy)*ToggleBox1*CheckButton1(Energy Equation)" #t)
(cx-gui-do cx-activate-item "Energy*Table1(Energy)*ToggleBox1*CheckButton1(Energy Equation)")
(cx-gui-do cx-activate-item "Energy*PanelButtons*PushButton1(OK)")
(cx-gui-do cx-set-list-tree-selections "NavigationPane*List_Tree1" (list "Setup|Materials"))
(cx-gui-do cx-set-list-tree-selections "NavigationPane*List_Tree1" (list "Setup|Materials"))
(cx-gui-do cx-activate-item "NavigationPane*List_Tree1")
(cx-gui-do cx-set-list-tree-selections "NavigationPane*List_Tree1" (list "Setup|Materials"))
(cx-gui-do cx-activate-item "Materials*Table1*ButtonBox2*PushButton1(Create/Edit)")
(cx-gui-do cx-activate-item "Create/Edit Materials*Table1*Frame1*Frame2*ButtonBox2*PushButton2(User-Defined Database)")
(cx-gui-do cx-activate-item "Open Database*PushButton2(Browse)")
(cx-gui-do cx-set-file-dialog-entries "Select File" '( "C:/R&D Share/Transient Layers/Reference Documents/vulcan-material-database.scm") "Database Files (*.scm)")
(cx-gui-do cx-activate-item "Open Database*PanelButtons*PushButton1(OK)")
(cx-gui-do cx-set-list-selections "User-Defined Database Materials*Table1*Frame1*Frame3*DropDownList1(Material Type)" '( 1))
(cx-gui-do cx-activate-item "User-Defined Database Materials*Table1*Frame1*Frame3*DropDownList1(Material Type)")
(cx-gui-do cx-set-list-selections "User-Defined Database Materials*Table1*Frame1*List1(Materials)" '( 1))
(cx-gui-do cx-activate-item "User-Defined Database Materials*Table1*Frame1*List1(Materials)")
(cx-gui-do cx-activate-item "User-Defined Database Materials*PanelButtons*PushButton6(Copy)")
(cx-gui-do cx-activate-item "User-Defined Database Materials*PanelButtons*PushButton1(Close)")
(cx-gui-do cx-activate-item "Create/Edit Materials*PanelButtons*PushButton1(Close)")
```

Each initial layer is turned on at 150C:

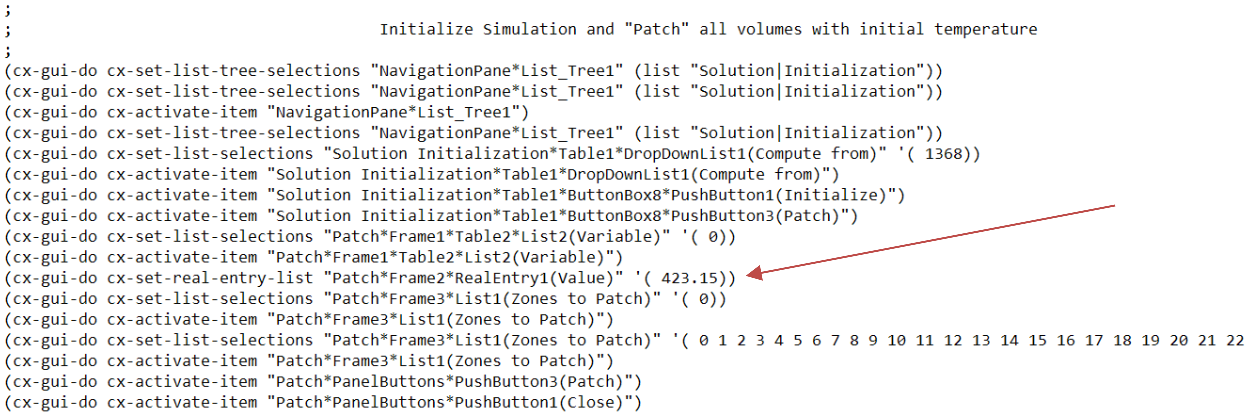

```
;
;                                          Initialize Simulation and "Patch" all volumes with initial temperature
;
(cx-gui-do cx-set-list-tree-selections "NavigationPane*List_Tree1" (list "Solution|Initialization"))
(cx-gui-do cx-set-list-tree-selections "NavigationPane*List_Tree1" (list "Solution|Initialization"))
(cx-gui-do cx-activate-item "NavigationPane*List_Tree1")
(cx-gui-do cx-set-list-tree-selections "NavigationPane*List_Tree1" (list "Solution|Initialization"))
(cx-gui-do cx-set-list-selections "Solution Initialization*Table1*DropDownList1(Compute from)" '( 1368))
(cx-gui-do cx-activate-item "Solution Initialization*Table1*DropDownList1(Compute from)")
(cx-gui-do cx-activate-item "Solution Initialization*Table1*ButtonBox8*PushButton1(Initialize)")
(cx-gui-do cx-activate-item "Solution Initialization*Table1*ButtonBox8*PushButton3(Patch)")
(cx-gui-do cx-set-list-selections "Patch*Frame1*Table2*List2(Variable)" '( 0))
(cx-gui-do cx-activate-item "Patch*Frame1*Table2*List2(Variable)")
(cx-gui-do cx-set-real-entry-list "Patch*Frame2*RealEntry1(Value)" '( 423.15))
(cx-gui-do cx-set-list-selections "Patch*Frame3*List1(Zones to Patch)" '( 0))
(cx-gui-do cx-activate-item "Patch*Frame3*List1(Zones to Patch)")
(cx-gui-do cx-set-list-selections "Patch*Frame3*List1(Zones to Patch)" '( 0 1 2 3 4 5 6 7 8 9 10 11 12 13 14 15 16 17 18 19 20 21 22
(cx-gui-do cx-activate-item "Patch*Frame3*List1(Zones to Patch)")
(cx-gui-do cx-activate-item "Patch*PanelButtons*PushButton3(Patch)")
(cx-gui-do cx-activate-item "Patch*PanelButtons*PushButton1(Close)")
```

Boundary Conditions…150C for 1st simulation:

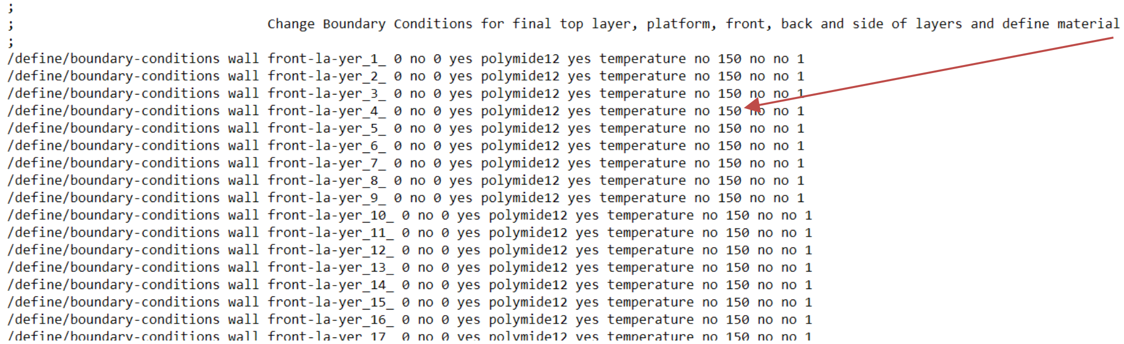

```
;
;                              Change Boundary Conditions for final top layer, platform, front, back and side of layers and define material
;
/define/boundary-conditions wall front-la-yer_1_  0 no 0 yes polymide12 yes temperature no 150 no no 1
/define/boundary-conditions wall front-la-yer_2_  0 no 0 yes polymide12 yes temperature no 150 no no 1
/define/boundary-conditions wall front-la-yer_3_  0 no 0 yes polymide12 yes temperature no 150 no no 1
/define/boundary-conditions wall front-la-yer_4_  0 no 0 yes polymide12 yes temperature no 150 no no 1
/define/boundary-conditions wall front-la-yer_5_  0 no 0 yes polymide12 yes temperature no 150 no no 1
/define/boundary-conditions wall front-la-yer_6_  0 no 0 yes polymide12 yes temperature no 150 no no 1
/define/boundary-conditions wall front-la-yer_7_  0 no 0 yes polymide12 yes temperature no 150 no no 1
/define/boundary-conditions wall front-la-yer_8_  0 no 0 yes polymide12 yes temperature no 150 no no 1
/define/boundary-conditions wall front-la-yer_9_  0 no 0 yes polymide12 yes temperature no 150 no no 1
/define/boundary-conditions wall front-la-yer_10_  0 no 0 yes polymide12 yes temperature no 150 no no 1
/define/boundary-conditions wall front-la-yer_11_  0 no 0 yes polymide12 yes temperature no 150 no no 1
/define/boundary-conditions wall front-la-yer_12_  0 no 0 yes polymide12 yes temperature no 150 no no 1
/define/boundary-conditions wall front-la-yer_13_  0 no 0 yes polymide12 yes temperature no 150 no no 1
/define/boundary-conditions wall front-la-yer_14_  0 no 0 yes polymide12 yes temperature no 150 no no 1
/define/boundary-conditions wall front-la-yer_15_  0 no 0 yes polymide12 yes temperature no 150 no no 1
/define/boundary-conditions wall front-la-yer_16_  0 no 0 yes polymide12 yes temperature no 150 no no 1
/define/boundary-conditions wall front-la-yer_17_  0 no 0 yes polymide12 yes temperature no 150 no no 1
```

“The bottom layer is shadowed the top of previous layer”…….The new layer is activated, the top and the bottom of the new layer become coupled, the top of the new layer has the gradients applied:

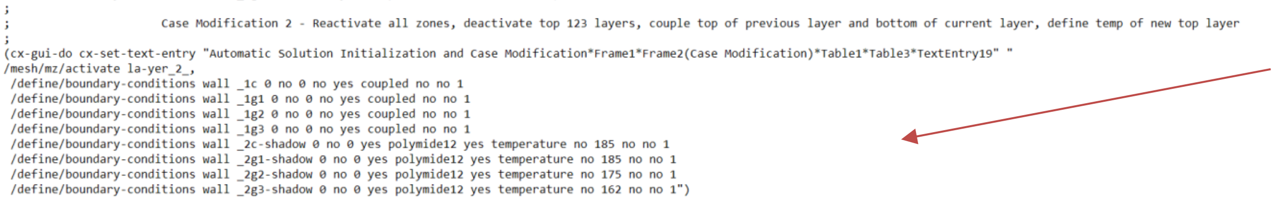

```
;
;                   Case Modification 2 - Reactivate all zones, deactivate top 123 layers, couple top of previous layer and bottom of current layer, define temp of new top layer
;
(cx-gui-do cx-set-text-entry "Automatic Solution Initialization and Case Modification*Frame1*Frame2(Case Modification)*Table1*Table3*TextEntry19" "
/mesh/mz/activate la-yer_2_,
 /define/boundary-conditions wall _1c 0 no 0 no yes coupled no no 1
 /define/boundary-conditions wall _1g1 0 no 0 no yes coupled no no 1
 /define/boundary-conditions wall _1g2 0 no 0 no yes coupled no no 1
 /define/boundary-conditions wall _1g3 0 no 0 no yes coupled no no 1
 /define/boundary-conditions wall _2c-shadow 0 no 0 yes polymide12 yes temperature no 185 no no 1
 /define/boundary-conditions wall _2g1-shadow 0 no 0 yes polymide12 yes temperature no 185 no no 1
 /define/boundary-conditions wall _2g2-shadow 0 no 0 yes polymide12 yes temperature no 175 no no 1
 /define/boundary-conditions wall _2g3-shadow 0 no 0 yes polymide12 yes temperature no 162 no no 1")
```

The top layer has temperatures applied based on FLIR camera.

The cool down then applies a convection coefficient to all boundaries of 5 W/m-K @ 40C:

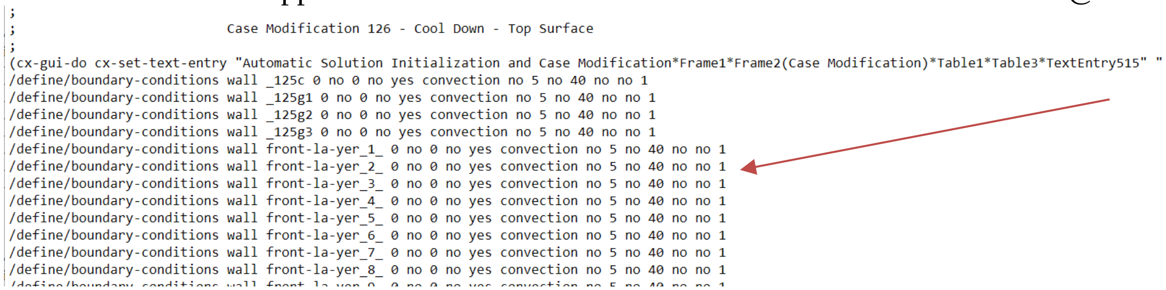

```
;
;                            Case Modification 126 - Cool Down - Top Surface
;
(cx-gui-do cx-set-text-entry "Automatic Solution Initialization and Case Modification*Frame1*Frame2(Case Modification)*Table1*Table3*TextEntry515" "
/define/boundary-conditions wall _125c 0 no 0 no yes convection no 5 no 40 no no 1
/define/boundary-conditions wall _125g1 0 no 0 no yes convection no 5 no 40 no no 1
/define/boundary-conditions wall _125g2 0 no 0 no yes convection no 5 no 40 no no 1
/define/boundary-conditions wall _125g3 0 no 0 no yes convection no 5 no 40 no no 1
/define/boundary-conditions wall front-la-yer_1_ 0 no 0 no yes convection no 5 no 40 no no 1
/define/boundary-conditions wall front-la-yer_2_ 0 no 0 no yes convection no 5 no 40 no no 1
/define/boundary-conditions wall front-la-yer_3_ 0 no 0 no yes convection no 5 no 40 no no 1
/define/boundary-conditions wall front-la-yer_4_ 0 no 0 no yes convection no 5 no 40 no no 1
/define/boundary-conditions wall front-la-yer_5_ 0 no 0 no yes convection no 5 no 40 no no 1
/define/boundary-conditions wall front-la-yer_6_ 0 no 0 no yes convection no 5 no 40 no no 1
/define/boundary-conditions wall front-la-yer_7_ 0 no 0 no yes convection no 5 no 40 no no 1
/define/boundary-conditions wall front-la-yer_8_ 0 no 0 no yes convection no 5 no 40 no no 1
/define/boundary-conditions wall front-la-yer_9_ 0 no 0 no yes convection no 5 no 40 no no 1
```

E3: ANSYS Fluent Macro Code (125 Layer Model)

The ability to simulate a multi-layer thermal problem comes at the cost of having to manually replicate the source code. The following is the ANSYS Fluent macro code that was used to create the many layers and instruct ANSYS to enable and disable layers as it progressed through the simulation. More detail on developing the solid model, the scheme for multi-layer simulation, and the results from Fluent are available in the following Sections: 4.3 Thermal Simulation, 6.4 ANSYS® Fluent Thermal Model and 7.3 ANSYS Fluent Thermal Model

```
/file/set-tui-version "18.2"
;
; Define Simulation as Transient, Enable Energy Model, Define Temperature in Celsius, & Import Vulcan Material Database, Copy Polymide12
;
(cx-gui-do cx-set-toggle-button2 "General*Table1*Table2(Solver)*ToggleBox5(Time)*Transient" #t)
(cx-gui-do cx-activate-item "General*Table1*Table2(Solver)*ToggleBox5(Time)*Transient")
(cx-gui-do cx-activate-item "General*Table1*Table3*PushButton2(Units)")
(cx-gui-do cx-set-list-selections "Set Units*List1(Quantities)" '( 90))
(cx-gui-do cx-activate-item "Set Units*List1(Quantities)")
(cx-gui-do cx-set-list-selections "Set Units*Frame3*List1(Units)" '( 1))
```

```
(cx-gui-do cx-activate-item "Set Units*Frame3*List1(Units)")
(cx-gui-do cx-activate-item "Set Units*PanelButtons*PushButton2(Cancel)")
(cx-gui-do cx-set-list-tree-selections "NavigationPane*List_Tree1" (list "Setup|Models|Energy (Off)"))
(cx-gui-do cx-set-list-tree-selections "NavigationPane*List_Tree1" (list "Setup|Models|Energy (Off)"))
(cx-gui-do cx-activate-item "NavigationPane*List_Tree1")
(cx-gui-do cx-set-list-tree-selections "NavigationPane*List_Tree1" (list "Setup|Models|Energy (Off)"))
(cx-gui-do cx-set-toggle-button2 "Energy*Table1(Energy)*ToggleBox1*CheckButton1(Energy Equation)" #t)
(cx-gui-do cx-activate-item "Energy*Table1(Energy)*ToggleBox1*CheckButton1(Energy Equation)")
(cx-gui-do cx-activate-item "Energy*PanelButtons*PushButton1(OK)")
(cx-gui-do cx-set-list-tree-selections "NavigationPane*List_Tree1" (list "Setup|Materials"))
(cx-gui-do cx-set-list-tree-selections "NavigationPane*List_Tree1" (list "Setup|Materials"))
(cx-gui-do cx-activate-item "NavigationPane*List_Tree1")
(cx-gui-do cx-set-list-tree-selections "NavigationPane*List_Tree1" (list "Setup|Materials"))
(cx-gui-do cx-activate-item "Materials*Table1*ButtonBox2*PushButton1(Create/Edit)")
(cx-gui-do cx-activate-item "Create/Edit Materials*Table1*Frame1*Frame2*ButtonBox2*PushButton2(User-Defined Database)")
(cx-gui-do cx-activate-item "Open Database*PushButton2(Browse)")
```

```
	(cx-gui-do cx-set-file-dialog-entries "Select File" '( "C:/R&D Share/Transient Layers/Reference Documents/vulcan-material-database.scm")
"Database Files (*.scm)")

	(cx-gui-do cx-activate-item "Open Database*PanelButtons*PushButton1(OK)")

	(cx-gui-do cx-set-list-selections "User-Defined Database Materials*Table1*Frame1*Frame3*DropDownList1(Material Type)" '( 1))

	(cx-gui-do cx-activate-item "User-Defined Database Materials*Table1*Frame1*Frame3*DropDownList1(Material Type)")

	(cx-gui-do cx-set-list-selections "User-Defined Database Materials*Table1*Frame1*List1(Materials)" '( 1))

	(cx-gui-do cx-activate-item "User-Defined Database Materials*Table1*Frame1*List1(Materials)")

	(cx-gui-do cx-activate-item "User-Defined Database Materials*PanelButtons*PushButton6(Copy)")

	(cx-gui-do cx-activate-item "User-Defined Database Materials*PanelButtons*PushButton1(Close)")

	(cx-gui-do cx-activate-item "Create/Edit Materials*PanelButtons*PushButton1(Close)")

	;

	;			Change Volumes from Fluid to Solid

	;
(cx-gui-do cx-set-list-tree-selections "NavigationPane*List_Tree1" (list "Setup|Cell Zone Conditions|la-yer_100_ (fluid,
id=695)"))

(cx-gui-do cx-set-list-tree-selections "NavigationPane*List_Tree1" (list "Setup|Cell Zone Conditions|la-yer_100_ (fluid,
id=695)""Setup|Cell Zone Conditions|la-yer_101_ (fluid, id=689)""Setup|Cell Zone Conditions|la-yer_102_ (fluid,
id=683)""Setup|Cell Zone Conditions|la-yer_103_ (fluid, id=677)""Setup|Cell Zone Conditions|la-yer_104_ (fluid,
id=671)""Setup|Cell Zone Conditions|la-yer_105_ (fluid, id=666)""Setup|Cell Zone Conditions|la-yer_106_ (fluid,
id=661)""Setup|Cell Zone Conditions|la-yer_107_ (fluid, id=656)""Setup|Cell Zone Conditions|la-yer_108_ (fluid,
```

id=651)""Setup|Cell Zone Conditions|la-yer_109_ (fluid, id=646)""Setup|Cell Zone Conditions|la-yer_10_ (fluid, id=711)""Setup|Cell Zone Conditions|la-yer_110_ (fluid, id=641)""Setup|Cell Zone Conditions|la-yer_111_ (fluid, id=636)""Setup|Cell Zone Conditions|la-yer_112_ (fluid, id=630)""Setup|Cell Zone Conditions|la-yer_113_ (fluid, id=624)""Setup|Cell Zone Conditions|la-yer_114_ (fluid, id=742)""Setup|Cell Zone Conditions|la-yer_115_ (fluid, id=736)""Setup|Cell Zone Conditions|la-yer_116_ (fluid, id=730)""Setup|Cell Zone Conditions|la-yer_117_ (fluid, id=724)""Setup|Cell Zone Conditions|la-yer_118_ (fluid, id=718)""Setup|Cell Zone Conditions|la-yer_119_ (fluid, id=712)""Setup|Cell Zone Conditions|la-yer_11_ (fluid, id=705)""Setup|Cell Zone Conditions|la-yer_120_ (fluid, id=706)""Setup|Cell Zone Conditions|la-yer_121_ (fluid, id=700)""Setup|Cell Zone Conditions|la-yer_122_ (fluid, id=694)""Setup|Cell Zone Conditions|la-yer_123_ (fluid, id=688)""Setup|Cell Zone Conditions|la-yer_124_ (fluid, id=682)""Setup|Cell Zone Conditions|la-yer_125_ (fluid, id=676)""Setup|Cell Zone Conditions|la-yer_12_ (fluid, id=699)""Setup|Cell Zone Conditions|la-yer_13_ (fluid, id=693)""Setup|Cell Zone Conditions|la-yer_14_ (fluid, id=687)""Setup|Cell Zone Conditions|la-yer_15_ (fluid, id=681)""Setup|Cell Zone Conditions|la-yer_16_ (fluid, id=675)""Setup|Cell Zone Conditions|la-yer_17_ (fluid, id=670)""Setup|Cell Zone Conditions|la-yer_18_ (fluid, id=665)""Setup|Cell Zone Conditions|la-yer_19_ (fluid, id=660)""Setup|Cell Zone Conditions|la-yer_1_ (fluid, id=622)""Setup|Cell Zone Conditions|la-yer_20_ (fluid, id=655)""Setup|Cell Zone Conditions|la-yer_21_ (fluid, id=650)""Setup|Cell Zone Conditions|la-yer_22_ (fluid, id=645)""Setup|Cell Zone Conditions|la-yer_23_ (fluid, id=640)""Setup|Cell Zone Conditions|la-yer_24_ (fluid, id=634)""Setup|Cell Zone Conditions|la-yer_25_ (fluid, id=628)""Setup|Cell Zone Conditions|la-yer_26_ (fluid, id=746)""Setup|Cell Zone Conditions|la-yer_27_ (fluid, id=740)""Setup|Cell Zone Conditions|la-yer_28_ (fluid, id=734)""Setup|Cell Zone Conditions|la-yer_29_ (fluid, id=728)""Setup|Cell Zone Conditions|la-yer_2_ (fluid, id=635)""Setup|Cell Zone Conditions|la-yer_30_ (fluid, id=722)""Setup|Cell Zone Conditions|la-yer_31_ (fluid, id=716)""Setup|Cell Zone Conditions|la-yer_32_ (fluid, id=710)""Setup|Cell Zone Conditions|la-yer_33_ (fluid, id=704)""Setup|Cell Zone Conditions|la-yer_34_ (fluid, id=698)""Setup|Cell Zone Conditions|la-yer_35_ (fluid, id=692)""Setup|Cell Zone Conditions|la-yer_36_ (fluid, id=686)""Setup|Cell Zone Conditions|la-yer_37_ (fluid, id=680)""Setup|Cell Zone Conditions|la-yer_38_ (fluid, id=674)""Setup|Cell Zone Conditions|la-yer_39_ (fluid, id=669)""Setup|Cell Zone Conditions|la-yer_3_ (fluid, id=629)""Setup|Cell Zone Conditions|la-yer_40_ (fluid, id=664)""Setup|Cell Zone Conditions|la-yer_41_ (fluid, id=659)""Setup|Cell Zone Conditions|la-yer_42_ (fluid, id=654)""Setup|Cell Zone Conditions|la-yer_43_ (fluid, id=649)""Setup|Cell Zone Conditions|la-yer_44_ (fluid, id=644)""Setup|Cell Zone Conditions|la-yer_45_ (fluid, id=639)""Setup|Cell Zone Conditions|la-yer_46_ (fluid, id=633)""Setup|Cell Zone Conditions|la-yer_47_ (fluid, id=627)""Setup|Cell Zone Conditions|la-yer_48_ (fluid, id=745)""Setup|Cell Zone Conditions|la-yer_49_ (fluid,

```
id=739)""Setup|Cell Zone Conditions|la-yer_4_ (fluid, id=623)""Setup|Cell Zone Conditions|la-yer_50_ (fluid,
id=733)""Setup|Cell Zone Conditions|la-yer_51_ (fluid, id=727)""Setup|Cell Zone Conditions|la-yer_52_ (fluid,
id=721)""Setup|Cell Zone Conditions|la-yer_53_ (fluid, id=715)""Setup|Cell Zone Conditions|la-yer_54_ (fluid,
id=709)""Setup|Cell Zone Conditions|la-yer_55_ (fluid, id=703)""Setup|Cell Zone Conditions|la-yer_56_ (fluid,
id=697)""Setup|Cell Zone Conditions|la-yer_57_ (fluid, id=691)""Setup|Cell Zone Conditions|la-yer_58_ (fluid,
id=685)""Setup|Cell Zone Conditions|la-yer_59_ (fluid, id=679)""Setup|Cell Zone Conditions|la-yer_5_ (fluid,
id=741)""Setup|Cell Zone Conditions|la-yer_60_ (fluid, id=673)""Setup|Cell Zone Conditions|la-yer_61_ (fluid,
id=668)""Setup|Cell Zone Conditions|la-yer_62_ (fluid, id=663)""Setup|Cell Zone Conditions|la-yer_63_ (fluid,
id=658)""Setup|Cell Zone Conditions|la-yer_64_ (fluid, id=653)""Setup|Cell Zone Conditions|la-yer_65_ (fluid,
id=648)""Setup|Cell Zone Conditions|la-yer_66_ (fluid, id=643)""Setup|Cell Zone Conditions|la-yer_67_ (fluid,
id=638)""Setup|Cell Zone Conditions|la-yer_68_ (fluid, id=632)""Setup|Cell Zone Conditions|la-yer_69_ (fluid,
id=626)""Setup|Cell Zone Conditions|la-yer_6_ (fluid, id=735)""Setup|Cell Zone Conditions|la-yer_70_ (fluid,
id=744)""Setup|Cell Zone Conditions|la-yer_71_ (fluid, id=738)""Setup|Cell Zone Conditions|la-yer_72_ (fluid,
id=732)""Setup|Cell Zone Conditions|la-yer_73_ (fluid, id=726)""Setup|Cell Zone Conditions|la-yer_74_ (fluid,
id=720)""Setup|Cell Zone Conditions|la-yer_75_ (fluid, id=714)""Setup|Cell Zone Conditions|la-yer_76_ (fluid,
id=708)""Setup|Cell Zone Conditions|la-yer_77_ (fluid, id=702)""Setup|Cell Zone Conditions|la-yer_78_ (fluid,
id=696)""Setup|Cell Zone Conditions|la-yer_79_ (fluid, id=690)""Setup|Cell Zone Conditions|la-yer_7_ (fluid,
id=729)""Setup|Cell Zone Conditions|la-yer_80_ (fluid, id=684)""Setup|Cell Zone Conditions|la-yer_81_ (fluid,
id=678)""Setup|Cell Zone Conditions|la-yer_82_ (fluid, id=672)""Setup|Cell Zone Conditions|la-yer_83_ (fluid,
id=667)""Setup|Cell Zone Conditions|la-yer_84_ (fluid, id=662)""Setup|Cell Zone Conditions|la-yer_85_ (fluid,
id=657)""Setup|Cell Zone Conditions|la-yer_86_ (fluid, id=652)""Setup|Cell Zone Conditions|la-yer_87_ (fluid,
id=647)""Setup|Cell Zone Conditions|la-yer_88_ (fluid, id=642)""Setup|Cell Zone Conditions|la-yer_89_ (fluid,
id=637)""Setup|Cell Zone Conditions|la-yer_8_ (fluid, id=723)""Setup|Cell Zone Conditions|la-yer_90_ (fluid,
id=631)""Setup|Cell Zone Conditions|la-yer_91_ (fluid, id=625)""Setup|Cell Zone Conditions|la-yer_92_ (fluid,
id=743)""Setup|Cell Zone Conditions|la-yer_93_ (fluid, id=737)""Setup|Cell Zone Conditions|la-yer_94_ (fluid,
id=731)""Setup|Cell Zone Conditions|la-yer_95_ (fluid, id=725)""Setup|Cell Zone Conditions|la-yer_96_ (fluid,
id=719)""Setup|Cell Zone Conditions|la-yer_97_ (fluid, id=713)""Setup|Cell Zone Conditions|la-yer_98_ (fluid,
id=707)""Setup|Cell Zone Conditions|la-yer_99_ (fluid, id=701)""Setup|Cell Zone Conditions|la-yer_9_ (fluid, id=717)"))
```

```
(cx-gui-do cx-set-list-tree-selections "NavigationPane*List_Tree1" (list "Setup|Cell Zone Conditions|la-yer_100_ (fluid,
id=695)""Setup|Cell Zone Conditions|la-yer_101_ (fluid, id=689)""Setup|Cell Zone Conditions|la-yer_102_ (fluid,
id=683)""Setup|Cell Zone Conditions|la-yer_103_ (fluid, id=677)""Setup|Cell Zone Conditions|la-yer_104_ (fluid,
id=671)""Setup|Cell Zone Conditions|la-yer_105_ (fluid, id=666)""Setup|Cell Zone Conditions|la-yer_106_ (fluid,
id=661)""Setup|Cell Zone Conditions|la-yer_107_ (fluid, id=656)""Setup|Cell Zone Conditions|la-yer_108_ (fluid,
id=651)""Setup|Cell Zone Conditions|la-yer_109_ (fluid, id=646)""Setup|Cell Zone Conditions|la-yer_10_ (fluid,
id=711)""Setup|Cell Zone Conditions|la-yer_110_ (fluid, id=641)""Setup|Cell Zone Conditions|la-yer_111_ (fluid,
id=636)""Setup|Cell Zo...
```

GLOSSARY

Brittle Fracture: Failure of a laser sintered specimen in tension within the elastic deformation range of a standard stress-strain curve. Fracture stress is less than yield stress with strains less than 10%. Typical fracture surfaces have a 45^o shear fracture.

Delamination: A special brittle fracture occurring at strains of <3% where the fracture surfaces are typically coincident with the interface boundary layer.

Fracture Limited Ductility: A fracture that occurs after the onset of strain hardening and typically before UTS and the onset of significant necking. Strains are typically 15-25%.

Full Plasticity Failure: Fracture occurring after the onset of necking at UTS. If this level of strain is reached, it is very common that failure will not occur until 40-60% strain.

Interface Boundary Layer: The interface between subsequent processed layers in the laser sintering process. This boundary is in the x-y plane and is the primary contributor to anisotropic material characteristics of specimens made in this process.

DSC: Differential Scanning Calorimetry is a thermoanalytical technique in which the difference in the amount of heat required to increase the temperature of a sample and reference is measured as a function of temperature.

ISO: International Standards Organization that develops and publishes international standards, especially in the context of quality management systems used in multiple manufacturing sectors.

AS9100: A widely adopted and standardized quality manufacturing system for use in the aerospace industry.

UTS: Ultimate Tensile Strength

EAB: Elongation at Break or Elongation at Fracture (EAF)

EAF: Elongation at Fracture or Elongation at Break (EAB)

XBar and R (range) Chart: In statistical quality control, the XBar and R chart is a type of control chart used to monitor variables data when samples are collected at regular intervals from a business or industrial process. The chart is advantageous when sample size constant and relatively small ($n \leq 10$). $R = x_{max} - x_{min}$ (NIST Staff, 2009)

Part Bed: Region of the polymer laser sintering machine that contains unsintered material and parts.

Feed Bed: Region of the polymer laser sintering machine that contains feedstock to be used to produce parts.

Feedstock: Powdered material used to produce parts in laser sintering.

Pyrometer or IR Sensor: A single color infra-red sensor used to determine the surface temperature in polymer laser sintering to control radiant heaters used to maintain a process setpoint.

BIBLIOGRAPHY

3D Systems Staff. (2018). *3D Systems Nylon Materials.* Retrieved from 3D Systems Corporate Website: https://www.3dsystems.com/sites/default/files/2017-01/DS_DuraForm_EX_US_0.pdf

3D Systems Staff. (2018). *3D Systems sPro 60 HD-HR*. Retrieved from 3D Systems Corporate Website: https://www.3dsystems.com/3d-printers/spro-60-hd

ALM Staff. (2018). *ALM Flame Retardnant Nylon FR-106*. Retrieved from ALM Corporate Website: http://alm-llc.com/project/fr-106/

Ansys Staff. (2018). *Ansys Fluent*. Retrieved from Ansys: https://www.ansys.com/products/fluids/ansys-fluent

ASM Engineering Materials Handbook (Vol. Plastics). (n.d.).

ASTM F42 Committee. (n.d.). *Standard Terminology for Additive Manufacturing Technologies.* Retrieved from ASTM International: https://www.astm.org/Standards/F2792.htm

ASTM Subcommittee D20-10. (2018). *ASTM D638-14 Standard Test Method for Tensile Properties of Plastics.* West Conshohocken, PA: ASTM International.

ASTM Subcommittee E28-01. (2018). *ASTM E83-16: Standard Practice for Verification and Classification of Extensometer Systems.* West Conshohocken, PA: ASTM International.

Bourell, D., Beaman, J., Ming, L., & Rosen, D. (2009). A Brief History of Additive Manufacturing and the 2009 Roadmap for Additive Manufacturing: Looking Back and Looking Ahead. *Proceedings of the RapidTech.* Istanbul, Turkey: US-Turkey Workshop on Rapid Technologies.

Caulfield, B., McHugh, P., & Lohfeld, S. (2006, September 1). Dependence of mechanical properties of polyamide components on build parameters in the SLS process. *Journal of Material Processing Technology, 182*(2007), 477-488.

Choren, J., Gervasi, V., Herman, T., Kamara, S., & Mitchell, J. (2001). SLS Powder Life Study. *SFF Symposium* (pp. 39-45). Austin, TX: The University of Texas at Austin.

Codd, E. (1970, Jun). A Relational Model of Data for Large Shared Data Banks. *Communications of the ACM, 13*(6), 377-387. Retrieved from Wikipedia: https://en.wikipedia.org/wiki/SQL

Design News Staff. (2010, May 18). Boeing Engineer Honored for Dreamliner 787 Components. *Design News*.

Drummera, D. W. (2015). Modelling of the Aging Behavior of Polyamide 12 powder. *AIP Conference Proceedings* (pp. 160007: 1-5). American Institute of Physics.

eFunda, Inc. . (2018, June 10). *Rapid Prototyping: An Overview*. Retrieved from eFunda: The Ultimate Online Reference for Engineers: http://www.efunda.com/processes/rapid_prototyping/

Egger, G., Gygax, P., Glardon, R., & Karapatis, N. (1999). Optimization of Powder Layer Density in Selective Laser Sintering. *Proceedings of the Solid Freeform Fabrication Symposium* (pp. 255-263). Austin, TX: The University of Texas at Austin.

F42.91, A. S. (2012). *ASTM F2792-12a: Standard Terminology for Additive Manufacturing Technologies*. West Conshohocken, PA: ASTM International.

Federal Aviation Administration. (2017). FAR 25.853, Vertical testing. In F. A. Administration, *Airworthiness Standard: Transport Category Airplanes* (pp. Part 25, Section 25.853). Washington, D.C.: Federal Aviation Administration.

FLIR Product Website. (2018). *FLIR A325sc*. Retrieved from FLIR Research and Science: http://ww4.flir.com/science/display/?id=46623

Gebhardt, A. (2011). *Understanding Additive Manufacturing* (First ed.). Munich, Germany: Hanser.

Gibson, I. a. (1997). Material properties and fabrication parameters in selective laser sintering process. *Rapid Prototyping Journal, Volume 3 Number 4*, 129-136.

Gibson, I., Rosen, D., & Stucker, B. (2015). *Additive Manufacturing Technologies, 2nd Edition.* New York: Springer.

Gornet, T. (2010). Microtoming of Laser Sintering Nylon Specimens. (D. Leigh, Interviewer) Louisville, KY: University of Louisville.

Guzman, A. R. (2006). Development of AZS Refractories for the Glass Industry. *AZojomo - The AZo Journal of Materials Online*, 9/15.

Hopkinson, N., Hague, R., & Dickens, P. (2006). *Rapid Manufacturning: An Industrial Revolution for the Digital Age.* West Sussex, England: John Wiley & Sons, Ltd.

Incropera, F., & De Witt, D. (1990). *Fundamentals of Heat and Mass Transfer.* New York: John Wiley & Sons.

International Standards Organization. (2016, Sep 20). *Quality Management Systems - Requirements for Aviation, Space, and Defense Organizations AS9100D.* Retrieved from SAE International Standards: https://www.sae.org/standards/content/as9100d/

ISO Central Secretariat . (2015). *ISO 9001:2015 - How to use it.* Geneva, Switzerland: International Standards Organization.

Jacobs, P. F. (1996). *Stereolithography and other RP&M Technologies.* Dearborn, MI: Society of Manufacturing Engineers.

Kang, S. (2005). In S. Kang, *Sintering: Densification, Grain Growth, and Microstructure.* Amsterdam, Boston, Heidelberg, London, et. al.: Elsevier Butterworth Heinemann.

Kim, G., & Oh, Y. (2008). A benchmark study on rapid prototyping processes and machines: quantitative comparisons of mechanical properties, accuracy, roughness, speed and material cost. *Journal of Engineering Manufacture*, 201-215.

Kim, K. D., Sperling, L., & and Klein, A. (1994, Aug 4). Reptation Time, Temperature, and Cosurfactant Effects on the Molecular Interdiffusion Rate during Polystyrene Latex Film Formation. (B. Hammouda, Ed.) *Macromolecules, 27*, 6841-6850.

Kruse, R. (2010). *Photos of Military Helicopters and Tiltrotors*. Retrieved from Website of Richard Kruse: https://richardkruse.com/Photos-Aviation-Helicopter.html

Leigh, D. (2011). *Effect of In-Plane Voiding on the Fracture Behavior of Laser Sintered Polyamide.* The University of Texas at Austin, College of Mechanical Engineering. Austin, TX: The University of Texas at Austin.

Leigh, D., & Gornet, T. (n.d.). Laser Sintering Powder Studies. SLS User's Group, Private Communication.

Levy, G. (2010). The Role and Future of the Laser Technology in the Additive Manufacturing Environment. *Laser Assisted Net Shape Engineering* (pp. 65-80). Erlangen, Germany: Elsevier Procedia.

Majewski, C., Zarringhalam, H., & Hopkinson, N. (2008). Effects of Degree of Particle Melt and crystallinity in SLS Nylon-12 parts. *SFF Symposium* (pp. 45-54). Austin, TX: The University of Texas at Austin.

Makerbot Staff. (2018). *The Makerbot Replicator Z18*. Retrieved from Makerbot Corporate Website: https://www.makerbot.com/3d-printers/replicator-z18/

MathWorks Staff. (2018). *Mathworks Matlab Overview*. Retrieved from Mathworks: https://www.mathworks.com/products/matlab.html

Milberg, E. (2017, September 18). *Boeing to Increase Production of 787 Dreamliner*. Retrieved from Composites Manufacturing: http://compositesmanufacturingmagazine.com/2017/09/boeing-increase-production-787-dreamliner-14-per-month-2019/

MTS Staff. (2018). *Tensile Testing*. Retrieved from MTS - Industry-Leading Testing and Sensing Solutions: https://www.mts.com/en/products/application/materials-testing/cord-fiber-yarn-thread/tensile/index.htm

Nelson, C., McAlea, K., & Gray, D. (1995). *Improvements in SLS Part Accuracy.* Austin, TX: DTM Corporation.

NI Staff. (2018). *CompactDAQ Chasis*. Retrieved from National Instruments Corporate Website: http://www.ni.com/en-us/shop/select/compactdaq-chassis

NI Staff. (2018). *Signal Express*. Retrieved from National Instruments Corporate Website: http://www.ni.com/labview/signalexpress/

NIST Staff. (2009). Shewhart X-bar and R and S Control Charts. In *NIST/Sematech Engineering Statistics Handbook.* National Institute of Standards and Technology.

Omega Staff. (2018). *Fine Diameter (0.01 in. - 0.04 in.) Rugged Thermocouple Transition Joint Probes*. Retrieved from Omega Corporate Website: https://www.omega.com/pptst/TJ36-PFA_CHB.html

Omron Staff. (2018). *E5DC*. Retrieved from Omron Industrial Automation: http://www.ia.omron.com/products/family/3242/

Parrini, P., & Romanini, G. (1976, May). Melt Rheology of some aliphatic polyamides. *Polymer, 17*(5), pp. 377-381.

Perkins, W., & Porter, R. (1981). *Solid-State Extrusion of Nylons 11 and 12: Processing, Morphology and Properties.* J. Mater Sci.

Polymerdatabase. (2018, Jan 13). *Nylon 11 Polyamide*. Retrieved from Polymer Database: http://polymerdatabase.com/polymers/nylon11.html

Rietzel, D., Aquite, W., Drummer, D., & Osswald, T. (2011). Polymer powders for Selective Laser Sintering - Production and Characterization. *Proceedings of the 44th Conference on Manufacturing Systems,* (pp. 1-6). Madison, WI.

Ristic, M., & Milosevic, S. (2006). Frenkel's Theory of Sintering. *Science of Sintering*, 7-11.

Roesler, J., Harders, H., & Baeker, M. (n.d.). *Mechanical Behaviour of Engineering Materials.*

Ruffo, M., Tuck, C., & Hague, R. (2006, May 2). Cost estimation for rapid manufacturing - laser sintering production for low to medium volumes. *J. Engineering Manufacture, 220 Part B*(Proc. IMechE).

Russenberg, S., Schmidt, L., Hosse, H., & H.J., S. (2012). Porosity as a key to increase material properties of laser sintered parts. *Innovative Developments in Virtual and Physical Prototyping*, 531-538.

Schmid, M. L. (2013). Commercial SLS Powders. (p. 8/36). Jacksonville, FL: Additive Manufacturing User's Group.

Schmid, M., Amado, A., & Wegener, K. (2014). Materials perspective of polymers for additive manufacturing with selective laser sintering. *Journal of Materials Research*, 1824-1832.

Schmid, M., Amado, F., Levy, G., & Wegener, K. (2013). Flowability of powders for Selective Laser Sintering investigated by Round Robin Test. *Proceedings of the 6th International Conference on Advanced Research in Virtual and Rapid Prototyping,* (pp. 95-99). Leiria, Portugal.

SME Staff. (2013). *Fundamentals of Manufacturing* (Third ed.). (P. D. Rufe, Ed.) Dearborn, MI: Society of Manufacturing Engineering.

Solidworks Staff. (2018). Retrieved from Dessault Systems Solidworks: www.solidworks.com

Starr, T., Gornet, T., & and Usher, J. (2011). The effect of process conditions on mechanical properties of laser sintered nylon. *Rapid Prototyping Journal*, 418-423.

Starr, T., Gornet, T., Usher, J., & Sherzer, M. (2008). Laser Sintering of PA-11 and PA-12 for Direct Digital Manufacturing. *SFF Symposium.* Austin, TX: The University of Texas at Austin.

TA Instruments Staff. (2018). *TA Instruments.* Retrieved from TA Instruments Thermal Analyzers: http://www.tainstruments.com/pdf/oldDSC.pdf

Tecplot Staff. (2018). *Tecplot 360*. Retrieved from Tecplot Data Visualization & Analysis: https://www.tecplot.com/products/tecplot-360/

The American Society of Mechanical Engineers (ASME). (2018, June 10). *ASME Codes Catalog*. Retrieved from ASME File Server: https://files.asme.org/Catalog/Codes/PDF/35946.pdf

Twisp. (2008, January 21). *Fracture Modes V2*. Retrieved 2011, from en.wikipedia.org: http://en.wikipedia.org/wiki/File:Fracture_modes_v2.svg

Vasquez, M. (2012). *Analysis and Development of New Materials for Polymer Laser Sintering.* Loughborough, UK: Loughborough University.

Vasquez, M., Haworth, B., & Hopkinson, N. (2013). *Methods for quantifying the stable sintering region in laser sintered polyamide-12.* Loughborough, U.K.: Loughborough University Institutional Repository.

Waldron, M. (1978). *Sintering.* London.

Wohlers, T. (2018). *Wohlers Report.* Ft. Collins, CO: Wohlers Associates.

Yuan, M., Bourell, D., & and Diller, T. (2011). Thermal Conductivity Measurements of Polyamide 12. *Solid Freeform Fabrication Symposium.* Austin, TX: The University of Texas at Austin.

Yusoff, W., & Thomas, A. (2008). The effect of employing an effective laser sintering scanning strategy and energy density value on eliminating "orange peel" on a selective laser sintered part. *International Association for Management of Technology*. International Islamic University Malaysia, Faculty of Manufacturing and Materials Engineering and Innovative Manufacturing Research Centre (IMRC), Cardiff University, Wales, UK.

VITA

David Keith Leigh obtained his undergraduate degree in mechanical engineering at The University of Texas at Austin in 1991 and his master’s degree in mechanical engineering in 2011. Upon graduation in 1991, he began a career in laser sintering and additive manufacturing with DTM Corporation. The technologies employed by DTM to design, manufacture, and develop the software, machines, and processes were based on the licensing of laser sintering patents from The University of Texas at Austin. After 5 years, David left DTM to start Harvest Technologies (Harvest) and was involved in the startups of Advanced Laser Materials (ALM), Integra Services (Integra), and 3DSIM. As the industry has grown, these four companies have been acquired: Harvest by Stratasys of Israel and Minnesota; ALM and Integra by EOS of Munich, Germany; and 3DSIM by ANSYS of Pennsylvania.

Permanent address (or email): 500 N. Loop 121, Belton, TX 76513
dkleigh@shinebranch.com

This dissertation was typed by David Keith Leigh.